# The Dynamical Evolution of Perturbed Near-Earth Binary Asteroids

by

**Alex J. Meyer**

B.S., University of Wisconsin Madison, 2019

M.S., University of Colorado Boulder, 2021

A thesis submitted to the
Faculty of the Graduate School of the
University of Colorado in partial fulfillment
of the requirements for the degree of
Doctor of Philosophy
Department of Aerospace Engineering Sciences
2024

Committee Members:
Daniel J. Scheeres, Chair
Jay W. McMahon
Hanspeter Schaub
Derek C. Richardson
Kleomenis Tsiganis

Meyer, Alex J. (Ph.D., Aerospace Engineering Sciences)

The Dynamical Evolution of Perturbed Near-Earth Binary Asteroids

Thesis directed by Prof. Daniel J. Scheeres

Near-Earth binary asteroids are typically comprised of a kilometer-sized rapidly rotating primary asteroid, orbited by a smaller secondary asteroid usually rotating synchronously with the orbit. Owing to the generally non-spherical shapes and proximity of the two asteroids, these systems experience strong spin-orbit coupling. This leads to complex and rich dynamics that are not fully understood, deserving of further study.

Not only are these systems the frequent target of ground-based observations, they are also targets of recent and upcoming missions, including NASA's DART and Lucy missions, and ESA's Hera mission. Due to this recent attention, it is necessary to build a more fundamental and thorough understanding of the dynamics of these systems. Typically, studies focus on the very long-term evolution of these systems. However, observations and missions demand a more in-depth study of the shorter-term dynamics. Furthermore, due to the recent DART mission and the frequent encounters between near-Earth binary asteroids and the terrestrial planets, it is also necessary to develop an understanding of how binary asteroid systems behave once perturbed in order to fully understand these systems.

By developing strategies to better link observations and numerical models of binary asteroids, it is possible to study the dynamics of real-world systems to inform missions and observations. This improves the scientific return from these campaigns. Using this approach, this thesis builds an understanding of the dynamics in a perturbed system, how those dynamics are manifested to an external observer, and how various internal physical parameters lead to those dynamics. This means observations of the orbit period, eccentricity, secondary libration, and orbit precession rate can constrain the physical and dynamical properties of the two asteroids.

This thesis develops models to simulate both the excitation and relaxation of the dynamics within binary asteroids. These are useful for understanding the current dynamical state of these systems. As one example, the near-Earth binary asteroid (35107) 1991VH appears to exist in a dynamically excited state. The application of these models predicts that this dynamical state is the result of a past close Earth encounter. Furthermore, applying models of energy dissipation constrains the physical structure of the secondary in this system, and it is likely relatively inefficient at dissipating energy.

As another case study, many of the analyses used throughout this thesis are directly applicable to NASA's DART mission, the first test of a kinetic impactor for planetary defense. The target of this mission was Dimorphos, the secondary in the binary asteroid (65803) Didymos. This simulation methodology is used to calculate the momentum transfer to the system, satisfying one of the Level One requirements of the mission. Furthermore, studying the short-term dynamics within the Didymos system reveals additional changes. By informing numerical simulations with observations, we conclude the DART impact caused significant reshaping in Dimorphos, as well as inducing significant non-principal axis rotation in the asteroid.

This thesis develops strategies to accurately model the short- and long-term dynamics of binary asteroids informed by real-world observations. These timescales range from days to thousands of years, and the application of these analyses reveals a complex interplay between the physical properties of the two asteroids and the rotational and orbital dynamics of the system. By developing a thorough understanding of the dynamics within these systems, we promote a greater scientific return from observations of and missions to these systems.

# Dedication

To my teachers.

Mom and Dad, my first, best, and most imporant teachers. I cannot thank them enough for their support.

Jacob, who taught me to do what I love, and Adam, who taught me to just be myself.

I was incredibly fortunate to have teachers who believed in me and encouraged me throughout my life. Ms. Wickman, Mr. Garrity, Ms. Demeuse, Ms. Graphos, Mr. Andrews, Ms. Kelly, Mr. Crane, Mr. Krings, Ms. Sparks, Mr. Couch, Ms. Duschek, Mr. Nedobeck, Ms. Counard, Ms. Hoffman, to name a few. They are the ones who put me on this trajectory.

# Acknowledgements

First and foremost, I could not have done this work without the steady guiding hand of my advisor, Dr. Scheeres. He was endlessly patient with my questions, and gave me the freedom and responsibility to run in whatever research direction I wanted at the time. And when I got lost and confused, he was ready and willing to redirect me back onto a sensible direction.

A huge thanks to my committee members, all of whom I have had the privilege of interacting with in either the classroom or research collaborations, sometimes both. They are some of the finest mentors I could ask for.

Another thanks to the DART team, especially Nancy Chabot and Andy Rivkin, who let me take as much responsibility on the mission as I wanted, and who frequently picked up my bar tab. I consider myself extremely fortunate to have been so involved with that mission.

Special thanks to my friends and coworkers within CSML, who made my time in grad school some of the most enjoyable years in my life, even with the pandemic in there. They are all very fine engineers and scientists. I'm lucky to have gotten to work with them.

I had a lot of support from my friends and family around the world and right here in Boulder. During some of the most challenging years of my life, they were always around to get a beer.

Last, and certainly not least, I could not have done this without the support (emotionally, mentally, financially) from my fiancée Lauren. Her patience is incredible.

# Contents

**Chapter**

Appendix

# Tables

**Table**

# Figures

**Figure**

# Chapter 1

# Introduction

In the most general terms, a binary asteroid is any system of two asteroids which are gravitationally bound to one another. The existence of these systems was hypothesized for decades, originally (and inaccurately) as an explanation for rapidly rotating asteroids formed from a collapse of binary asteroids [1]. Concrete evidence for these systems came in 1979 as a result of stellar occultations of asteroids, suggesting the existence of minor planet moons [2]. Shortly after, additional evidence pointed to the existence of these systems, specifically the Trojan asteroid (642) Hektor [3]. While the binary nature of (642) Hektor was not verified until 2006 [4], the existence of binary asteroids was confirmed by the Galileo spacecraft in 1993 during its flyby of (243) Ida en route to Jupiter, where it discovered the asteroid's satellite Dactyl [5].

In the 30 years since the first discovery of binary asteroids, hundreds of these systems have been found throughout the solar system, including near-Earth and main belt asteroids [6], comets [7], Jupiter Trojans [8], Centaurs, [9] and Kuiper belt objects [10]. The physical and dynamical characteristics of binaries are diverse throughout these populations. In this thesis we specifically study the binary asteroids found among near-Earth asteroids (NEAs) and small main-belt asteroids (MBAs). The results obtained in this work can be generalized to the dynamics of binary asteroids throughout the solar system.

NEA and small MBA binaries are overwhelmingly made up of a rapidly rotating primary orbited by a smaller secondary. The primary is usually oblate with a kilometer-scale diameter, while the secondary can be elongated or oblate, usually with a diameter smaller than $\sim 60\%$ of the primary's diameter [6]. Ground-based observations suggest the secondary is usually prolate (having an elongated shape) with an upper limit of $a/b \lesssim 1.5$ for ellipsoidal semiaxes $a > b > c$ [11, 6]. However, these observations are biased against detection of low-elongation secondaries, and the discovery of the nearly perfectly oblate shape of Dimorphos by the DART mission demonstrates the existence of low-elongation secondaries [12]. Regardless of the secondary's elongation, it is almost always found in the tidally locked, 1:1 spin-orbit resonance, usually in a physically circular orbit with a radius of less than 10 primary radii [6]. This state is frequently called the singly synchronous equilibrium, as the secondary is rotating synchronously with the orbit period even though the primary is rotating rapidly.

An example of a typical NEA binary is shown in Fig. 1.1. This shows the radar-derived shape models of (66391) Moshup and its secondary Squannit, one of the best-characterized NEA binaries [13]. The primary is oblate with a characteristic equatorial ridge, while the secondary is more elongated. The primary has an effective diameter of 1.5 km and rotates with a spin period of 2.8 hours. The secondary is in a geometrically circular orbit with a separation distance of 2.5 km and rotates synchronously with the orbit period of 17.4 hours, so that its long axis (equivalently, axis of minimum inertia) is pointing toward the primary. Due to the system's heliocentric orbit, libration in the secondary is possible, where the long axis has small angular deviations away from exactly pointing toward the secondary [13, 14]. This is an example of a very typical NEA binary.

Among NEAs and small MBAs, binary asteroids are relatively common, making up at least 15% of this population [15, 16]. That fraction increases to 65% for fast rotators with a diameter larger than 300 m [16]. Asteroid pairs are binary asteroids which have separated, placing the two asteroids on separate but similar heliocentric orbits [17]. The population fraction of these objects is difficult to calculate, but around one hundred of these objects have been identified [18]. Contact binary asteroids, which are made up of two asteroids that have merged into a bilobed object, make up an additional 30% of NEAs [19]. As these are likely collapsed binary asteroids [20], understanding the evolution of NEA binaries is important for understanding the lifecycle of a large fraction of all NEAs. Given the relatively short 10 Myr expected lifetime of NEAs [21],

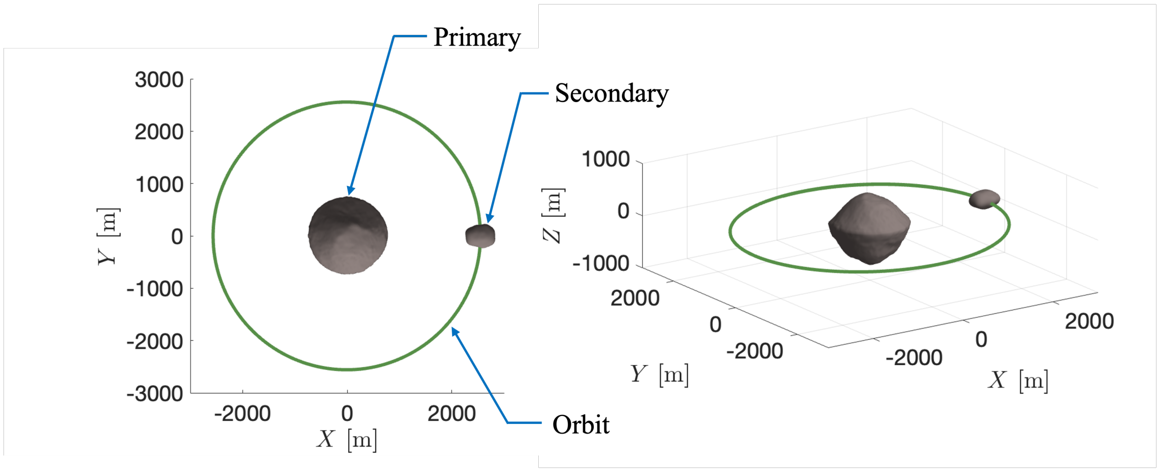

Figure 1.1: An overview of the binary asteroid (66391) Moshup showing (left) a top-down view and (right) an isometric view. The primary is oblate with an equatorial ridge, while the secondary is elongated with its minimum-inertia axis aligned to the primary. The orbit is geometrically circular with a separation distance of $\sim 3$ primary radii.

binary asteroids must have an efficient formation mechanism to maintain this population fraction.

## 1.1 Formation and Evolution

### 1.1.1 Formation

Since their discovery, a wide range of theories have emerged to explain the formation of binary asteroids. These theories mainly rely on the understanding that the overwhelming majority of small ($\lesssim 10$ km) NEAs and MBAs are rubble piles, meaning they are made up of gravitationally bound particles with high bulk porosity between the constituent bodies, rather than a single monolithic body [22]. One of the first major theories of binary asteroid formation relied on tidal disruption of rubble piles by close planetary encounters [23, 24]. In this model, tidal forces can rip apart a rubble pile, resulting in a binary asteroid. However, it was later shown that tidal disruption can only account for $1-2\%$ of NEAs being binaries, and thus a more prevalent formation mechanism is required [25].

Shortly after, another formation model was proposed in which material is shed from the equator of a rapidly rotating rubble pile [26]. This is driven by the YORP effect, in which asymmetric bodies absorb and re-radiate solar radiation resulting in a net torque on the asteroid, causing a spin-up or spin-down of the asteroid [27]. YORP can increase the spin of an object until it becomes structurally unstable, resulting in mass loss which can gradually re-accumulate in orbit as a satellite. A related theory suggests that a secondary could form after a single large landslide event on a rapidly rotating asteroid, in which all the secondary material is put into orbit at once [28, 29]. This version of the theory removes the issue of the inherent randomness of YORP due to its extreme sensitivity to the asteroid's shape [30]. This stochastic YORP torque could significantly extend the required time for binary asteroid formation. Either way, the hypothesis of formation via YORP spin-up is supported by the typically oblate shape and rapid rotation of the primary.

A similar theory of binary formation is through fission of a progenitor asteroid. In this theory, the rapidly rotating primary undergoes tensile failure in which a single chunk of the body is thrown off into orbit [31, 32, 33]. Depending on the mass ratio of the secondary, the system can be energetically unstable and the secondary is ejected from the system forming an asteroid pair [34, 17]. This mass ratio is approximately 0.2, below which the fissioned system is unstable. However, most NEA and small MBA binaries are also below this mass ratio, meaning some form of rapid energy dissipation would be required for small mass ratio binaries to form by fission, such as a secondary fission event [31].

While formation by tidal disruption can be effectively eliminated as a formation mechanism for the majority of binary asteroids, the mass shedding and fission formation events cannot so easily be dismissed. Given the prevalence of these bodies in the NEA population, it is generally accepted that YORP plays a large part in the evolution of rubble piles and the formation of binary asteroids, but the exact details of this process are ambiguous [35]. It's possible all of these pathways are in play, and depending on the material properties of the rapidly spinning body, different evolutionary paths of rubble piles could emerge [36]. In this context, the lines between asteroid pairs, binary asteroids, and contact binary asteroids blur. As such, understanding the evolution of binary asteroids is part of the larger picture of understanding the evolution of rubble pile asteroids as a whole [37].

### 1.1.2 Evolution

Regardless of the formation mechanism, tidal torques within the system tend to rapidly synchronize the secondary's rotation rate with the orbit period, placing the system in the 1:1 spin-orbit resonance [38]. Further energy dissipation via tidal torque will usually reduce the eccentricity of the system and expand the semimajor axis [39]. This is where most, but not all, NEA and small MBA binaries are found: with a rapidly rotating primary and a secondary in a physically circular orbit in the 1:1 spin-orbit resonance. However, despite the relatively rapid rate of energy dissipation within binary asteroids [40], some of these small binaries are still found with eccentric orbits and asynchronous secondaries [6]. The source of these 'excited' systems is unclear, and one topic of this thesis.

Singly synchronous NEA and small MBA binaries typically have a small mass ratio; for larger MBA binaries and binaries found within the Trojans or Kuiper belt, the mass ratio can be closer to unity, suggesting a different formation mechanism altogether. In these systems, the secondary is large enough to impart sufficient tidal torque on the primary such that its spin rate also becomes synchronous with the orbit period. Such a system is called a doubly-synchronous binary, and is the ultimate end-point of energy dissipation [40, 20].

However, because of the small mass ratio within NEA and small MBA binaries, these systems never reach the doubly-synchronous state [20]. But once the secondary becomes synchronized with the orbit period, an imbalance in solar radiation can cause its orbit to expand or shrink [41]. This is essentially an extension of YORP where the secondary effectively acts as an asymmetric appendage of the primary, causing the orbit to spin-up or spin-down; as such this has been termed the binary-YORP (BYORP) effect. BYORP can be either expansive or diminutive, growing or shrinking the semimajor axis. If BYORP is expansive, it works in parallel with tidal dissipation to increase the system's semimajor axis. In these systems, the orbit expands until it becomes wide enough that the torques are no longer strong enough to hold the secondary in synchronous rotation. The secondary then becomes asynchronous, shutting off the BYORP effect and forming a wide asynchronous binary [42]. It is possible the system can resynchronize in the opposite orientation, switching the BYORP effect to cause inward migration.

On the other hand, if inward BYORP is stronger than tides, the system migrates inward, leading to a potential merger between the two bodies [11]. However, there exists a balance between expansive tides and contractive BYORP. When these forces are balanced, the semimajor axis stops its secular evolution and can be constant over long time periods [43]. This is typically called the BYORP-tide equilibrium. However, resonances between the primary's rotation and the orbit period (equivalently the secondary's rotation) can cause this state to eventually become unstable [44].

## 1.2 The Full Two-Body Problem

Given the generally non-spherical shapes of the two asteroids and their proximity in their mutual orbit, the dynamics of binary asteroids are driven by strong spin-orbit coupling [45]. In this dynamical model, the attitude and orbit of the bodies cannot be separated, so the system has 12 degrees of freedom. We call this model the full two-body problem (F2BP), and it is a source of rich and complex dynamics worthy of further study.

The system becomes somewhat simpler if the equations of motion are written in the relative problem using the primary's body-fixed coordinate frame [46]. From here, further simplifications can be made to analytically study the F2BP. Limiting the motion to the planar case is one option, as the assumption that the angular momentum vectors of the primary, secondary, and orbit are all aligned is reasonable. The planar F2BP, derived in [34], can be effectively used to study the singly synchronous equilibrium in which most NEA binaries are found. Unfortunately, this construction necessarily limits the rotation to major principal axis spin. Assuming the primary to be spherical is a separate simplification that allows for an analytic study of the dynamics while allowing for out-of-plane motion and rotation of the secondary [47]. Since the primary in binary asteroids is usually spheroidal, this is another reasonable assumption. This is generally called the sphere-restricted full two-body problem.

Despite these simplifications, a comprehensive analysis of the fully coupled spin-orbit dynamics in binary asteroids has eluded analytic approaches due to the complexity of the full equations of motion. Instead, numerical methods have been developed to study this problem. The first step in solving this problem was the derivation of the mutual gravitational potential between two homogeneous polyhedra [48]. This expansion allows one to numerically calculate the force between two arbitrary bodies modeled as polyhedra at any relative orientation. However, this approach is computationally intensive, particularly for high-fidelity shape models which are required to obtain accurate results. This approach can be generalized to include an arbitrary mass distribution within the bodies [49]. This model was used to complete a comprehensive dynamical study of a binary asteroid, focused on (66391) Moshup [14, 50]. The computational efficiency of this approach was improved by introducing a recursive algorithm to the approximation [51]. Following this, the use of a series expansion of the products of inertia of the two bodies was introduced [52], further improving computational efficiency by removing the need to sum over the entire polyhedral body at every timestep. Using the products of inertia approach in a recursive algorithm then efficiently calculates the mutual potential, force, and torque between two arbitrary rigid bodies [53]. This algorithm was implemented by [54] as the General Use Binary Asteroid Simulator (GUBAS), which is open source and freely available online [55]. GUBAS is the dynamical tool adopted by NASA's DART mission to simulate binary asteroid dynamics [56], and is used heavily in this thesis. GUBAS has been benchmarked against other F2BP codes [56, 57], and while it assumes rigid body dynamics, effects from non-rigid dynamics are shown to have no large impact on the overall system dynamics despite a likely rubble pile structure [58].

A major concern that rises as a result of the spin-orbit coupling in binary asteroids is the orbital dynamics of the system are strongly non-Keplerian [34]. Thus, it is actually unclear how observations of these systems should be incorporated into models. Gound-based observations typically take the form of optical lightcurve measurements [16] or radar range-Doppler measurements [13]. Both strategies provide accurate measurements of the mutual orbital period of a binary asteroid. But because of the non-Keplerian dynamics of these systems, it is ambiguous how these measurements should be used. Furthermore, a physically circular orbit actually has non-zero Keplerian eccentricity [34]. Thus, it requires careful consideration while using ground-based measurements of these systems to inform dynamical modeling, a topic we address in this thesis.

## 1.3 Relevance and Applications

Despite the complexities involved in binary asteroid dynamics, the size of the mutual orbit and relatively rapid orbit period make these systems essentially self-contained laboratories for studies on gravity and the internal structure of asteroids. This was one of the primary reasons the binary asteroid Didymos was selected as the target for the Double Asteroid Redirection Test (DART) mission, which tested the viability of a kinetic impactor for the means of planetary defense [59]. The short orbit period made measurements of the change imparted by DART much easier to measure than a heliocentric orbit [60].

The secular evolution of the orbit can also be used to place constraints on the interior structure and energy dissipation rates of rubble pile asteroids [61]. Furthermore, the gravitational effects of the secondary on the primary can also be used to study seismology and mechanical behavior within rubble piles [62].

The different dynamical states found within NEA binaries can also be used to help understand the evolution of rubble piles. For example, comparing a system in the synchronous equilibrium with one that is dynamically excited can elucidate the parameters that lead down different formation and evolutionary paths. This was one of the primary goals of the Janus mission [63].

All in all, binary asteroids provide excellent opportunities to study the lifecycle of rubble pile asteroids. The ability to leverage the unique dynamics within these systems makes them advantageous for studying the interior structure and mechanics of rubble piles. And the applications for planetary defense range from using these systems as test sites to understanding the requirements of actually deflecting binary asteroids themselves. As a result, binary asteroids have recently been selected as numerous mission targets, including DART [59], Janus [63], Hera [64], and Lucy [65], as well as several mission proposals [66, 67]. While missions offer extremely high quality data of these systems, ground-based observations are also useful strategies for studying these systems.

Indeed, given the relative ease of ground-based observations, this thesis focuses primarily on using ground-based data, with supplements from in-situ spacecraft data.

## 1.4 Dissertation Overview

### 1.4.1 Thesis Statement

The study of near-Earth binary asteroid dynamics enables the detailed interpretation of ground-based observations of these systems, leading to a greater scientific return from observation campaigns and the enabling of new campaigns. This promotes a more thorough understanding of the evolution of binary asteroids over timescales ranging from days to thousands of years.

### 1.4.2 Outline

In Chapter 2, we introduce the full two-body problem and various models used to simulate the dynamics in spin-orbit coupled systems. This chapter also presents three archetypal binary asteroids that will be used throughout this work as case studies to motivate analyses. We also outline a strategy for connecting observations of these systems to dynamical models. Chapter 3 then presents an in-depth discussion of the dynamics of a system once it has been perturbed. This discussion includes the behavior of the orbital elements and the orbit period. We also compare analytic to numeric approaches to modeling these systems. In the spin-orbit coupled system, perturbations to the orbit and spin of the secondary are closely tied together, which we also discuss in this chapter. Then, in Chapter 4, we derive methods of modeling energy dissipation within these systems, and analyze how perturbed binary asteroids return to an equilibrium state. We discuss the effects of close planetary encounters on the dynamics of binary asteroids in Chapter 5, showing the various possible outcomes of a close flyby. We also specifically apply this approach as a possible explanation for the current dynamical state of (35107) 1991VH. In Chapter 6, we apply the tools developed throughout this thesis to the DART mission's kinetic impact of (65803) Didymos. This demonstrates the practical application of this research, and presents interesting findings on the current dynamical state of the system. Finally, we conclude and discuss future work in Chapter 7.

### 1.4.3 Contributions

This research is focused on modeling and understanding the dynamics of binary asteroids, and we have made several contributions toward this goal. Importantly, the development of a strategy for connecting observations to models, along with an algorithm implementing this strategy, allows us to accurately model real-world binary asteroid systems outside of the traditional Keplerian treatment of these systems, which is inaccurate. As a result of this approach, we are able to model the dynamical history of (35107) 1991VH to investigate the cause of its current dynamical state, as well as modeling the DART impact into (65803) Didymos, which was used to calculate the momentum enhancement factor of the impact, completing one of the level one requirements of the mission.

Other contributions include developing a thorough understanding of how different parameters within the system are manifested in ground-based observations. This improves the scientific return of observation campaigns by providing context to the dynamical behaviors that may appear in these systems, and the cause of those behaviors. This was used to determine the level of reshaping within Dimorphos, the DART target, as the apsidal precession rate of the orbit is directly connected to the shape and spin of the secondary. We also investigated the relationship between the orbit and libration within a binary asteroid, so accurate measurements can constrain the inertias of the secondary by relating these periods.

Another contribution we made is applying energy dissipation models to binary asteroids to study their secular evolution. This is a key contribution for the Hera mission, which may be able to measure energy dissipation rates within Didymos by applying this model. In turn, this constrains the internal structure of the asteroid, which is poorly understood for rubble piles.

We also developed a high-fidelity model for simulating the effect of gravitational third-bodies on the internal dynamics of binary asteroids. This is useful for understanding the effect of solar gravity, as well as more dramatic close planetary encounters. The latter is especially useful, as

NEAs are dominated by close encounters with the terrestrial planets.

One of the major contributions of this thesis is the application to the DART mission. Using our approach, we calculated the post-impact orbit in Didymos and determined that Dimorphos was globally reshaped by the impact and is likely currently in a state of rotational instability. This is another important consideration for the Hera mission, which will perform proximity operations around this secondary.

By developing models to study the perturbed dynamics within near-Earth binary asteroids, we have gained a thorough understanding of the evolution of these systems. The strategies and understanding developed in this thesis can be applied to any binary asteroid system to better understand its past, current, and future dynamical state.

### 1.4.4 Publications

The following is a list of publications, including peer-reviewed journal articles and letters, along with conference papers, posters, and talks.

#### 1.4.4.1 Journal publications

(1) **Meyer, A. J.**, & Scheeres, D. J. (2024). The Strength and Shapes of Contact Binary Objects. The Astrophysical Journal Letters, 963(1), L14.

(2) Pravec, P., **Meyer, A. J.**, Scheirich, P., Scheeres, D. J., Benson, C., & Agrusa, H. F. (2024). Rotational Lightcurves of Dimorphos and Constraints on its Post-DART Impact Spin State. Icarus, 418, 116138.

(3) Naidu, S. P., Chesley, S. R., Moskovitz, N., Thomas, C., **Meyer, A. J.**, Pravec, P., ... & Chabot, N. L. (2024). Orbital and physical characterization of asteroid dimorphos following the DART impact. The Planetary Science Journal, 5(3), 74.

(4) Chabot, N. L., Rivkin, A. S., Cheng, A. F., Barnouin, O. S., Fahnestock, E. G., Richardson, D. C., ...**Meyer, A. J.**, .... & Zhang, Y. (2024). Achievement of the planetary defense

investigations of the Double Asteroid Redirection Test (DART) mission. The Planetary Science Journal, 5(2), 49.

(5) Cueva, R. H., McMahon, J. W., **Meyer, A. J.**, Scheeres, D. J., Hirabayashi, M., Raducan, S. D., ... & Merrill, C. C. (2024). The Secular Dynamical Evolution of Binary Asteroid System (65803) Didymos Post-DART. The Planetary Science Journal, 5(2), 48.

(6) Scheirich, P., Pravec, P., **Meyer, A. J.**, Agrusa, H. F., Richardson, D. C., Chesley, S. R., ... & Moskovitz, N. A. (2024). Dimorphos Orbit Determination from Mutual Events Photometry. The Planetary Science Journal, 5(1), 17.

(7) Agrusa, H. F., Zhang, Y., Richardson, D. C., Pravec, P., Ćuk, M., Michel, P., ...**Meyer, A. J.**... & Sánchez, P. (2024). Direct $N$-body simulations of satellite formation around small asteroids: insights from DART's encounter with the Didymos system. The Planetary Science Journal, 5(2), 54.

(8) **Meyer, A. J.**, Agrusa, H. F., Richardson, D. C., Daly, R. T., Fuentes-Muñoz, O., Hirabayashi, M., ... & Scheeres, D. J. (2023). The Perturbed Full Two-Body Problem: Application to Post-DART Didymos. The Planetary Science Journal, 4(8), 141.

(9) Cheng, A. F., Agrusa, H. F., Barbee, B. W., **Meyer, A. J.**, Farnham, T. L., Raducan, S. D., ... & Zanotti, G. (2023). Momentum transfer from the DART mission kinetic impact on asteroid Dimorphos. Nature, 616(7957), 457-460.

(10) **Meyer, A. J.**, Scheeres, D. J., Agrusa, H. F., Noiset, G., McMahon, J., Karatekin, Ö., ... & Nakano, R. (2023). Energy dissipation in synchronous binary asteroids. Icarus, 391, 115323.

(11) Fuentes-Muñoz, O., **Meyer, A. J.**, & Scheeres, D. J. (2022). Semi-analytical near-Earth objects propagation: the orbit history of (35107) 1991 VH and (175706) 1996 FG3. The Planetary Science Journal, 3(11), 257.

(12) Agrusa, H. F., Ballouz, R., **Meyer, A. J.**, Tasev, E., Noiset, G., Karatekin, Ö., ... & Hirabayashi, M. (2022). Rotation-induced granular motion on the secondary component of binary asteroids: Application to the DART impact on Dimorphos. Astronomy & Astrophysics, 664, L3.

(13) Richardson, D. C., Agrusa, H. F., Barbee, B., Bottke, W. F., Cheng, A. F., Eggl, S., ...**Meyer, A. J.**... & Zhang, Y. (2022). Predictions for the Dynamical States of the Didymos System before and after the Planned DART Impact. The planetary science journal, 3(7), 157.

(14) Nakano, R., Hirabayashi, M., Agrusa, H. F., Ferrari, F., **Meyer, A. J.**, Michel, P., ... & Zhang, Y. (2022). NASA's Double Asteroid Redirection Test (DART): mutual orbital period change due to reshaping in the near-earth binary asteroid system (65803) Didymos. The planetary science journal, 3(7), 148.

(15) **Meyer, A. J.**, Gkolias, I., Gaitanas, M., Agrusa, H. F., Scheeres, D. J., Tsiganis, K., ... & Michel, P. (2021). Libration-induced orbit period variations following the DART impact. The planetary science journal, 2(6), 242.

(16) Agrusa, H. F., Gkolias, I., Tsiganis, K., Richardson, D. C., **Meyer, A. J.**, Scheeres, D. J., ... & Davis, A. B. (2021). The excited spin state of Dimorphos resulting from the DART impact. Icarus, 370, 114624.

(17) **Meyer, A. J.**, & Scheeres, D. J. (2021). The Effect of Planetary Flybys on Singly Synchronous Binary Asteroids. Icarus, 367, 114554.

#### 1.4.4.2 Papers in Revision or in Preparation

(1) Richardson, D. C., Agrusa, H. R., Barbee, B., Cueva, R. C., Ferrari, F., Jacobson, S. A., ... **Meyer, A. J.**... & Zannoni, M. (2024). The Dynamical State of the Didymos System Before and After the DART Impact. Accepted to The Planetary Science Journal.

(2) **Meyer, A. J.**, & Scheeres, D. J. (2024). Apsidal Precession in Binary Asteroids. Accepted to Astronomy & Astrophysics.

(3) **Meyer, A. J.**, Fuentes-Muñoz, O., Gkolias, I., Tsiganis, K., Pravec, P., Naidu, S., & Scheeres, D. J. (2024). An Earth Encounter as the Cause of Chaotic Dynamics in Binary Asteroid (35107) 1991VH. Submitted.

(4) Bottke, W. F., **Meyer, A. J.**, Vokrouhlický, D., Nesvorný, D., Bierhaus, B., Hoover, R., ... & Lauretta, D. (2024). Surface Ages for the Sample Return Asteroids Bennu, Ryugu, and Itokawa. In Prep.

#### 1.4.4.3 Conference Papers, Presentations, and Posters

(1) Meyer, A. J., Pravec, P., Scheirich, P., Benson, D., & Scheeres, D. J. (2024). "The Rotational State of Dimorphos After the DART Impact." In AAS/Division of Dynamical Astronomy Meeting. **Awarded Duncombe Prize**.

(2) Meyer, A. J., & Scheeres, D. J. (2024). "The Strength and Shapes of Contact Binaries." LPI Contributions, 3040, 1518

(3) Meyer, A. J., & Scheeres, D. J. (2024). "The Transient Dynamical Evolution of Near-Earth Binary Asteroids." 30th Meeting of the NASA Small Bodies Assesment Group. **Early Career Invited Talk**.

(4) Meyer, A. J., Pravec, P., Scheirich, P., Gkolias, I., Tsiganis, K., . . . , & Scheeres, E. J. (2023). "The Dynamical Evolutoin of the Chaotic Binary Asteroid (35107) 1991VH." In Asteroids, Comets, and Meteors.

(5) Meyer, A. J., Agrusa, H. F., Barbee, B., Gkolias, I., Tsiganis, K., . . . , & Scheeres, D. J. (2023). "Leveraging Observations to Model the Dynamics of the Didymos System After the DART Impact." In AAS/Division of Dynamical Astronomy Meeting. **Invited talk**.

(6) Meyer, A. J., Gkolias, I., Tsiganis, K., Noiset, G, Karatekin, Ö., . . . , & Scheeres, D. J. (2023). “Energy Dissipation in Didymos Prior to Hera’s Arrival.” In 8th IAA Planetary Defense Conference

(7) Meyer, A. J., Noiset, G., Karatekin, Ö., McMahon, J., Agrusa, H. F., Nakano, R., ... & Scheeres, D. J. (2023). ”Tidal Dissipation in Didymos Following the DART Impact.” LPI Contributions, 2806, 2105.

(8) Meyer, A. J., & Scheeres, D. J. (2023). ”The Transient Dynamical Evolution of Near-Earth Binary Asteroids.” AAS/Division for Planetary Sciences Meeting Abstracts. Vol. 55. No. 8.

(9) Meyer, A. J., Scheeres, D. J., Gkolias, I., Gaitanas, M., Tsiganis, K., Agrusa, H. F., ... & Sanchez, P. (2022). ”Orbit Period Variations of Dimorphos After the DART Impact.” In AGU Fall Meeting Abstracts (Vol. 2022, pp. P55F-1633).

(10) Meyer, A. J., Gkolias, I., Tsiganis, K., Scheeres, D., Naidu, S., Pravec, P., & Benson, C. (2022). “Chaotic Rotation in Binary Asteroids.” In AAS/Division for Planetary Sciences Meeting Abstracts (Vol. 54, No. 8, pp. 202-05).

(11) Meyer, A. J., & Scheeres, D. J. (2022). “Dissipation of energy in Didymos following the DART impact.” 44th COSPAR Scientific Assembly. Held 16-24 July, 44, 182.

(12) Meyer, A. J., Scheeres, D., & Benson, C. (2022). “Modeling the Chaotic Dynamics of Binary Asteroid 1991 VH.” In AAS/Division of Dynamical Astronomy Meeting (Vol. 54, No. 4, pp. 200-03).

(13) Meyer, A. J., Scheeres, D. J., Gkolias, I. G., Gaitanas, M., Agrusa, H. F., ... & Michel, P. (2022). “Libration-Induced Orbit Period Variations Following the DART Impact.” LPI Contributions, 2678, 2225.

(14) Meyer, A. J., and Scheeres, D. J. (2022) ”Estimation of Binary Asteroid Gravity Using Mutual Orbit Observations.” AIAA Scitech Forum.

(15) Meyer, A., Scheeres, D., Gkolias, I., Agrusa, H., & Tsiganis, K. (2021). “Libration and Orbit Period Variation in Didymos Following the DART Impact.” In AAS/Division for Planetary Sciences Meeting Abstracts (Vol. 53, No. 7, pp. 113-03).

(16) Meyer, A. J., Scheeres, D. J., Naidu, S., Benner, L., Pravec, P., & Scheirich, P. (2021). “Modeling Fully Coupled Dynamics of Janus Binary Asteroid Mission Targets.” In AAS/Division of Dynamical Astronomy Meeting (Vol. 53, No. 5, pp. 405-06).nse Conference (p. 232).

(17) Meyer, A. J., & Scheeres, D. J. (2021). ”The Effect of Planetary Flybys on Singly Synchronous Binary Asteroids.” In 7th IAA Planetary Defense Conference (p. 232).

(18) Meyer, A. J., & Scheeres, D. J. (2020) ”Formations with frozen relative orbits in the presence of strong solar radiation pressure.” Astrodynamics Specialist Conference.

(19) Meyer, A. J., & Scheeres, D. J. (2020). “The Effect of Planetary Flybys on Singly Synchronous Binary Asteroids.” In AAS/Division for Planetary Sciences Meeting Abstracts (Vol. 52, No. 6, pp. 217-02).

# Chapter 2

# Dynamical Models and Case Studies

## 2.1 Introduction

The study of spin-orbit coupling and the full two-body problem (F2BP) dates back to the study of the Earth-moon system and explanations for the moon's libration [68]. A complete description of the motion in systems governed by spin-orbit coupling requires 12 degrees of freedom (3 rotational and 3 translational for each body), and the equations describing the rotational and translational motion cannot be separated from one another [45]. Close binary asteroids are governed by these equations given their proximity and irregular shapes. In this chapter, we present the mathematical equations of the F2BP, as well as certain simplifications that allow us to to perform analytical investigations and improve computational efficiency. In a study of the equilibrium configuration within the F2BP, we will find these systems are non-Keplerian. To handle this difficulty, we will introduce a set of 'observable elements' that can be used to connect observations of binary asteroids to numerical modeling. By using observations of the mutual orbit period to calculate the mass of these systems, we will demonstrate the importance of considering these non-Keplerian effects. Finally, we will introduce 3 binary asteroid systems that will be used as case studies throughout this thesis: (175706) 1996 FG3 as an example of a system in equilibrium, (65803) Didymos as an example of a recently perturbed system, and (35107) 1991 VH as an example of a system experiencing chaotic dynamics.

## 2.2 The Full Two-Body Problem

In general, the gravitational potential energy between two arbitrary rigid bodies is written as

$$U = \int_A \int_B \left( \frac{\mathrm{d}m_A \mathrm{d}m_B}{|\vec{r} + \mathbf{C_B}\vec{r}_B - \mathbf{C_A}\vec{r_A}|} \right), \tag{2.1}$$

where $\vec{r}$ tracks the barycenter of body $B$ with respect to the barycenter of body $A$, $dm_A$ and $dm_B$ are infinitesimal mass elements in body $A$ and $B$, respectively, and $\mathbf{C_A}$ and $\mathbf{C_B}$ are the tensors transforming a vector in the body-fixed coordinates of $A$ and $B$ to the inertial frame, respectively. An illustration of these components is shown in Fig. 2.1.

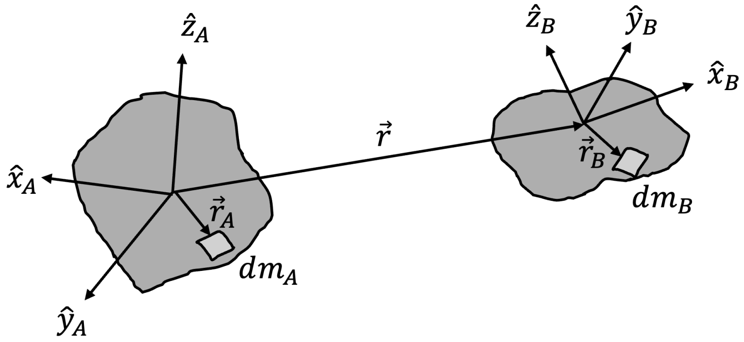

Figure 2.1: Graphic of the F2BP, showing the primary (body $A$), secondary (body $B$), their respective body-fixed coordinates, and their relative position. Infinitesimal mass elements are shown in each body, along with their location relative to the body's barycenter.

Thus, inherently we have defined 3 frames for this problem, two body-fixed and one inertial. These are formally defined as,

$$\mathcal{A} : [\mathcal{O}_A; \hat{x}_A, \hat{y}_A, \hat{z}_A], \tag{2.2}$$

$$\mathcal{B} : [\mathcal{O}_B; \hat{x}_B, \hat{y}_B, \hat{z}_B], \tag{2.3}$$

$$\mathcal{N} : [\mathcal{O}_A; \hat{x}, \hat{y}, \hat{z}]. \tag{2.4}$$

The origin of each frame is denoted by $\mathcal{O}_A$ or $\mathcal{O}_B$, which correspond to the barycenter of $A$ and $B$ respectively. Note we have attached our inertial frame to the barycenter of the primary, in anticipation of reducing the problem to the relative system. These frames are used to easily construct the transformation tensors,

$$\mathbf{C_A} = [\hat{x}_A, \hat{y}_A, \hat{z}_A], \tag{2.5}$$

$$\mathbf{C_B} = [\hat{x}_B, \hat{y}_B, \hat{z}_B]. \tag{2.6}$$

### 2.2.1 Equations of Motion

In the most general, frame-agnostic form, the equations of motion are defined as

$$\ddot{\vec{r}} = -\frac{1}{m}\frac{\partial U}{\partial \vec{r}}, \tag{2.7}$$

$$\dot{\vec{L}}_A = \vec{M}_A, \tag{2.8}$$

$$\dot{\vec{L}}_B = \vec{M}_B, \tag{2.9}$$

where $m$ is the reduced mass defined as

$$m = \frac{m_A m_B}{m_A + m_B}. \tag{2.10}$$

$\vec{L}_A$ is the angular momentum of body $A$ and similarly for $\vec{L}_B$ with body $B$. $\vec{M}_A$ is the torque on $A$ caused by $B$, and vice versa for $\vec{M}_B$.

A more useful form of equations describing the F2BP were derived for the relative problem, in which we describe our system in the body-fixed frame of the primary, eliminating three degrees of freedom [46, 53]. These equations are easier to implement in numerical algorithms. In this construction, the equations of motion are,

$$\ddot{\vec{r}} = -\dot{\vec{\omega}}_A \times \vec{r} - 2\vec{\omega}_A \times \dot{\vec{r}} - \vec{\omega}_A \times \vec{\omega}_A \times \vec{r} - \frac{1}{m}\frac{\partial U}{\partial \vec{r}}, \tag{2.11}$$

$$\dot{\vec{L}}_A = \vec{L}_A \times \vec{\omega}_A + \vec{M}_A, \tag{2.12}$$

$$\dot{\vec{L}}_B = \vec{L}_B \times \vec{\omega}_A + \vec{M}_B. \tag{2.13}$$

In Eqs. 2.11 - 2.13 the dot indicates a time derivative taken in the $\mathcal{A}$ frame.

Evaluation of the mutual potential between two arbitrary bodies is difficult. For this reason, we use GUBAS to integrate the F2BP equations of motion. This uses the algorithm developed in [53] to evaluate the mutual potential and its derivatives up to an arbitrary degree-and-order.

### 2.2.2 Planar F2BP

One of the most useful simplifications to the F2BP comes in the form of limiting the system to planar motion. Under this assumption, the angular momentum of the primary, secondary, and orbit are all colinear, and the translation and rotation of the bodies occurs in the plane perpendicular to these momenta vectors. We can make an additional assumption of purely elllipsoidal bodies to allow us a more in-depth investigation of the F2BP. This formulation is especially useful for studying the equilibrium configuration of binary asteroids, as the singly synchronous configuration equilibrium only consists of planar motion and rotation. A diagram of this system is shown in Fig. 2.2. In this problem we have reduced the system to only 4 degrees of freedom: the relative separation and rotation of the system, along with the relative orientation of the two bodies.

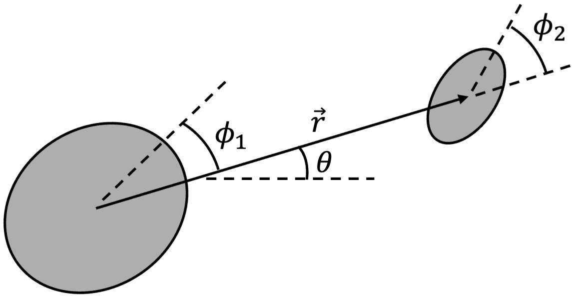

Figure 2.2: Graphic of the planar F2BP, showing the relative position and orientation of the two ellipsoids.

With these simplifications, we can write the second degree-and-order potential energy in a relatively simple form [34],

$$\begin{aligned} U(r, \phi_1, \phi_2) = -\frac{\mathcal{G} m_A m_B}{r} \Bigg[ 1 + \frac{1}{2r^2} \bigg( &\mathrm{Tr}(\bar{\mathbf{I}}_A) + \mathrm{Tr}(\bar{\mathbf{I}}_B) - \frac{3}{2} \big[ \bar{I}_{A,x} + \bar{I}_{A,y} \\ &- \cos 2\phi_1 (\bar{I}_{A,y} - \bar{I}_{A,x}) + \bar{I}_{B,x} + \bar{I}_{B,y} - \cos 2\phi_2 (\bar{I}_{B,y} - \bar{I}_{B,x}) \big] \bigg) \Bigg]. \end{aligned} \tag{2.14}$$

Note the potential energy is independent of the angle $\theta$. The bar over the inertias indicates mass-normalized, and the subscripts $x$, $y$, and $z$ correspond to the minimum, intermediate, and maximum principal inertia values.

The kinetic energy is

$$T = \frac{1}{2} I_{A,z} (\dot{\phi}_1 + \dot{\theta})^2 + \frac{1}{2} I_{B,z} (\dot{\phi}_2 + \dot{\theta})^2 + \frac{1}{2} m \dot{r}^2 + \frac{1}{2} m (r\dot{\theta})^2, \tag{2.15}$$

and using the Lagrangian $L = T - U$, we obtain the equations of motion of the planar-ellipsoid system [34]. These equations are

$$\ddot{r} = \dot{\theta}^2 r \frac{1}{m} \frac{\partial U}{\partial r} \tag{2.16}$$

$$\ddot{\phi}_1 = -\left(1 + \frac{mr^2}{I_{A,z}}\right) \frac{1}{mr^2} \frac{\partial U}{\partial \phi_1} - \frac{1}{mr^2} \frac{\partial U}{\partial \phi_2} + 2\frac{\dot{r}\dot{\theta}}{r} \tag{2.17}$$

$$\ddot{\phi}_2 = -\left(1 + \frac{mr^2}{I_{B,z}}\right) \frac{1}{mr^2} \frac{\partial U}{\partial \phi_2} - \frac{1}{mr^2} \frac{\partial U}{\partial \phi_1} + 2\frac{\dot{r}\dot{\theta}}{r} \tag{2.18}$$

$$\ddot{\theta} = \frac{1}{mr^2} \left( \frac{\partial U}{\partial \phi_1} + \frac{\partial U}{\partial \phi_2} \right) - 2\frac{\dot{r}\dot{\theta}}{r}. \tag{2.19}$$

As we will see later, this formulation is useful for studying the system's equilibrium dynamics. However, the major shortfall of this simplification is that it ignores any out-of-plane motion, particularly any non-principal axis (NPA) rotation of the secondary, which is an important characteristic of the perturbed dynamics of binary asteroids. Another shortfall is these equations are limited to studying the motion of two ellipsoids under the influence of their mutual second degree-and-order gravity field, which restricts the possible applications of this model.

### 2.2.3 Sphere-restricted F2BP

Another useful simplification of the F2BP is the sphere-restricted F2BP, in which we consider one of the two bodies to be a sphere [69]. This system is shown in Fig. 2.3, illustrating that we now consider the central body to be the non-spherical body. In practice, we usually assign the non-spherical body to the secondary, since the primary is roughly spheroidal in most systems. This means the equations of motion for this system are written in the secondary's body-fixed frame.

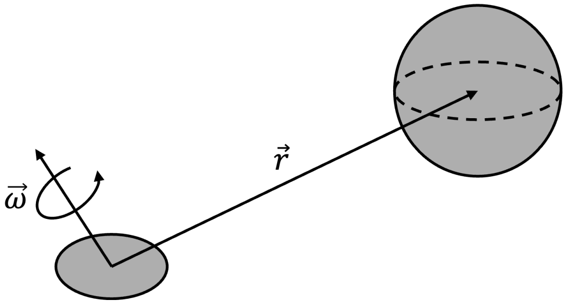

Figure 2.3: Graphic of the sphere-restricted F2BP, showing the relative position of the two bodies and the rotation of the non-spherical body.

These equations are simply written for the non-inertial body-fixed frame of the secondary [69],

$$\ddot{\vec{r}} + 2\vec{\omega}_B \times \dot{\vec{r}} + \dot{\vec{\omega}}_B \times \vec{r} + \vec{\omega}_B \times (\vec{\omega}_B \times \vec{r}) = \frac{\mathcal{G}}{m}\frac{\partial U}{\partial \vec{r}} \tag{2.20}$$

$$\mathbf{I}_B\dot{\vec{\omega}}_B + \vec{\omega}_B \times \mathbf{I}_B\vec{\omega}_B = \mathcal{G}\vec{r} \times \frac{\partial U}{\partial \vec{r}}. \tag{2.21}$$

These equations are written for any arbitrary shape of the secondary. However, for this simplified system, it generally does not make sense to use a secondary shape more complicated than an ellipsoid. Taking the secondary as an ellipsoid, its potential energy can be written using MacCullagh's formula for a second degree-and-order gravity field [70],

$$U = -\frac{\mathcal{G}m_A m_B}{r} - \frac{\mathcal{G}m_A(\bar{I}_{B,x} + \bar{I}_{B,y} + \bar{I}_{B,z} - 3\Phi)}{2r^3} \tag{2.22}$$

where

$$\Phi = \frac{\bar{I}_{B,x}x^2 + \bar{I}_{B,y}y^2 + \bar{I}_{B,z}z^2}{r^2} \tag{2.23}$$

with the location of the spherical primary denoted by the cartesian coordinates $x$, $y$, $z$ defined in the secondary's body-fixed frame. Alternatively, a more accurate representation of the potential energy could be used, for example spherical harmonics [70].

While the benefit of the sphere-restricted F2BP is the consideration of the full three-dimensional rotation of the secondary, this representation also has drawbacks. Namely, we cannot consider any shape effects of the primary, which could be problematic as the primary is usually oblate which affects both the instantaneous and secular dynamics of the system (i.e. the orbit precession).

### 2.2.4 Equilibrium Dynamics

In studying the equilibria of the F2BP, we focus on the planar F2BP equations of motion. These have been defined and studied in [34], and we briefly summarize the conditions here for completion. In an equilibrium, we require all partial derivatives of the total energy to equal zero [69]. These partials are

$$E_r = -mr\frac{h^2 - (I_{A,z}\dot{\phi}_1 + I_{B,z}\dot{\phi}_2)^2}{I_z^2} + U_r \tag{2.24}$$

$$E_{\phi_i} = U_{\phi_i} \tag{2.25}$$

$$E_{\dot{r}} = m\dot{r} \tag{2.26}$$

$$E_{\dot{\phi}_i} = I_{i,z}\dot{\phi}_i - \frac{I_{i,z}(I_{A,z}\dot{\phi}_1 + I_{B,z}\dot{\phi}_2)}{I_z} \tag{2.27}$$

where $h$ is the total angular momentum of the system and $I_z = I_{A,z} + I_{B,z} + mr^2$ is the total moment of inertia of the system about the $z-$axis. The total angular momentum is equal to

$$h = I_z\dot{\theta} + I_{A,z}\dot{\phi}_1 + I_{B,z}\dot{\phi}_2. \tag{2.28}$$

In an equilibrium, we have all velocities equal to zero: $\dot{r} = \dot{\phi}_1 = \dot{\phi}_2 = 0$, which immediately satisfies our requirements $E_{\dot{r}} = 0$ and $E_{\dot{\phi}_i} = 0$. Next we calculate the partials of the potential energy,

$$\begin{aligned} U_r = \frac{\mathcal{G}m_A m_B}{r^2}\Bigg[1 + \frac{3}{2r^2}\Bigg(&\mathrm{Tr}(\bar{\mathbf{I}}_A) + \mathrm{Tr}(\bar{\mathbf{I}}_B) - \frac{3}{2}\big[\bar{I}_{A,x} + \bar{I}_{A,y} \\ &- \cos 2\phi_1(\bar{I}_{A,y} - \bar{I}_{A,x}) + \bar{I}_{B,x} + \bar{I}_{B,y} - \cos 2\phi_2(\bar{I}_{B,y} - \bar{I}_{B,x})\big]\Bigg)\Bigg]. \end{aligned} \tag{2.29}$$

$$U_{\phi_i} = \frac{3\mathcal{G}m_A m_B}{2r^3}\sin 2\phi_i(I_{i,y} - I_{i,x}). \tag{2.30}$$

From the requirement $E_{\phi_i} = 0$, this tells us in an equilibrium we have $\phi_i = 0, \pm\pi/2, \pi$, meaning the principal axes of the two bodies are aligned. Our final constraint, $E_r = 0$, will allow us to calculate the spin rate of the system for a given separation to place us in an equilibrium. Since we have now $h = I_z\dot{\theta}$, we obtain

$$\begin{aligned}\dot{\theta}^{*2} = \frac{\mathcal{G}(m_A + m_B)}{r^3}\Bigg[1 + \frac{3}{2r^2}\Bigg(&\mathrm{Tr}(\bar{\mathbf{I}}_A) + \mathrm{Tr}(\bar{\mathbf{I}}_B) - \\ &\frac{3}{2}\left[\bar{I}_{A,x} + \bar{I}_{A,y} - \pm_1(\bar{I}_{A,y} - \bar{I}_{A,x}) + \bar{I}_{B,x} + \bar{I}_{B,y} - \pm_2(\bar{I}_{B,y} - \bar{I}_{B,x})\right]\Bigg)\Bigg],\end{aligned} \tag{2.31}$$

giving us four potential equilibrium configurations depending on $\phi_1$ and $\phi_2$. These are discussed in [34], who demonstrates that the stable equilibrium occurs when the minimum principal-inertia directions of the two bodies are aligned ($\phi_1 = \phi_2 = 0$).

However, we note this is for the doubly-synchronous system. Among NEAs, this tidal end state is not reached, as the primary is rotating rapidly. This will lead us to a slightly modified equilibrium condition. We assume the primary's rapid rotation averages out, so we set $I_{A,x} = I_{A,y} = I_{A,s}$, approximating the primary as a spheroid. Under this assumption, we can write

$$\dot{\theta}^{*2} = \frac{\mathcal{G}(m_A + m_B)}{r^3}\left(1 + \frac{3}{2r^2}\left(\bar{I}_{A,z} - \bar{I}_{A,s} + \bar{I}_{B,y} + \bar{I}_{B,z} - 2\bar{I}_{B,x}\right)\right) \tag{2.32}$$

for the energetically stable equilibrium. Most notably, this is not equal to the mean motion even though we have $\dot{r} = 0$. This tells us the secondary is trapped at either periapsis or apoapsis depending on the system's moments of inertia, and the orbit precesses at this rate [34]. Specifically, if $\bar{I}_{A,z} + \bar{I}_{B,y} + \bar{I}_{B,z} > \bar{I}_{A,xy} + 2\bar{I}_{B,x}$, then $\dot{\theta}^* > \sqrt{\mu/r^3}$, the secondary is trapped at periapsis, and the orbit precesses faster than the Keplerian circular orbit rate. Alternatively, if $\bar{I}_{A,z} + \bar{I}_{B,y} + \bar{I}_{B,z} < \bar{I}_{A,xy} + 2\bar{I}_{B,x}$, we have the opposite case: the secondary is trapped at apoapsis and the orbit precesses slower than the Keplerian circular orbit rate. In this work we focus on the former, where the secondary is trapped at periapsis, but in either case, the true anomaly is constant (equal to 0 or $\pi$) while the argument of periapsis tracks the secondary. For typical shapes of binaries, the secondary is trapped at periapsis.

This implies the orbit will have non-zero Keplerian eccentricity at equilibrium, despite being physically circular. For a system trapped at periapsis, the equilibrium Keplerian eccentricity is calculated from the orbit angular momentum and energy as [34, 71]

$$e^*_{\text{Kep}} = \frac{3(\bar{I}_{A,z} - \bar{I}_{A,xy} - 2\bar{I}_{B,x} + \bar{I}_{B,y} + \bar{I}_{B,z})}{2r^2}, \tag{2.33}$$

while the equilibrium Keplerian semimajor axis is [34, 71]

$$a^*_{\text{Kep}} = r\left(1 - \frac{3(\bar{I}_{A,z} - \bar{I}_{A,xy} - 2\bar{I}_{B,x} + \bar{I}_{B,y} + \bar{I}_{B,z})}{2r^2}\right)^{-1}. \tag{2.34}$$

This semimajor axis is larger than the separation distance in the physically circular orbit owing to the spin-orbit coupling as long as $\bar{I}_{A,z} + \bar{I}_{B,y} + \bar{I}_{B,z} > \bar{I}_{A,xy} + 2\bar{I}_{B,x}$, i.e. the secondary is trapped at periapsis.

Here we begin to see the problem of modelling the system's dynamics as Keplerian, and the disconnect between dynamical models and observations of these systems. For a system in equilibrium, an observer would see a constant separation distance between the two asteroids, and in orbit fitting set the eccentricity equal to 0 and the semimajor axis equal to the separation distance. This then leads to erroneous mass estimates of the system while ignoring the effects of the non-spherical bodies. Thus, we require an effective strategy for summarizing the dynamics of these systems consistent with the bodies' masses.

## 2.3 Case Study Systems

Throughout this thesis, we will primarily focus on three specific NEA binaries to illustrate examples. These three systems, (175706) 1996FG3, (65803) Didymos, and (35107) 1991VH each represent a distinctly different dynamical regime among NEAs. 1996FG3 is an example of a system in the singly synchronous spin-orbit resonance with its secondary in the BYORP-tide equilibrium [72]. Didymos is a system previously in the singly synchronous spin-orbit resonance, but experienced a recent perturbation in the form of the DART impact [60, 73, 74, 75]. 1991 VH is a system with its secondary rotating asynchronously and likely experiencing NPA rotation, resulting in an exchange of angular momentum between the orbit and the secondary [6, 76, 77, 78]. These three systems are all well characterized since they have all been selected as mission targets [59, 63].

### 2.3.1 1996FG3

1996FG3 is a NEA binary with its secondary in the 1:1 spin-orbit resonance, likely in the BYORP-tide equilibrium, meaning its semimajor axis is not secularly evolving [72]. The radar-derived polyhedral shape model of the primary and secondary are shown in Fig. 2.4 (L. Benner, *Private Communication*), making 1996FG3 one of only a few binary asteroids for which a shape model of the secondary exists.

The mutual orbit period is 16.15 h with a semimajor axis of 2433 m and no eccentricity [6, 72]. The primary has a spin period of 3.49 h, and the secondary's rotation period is equal to the orbit period. The volume-equivalent diameter is 1900 m for the primary and 500 m for the secondary.

Using these measurements of semimajor axis and eccentricity as the observable elements, and the orbit period as the stroboscopic orbit period, we obtain an estimate of the system's bulk density of 0.7 g/cm$^3$. This low density is consistent with a rubble pile, but may be under-estimated as the primary's shape model likely over-estimates the volume of the primary.

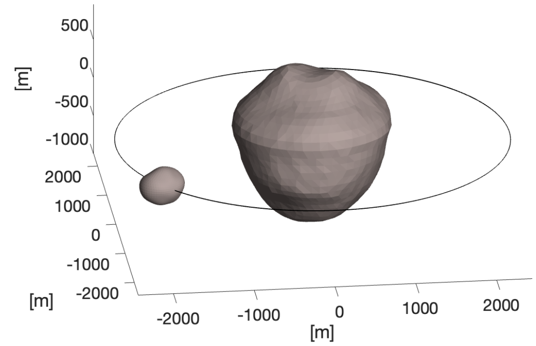

Figure 2.4: Graphic of (175706) 1996FG3, demonstrating an example of a binary asteroid in the singly-synchronous and BYORP-tide equilibrium.

### 2.3.2 Didymos

Didymos was the target of NASA's DART mission, a test of a kinetic impactor as a viable means of planetary defense [59, 79]. Specifically, DART impacted Dimorphos, the secondary of Didymos. Prior to the impact, Dimorphos was likely in the 1:1 spin-orbit resonance [80]. However, the DART impact perturbed the system away from the singly synchronous equilibrium, allowing for an excellent case study of a perturbed binary asteroid.

The shape models of Didymos and Dimorphos are shown in Fig. 2.5. This shows the primary [81] and secondary [12]. We have scaled the radar-derived primary shape model to match the dimensions of Didymos seen by DART, which deviate from the nominal shape model but are within its formal uncertainties [12, 81]. We also plot both the pre-impact and post-impact orbits to illustrate the change to the system caused by the DART impact.

Prior to the impact, the mutual orbit period was 11.92 h [74]. The semimajor axis was around 1189 m with an eccentricity less than 0.03, but likely in a physically circular orbit [73, 74, 80, 82]. The primary's rotation period was 2.26 h, and the secondary's rotation period was assumed to be synchronous. The volume-equivalent diameter is around 780 m for the primary and 150 m for the secondary [12].

The pre-impact shape of Dimorphos is interesting, as it was nearly a perfectly oblate spheroid, leading to a non-detection of its rotation period in photometric observations [12, 83]. However, a detection of BYORP drift prior to the DART impact is a convincing argument for it to be synchronous with the orbit period prior to the impact [80, 74]. Using these pre-impact values, we come up with a high bulk density around 2.8 g/cm$^3$. This high value has implications for the structure and porosity of the system, but should be validated by the ESA Hera mission [64].

Determining the post-impact parameters of Didymos is a major portion of this thesis work. From photometric and radar observations, the post-impact orbit period is determined to be 11.37 h [60]. Using the change in orbit period and the bulk density calculated using the pre-impact system, the post-impact observable semimajor axis is around 1152 m, and the observable eccentricity is around 0.027 [84]. The post-impact apsidal precession drift rate is around 7°/d, which is much slower than would be expected from the oblate shape of Didymos. This leads to the conclusion that Dimorphos must be more elongated than its pre-impact shape, with an elongation around $a/b \approx 1.3$. These results will be discussed in greater detail in Chapter 6.

The DART impact is characterized by the momentum enhancement factor $\beta$, defined as

$$\beta = \frac{-m_B \Delta v_T}{m_{\mathrm{DART}} v_{\mathrm{DART}}}, \tag{2.35}$$

when limited to planar motion, where $\Delta v_T$ is the instantaneous change in Dimorphos's orbital velocity in the tangential direction. $m_{DART}$ and $v_{DART}$ are the mass and relative velocity of the DART spacecraft, respectively. The negative sign is a result of the retrograde impact, causing the secondary to slow in its orbit. In this work we will use a DART mass of 535 kg and a relative velocity of 6.6 km/s.

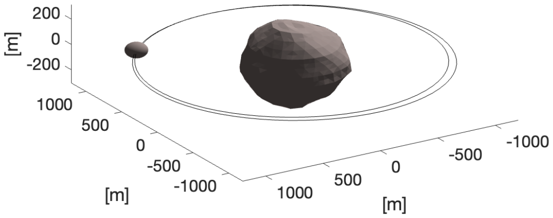

Figure 2.5: Graphic of (65803) Didymos, demonstrating an example of a binary asteroid that was previously in a singly-synchronous equilibrium but recently perturbed by the DART impact.

### 2.3.3 1991VH

The NEA binary (35107) 1991VH is relatively unique among binary asteroids as its secondary is rotating asynchronously with with orbit period [6]. Furthermore, the secondary's rotation period and the mutual orbit period appear to be evolving over time [78]. Dating back to 1997, the data are summarized in Table 2.1.

Table 2.1: The observed secondary rotation and orbit period of 1991VH. Uncertainties are $\leq 0.02$ hr. The bracketed value is not unique, and solutions exist between 7 and 29 hours. Orbit periods for all 2020 dates were determined from all the January-March data. Data taken from [78].

| Epoch UT | Secondary Period (hr) | Orbit Period (hr) |
|---|---|---|
| 1997-03-17 | n/a | 32.69 |
| 2003-02-25 | 12.84 | 32.63 |
| 2008-07-01 | (14.18) | 32.8 |
| 2020-01-27 | 11.57 | 32.50 |
| 2020-02-18 | 11.78 | 32.50 |
| 2020-02-26 | 11.55 | 32.50 |
| 2020-03-02 | 11.61 | 32.50 |

Several estimates of the orbit eccentricity provide $e = 0.05 \pm 0.02$ [16, 85, 77]. Estimates of the orbit semimajor axis range from $a = 3.24$ km [6] to $a = 3.26$ km [77]. Both photometric and radar observations give a volume-equivalent diameter of the primary of 1.2 km [6, 77], with radar observations revealing the primary to be top-shaped. The system is illustrated in Fig. 2.6.

Photometric observations suggest the secondary has a diameter of 450 m with an elongation of $a/b = 1.33 \pm 0.1$ [6], while radar observations give a more elongated value of $a/b = 1.5$ [76].

Among NEA binaries, only around 15% have a measured asynchronous spin rate, making 1991VH relatively unique in this population. In Fig. 2.7, we plot the difference between the orbit period and secondary rotation period for the population of binary asteroids, as a function of the separation distance between the two asteroids. Among close binary asteroids, which we define here as having $a/D_A < 5$, 1991VH has the largest difference between orbit period and secondary rotation period, and the only close system with a difference larger than 10 hours. Here $a$ is the binary asteroid semimajor axis and $D_A$ is the diameter of the primary. Any of the systems which have a larger discrepancy between these periods are wide systems with orbit periods on the order of 100 hours. Explaining this unique dynamical state is one focus of this thesis work.

## 2.4 Observable Elements

For comparison between observations and our models, we define 'observable elements' that are meant to parallel how ground-based observations are taken through lightcurves and radar data.

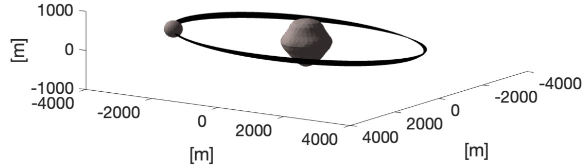

Figure 2.6: Graphic of (35107) 1991VH, demonstrating an example of a binary asteroid with an asynchronous secondary experiencing NPA rotation.

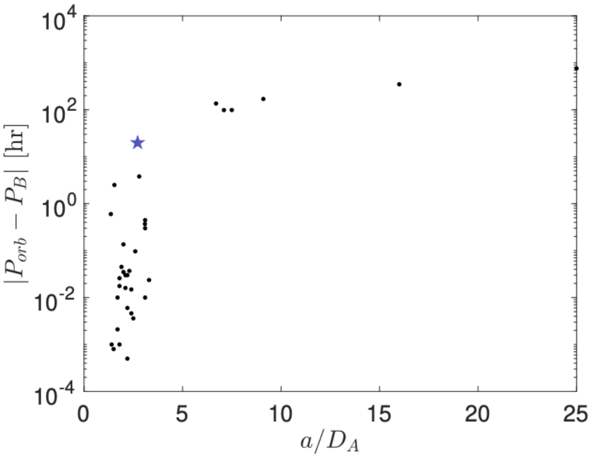

Figure 2.7: The difference in secondary rotation period and mutual orbit period as a function of separation distance. The star is 1991VH.

Thus, these elements are defined using only physical characteristics that are seen by an external observer; specifically, the separation distance. The observable semimajor axis is defined as [84]

$$a_{\text{obs}} = \frac{R_{\text{max}} - R_{\text{min}}}{2} \tag{2.36}$$

and the observable eccentricity as

$$e_{\text{obs}} = \frac{R_{\text{max}} - R_{\text{min}}}{R_{\text{max}} + R_{\text{min}}} \tag{2.37}$$

where $R_{\max}$ is the maximum separation distance between the two bodies within some time interval, and similarly for $R_{\min}$ as the minimum in that same time interval. Thus, these elements only use the observable quantity of separation distance, so they can be directly compared to ground-based observations. The drawback of these elements is they are similar to an averaged element, in that they require a time domain to define one realization. Typically we use the orbit period as the time interval for calculating these elements.

However, this still leaves the question of how best to represent the orbit period, which is one of the most important parameters of a binary asteroid as this is the most readily-available and accurate measurement of these systems [16]. The Keplerian orbit period will be misleading given the deviation of the semimajor axis from the separation distance. Instead, we define the 'stroboscopic' orbit period, which is simply the time required for the secondary to complete one full revolution around the primary in inertial space [84]. This mimics how lightcurves are taken of these systems, and again relies solely on the parameters of the system that are visible to an external observer. The stroboscopic orbit period can be easily calculated as the difference between successive crossings of an inertial plane by the secondary, and so is thus occasionally called the plane-crossing orbit period.

### 2.4.1 Equilibrium Comparison

We now investigate the equilibrium configuration of 1996FG3. While observable elements are designed to describe binary asteroids taking into account the F2BP, an alternative option is geometric elements, which are analytic and take into account the oblateness of the primary [86]. We compare these elements to the classical Keplerian representation in Fig. 2.8. When plotting the semimajor axis, we also plot the separation distance. Due to small librations in the system, the separation distance is not constant but varies on the order of several meters. We see the observable semimajor axis is equal to the average separation distance, whereas the geometric semimajor axis is a few meters larger. The Keplerian semimajor axis is too large by over 10 meters.

In Fig. 2.8 we also plot the eccentricity. Again, the eccentricity fluctuates thanks to small librations in the secondary. But the observable eccentricity is very small, oscillating just above 0. The geometric eccentricity is again slightly larger than this, while the Keplerian eccentricity is much larger.

None of these representations is ‘incorrect,’ but here we demonstrate their differences. Keplerian elements see significant deviations from the physical system. Geometric elements do a better job of describing the physical system, but observable elements are the closest match as these elements were designed to reproduce what an external observer would see.

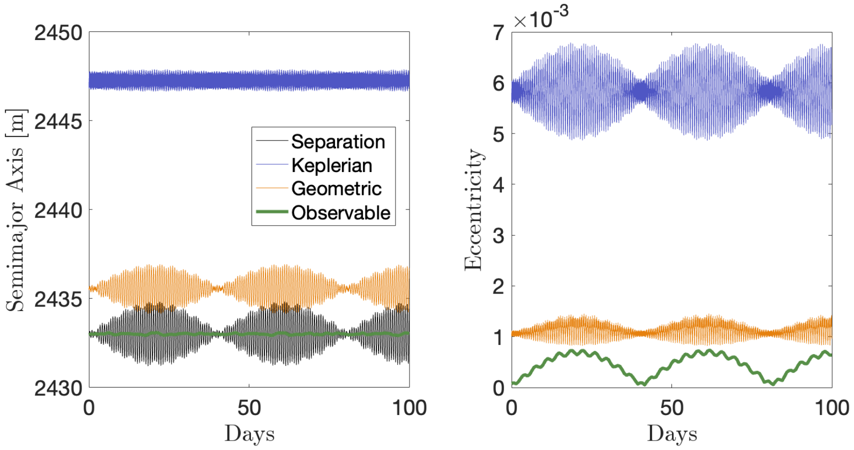

Figure 2.8: The Keplerian, geometric, and observable elements for 1996FG3

We next contrast the representations of the orbit period in Fig. 2.9. The measured orbit period of the system is 16.15 hours [6]. The stroboscopic orbit period is equal to this value exactly and remains constant. The geometric orbit period, calculated using the geometric semimajor axis, is about 5 minutes longer than this value and sees fluctuations. While these are a close match, the uncertainty on the orbit period in binary asteroids is usually on the order of 1 minute or less, so this difference is significant [78]. The traditional Keplerian orbit period calculated using the Keplerian semimajor axis is around 12 minutes longer, illustrating its shortfall in accurately characterizing the system.

These examples illustrate that observable elements are the best way to connect physical observations of binary asteroids to dynamical models, and they are self consistent throughout all

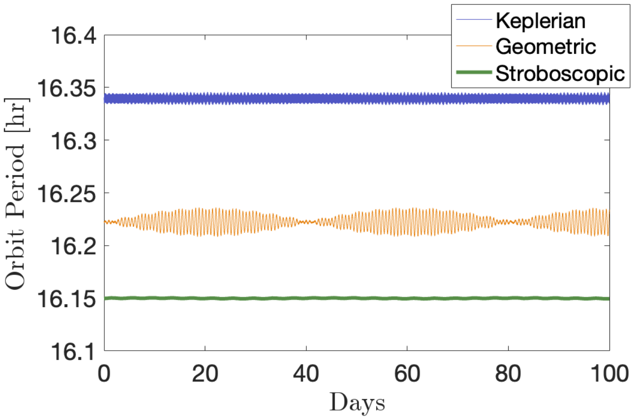

Figure 2.9: The Keplerian, geometric, and stroboscopic orbit period for 1996FG3

aspects of the system.

### 2.4.2 Mass Calculation

As a final point of comparison, we calculate the error in the mass estimate of a 1996FG3-like system as a function of the separation distance. This compares the difference in mass estimates given a measurement of the orbit period using Keplerian and F2BP dynamics. This is plotted in Fig. 2.10. For the shapes of the primary and secondary of 1996FG3, we see an exponential relationship between the mass error and separation distance. For close systems, the mass obtained with Keplerian dynamics is several percent compared to the mass obtained using the F2BP, specifically Eq. 2.32. However, as the separation distance increases, the error quickly drops off. Thus, for wide binary asteroids with a separation of 5 primary radii or larger, there should be negligible error from using Keplerian dynamics in mass estimation.

## 2.5 Numerical Integrators

The various models described in this Section are implemented in several integrators. The primary integrator utilized to propagate the F2BP is a Lie-Group Variational Integrator (LGVI). This symplectic integrator is implemented in GUBAS and allows for very efficient computation. To ensure accuracy, we iterate the integration step size until we reach convergence in our results.

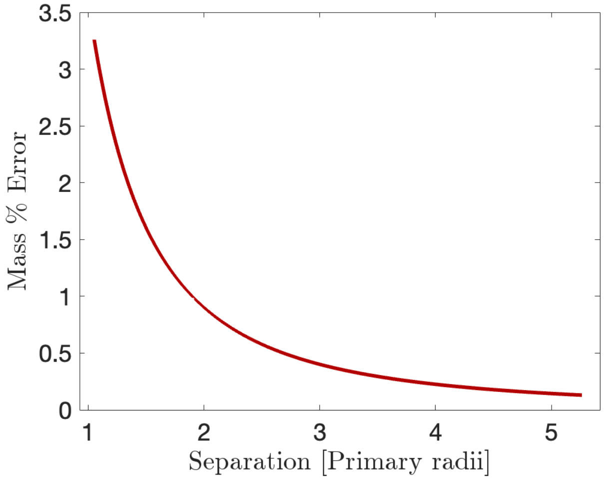

Figure 2.10: The percent error in assuming Keplerian dynamics for 1996FG3 as a function of separation distance

Typically, this required a 30 second time step, producing high-fidelity results.

For more efficient computation, that is, implementing the planar or sphere-restricted F2BP, we typically use an Adams-Bashforth-Moulton variable-step, variable-order integrator. This is implemented in MATLAB's *ode113* algorithm. This integrator is fast and accurate, and is typically applied in orbital dynamics problems. To ensure accuracy in its implementation, we decrease the tolerance on the integration until the system's total angular momentum is conserved to within some tolerance. For long-term simulations, we adopt a tolerance of $1 \times 10^{-6}\%$.

Finally, the last integrator is used to calculate perturbations to binary asteroids from additional gravitational bodies. This is another Adams-Bashforth-Moulton integrator that is also implemented in GUBAS. This is a four-step predictor-corrector algorithm that is less sophisticated than MATLAB's *ode113*, but serves to relatively accurately and efficiently integrate the perturbed problem. As this is not a symplectic integrator, we reduce the constant integrator step size until angular momentum is conserved.

## 2.6 Conclusion

In this chapter we have formally defined the F2BP, along with two more simplified approximations of the F2BP. The planar F2BP can take into account non-spherical shapes in both the primary and secondary, but is of course limited to planar motion and rotation. The sphere-restricted F2BP does allow for full three-dimensional rotation, but at the cost of limiting one of the bodies to be spherical. Both simplified systems have their own uses in which they are appropriate. We then outlined the three case study systems that motivate the work in this thesis: 1996FG3 is an example of a system in equilibrium, Didymos recently underwent a perturbation out of equilibrium, and 1991VH is asynchronous and likely experiences chaotic dynamics.

There are a few ways of describing the dynamics of these systems, but we showed the best way to connect numerical models to real-world observations is through the use of 'observable elements' and the stroboscopic orbit period. These elements are meant to parallel how observations are taken of these systems. We then finished by demonstrating the advantage of using these elements.

# Chapter 3

# Perturbed Dynamics

## 3.1 Introduction

Using various models of the F2BP, equilibrium states of binary asteroids have been studied extensively in the literature [43, 69, 71, 87, 88], but there are few studies on the perturbed dynamics. Of the studies of perturbed binary dynamics, many focus solely on the rotational dynamics of the secondary; some limited to planar, major principal axis rotation [44, 71, 76, 89], and others allowing for full three-dimensional rotation [90, 91, 92, 93]. However, studies on the mutual orbit dynamics of perturbed systems are lacking. Furthermore, there also lacks a comprehensive study of the effects of the secondary rotation on the orbit dynamics, and vice versa. But because of the strong spin-orbit coupling, this dynamical feedback is important to consider. This knowledge gap is a major focus of this thesis.

This chapter offers an analysis of the perturbed dynamics within the F2BP. Due to spin-orbit coupling within the system, we are particularly concerned with the interaction between the secondary and the orbit. The primary can usually be considered insulated form perturbations, as its rapid rotation and general axial-symmetry tend to decouple it from the rest of the system. However, due to commensurate angular momenta between the secondary and the orbit, we frequently see a complex interplay between these components. In this chapter we start with an analysis of the orbit dynamics, analyzing the behavior of the orbit elements under perturbations. We will find a threshold that allows the true anomaly to break out of its state of oscillation found in the equilibrium. This leads to libration in the secondary, with a resulting exchange of angular momentum leading to a non-constant orbit period. We also study the precession of an eccentric orbit, which is driven by both the primary and secondary shapes. We then build up our analysis to focus on the spin state of the secondary, and show in detail how the secondary and orbit are coupled. In particular, the onset of non-principal axis (NPA) rotation in the secondary can have significant and measurable effects on the orbit.

## 3.2 True Anomaly

As we saw in Section 2.2.4, the true anomaly is constant and equal to 0° in the 1:1 spin-orbit resonance equilibrium. However, there is a transition point where the true anomaly switches from librating about zero to circulating and tracking the secondary. At this point there is a sharp decrease in the rate of precession of the argument of periapsis where it abruptly changes from precessing at the orbit rate to precessing at a rate dominated by the oblateness of the primary and elongation of the secondary [50, 94, 95]. Here we calculate the perturbation to the orbit necessary to reach this transition point.

The equilibrium spin rate corresponds to an equilibrium specific orbital angular momentum:

$$h^* = r^2\dot{\theta}^*. \tag{3.1}$$

To calculate the perturbation needed to push the system out of equilibrium and allow the true anomaly to track the secondary, we can substitute the mean motion into a perturbed form of Eq. 3.1,

$$h^* + \Delta h = r^2\sqrt{\frac{\mu}{r^3}} \tag{3.2}$$

and solve for the perturbation $\Delta h$,

$$\Delta h = r^2\sqrt{\frac{\mu}{r^3}} - h^*. \tag{3.3}$$

We compare this analytic result to numerical GUBAS simulations of an orbit perturbation to an equilibrated Didymos. The numerical simulations begin with the nominal Didymos system as described in Section 2.3.2, then apply a tangential $\Delta v_T$ to perturb the orbit. Over the simulation time we record the maximum true anomaly value. The results are shown in Fig. 3.1, where the maximum true anomaly $f$ is plotted as a function of the perturbation $\Delta h$. As the magnitude of $\Delta h$ increases, the maximum allowable true anomaly increases. Outside of a perfect equilibrium where $f = 0$, the true anomaly oscillates around 0 until the critical perturbation pushes the maximum true anomaly over 90°, allowing it to circulate and track the secondary. At this point there is a discontinuity where the maximum true anomaly is 180°. In Fig. 3.1, the vertical dashed line corresponds to the analytic value calculated from Eq. 3.3 using the nominal Didymos system (ignoring uncertainties). We see excellent agreement between this analytic value and the numerical simulations, which are plotted as individual data points.

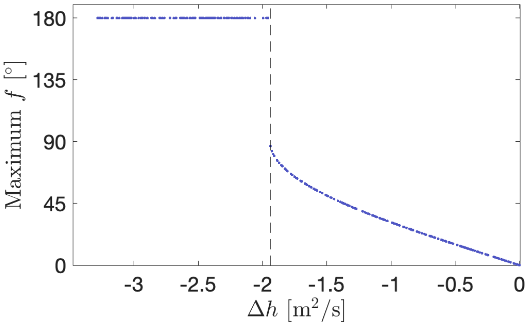

Figure 3.1: The maximum true anomaly as a function of the change in specific orbital angular momentum for an orbit perturbation. There is a discontinuity where the perturbation to the orbit changes the orbital angular momentum enough to push the system out of an equilibrium and the true anomaly switches from librating to circulating. Data points are numerical simulations and the dashed line is the analytic prediction.

This perturbation corresponds to decreasing the orbit period, but it is also possible to perturb the orbit out of an equilibrium by increasing the orbit period. This approach requires more consideration. Note that setting $\dot{\theta} = \sqrt{\frac{\mu}{r^3}}$ is equivalent to decreasing the semimajor axis from the equilibrium value $a^*_{\text{Kep}}$ to the separation distance $r$, which is the equilibrium observable semimajor axis. For the opposite perturbation, we instead increase the observable semimajor axis to be equal to the Keplerian semimajor axis. In other words we set

$$\dot{\theta} = \sqrt{\frac{\mu}{r^2}\left(\frac{2}{r} - \frac{1}{2a^*_{\text{Kep}} - r}\right)}. \tag{3.4}$$

This corresponds to a perturbation of

$$\Delta h = r^2 \sqrt{\frac{\mu}{r^2}\left(\frac{2}{r} - \frac{1}{2a^*_{\text{Kep}} - r}\right)} - h^*. \tag{3.5}$$

Fig. 3.2 shows the full range of perturbations, both increasing and decreasing the orbit period. Numerical simulations calculated with GUBAS are plotted as data points along with the analytical solutions from Eqs. 3.3 and 3.5 as dashed lines. We see good agreement between these analytical solutions and the numerical results. Thus, we have established novel analytical equations to calculate the critical perturbation to the orbit necessary to break out of an equilibrium configuration and allow the true anomaly to track the secondary rather than librate about 0°. This perturbation is equivalent to changing the binary semimajor axis by $\pm(a^*_{\text{Kep}} - r)$, which is illustrated in Fig. 3.3.

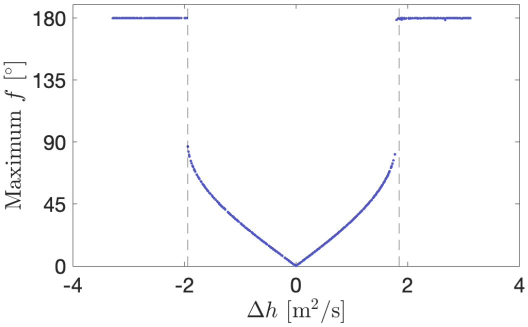

Figure 3.2: The maximum true anomaly as a function of the change in specific orbital angular momentum for an orbital perturbation. The discontinuities correspond to perturbations sufficient to push the orbit out of equilibrium and allow the true anomaly to track the secondary. The vertical dashed lines correspond to the analytical solutions from Eq. 3.3 (left, indicating a decrease in the orbit period) and Eq. 3.5 (right, indicating an increase in the orbit period). Numerical simulations are plotted as individual points, and show strong agreement with the analytical formulae.

## 3.3 Lagrange Planetary Equations

In their analysis of the binary asteroid (66391) Moshup, [50] developed Lagrange Planetary Equations (LPEs) for a binary system using a second-degree mutual potential. LPEs can provide a simple alternative to the full GUBAS integration. These equations have the advantage of an analytic

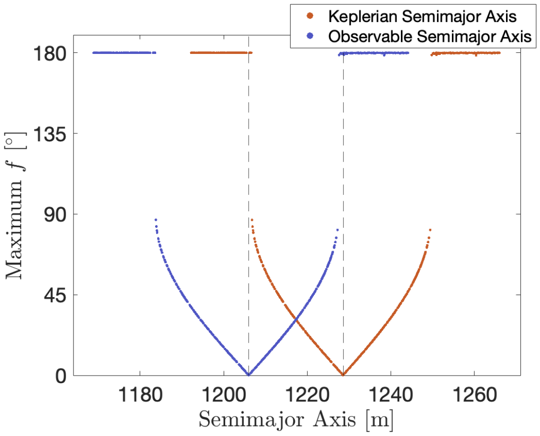

Figure 3.3: The maximum true anomaly as a function of the change in both the observable and Keplerian semimajor axis. This illustrates how pushing a system out of equilibrium is equivalent to changing the semimajor axis by the difference between the observable and Keplerian values.

method to calculate quantities such as the orbit precession without relying on more expensive numerical simulations. We do not reproduce the full set of LPEs here, but refer the reader to Eqs. 44–48 in [50]. Because the Didymos mutual orbit is assumed planar (i.e., the orbit angular momentum is aligned with the total angular momentum), we use the longitude of periapsis rather than the argument of periapsis and the longitude of the ascending node to avoid the singularity in the longitude of the ascending node. The longitude of periapsis is defined as the sum of these two classical Keplerian angles ($\varpi = \omega + \Omega$). For a planar system, the relevant LPEs simplify to:

$$\dot{a}_{\text{Kep}} = 0 \tag{3.6}$$

$$\dot{e}_{\text{Kep}} = 0 \tag{3.7}$$

$$\dot{\varpi} = \frac{3\sqrt{\mu}}{2a_{\text{Kep}}^{7/2}(1-e_{\text{Kep}}^2)^2}\left(\bar{I}_{A,z} - \bar{I}_{A,s} - 2\bar{I}_{B,x} + \bar{I}_{B,y} + \bar{I}_{B,z}\right) \tag{3.8}$$

$$\dot{M} = \sqrt{\frac{\mu}{a_{\text{Kep}}^3}} + \frac{3\sqrt{\mu}}{2a_{\text{Kep}}^{7/2}(1-e_{\text{Kep}}^2)^2}\left(\bar{I}_{A,z} - \bar{I}_{A,s} - 2\bar{I}_{B,x} + \bar{I}_{B,y} + \bar{I}_{B,z}\right). \tag{3.9}$$

First, we apply the averaged LPEs to an equilibrated Didymos system and compare to numerical simulations: see Fig. 3.4. While there is agreement for the Keplerian semimajor axis and eccentricity, which remain constant, the LPEs do not correctly capture the average behavior of the geometric angles. Specifically, in the LPE solution the longitude of periapsis precesses and the true anomaly circulates, while in reality the true anomaly librates and the longitude of periapsis circulates. Thus, the LPEs are a poor representation of the dynamics when the true anomaly is librating.

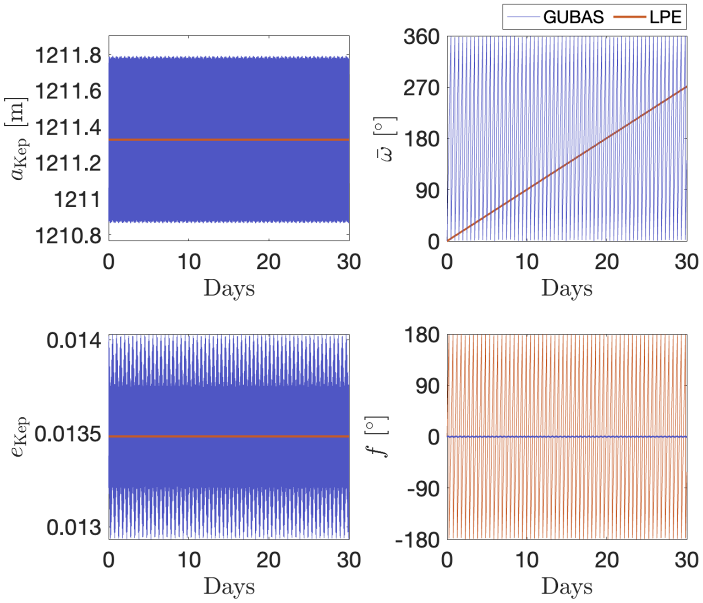

Figure 3.4: The semimajor axis (top left), eccentricity (bottom left), longitude of periapsis (top right), and true anomaly (bottom right) of a numerical GUBAS simulation compared to the analytical LPE solution for an equilibrated system. The LPE solution shows the true anomaly circulating, while in reality this angle should be zero and the longitude of periapsis should be circulating.

Compare this to an excited system, where there is better agreement between the LPEs and GUBAS solutions, as seen in Fig. 3.5. The LPEs correctly compute the average values of semimajor axis and eccentricity, however they do not capture the fluctuations that these variables experience. In the perturbed system, the LPEs also correctly calculate the behavior of the longitude of periapsis, where this angle precesses. For the true anomaly, again the LPEs correctly show this angle circulating, although with a period slightly different from the numerical solution. Nonetheless, the LPEs are an effective approach for quickly calculating the precession period without the need for expensive simulations, as long as the system is not in an equilibrium state. One shortfall of the LPEs is they ignore any triaxiality of the secondary [50]. For an oblate spheroidal shape like Dimorphos [12, 83], this is a fine assumption, but for more elongated secondaries experiencing libration, the LPEs will incorrectly calculate the precession rate.

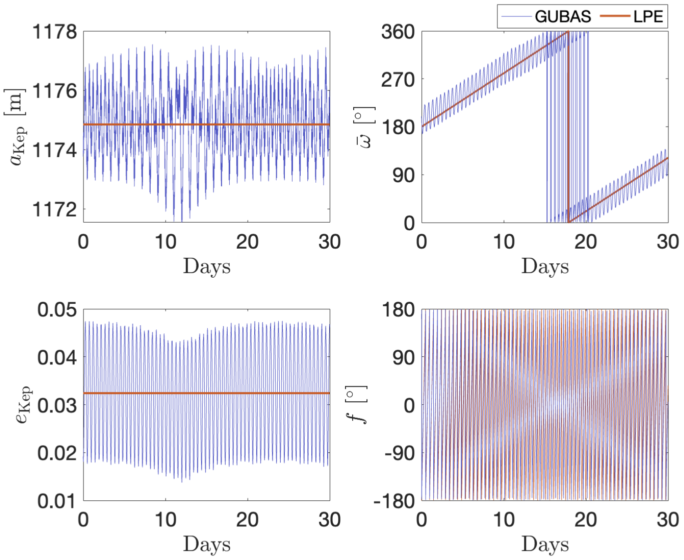

Figure 3.5: The semimajor axis (top left), eccentricity (bottom left), longitude of periapsis (top right), and true anomaly (bottom right) of a numerical GUBAS simulation compared to the analytical LPE solution for a perturbed system. Because the system is perturbed, both GUBAS and the LPE correctly show the true anomaly circulating and the longitude of periapsis precessing.

The cause of the LPEs' shortfalls for the relaxed system stems from their definition. The LPEs are calculated by averaging over the mean anomaly. However, this is not appropriate for a system in equilibrium, as the mean anomaly remains equal to zero. Rather than using LPEs for a system in equilibrium, one can instead simply use Eq. 2.32 in place of $\dot{\bar{\varpi}}$. Once a system is perturbed out of the equilibrium and the mean anomaly is allowed to circulate, the LPEs become more accurate. However, for a significantly triaxial secondary experiencing libration, a higher-fidelity model should be used, for example the analytic correction defined in [94] or the semi-analytic model in [11]. Given the limited scope of applicability of the averaged LPEs, we caution their use in the analysis of binary asteroid dynamics.

## 3.4 Orbit Period Variations

Due to spin-orbit coupling in binary asteroids, libration within the secondary will affect the orbit [96]. We define libration as angular deviations between the secondary's longest axis (minimum principal inertia axis) and the line connecting the primary to the secondary. Libration in the secondary results in oscillations within its spin rate. To enforce angular momentum conservation, this results in an equivalent angular momentum fluctuation in the orbit. The result is a non-constant orbit period. We will focus on Didymos and the DART impact to illustrate this effect.

Coupling between the libration of the secondary and the orbit period stems from the conservation of angular momentum. To investigate this, we assume the spin angular momentum of the primary is essentially unchanged by the DART impact. We turn to GUBAS numerical simulations to verify this assumption. Based on GUBAS simulations with a $\beta$ factor equal to 3, The secondary's spin angular momentum changes by around 3.6% while the orbital angular momentum changes by about 1.2% as a result of the impact. These changes are much larger compared to the primary's spin angular momentum change of around $2 \times 10^{-4}\%$, and thus we ignore any change in the primary's angular momentum. Despite the primary's large angular momentum, most of the change in momentum does indeed occur in the secondary and orbit. To investigate the momentum exchange, we define the free angular momentum as the total angular momentum minus the contribution by the primary:

$$h_{\text{free}} = h_{\text{total}} - h_A. \tag{3.10}$$

Under our assumption of constant primary angular momentum, $h_{free}$ is constant in the absence of external perturbations. In the planar F2BP system, the free angular momentum can be written as

$$h_{\text{free}} = \bar{I}_z\dot{\theta} + \bar{I}_{B,z}\dot{\phi}_2. \tag{3.11}$$

We can rearrange this equation to get a direct relationship between the orbital rate and the libration rate:

$$\dot{\theta} = \frac{h_{\text{free}} - \bar{I}_{B,z}\dot{\phi}_2}{\bar{I}_z}. \tag{3.12}$$

When the system is in equilibrium, the orbit rate is constant as defined in Eq. 2.32, and the libration angle $\phi_2 = 0$ over all time. For a given angular momentum value, Eq. 2.32 then defines the required separation distance.

In this analysis we will assume the DART impact to be head-on through the secondary's center of mass, so only the orbital angular momentum is instantaneously changed by the impulse. Furthermore, we assume the pre-impact system is in an equilibrium configuration, and therefore the separation distance is constant. Thus, the impulse to the free angular momentum is equal to

$$\Delta h = \frac{m_A m_B}{m_A + m_B} r \Delta v_T. \tag{3.13}$$

Substituting our simple, planar definition for $\beta$ (Eq. 2.35) into this expression gives the free angular momentum perturbation as a function of $\beta$:

$$\Delta h = -\beta r \frac{m_A}{m_A + m_B} m_{\text{DART}} v_{\text{DART}}, \tag{3.14}$$

where again the negative sign is due to the retrograde impact. Finally, we add this perturbation to the equilibrium free angular momentum value for use in the equations of motion,

$$h_{\text{free}} = h^* + \Delta h. \tag{3.15}$$

Using this expression for the free angular momentum allows $r$, $\dot{\theta}$, and $\phi_2$ to oscillate around their equilibrium values, allowing for the exchange of momentum between the orbit and the secondary's spin.

Assuming the system is initially at equilibrium with a separation distance of 1200 m, we have all the initial conditions necessary to integrate the equations of motion using the planar F2BP. In these simulations we will assume the secondary to have the axial ratios $a/b = 1.3$, $b/c = 1.1$. We simulate the impact by instantaneously perturbing the free angular momentum for a given value of $\beta$. When the free angular momentum is perturbed through $\beta$, the system deviates from the equilibrium configuration. The inertia tensor of the secondary is calculated using its bulk diameter and axis ratios, while the inertia tensor of the primary is calculated by approximating the primary's full shape model as an oblate spheroid. Thus, we have all the quantities needed to propagate the equations of motion using the planar F2BP model.

The libration amplitude is calculated using the time history of $\phi_2$ over the full time domain. A 20° libration means the secondary is oscillating by ±20° around the line $r$, as is the case in Fig. 3.7.

The orbit rate $\dot{\theta}$ is plotted for the $\beta = 3$ case in the lower left of Figs. 3.6 and 3.7, where we immediately see it varies over time. In order to calculate the orbit periods, we use an event function during the integration of the equations of motion. The event function checks the integration of Eq. 3.12 and calculates the precise times $\theta$ has reached $2\pi$. By differencing these sequential times, we calculate the orbit period, or the time required for the secondary to move by $2\pi$ radians in inertial space. This is the stroboscopic orbit period

Figs. 3.6 and 3.7 show the result of this numeric integration approach, plotting the orbit period as a function of time in the lower right plots. These results clearly show that the orbit period is not constant when the system is perturbed from its equilibrium and experiencing libration. Furthermore, the two scales in these figures demonstrate a range of constituent frequencies driving the oscillations within the system.

### 3.4.1 Constituent Frequencies

We next examine the underlying frequencies governing the fluctuations around the equilibrium. Using the angular momentum integral, we can remove $\theta$ from the equations of motion through Eq. 3.12. Additionally, the assumption of an axially symmetric primary also removes $\phi_1$ from the state. Thus, we can reduce the planar F2BP equations down to 2 degrees of freedom: $r$ and $\phi_2$.

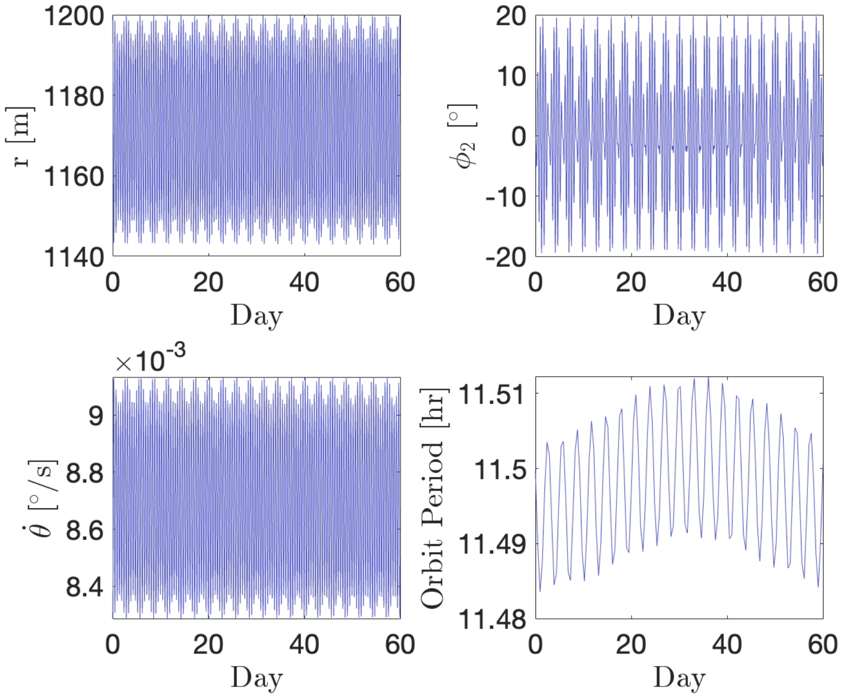

Figure 3.6: The separation (top left), libration (top right), orbital rate (bottom left), and orbital period (bottom right) for the case $\beta = 3$ for a time of 60 days.

Defining our state as

$$X = \begin{bmatrix} r \\ \phi_2 \\ \dot{r} \\ \dot{\phi}_2 \end{bmatrix}, \tag{3.16}$$

we can write the equations of motion in the form

$$\dot{X} = f(X). \tag{3.17}$$

To linearize the equations of motion, we define the Jacobian

$$A = \frac{\partial f}{\partial X}. \tag{3.18}$$

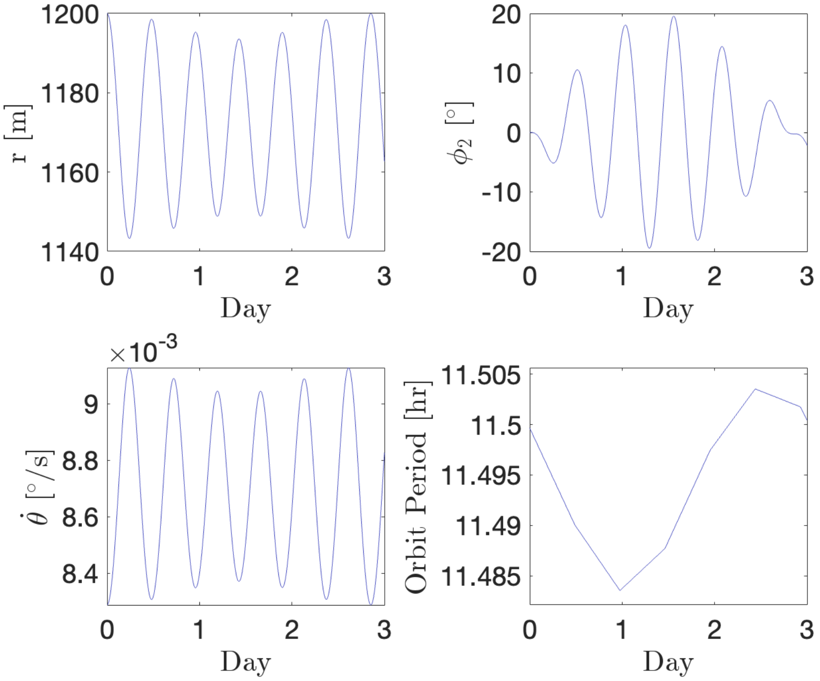

Figure 3.7: A closeup view of the separation (top left), libration (top right), orbital rate (bottom left), and orbital period (bottom right) for the case $\beta = 3$ for a time of 3 days.

This gives

$$A = \begin{bmatrix} 0 & 0 & 1 & 0 \\ 0 & 0 & 0 & 1 \\ \frac{\partial \ddot{r}}{\partial r} & \frac{\partial \ddot{r}}{\partial \phi_2} & 0 & \frac{\partial \ddot{r}}{\partial \dot{\phi}_2} \\ \frac{\partial \ddot{\phi}_2}{\partial r} & \frac{\partial \ddot{\phi}_2}{\partial \phi_2} & \frac{\partial \ddot{\phi}_2}{\partial \dot{r}} & \frac{\partial \ddot{\phi}_2}{\partial \dot{\phi}_2} \end{bmatrix}. \tag{3.19}$$

By substituting in values for the semimajor axis and angular momentum after the perturbation, the eigenvalues of Eq. 3.19 give the natural frequencies of the system. For the case of $\beta = 3$, the new semimajor axis is 1170 m. After evaluation and spectroscopic decomposition of the Jacobian, the two natural frequencies are 11.4 h and 13.5 h. These correspond to the mean motion and frequency of free libration. The proximity of these two natural frequencies will result in beating; we can calculate the period of the beating by

$$T_{\text{beat}} = \frac{1}{T_1 - T_2} \tag{3.20}$$

where $T_1$ and $T_2$ are the two natural frequencies of the system. In this simulation, this gives us a beating period of 3 days.

After examination of Fig. 3.7, the 3 day beating period in the libration angle is obvious. This drives the short-period oscillation within the orbit period. Thus, an analysis of the linearized dynamics will reveal the libration frequency in the perturbed system.

There is also a long-period mode within the orbit period, for this simulation about equal to 60 days. This is not due to any angular momentum exchange, but is actually the apsidal precession period of the orbit. Because our observer is fixed in an inertial frame, the orbit period appears to oscillate as the orbit precesses and periapsis is pointing in different directions. We provide a more detailed discussion of the orbital precession in binary asteroids in Section 3.5.

Thus, the orbit period varies with dominant frequencies driven by the libration and the precession. For this simulation, we fit the 3 day and 60 day periods to produce an analytic approximation of the orbit period; this is shown in Fig. 3.8. Thus, the orbit period can provide additional information about the system, such as its precession rate and secondary shape, provided a high enough signal-to-noise ratio is obtained to produce high-quality observational data.

### 3.4.2 Secondary Shapes

Expanding our analysis to different secondary elongations, we plot the periods of the natural frequencies as a function of $a/b$ in Fig. 3.9, along with the beating period these frequencies produce. These periods, along with the apsidal precession period of the orbit, will drive the variations in the orbit period as seen by an external observer. Here we see these frequencies have a strong dependence on the secondary shape. The beating period is maximum around $a/b = 1.4$, which is near a major resonance within the system as we will see in Sec. 3.6.

The time history of the stroboscopic orbit period for 5 different secondary elongations are shown in Fig. 3.10. The secondary shapes range from $a/b = 1.1$ to $a/b = 1.5$. This demonstrates how the underlying frequencies within the system are very sensitive to the shape of the secondary, highlighting the importance of this parameter in binary asteroid dynamics.

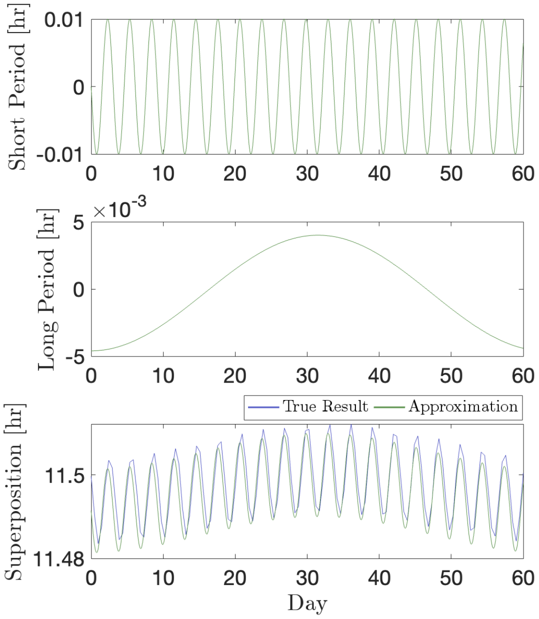

Figure 3.8: The decomposition of the orbit period variations into its two constituent modes. The decomposition is computed using a discrete Fourier transform. The short-period mode (top), long-period mode (middle), and the superposition of the two modes (bottom) are plotted, with the superposition overlaid on the actual orbit period calculation.

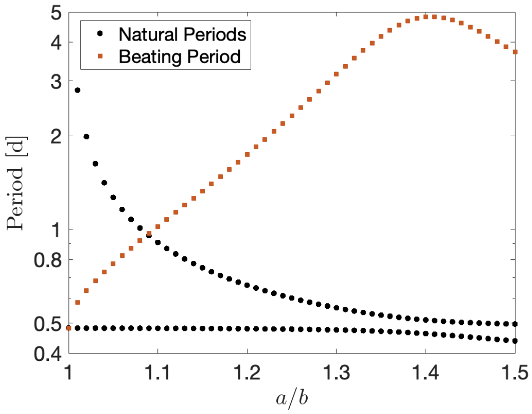

Figure 3.9: The periods of libration calculated from the linear dynamics. The two natural frequencies in the system produce the periods shown in black circles, while the beating period between the two is plotted as red squares.

Expanding even further, we test different combinations of $a/b$ and $\beta$ and examine how the libration and orbit period change. Fig. 3.11a shows the libration amplitude as a function of both

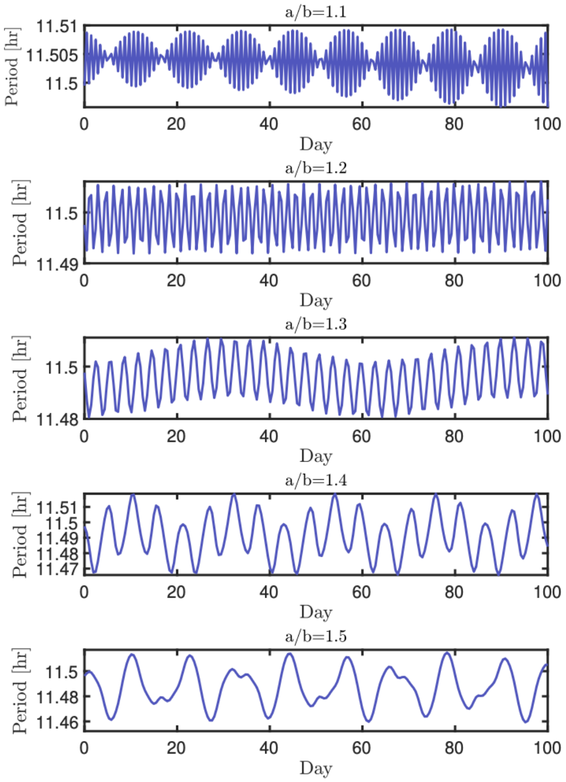

Figure 3.10: The time history of the orbit periods for 5 different secondary elongations. This shows how different shapes produce different underlying frequencies within the orbit period.

$a/b$ and $\beta$, while Fig. 3.11b shows the corresponding variation in the orbit period. Immediately apparent is that increasing $\beta$ increases both the libration amplitude and the orbit period variations. There are resonances near $a/b = 1.1$, and $a/b = 1.4$ where the libration and orbit period variation are excited for all values of $\beta$. We will discuss this resonance in greater detail in Sec. 3.6.

As $a/b$ changes, the moments of inertia of the secondary change as well. Also, the natural frequencies of oscillations in the secondary change with $a/b$ [90]. Thus, it is unsurprising that the libration magnitude changes with $a/b$. However, it is interesting that there is not a monotonic dependence on $a/b$. Instead, we see a dependence consistent with the trend in beating period shown in Fig. 3.9.

Fig. 3.11 illustrates the close relationship between libration and orbit period variations. As the libration amplitude increases, the range in orbit period also increases. This is caused by a larger exchange of angular momentum between the two. We see some interesting trends when we also consider the libration periods plotted in Fig. 3.9. The resonance at $a/b = 1.1$ where the libration amplitude and orbit period variations spike appears to correlate with the point where the beating period in libration is equal to one of the natural frequencies of the system (i.e. the two curves cross in Fig. 3.9). The increase in libration amplitude and orbit period variations also follow the curve of the beating period, where the longer period corresponds to a larger libration amplitude and variations in the orbit period.

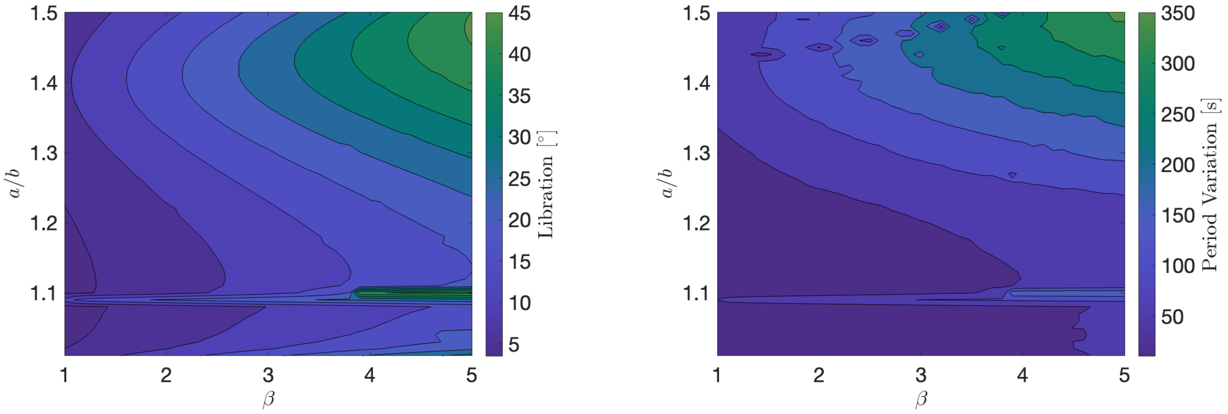

(a) Libration Amplitude as a Function of Elongation and $\beta$

(b) Libration Amplitude as a Function of Elongation and $\beta$

Figure 3.11: (a) The libration amplitude as a function of the axis ratio $a/b$ and the $\beta$ parameter. (b) The variation in orbit period as a function of the axis ratio $a/b$ and the $\beta$ parameter. The effects of resonances near $a/b = 1.1$ and $a/b = 1.4$ are apparent.

We have demonstrated that in perturbed systems, the orbit period is not constant. It experiences variations driven by the libration and precession of the system, and these relationships can be very complex. However, if these variations are detected, they can provide additional information about the system not otherwise apparent from lightcurve observations.

## 3.5 Orbit Precession

The secular precession rate of an orbit is an important quantity driven by the physical characteristics of the system. It is well understood that the oblateness of the primary body plays a major role in the precession rate [70]. This fact is frequently used to estimate mass distributions within the body given an observed orbital precession rate. However, the typical assumption in these problems is that the secondary body is small and massless in comparison to the primary. This is not the case for binary asteroids, in which the secondary can be a significant fraction of the total mass in the system [6]. Furthermore, the secondary is typically elongated, and its non-spherical shape can have an important influence on the system dynamics, especially in a perturbed system [84, 11].

The topic of orbital precession in systems with irregular satellites has been previously discussed in the literature, with some emphasis on the Martian moon Phobos [94]. However, these studies do not account for free libration in the system, instead focusing only on the libration caused by the orbit's eccentricity (i.e., forced libration). Furthermore, Phobos's mass fraction is very small, being around 7 orders of magnitude smaller than Mars.

The groundwork for an analytic expression of the apsidal precession rate around an elongated body was done by [97, 98] through an application of the classical Gauss Planetary Equations. The radial and tangential accelerations due to the perturbation of the elongated body were derived in [34]. Using these, the time derivative of the longitude of periapsis, or equivalently the apsidal precession rate, as applied to binary asteroids was then finalized in [11]. The apsidal precession resulting from the body's oblateness is a classical result [70], so here we focus only on the effect of the body's prolateness. For convenience we repeat the expression here, with corrections to minor errors in the derivation. The equation is non-dimensionalized, using the radius of the primary as the unit of length and the total system mass as the mass unit, leading to the unit of time equal to $1/2\pi$ of the orbit period at the equator of the primary [11]:

$$\dot{\varpi} = \frac{\sqrt{a(1-e^2)}}{e} \frac{\bar{I}_{B,y} - \bar{I}_{B,x}}{r^4} \left[ \frac{9}{4} \cos 2\phi_2 \cos f + \frac{3}{2} \sin 2\phi_2 \sin f \frac{2 + e\cos f}{1 + e \sin f} \right]. \tag{3.21}$$

Apart from the classical precession rate driven by oblateness, this expression shows the driving quantities in apsidal precession. Beyond the semimajor axis, $a$, eccentricity $e$, and separation $r$, we also see the precession rate depends on the $C_{22}$ gravity term of the secondary (here equivalently written as $\bar{I}_{B,y} - \bar{I}_{B,x}$), the libration angle $\phi_2$, and the orbital position, measured by true anomaly $f$. Here we can directly observe increasing the secondary's $C_{22}$ increasing the apsidal precession rate. The libration angle is the angle between the longest axis and the position vector, also written mathematically as:

$$\phi_2 = \gamma - f - \varpi \tag{3.22}$$

where $\gamma$ is the elongated body's orientation in inertial space and $\varpi$ is the longitude of periapsis.

Interestingly, Eq. 3.21 includes the relative orientation of the prolate body, meaning the spin rate will affect the orbit's precession rate. This can be used to our advantage, for if the precession rate of the orbit is measured, it can help constrain the spin rate and libration amplitude of the secondary in a binary asteroid.

Another point of interest is the role the true anomaly plays in the precession rate. We have already established that in the synchronous equilibrium of binary asteroids, the true anomaly is equal to zero and the secondary is trapped at periapsis, with the longitude of periapsis precessing at the orbit rate. This is also reflected in Eq. 3.21, where if the true anomaly and libration angle are equal to zero the apsidal precession rate is rapid, equal to the orbit rate. For small perturbations, the true anomaly and the libration angle oscillate about 0°. In this case, the precession rate is not constant, but is still rapid, since the longitude of periapsis is still circulating while the true anomaly oscillates. We have derived this critical point where the true anomaly switches from oscillation to circulation in Sec. 3.2.

Unfortunately, this expression relies on both $\phi_2$ and $f$, which are not independent and lack an explicit relationship between the two. Thus, they must be integrated together using proper equations of motion, for example the model in [34] or [11]. Furthermore, the semimajor axis, eccentricity, and separation all also depend on these two quantities, and the semimajor axis and eccentricity in particular are not constant. We illustrate the relationships between these parameters in Fig. 3.12, which shows complex dependencies between true anomaly, libration, separation distance, semimajor axis, and eccentricity.

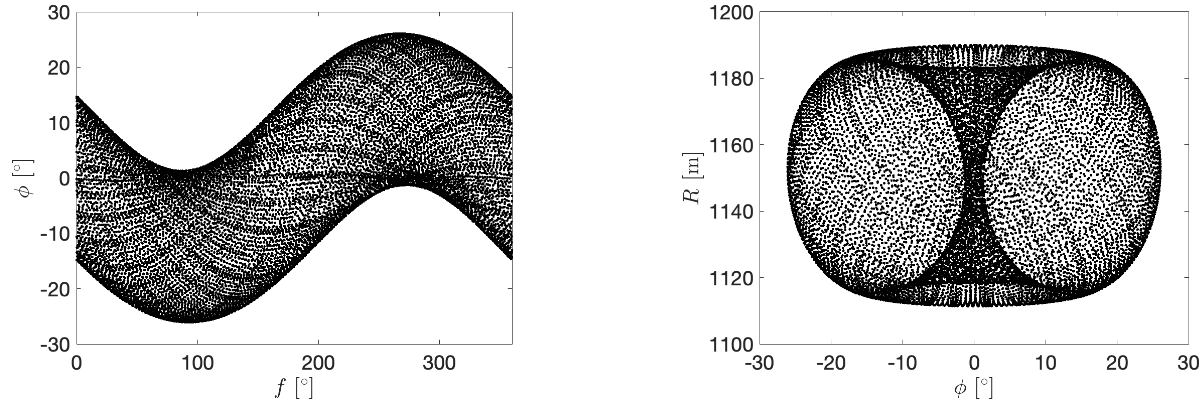

(a) Libration as a function of true anomaly (b) Separation as a function of libration

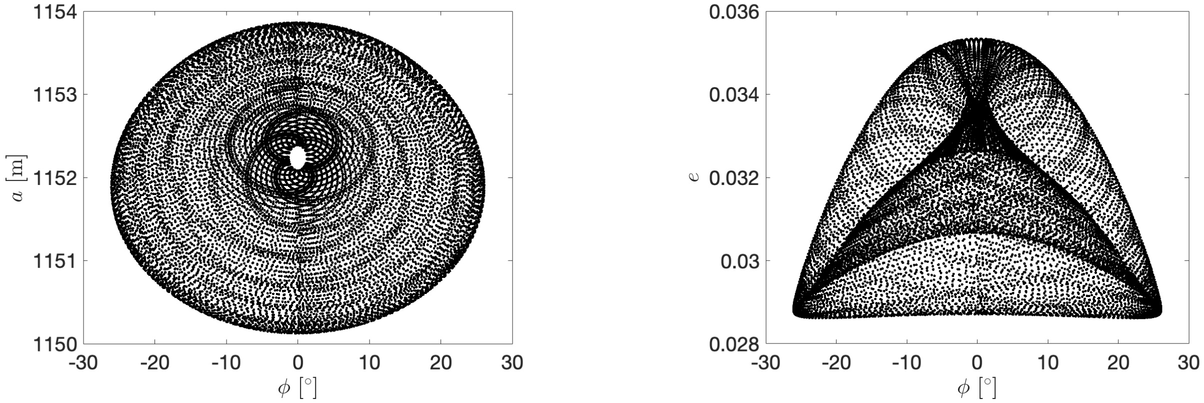

(c) Semimajor axis as a function of libration (d) Eccentricity as a function of libration.

Figure 3.12: Plots from the sphere-ellipsoid model showing the relationship between (a) the libration and true anomaly, (b) separation and libration, (c) semimajor axis and libration, and (d) eccentricity and libration. This illustrates the complicated relationships between these quantities.

One may attempt to average Eq. 3.21 over one orbit period. However, as demonstrated in Fig. 3.12 and discussed in Sec. 3.4.1, there are in reality several frequencies, specifically the frequency of the true anomaly and the frequency of libration. Thus, averaging over one orbit period will not capture the true secular behavior, except for the specific case where the libration frequency is resonant with the orbit mean motion (for a synchronous secondary, this is the case of only forced libration). Alternatively, one may average over one precession period. However, in a purely analytical approach we still run into the problem of the complex relationships between $f$

and $\phi_2$. To investigate this, we note there are two terms in Eq. 3.21. We carried out numerical simulations and averaged both these terms separately. In general, both terms contribute to the secular behavior (i.e. neither term averages to zero).

For an analytical approach, we turn to another expression for the apsidal precession rate, derived in [95]. This model also includes the effects of secondary elongation and libration, but only considers the forced libration within the system. The benefit of reducing the model to only incorporating the forced libration is the relationship between $\phi_2$ and $f$ becomes much simpler, and we can average over 1 orbit period. However, unfortunately we cannot use this equation when free libration is present in the system.

For now, we will restrict our dynamics to perfectly planar, so the angular momentum of the secondary and orbit are aligned. Because we cannot analytically solve Eq. 3.21, we will use the spherical-restricted F2BP to calculate the orbital elements and the libration angle. We approximate the apsidal precession rate using a linear fit of the numerically obtained longitude of periapsis. In our dynamics, we start the secondary aligned with the primary ($\phi_{2,0} = 0^\circ$) and perturb the velocity to add a small amount of eccentricity to the system. This is similar to the effect of the DART impact in the Didymos binary asteroid system.

We apply a $\Delta V$ of -3 mm/s to the secondary (retrograde to the orbital motion), similar to the value caused by the DART impact [75]. Along with this perturbation, we also apply a perturbation to the secondary's spin rate $\delta\dot{\phi}_2$. We then integrate the system forward in time for 60 days and calculate the precession rate by linearly fitting to the secular drift in the longitude of periapsis over this time.

Figure 3.13 shows the results of these simulations. Panel (a) plots the precession rate as a function of the spin perturbation, while panel (b) shows the precession rate as a function of the libration amplitude $\Phi_2$. The relationship between the libration amplitude and the spin perturbation is shown in panel (c). Finally, panel (d) shows the eccentricity as a function of the spin perturbation. This demonstrates how the precession rate does depend on the secondary's spin, and it's not only driven by the changing eccentricity.

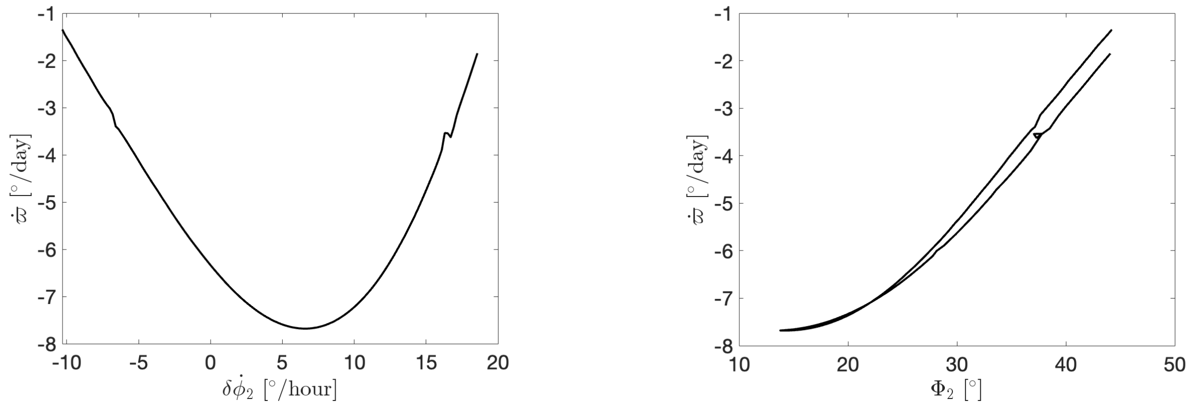

(a) Precession rate as a function of spin perturbation

(b) Precession rate as a function of libration amplitude

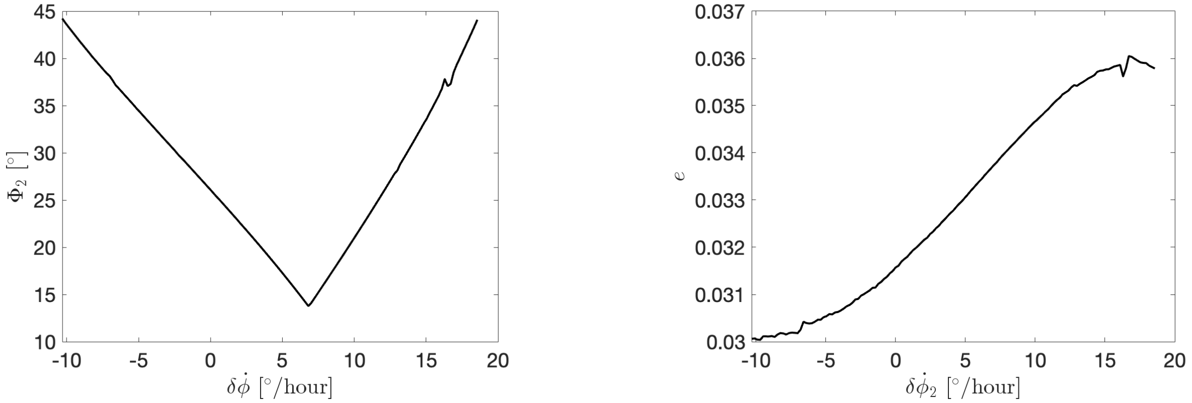

(c) Libration amplitude as a function of spin perturbation

(d) Eccentricity as a function of spin perturbation

Figure 3.13: Plots of numeric results showing (a) the precession rate as a function of the spin perturbation, (b) the precession rate as a function of the libration amplitude, (c) the libration amplitude as a function of the spin perturbation, and (d) the eccentricity as a function of the spin perturbation.

From Figure 3.13, there is a critical spin perturbation which results in the largest apsidal regression. This occurs at the same perturbation which minimizes the libration amplitude, meaning this is the secondary spin rate which eliminates free libration, leaving only the forced libration. Increasing libration amplitude, or equivalently perturbing the secondary spin away form this value, results in decreasing the absolute rate of precession (moving closer to zero secular drift). We also see how the secondary's spin perturbation has a small effect on the eccentricity. Increasing the secondary's spin rate results in a higher eccentricity.

In Figure 3.13, we see some discontinuities in the precession rate for a spin perturbation around 16°/hour, and to a lesser extent also around -6°/hour. These appear to be due to a resonance between the average orbit period and the average secondary spin period, but they only have a small effect on the dynamics.

These results demonstrate that apsidal precession within a binary asteroid is strongly affected by the secondary. While the contribution of the shape of the secondary is relatively easy to compute, there is also a contribution from the secondary's spin rate. Indeed, the secondary's libration angle at a specific point in the orbit will have an effect on the apsidal precession rate. Thus, perturbations to the spin of a secondary will change the precession rate, along with perturbations to the eccentricity. In fact, these are not independent, as changes to the secondary's spin will affect the eccentricity, and vice versa. This once more highlights the coupled spin-orbit dynamics in these systems.

### 3.5.1 Comparison with Analytic Models

Next we compare these results with the analytic equations for apsidal precession rate. To calculate the precession rate using 3.21, we integrate our equations of motion to get a time history for true anomaly and libration angle, then average the time history of $\dot{\varpi}$ to come up with an average apsidal precession rate. In using the model in [95], we calculate the libration amplitude by averaging the local maximums within the libration angle time history. Since there are a range of frequencies and amplitudes within the libration angle [96], this approach gives a more representative value for the libration amplitude.

The comparison between these three approaches in shown in Fig. 3.14. We see fairly good agreement using Eq. 3.21, although the curve is noisier than the numerical solution thanks to the averaging approach. The forced libration solution from [95] diverges sharply from the numerical solution. This is expected, since this equation only considers the forced libration. When the numerical solution only has forced libration, then the model in [95] matches the numerical solution closely. In this system, a spin perturbation around 7°/hour eliminates free libration from the system, only leaving the forced libration. Around this point, all three models have a close match for the precession rate.

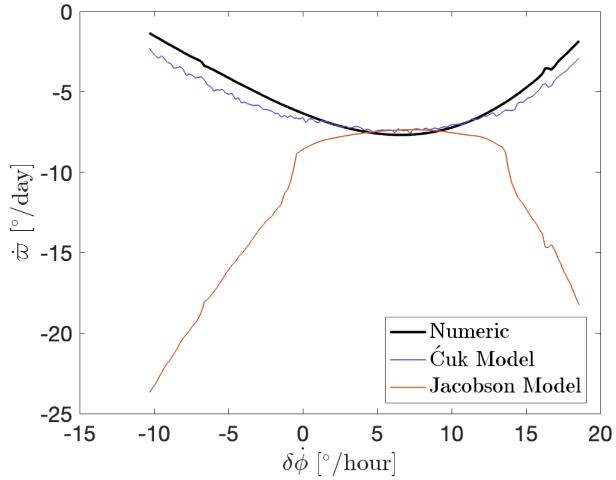

Figure 3.14: A comparison between the numerically calculated apsidal precession rate and the analytic expressions. The Ćuk Model corresponds to Eq. 3.21 and the Jacobson Model corresponds to the result in [95].

## 3.6 Resonances and Out-of-Plane Rotation

So far we have shown how the secondary rotation can affect the orbit dynamics in a binary asteroid. However, this discussion has been limited to only major principal axis rotation. We now begin to investigate how NPA rotation in the secondary changes these results. The first important consideration is understanding what system parameters make the secondary susceptible to NPA rotation. The main driver of this is resonances within the system. In Section 3.4.1 we showed how to calculate the natural frequencies within the planar system. We now extend that to three dimensions using the spherical-restricted F2BP.

The potential energy between two bodies taken to a second order approximation is [69]

$$U = \frac{-Gm_A m_B}{r} - \frac{\mathcal{G}}{2r^3}[m_A \mathrm{Tr}(I_B) + m_B \mathrm{Tr}(I_B)] + \frac{3\mathcal{G}}{2r^5}\vec{r}\cdot[m_A \mathbf{C_B}^T \mathbf{I}_B \mathbf{C_B} + m_B \mathbf{C_A}^T \mathbf{I}_A \mathbf{C_A}]\cdot\vec{r}. \quad (3.23)$$

For the spherical restricted F2BP, body $A$ is a sphere while body $B$ is an arbitrary 3D massive asteroid. Since body $A$ is a sphere, the term $\vec{r}\cdot\mathbf{C_A}^T\mathbf{I}_A\mathbf{C_A}\cdot\vec{r}$ can simply be written as $r^2 I_S$ where

$I_S$ is the diagonal entry of $\mathbf{I}_A$ (i.e., the moment of inertia of a uniform sphere) and $\mathrm{Tr}(\mathbf{I}_A)$ reduces to $3I_S$.

If the position vector $\vec{r}$ is written in the frame of body $B$, $\mathbf{C_B}$ then becomes the identity matrix. With these simplifications, the second order potential energy becomes

$$U = \frac{-\mathcal{G}m_A m_B}{r} - \frac{\mathcal{G}}{2r^3}[m_A \mathrm{Tr}(\mathbf{I}_B)] + \frac{3\mathcal{G}}{2r^5}\vec{r}\cdot[m_A\mathbf{I}_B]\cdot\vec{r}. \tag{3.24}$$

Defining the state vector as $X = [\vec{r}, \dot{\vec{r}}, \vec{\omega}]^T$, the state dynamics can thus be written as

$$\dot{\vec{X}} = \begin{bmatrix} \dot{\vec{r}} \\ -2\tilde{\vec{\omega}}\dot{\vec{r}} + \tilde{\vec{r}}\dot{\vec{\omega}} - \tilde{\vec{\omega}}\tilde{\vec{\omega}}\vec{r} - \frac{\partial U}{\partial \vec{r}} \\ \mathbf{I}_B^{-1}\left[-\tilde{\vec{\omega}}\mathbf{I}_B\vec{\omega} + m\vec{r}\times\frac{\partial U}{\partial \vec{r}}\right] \end{bmatrix} = \vec{F}(\vec{X}) \tag{3.25}$$

and the equilibrium conditions are

$$\dot{\vec{r}} = 0 \tag{3.26}$$

$$\tilde{\vec{\omega}}\tilde{\vec{\omega}}\vec{r} = -\frac{\partial U}{\partial \vec{r}} \tag{3.27}$$

$$\tilde{\vec{\omega}}\mathbf{I}_B\vec{\omega} = m\vec{r}\times\frac{\partial U}{\partial \vec{r}}. \tag{3.28}$$

Here we are using the notation where the tilde operator corresponds to the $3\times 3$ skew-symmetric cross-product matrix. With these equilibrium conditions, the linearized dynamics matrix at equilibrium can be calculated as

$$\left.\frac{\partial \vec{F}}{\partial \vec{X}}\right|_{\vec{X}_0} = \left[\begin{array}{c|c|c} [\mathbf{0}]_{3\times3} & [\mathbf{U}]_{3\times3} & [\mathbf{0}]_{3\times3} \\ \hline m\tilde{\vec{r}}\mathbf{I}_B^{-1}\left[\tilde{\vec{r}}\frac{\partial^2 U}{\partial \vec{r}^2} - \widetilde{\frac{\partial U}{\partial \vec{r}}}\right] - \tilde{\vec{\omega}}\tilde{\vec{\omega}} - \frac{\partial^2 U}{\partial \vec{r}^2} & -2\tilde{\vec{\omega}} & \tilde{\vec{r}}\mathbf{I}_B^{-1}\left[-\tilde{\vec{\omega}}\mathbf{I}_B + \widetilde{\mathbf{I}_B\vec{\omega}}\right] + \tilde{\vec{\omega}}\tilde{\vec{r}} + \widetilde{\tilde{\vec{\omega}}\vec{r}} \\ \hline m\mathbf{I}_B^{-1}\left[-\widetilde{\frac{\partial U}{\partial \vec{r}}} + \tilde{\vec{r}}\frac{\partial^2 U}{\partial \vec{r}^2}\right] & [\mathbf{0}]_{3\times3} & \mathbf{I}_B^{-1}\left[-\tilde{\vec{\omega}}\mathbf{I}_B + \widetilde{\mathbf{I}_B\vec{\omega}}\right] \end{array}\right]. \tag{3.29}$$

This gives the linearized dynamics equation

$$\begin{bmatrix} \delta\dot{\vec{r}} \\ \delta\ddot{\vec{r}} \\ \delta\dot{\vec{\omega}} \end{bmatrix} = \frac{\partial \vec{F}}{\partial \vec{X}}\bigg|_{\vec{X}_0} \begin{bmatrix} \delta\vec{r} \\ \delta\dot{\vec{r}} \\ \delta\vec{\omega} \end{bmatrix}. \tag{3.30}$$

Reference [50] carries out the operations in the dynamics matrix to obtain a simplified expression, from which they derive equations for the four fundamental frequencies after reducing the matrix to $8 \times 8$. We will walk through the process of reducing this matrix using the angular momentum integral. However, rather than obtaining expressions for the frequencies, we will directly solve for them using spectral decomposition of the reduced dynamics matrix.

The magnitude of the angular momentum provides an integral of motion allowing us to reduce the dynamics matrix from $9{\times}9$ to $8{\times}8$. In practice, this leads to eliminating the $\omega_3$ ($x_9$) contribution, which would otherwise result in a zero eigenvalue. To reduce the matrix, we can break the problem up as

$$\delta\dot{\vec{X}} = \begin{bmatrix} A_y & A_{8\times1} \\ A_{1\times8} & A_9 \end{bmatrix} \begin{bmatrix} \delta\vec{y} \\ \delta x_9 \end{bmatrix} \tag{3.31}$$

where $\vec{X}$ is the state, $\vec{y}$ is the first 8 states (excluding $x_9$), and the full dynamics matrix is called $A$, which we have broken up into convenient submatrices. This allows us to write

$$\delta\dot{\vec{y}} = A_y\delta\vec{y} + A_{8\times1}\delta x_9. \tag{3.32}$$

The angular momentum magnitude integral, $h$, is linearized and written as,

$$\frac{\partial h}{\partial \vec{X}}\delta\vec{X} = 0, \tag{3.33}$$

where the angular momentum vector is defined as

$$\vec{h} = \mathbf{I}_B\vec{\omega} + m\vec{r} \times (\dot{\vec{r}} + \vec{\omega} \times \vec{r}). \tag{3.34}$$

This can be expanded by splitting the state,

$$\frac{\partial h}{\partial \vec{y}}\delta\vec{y} + \frac{\partial h}{\partial x_9}\delta x_9 = 0. \tag{3.35}$$

Finally, we can write

$$\delta x_9 = \frac{\partial h}{\partial \vec{y}} \delta \vec{y} \left( \frac{-\partial h}{\partial x_9} \right)^{-1}. \tag{3.36}$$

After substitution, we obtain

$$\delta \dot{\vec{y}} = A^* \delta \vec{y}, \tag{3.37}$$

with

$$A^* = \left( A_y - A_{8\times 1} \frac{\partial h}{\partial \vec{y}} \left( \frac{-\partial h}{\partial x_9} \right)^{-1} \right). \tag{3.38}$$

At an equilibrium point it becomes simple to calculate the $A^*$ matrix and in turn find its spectral decomposition, with the zero eigenvalue corresponding to $\omega_3$ removed. The presence of real components in any of the eigenvalues of $A^*$ would correspond to unstable motion. Furthermore, the eigenvalues can be leveraged to find resonances between the system's fundamental frequencies. Using this approach, we can compute the fundamental frequencies of the secondary's motion as a function of its axial ratios $a/b$ and $b/c$.

We performed a grid search over the full solution space of axis ratios, ranging from $1 < a/b < 1.5$ and $1 < b/c < 1.5$. These limits are informed by observations [6]. For each value of $a/b$ and $b/c$, the inertia tensor is computed for a uniform triaxial ellipsoid. The matrix $A^*$ (Eq. 3.38) is then evaluated for each value of $a/b$ and $b/c$ at their respective equilibrium points. We find that all eigenvalues over this solution space are purely imaginary, which at first seem to indicate stable motion about the equilibrium point.

Because the spectral decomposition produces eight conjugate frequencies, there are only four unique values leading to four fundamental frequencies. Beyond the orbital frequency (mean motion) and in-plane free libration we calculated in the planar problem (see Sec. 3.4.1), we now add two out-of-plane frequencies, relating to the precession and nutation of the secondary [90].

Although the eigenvalue analysis only produces imaginary eigenvalues for all shapes (initially indicating rotational stability), we find a multitude of resonances among the fundamental frequencies upon closer examination. These resonances indicate areas in the solution space in which this linear model is no longer accurate, and nonlinear effects become important. Figure 3.15 shows each resonance between the various fundamental frequencies up to 5:1. Shapes near these resonances are susceptible to NPA rotation given small perturbations to the system. These resonances are similar to those analytically computed for gravity gradient torques [99]. Notably, we see resonances at $a/b = 1.1$ and $a/b = 1.4$. We have already seen evidence of these resonances in Sec. 3.4.

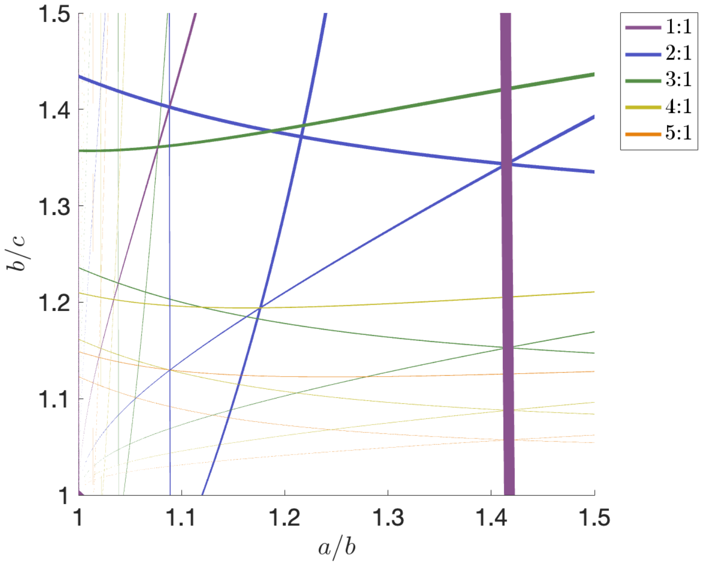

Figure 3.15: The resonances of the four fundamental frequencies up to 5:1. The line weight is a reflection of the size of each resonance region. Thus, thicker lines allow for a wider range of secondary shapes to excite that resonance.

### 3.6.1 Secondary NPA Rotation

To discuss NPA rotation in the secondary, we need to expand our description of the secondary's attitude. In planar cases we can describe this using a single libration angle. Allowing for full three-dimensional rotation requires a more careful description. To accomplish this, we define an additional coordinate frame, the rotating Hill frame. In this Hill frame, the $x$-axis points from the primary to the secondary, the $z$-axis is aligned with the orbit's angular momentum vector, and the $y$-axis completes the triad. Formally, this is defined as:

$$\mathcal{H} : [\mathcal{O}_A; \hat{r}, \hat{\theta}, \hat{h}_{orb}]. \tag{3.39}$$

We describe the secondary's attitude relative to this frame using the classical set of 1-2-3 Euler angles, corresponding to roll, pitch, and yaw. An illustration of this is shown in Fig. 3.16. For a system in the singly synchronous configuration, all three Euler angles are equal to zero over all time. In planar rotation, $\theta_3$ is equal to the libration angle.

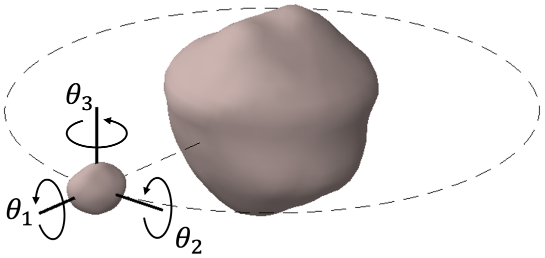

Figure 3.16: The 1-2-3 Euler angles measuring the secondary's attitude in roll-pitch-yaw relative to the rotating Hill frame.

NPA rotation in the secondary can take a wide range of forms. To investigate this, we simulate a range of perturbed Didymos-Dimorphos systems after the DART impact. This is a Monte Carlo suite of simulations allowing for uncertainties within the physical shapes and sizes of the asteroids, the orbit parameters, and the DART impact geometry. The result is three general regimes of NPA rotation.

To explore the regimes of possible NPA rotation, we plot the average of the magnitude of the pitch angle $|\bar{\theta}_2|$ as a function of the average of the magnitude of the yaw angle $|\bar{\theta}_3|$, shown in Fig. 3.17.

Immediately, we see a clustering of small $|\bar{\theta}_2|$ and small $|\bar{\theta}_3|$. We define this as regime 1, which is characterized by small out-of-plane rotation, and is near to principal axis rotation. We do not plot $|\bar{\theta}_1|$ as it does not provide much additional information, but we note regime 1 does permit the barrel instability, in which the secondary can roll about its long axis [91]. While there is technically NPA rotation within this regime, it is not large. Thus, we call this regime 'no tumbling'.

Above this region, we see a clustering of systems with larger $|\bar{\theta}_2|$ values, still with relatively small $|\bar{\theta}_3|$ values. These systems see a large out-of-plane rotation, but are still pointing on average toward the primary (i.e. $\theta_3 < 90°$), thus regime 2 is characterized by NPA rotation generally within the on-average synchronous configuration. Occasionally, the secondary may actually flip around and experience NPA rotation in the anti-synchronous configuration. Because of the similarity of these states we do not make a distinction between them, and thus the scattering of points to the right of the upper point cluster are still considered in regime 2 of NPA rotation. The barrel instability is common in this regime. This regime is not formally defined, and thus there is a transition region between regime 1 and regime 2. The NPA rotation in this regime is significant, but still generally limited to within on-average synchronous or anti-synchronous rotation. We call this regime ‘epicyclic tumbling’.

Lastly, we define a third regime of NPA rotation, characterized by more chaotic rotation. In this regime we cannot say the secondary is on-average synchronous or anti-synchronous. We call this regime ‘fully tumbling’, as the attitude of the secondary is completely unpredictable.

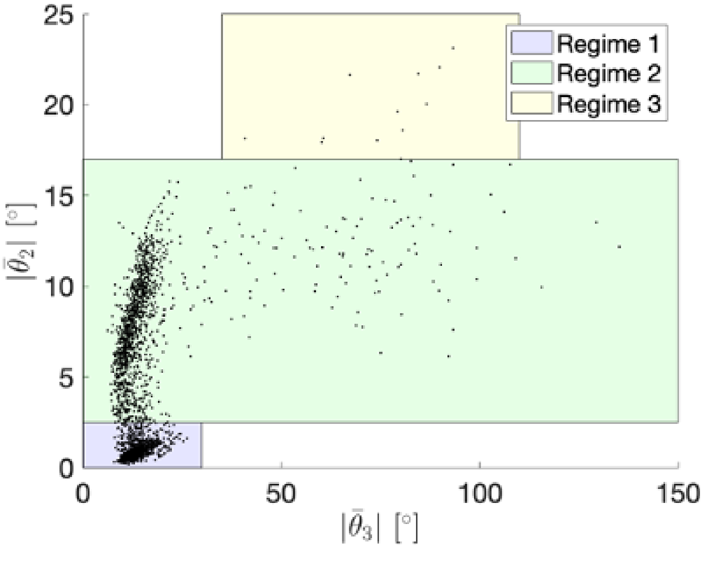

Figure 3.17: The three regimes of NPA rotation, plotted as a function of average yaw and pitch angles. The shaded regions are not hard cutoffs, but serve to aid interpretation.

### 3.6.2 Effect on Eccentricity

When the secondary enters into NPA rotation, the rotational angular momentum of the secondary will decrease on average as its spin axis moves away from its major principal inertia axis. As a result, the orbital angular momentum will on-average increase to compensate, which reduces the orbit's eccentricity. If the increase in orbital angular momentum, and corresponding decrease in eccentricity, is sufficient, it can cause the orbit to move back to an equilibrium configuration where the true anomaly begins librating again and the argument of periapsis tracks the secondary. Thus, unstable secondary rotation actually leads the orbit closer to equilibrium dynamics. The nearest equilibrium orbit to the perturbed orbit is at the same value of observable semimajor axis (i.e. orbital energy) but at the equilibrium eccentricity.

To illustrate this point, we use an example of a system where the secondary is near a resonance. The relative 1-2-3 Euler angles, corresponding to roll-pitch-yaw of the secondary, are shown in Fig. 3.18a. This system demonstrates an attitude instability as the secondary is in a state of epicyclic tumbling beginning around 40 days into the simulation. As an illustration, the Euler angles reveal that, even while the secondary is tumbling, it still remains either generally aligned or anti-aligned with Didymos. It occasionally switches between states where its long axis is on-average pointing toward Didymos ($\theta_1$ and $\theta_3$ oscillating around $0^\circ$) to pointing away from Didymos ($\theta_1$ and $\theta_3$ oscillating around $180^\circ$).

The specific orbital and secondary angular momenta of this system are plotted in Fig. 3.18b. As the secondary enters a state of tumbling, the orbital angular momentum increases on average. The dashed black line in Fig. 3.18b corresponds to the calculated angular momentum of the nearest equilibrium orbit from Eq. 3.2 using the post-impact observable semimajor axis. The orange line is a 1-day average of the angular momentum to aid in interpretation. As the secondary tumbles, there is an exchange of angular momentum between the secondary and the orbit.

As the secondary begins tumbling, the specific orbit angular momentum increases to its equilibrium value. At the same time, the Keplerian eccentricity decreases to its equilibrium value, as shown in Fig. 3.18c, where the dashed black line is the calculated equilibrium eccentricity from Eq. 2.33. The time period when the specific orbital angular momentum is equal to its equilibrium value is roughly the same time period when the Keplerian eccentricity is equal to its equilibrium value. This is also roughly the same time period when the true anomaly, shown in Fig. 3.18d, returns to a state of libration, before once again tracking when the orbital angular momentum again decreases and the osculating eccentricity increases. As the secondary enters a tumbling state, the orbital angular momentum increases on average. We see an exchange of angular momentum between the orbit and the secondary when the secondary is tumbling. At some threshold, the true anomaly switches from circulating to librating, then back to circulating as angular momentum is exchanged between the orbit and secondary. Comparing the true anomaly to the orbit angular momentum, this threshold is near when the orbital angular momentum crosses its nearest equilibrium value, or equivalently when the osculating eccentricity decreases to its equilibrium value.

Thus, we have demonstrated how the onset of tumbling in the secondary can have significant effects on the orbit dynamics, a general result beyond the application to Didymos and DART. We note this decrease in eccentricity is not caused by enhanced dissipation (e.g. [100]), which is not modeled here, but by the commensurability between the secondary and orbit angular momenta. The angular momentum lost by the secondary is sufficient to directly decrease the orbit's eccentricity. As the secondary begins tumbling, the decrease in eccentricity is substantial and rapid as the orbit becomes more circular and settles into the nearest equilibrium orbit. Thus, the onset of tumbling in the secondary may be observable from the ground in lightcurve data. As the system continues to evolve, this exchange in angular momentum can continue, causing the eccentricity to fluctuate. Furthermore, the true anomaly can then switch between epochs of circulating and librating, depending on the orbit's angular momentum. These dynamics are a direct result of the spin-orbit coupling in these systems.

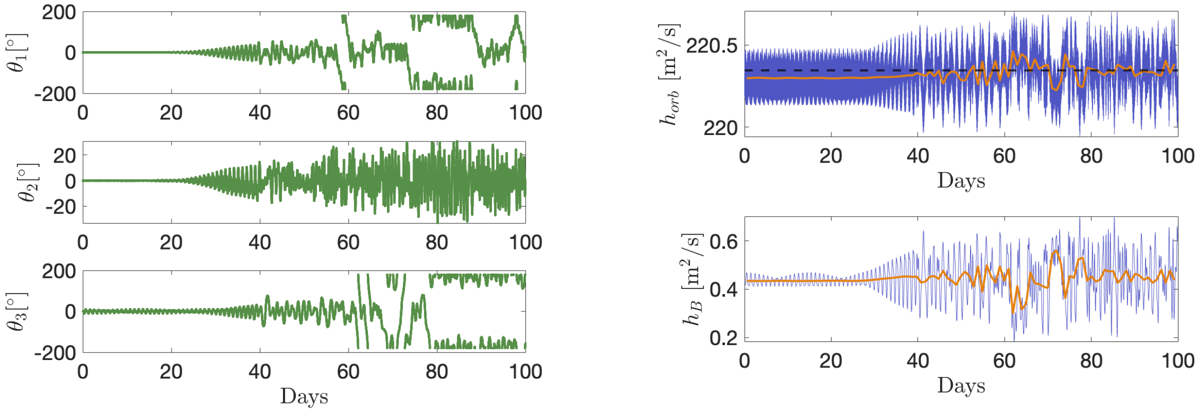

(a) Euler Angles for a Tumbling Secondary

(b) Orbit Angular Momentum for a Tumbling Secondary

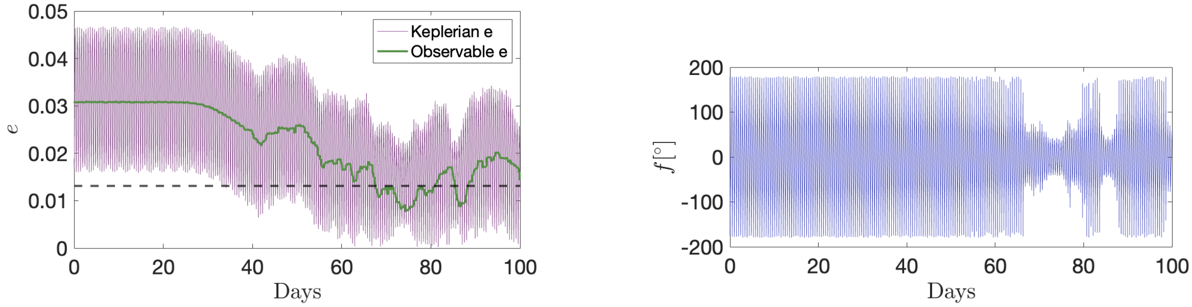

(c) Eccentricity for a Tumbling Secondary

(d) True Anomaly for a Tumbling Secondary

Figure 3.18: (a) The relative 1-2-3 Euler angles (roll-pitch-yaw) of the secondary of an unstable system that begins tumbling. Significant NPA rotation begins at around 40 days into the simulation. (b) The specific orbital angular momentum (top) and secondary angular momentum (bottom) of a system that begins tumbling. The dashed line corresponds to the nearest equilibrium orbit, and the orange line is a 1-day moving average of the angular momentum. (c) The Keplerian and observable eccentricity of a system that begins tumbling. As the secondary enters a tumbling state, the eccentricity decreases as the orbital angular momentum increases. The dashed line corresponds to the equilibrium Keplerian value. (d) The true anomaly of a system that begins tumbling.

### 3.6.3 Effect on Orbit Period

As discussed in Sec. 3.4, the stroboscopic orbit period is not constant in a perturbed system. While the secondary is in stable libration, the orbit period fluctuates at frequencies determined by the libration and precession.

The stroboscopic orbit period for a tumbling secondary in Didymos is plotted in Fig. 3.19 over time. We see the expected orbit period variations dominated by the orbit's precession and secondary libration prior to tumbling, but as the secondary enters epicyclic tumbling, the amplitude of orbit period variations increases significantly and the periodicity is lost. This implies that, along with a decrease in observed eccentricity, large deviations from expected mutual event timings in lightcurves can also indicate tumbling. Thus, we have established two independent indications of tumbling that are observable in lightcurve observations: a rapid decrease in the observable eccentricity followed by relatively large, aperiodic variations in the stroboscopic orbit period. So even if the spin state of the secondary is not directly observable from the ground, it is still possible to predict if it is tumbling or not from other features in the lightcurves. However, given observational errors and noise, it may be difficult to detect these characteristics in ground-based lightcurves [96].

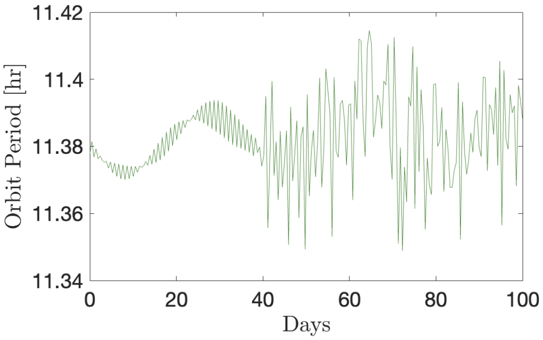

Figure 3.19: Stroboscopic orbit period over time for the tumbling case study in the previous section. Prior to the onset of tumbling, the orbit period experiences small, periodic variations. As the secondary begins to tumble, the amplitude of orbit period variations increases and the periodicity is absent.

### 3.6.4 Effect on Precession Rate

Next we examine the role played by out of plane rotation on the orbital precession rate. Specifically, we are interested in how the apsidal precession rate is affected by NPA rotation, and will continue using Didymos as an illustration.

An example of NPA rotation with no tumbling is shown in Figure 3.20. We see generally well-behaved dynamics, with NPA rotation starting around 70 days into the simulation. However, the NPA rotation is small, and as a result we see nearly constant semimajor axis and eccentricity, and an on-average constant apsidal precession rate. Thus, this level of NPA rotation has no significant effect on the precession rate.

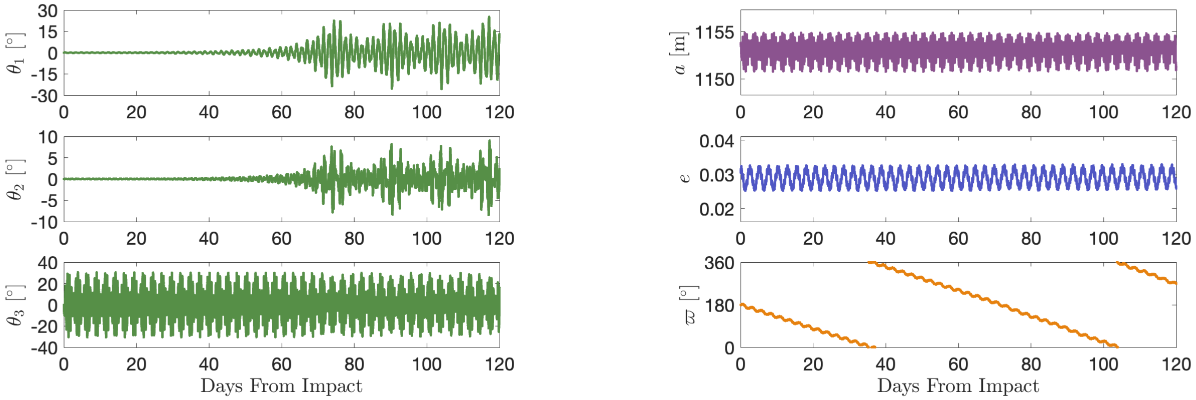

(a) Precession rate as a function of spin perturbation

(b) Precession rate as a function of libration amplitude

Figure 3.20: Illustration of no tumbling in NPA rotation, characterized by small out-of-plane Euler angles, a constant precession rate, and relatively constant eccentricity

In epicyclic tumbling, the libration amplitude varies as angular momentum is exchanged between the secondary and the orbit, and as a result the apsidal precession rate can vary as well. An example of epicyclic tumbling is shown in Figure 3.21. The barrel instability begins around 40 days into the simulation and is shown by ‘flipping’ of the roll angle. As angular momentum is exchanged between the secondary and orbit, we see a corresponding drop in eccentricity, as discussed in Sec. 3.6.2. The semimajor axis sees a small amount of variation, and the apsidal precession rate can fluctuate significantly away from the average rate. Since the eccentricity is not constant, we see corresponding changes to the apsidal precession rate as expected.

An example of constant tumbling is shown in Figure 3.22. Here we see no real structure to the Euler angles, and all 3 see significant amplitudes. This corresponds to fully chaotic secondary rotation. The semimajor axis sees more variation, along with the eccentricity. Interestingly, the longitude of periapsis does not have much of a secular drift. It usually remains around some value before rapidly jumping to a new value, without any consistent precession.

From these examples it is evident that NPA rotation of the secondary has a substantial impact

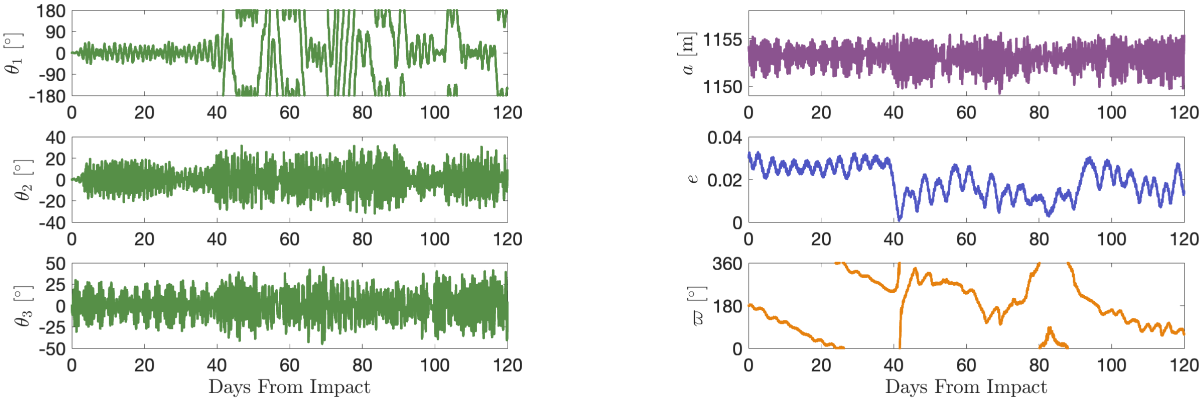

(a) Precession rate as a function of spin perturbation

(b) Precession rate as a function of libration amplitude

Figure 3.21: Illustration of epicyclic tumbling in NPA rotation, characterized by significant out-of-plane Euler angles and occasional rapid increases in the precession rate, and rapid changes in the eccentricity.

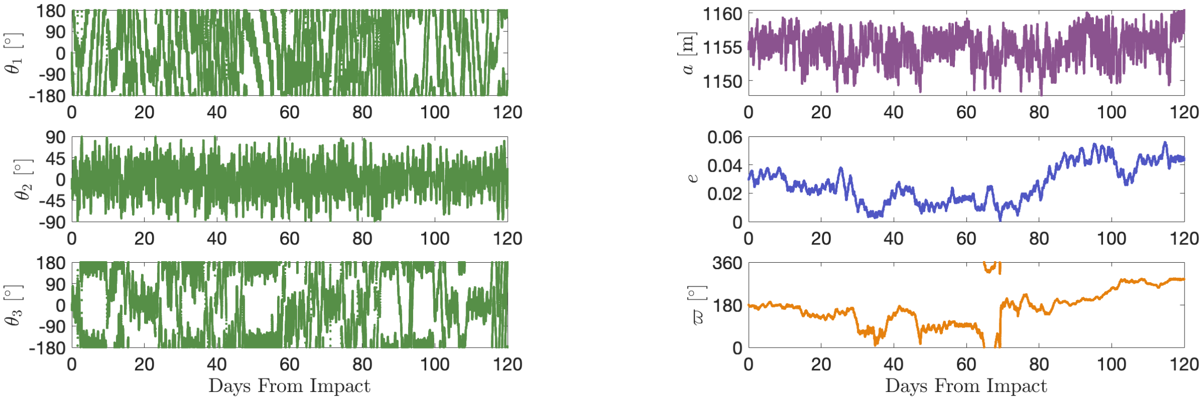

(a) Precession rate as a function of spin perturbation

(b) Precession rate as a function of libration amplitude

Figure 3.22: Illustration of constant tumbling in NPA rotation, characterized by large and uncorrelated out-of-plane Euler angles, and relatively constant precession rate and eccentricity.

on the apsidal precession of the orbit. While rotation within the no tumbling regime does not have much of an effect, epicyclic tumbling can cause significant departures from the expected precession rate, and constant tumbling can destroy this secular drift altogether. Thus, measurements of the apsidal precession rate in binary asteroids can also elucidate the secondary's rotational stability.

## 3.7 Conclusion

This chapter has explored the spin-orbit coupled dynamics within a perturbed binary asteroid. We calculated the perturbation necessary to allow the true anomaly to transition from libration to circulation. As the angular momentum is perturbed from the equilibrium value, an exchange of angular momentum between the secondary and the orbit begins, driven by libration in the secondary. The natural frequencies of libration strongly depend on the shape of the secondary. Larger librations in the secondary mean larger variations in its spin rate, which also manifests as larger fluctuations within the orbit period.

Both the secondary's shape and rotation play a major role in determining the apsidal precession rate of the orbit. The precession rate is maximized (to be specific, the fastest regression rate) when any free libration is eliminated from the system. Thus, free libration has a major effect on the precession rate and eccentricity of the orbit.

When natural frequencies within the system are in resonance, the secondary is susceptible to entering a state of NPA rotation. This generally falls into one of three categories: no tumbling, epicyclic tumbling, or constant tumbling. The onset of NPA rotation can have major effects on the orbit. The corresponding on-average decrease in secondary angular momentum manifests in the orbit as a rapid reduction in eccentricity, sometimes to the point where the true anomaly returns to oscillation around periapsis. The variations in the orbit period can become large and chaotic due to the angular momentum exchange, and the precession rate can rapidly change or disappear altogether. These changes in the orbit are an indicator of NPA rotation in the secondary without any need to directly observe its rotational state.

# Chapter 4

# Internal Dissipation

## 4.1 Introduction

While the dynamics of a perturbed binary asteroid are important to study, these dynamics are transient. Internal energy dissipation within these systems will inevitably evolve the dynamics back to an equilibrium configuration. There are two main mechanisms of energy dissipation we will consider in this chapter, both stemming from the deformation of the bodies. The first is tidal torque, in which the tidal forces of both bodies act to move the system into a synchronous equilibrium [38, 40, 70]. The second is non-principal axis (NPA) rotation, in which rotation about any axis other than the major principal axis will dissipate energy until the major principal axis is aligned with the angular momentum [101, 102, 103, 104, 105]. Both these mechanisms will drive the system toward the doubly synchronous equilibrium in which the two asteroids are mutually tidally locked, with their spin angular momentum vectors aligned with their major principal axes and the orbit angular momentum vector [39]. However, for NEAs and small MBAs, the primary will not synchronize with the orbit as it is counteracted by YORP and the small size of the secondary leads to very long dissipation times. Contrasted with the relatively short lifespan of NEAs, these systems do not reach the doubly-synchronous equilibrium.

While many studies focus on energy dissipation in the two-body problem, they generally ignore the specific dynamical regime that Didymos will inhabit after the DART impact: a system which is generally synchronous but with nonzero libration of the secondary [40, 38]. Here we define libration as any angular deviation of the secondary's long axis away from the tidally locked configuration, but smaller than 90° so the secondary remains on-average synchronous. Generally there are two modes of libration: free and forced [70]. While forced libration is driven by eccentricity, free libration is governed by the average libration over an orbit period and is thus eccentricity-agnostic [106]. Given the strongly coupled nature of binary asteroids, we make no distinction between these two modes and simply adopt the physical libration angle. More recently, [107] analyzed energy dissipation in a tidally perturbed librating body. This is the same regime we are interested in here, but we attempt to relax the small-libration assumption from that work and extend results to binary asteroids, which orbit much closer than planet-moon systems. Another noteworthy study is that of [31], who apply a tidal torque model to binary asteroids. However, this analysis is limited to 2 dimensions, whereas we are interested in the full 3 dimensional dynamics. [100, 92] study tidal dissipation in coupled systems with some attention spent on the libration state, and our work falls in a similar vein but we focus on how different shapes and stiffness of the secondary affect the dissipation process.

## 4.2 Dissipation Models

In studying dissipation, we use the sphere-restricted F2BP. It is important to consider three-dimensional rotation, as this can have an effect on the dissipation rate. However, studies of energy dissipation necessarily span a long time period, so we use the sphere-restricted F2BP to allow for studies over longer time domains while allowing for the full three-dimensional rotation.

We introduce the methods of dissipation through non-rigid processes, both through tidal torque and NPA rotation, which rise from a combination of deformation, rotation, and translation of the bodies [108]. We ignore any surface motion on both the primary and secondary, which includes rotation-induced granular motion on the secondary's surface and any associated body reshaping, which changes the gravitational potential energy [58, 109], tidal saltation and YORP-induced landslides on the primary [110], and boulder movement on either body [111], which would also dissipate energy. We will assume any reshaping and surface motion to be small and intermittent, and the energy dissipated by these events to be negligible over time.

We will primarily focus on Didymos in this chapter, as the question of how long-lived its excited dynamical state will be following the DART impact is of interest to Hera [64], as well as interesting to the small body community in general, as this can help constrain the internal properties of rubble piles.

### 4.2.1 Tidal Torque

To describe energy dissipation from the system, we introduce equations for tidal torque to add to our dynamical model. In selecting a basic model for tidal torque, we have two choices: the constant $Q$ model, in which the rate of dissipation is driven by the ratio of tidal quality factor $Q$ and the simple Love number $k_2$ [70], or the constant time lag model, in which the angle between the tidal bulge and the line connecting the two bodies is a constant $\Delta t$ [112, 113]. Based on the physics of our problem setup, the secondary will librate about the synchronous configuration, and thus a constant lag angle would be inappropriate, as the lag angle should oscillate as a result of the libration. For this reason we select the constant $Q$ model, which is the same model adopted by [31], in which the tidal torque is defined as:

$$\Gamma = -\text{sign}(\omega - \omega_{orb}) \frac{3}{2} \left( \frac{3}{4\pi\rho} \right)^2 \frac{G M_A^2 M_B^2}{r^6 R} \frac{k}{Q} \tag{4.1}$$

where the body's angular velocity is $\omega$, the orbit's angular rate is $\omega_{orb}$, $R$ is the reference radius for the body, $\rho$ is its density, and $Q/k$ is the tidal dissipation ratio. The tidal quality factor $Q$ is related to the tidal bulge lag angle ($Q \sim 1/\sin\epsilon$), while the Love number $k_2$ describes the level of body deformation due to the tidal potential. Henceforth we drop the subscript 2 on the Love number for simplicity. A large value of $Q/k$ corresponds to a more stiff body that dissipates more slowly. In reality, the tidal dissipation is far more complicated than simply selecting constant values for the unknown $Q/k$ values. As pointed out by [114], tidal dissipation in binary asteroids, including rubble piles, may be governed primarily by the body's viscosity, rather than rigidity. Others, including [38] and [115], argue that friction is a critical parameter. Since there is no current estimate for the viscosity of rubble pile asteroids, we adopt the friction approach. Furthermore, while many studies assume the quality number $Q$ to be constant, this parameter depends on the tidal frequency. Further complicating this relationship is the fact that the tidal quality number is not a linear function of the tidal frequency, and can either increase or decrease with the frequency [116]. We also are left with the problem of the tidal lag angle oscillation. To address this we adopt the same solution as [31]; we will linearize the tidal torque around the point where $(\omega - \omega_{orb})$ is near zero so the torque does not immediately switch signs as the secondary librates (see Appendix C therein for details on this linearization). This linearization is necessary, as the tidal bulge is a physical phenomenon and requires a finite time to cross between leading or trailing the tide-raising body.

Note that [40] point out the simple tidal model assumes the two bodies are widely separated, whereas the separation between Didymos and Dimorphos is only slightly larger than 3 primary radii. In their work, [40] calculate that higher order terms in the tidal potential speed up the process of tidal evolution. However, they also find that uncertainties in the system, particularly surrounding $Q/k$, dominate over the higher order tidal expansion. Thus, we continue with the simple tidal model given the large uncertainty associated with the system bulk density and physical properties, while keeping in mind higher order terms in the tidal model will only increase the rate of damping in the system. Thus, the error associated with this tidal model is considered to be secondary to the considerable uncertainty on the $Q/k$ coefficient for our purposes.

Unfortunately, given the lack of knowledge on the physical parameters of rubble piles, particularly their viscosity, we cannot calculate an accurate value for $Q/k$. For lack of a better option, we surrender ourselves to the typical simplifications surrounding the factor $Q/k$, and we turn to the work by [115, 43], who derive an estimate for a constant $Q/k$ for rubble pile binary asteroids, which can be approximated by

$$\frac{Q}{k} \approx 300R \tag{4.2}$$

for $R$ in meters. This leads to a value for Didymos $Q_A/k_A \approx 1 \times 10^5$ and for Dimorphos $Q_B/k_B \approx 2.5 \times 10^4$. These values, and the linear scaling with radius, are consistent with constraints calculated using the age of binary asteroids [61]. Note this expression for $Q/k$ is frequency independent and derived for a non-synchronous binary system. However, we again emphasize there is large uncertainty associated with these values so this definition serves as a first-order approximation, as the error from uncertainties dominates over the error from the assumptions. Furthermore, these values are consistent with existing estimates for small bodies in the literature [43, 72, 117, 118]. However, there is not a consensus on this linear scaling. For example, [38] propose an inverse scaling of $Q/k$ with $R$, and even in their own work [115] point out a scaling with $R^{3/2}$ may be more accurate. Another consideration is if Dimorphos turns out to be monolithic instead of a rubble pile, its $Q/k$ value would likely be orders of magnitude higher [38]. Hence, the large uncertainty in $Q/k$ dominates over other errors associated with our model, and it is futile to develop a high fidelity tidal model while limited by this unknown parameter.

Returning to the tidal torque equation, this model is still only defined in 2-dimensions and we wish to extend this to a full 3-dimensional analysis, as out-of-plane rotation of the secondary is a possibility. This can be done with only a few corrections to the classic model. To start, we need to define a vector for the torque direction. The torque will act to push the spin rates of the asteroids into the synchronous equilibrium, but physically cannot act in the direction of the position vector of the secondary relative to the primary. We define the relative spin rate of a body:

$$\dot{\vec{\phi}} = \vec{\omega} - \vec{\omega}_{orb}. \tag{4.3}$$

We can then use this spin vector as the vector along which the torque acts, with a small correction so the torque in the radial direction is zero:

$$\hat{\Gamma} = -\frac{\dot{\vec{\phi}} - (\dot{\vec{\phi}} \cdot \hat{r})\hat{r}}{|\dot{\vec{\phi}} - (\dot{\vec{\phi}} \cdot \hat{r})\hat{r}|} \tag{4.4}$$

This formulation also takes care of the sign of the torque, as the torque will generally act in the direction opposite the relative spin rate, so that a secondary rotating faster than the orbit rate is slowed, while a secondary rotating slower will be sped up. Furthermore, any out-of-plane rotation is countered by the torque, with the exception of any spin about the relative position vector, as tidal torque can only act perpendicular to this direction. Thus, we don't need any further consideration on the sign of the torque and can remove the $-\text{sign}(\omega - \omega_{orb})$ expression from Eq. 4.1 and substitute Eq. 4.4 in its place.

While we formulated the 3D torque expression with the secondary in mind, it is also equally applicable to the primary, as tidal dissipation will ultimately drive the system to the doubly synchronous state. So we have developed expressions for the torque on both bodies. However, to accurately express the equations of motion we also need to consider the torque on the orbit. By the conservation of angular momentum, the torque on the orbit is simply

$$\vec{\Gamma}_{orb} = -(\vec{\Gamma}_A + \vec{\Gamma}_B). \tag{4.5}$$

However, to include this in the orbital equation of motion we will need to calculate this torque's effect on $\ddot{\vec{r}}$. Turning to the orbital angular momentum we know

$$\dot{\vec{H}} = \frac{d}{dt}(m\vec{r} \times \dot{\vec{r}}) = \vec{\Gamma}_{orb} \tag{4.6}$$

where $m = \frac{M_A M_B}{M_A + M_B}$. This gives

$$m\vec{r} \times \ddot{\vec{r}} = \vec{\Gamma}_{orb}. \tag{4.7}$$

We would like to solve this equation for $\ddot{\vec{r}}$ to update the orbital equation of motion with the tidal torque. We note that

$$\vec{r} \times (\vec{r} \times \ddot{\vec{r}}) = (\vec{r} \cdot \ddot{\vec{r}})\vec{r} - (\vec{r} \cdot \vec{r})\ddot{\vec{r}} = \vec{r} \times \frac{\vec{\Gamma}_{orb}}{m}, \tag{4.8}$$

which can be arranged to find

$$\ddot{\vec{r}} = \frac{\vec{\Gamma}_{orb} \times \vec{r}}{mr^2} + \frac{\vec{r} \cdot \ddot{\vec{r}}}{r^2}\vec{r}. \tag{4.9}$$

However, this is not a unique solution, as for any real number $K$ we can find

$$\ddot{\vec{r}} = \frac{\vec{\Gamma}_{orb} \times \vec{r}}{mr^2} + K\frac{\vec{r} \cdot \ddot{\vec{r}}}{r^2}\vec{r} \tag{4.10}$$

is also a valid solution as a result of the dot product. Thus, we must solve the problem of a non-unique solution. We note that whenever the torque $\Gamma_{orb}$ is equal to zero, there should be no contribution to the equation of motion. So we choose $K = 0$ to enforce this constraint (alternatively, we force the acceleration to be perpendicular to the position vector, so that $\vec{r} \cdot \ddot{\vec{r}} = 0$), and we are left with

$$\ddot{\vec{r}} = \frac{\vec{\Gamma}_{orb} \times \vec{r}}{mr^2} = \vec{\gamma}_{orb}. \tag{4.11}$$

We have introduced the term $\vec{\gamma}_{orb}$ as the acceleration due to the torque on the orbit. This makes sense given the physical context, where the tides should not have any effect in the radial direction. Note that this formula must be calculated in an inertial frame as it is derived from the orbit angular momentum. Once computed in an inertial frame, it can be transformed into the secondary body-fixed frame for use in the equations of motion.

### 4.2.2 NPA Rotation

Any NPA rotation of the secondary will act to dissipate energy while keeping its angular momentum constant, until its maximum principal inertia axis is aligned with its angular momentum. There is a wide variety of work that has considered this problem [101, 103, 104, 105], but for the most applicable to this work we turn to [102], who calculate the rate of energy dissipation in a triaxial ellipsoid rotating in either long-axis mode or short-axis mode. The full expression for energy dissipation in a triaxial ellipsoid undergoing NPA rotation is quite complicated, and we report a condensed version here,

$$\dot{E}_{NPA} = \frac{a^4 \rho M_B \tilde{\omega}_B^5}{\mu Q} \Psi, \tag{4.12}$$

where $a$ is the secondary's longest semiaxis, $\tilde{\omega}_B$ is its nominal rotation rate, and $\Psi$ is a complicated function of the secondary's shape, Poisson's ratio, and an elliptic modulus. We omit the details here and refer the reader to [102] for the full expression. This expression uses the Lamé constant $\mu$ instead of the Love number $k$, but we can relate our $Q/k$ to $\mu Q$ through [70, 115]:

$$\mu Q \sim \mathcal{G} \frac{Q}{k} \rho^2 R^2. \tag{4.13}$$

At the risk of sounding repetitive, we again highlight the shortfall of this relationship as pointed out by [114], as $Q$ is frequency dependent. Thus, the $Q$ selected for the tidal dissipation model is not necessarily the same $Q$ for NPA rotation, again introducing considerable uncertainty. However, we assume the driving frequencies for tidal and NPA dissipation are the same, and again for lack of a better option we adopt the same $Q$ for both methods of dissipation.

Because our dynamics only include rigid body motion, we must add a torque to simulate the effects of nonrigid energy dissipation. In the secondary's body-fixed frame, the torque does not change the secondary's angular momentum magnitude, only rotates it until it is aligned with the secondary's major principal inertia axis.

To obtain the torque, we start with the energy dissipation equation

$$\dot{E} = \vec{\omega}_B \cdot I_B \dot{\vec{\omega}}_B. \tag{4.14}$$

Next, we expand the equation $\dot{\vec{H}}_B = \vec{\Gamma}_{NPA}$ for secondary angular momentum $H_B$:

$$\vec{\Gamma}_{NPA} = I_B \dot{\vec{\omega}}_B + \vec{\omega}_B \times I_B \vec{\omega}. \tag{4.15}$$

By taking the dot product of this equation with $\vec{\omega}_B$, we can find an expression for the effective torque as a function of $\dot{E}$:

$$\vec{\omega}_B \cdot \vec{\Gamma}_{NPA} = \dot{E}_{NPA}. \tag{4.16}$$

Of course, due to the dot product, this is not a complete expression as we still need to define the direction of the effective torque $\vec{\Gamma}_{NPA}$. Since NPA dissipation will not change the angular momentum magnitude, only the angular momentum's direction relative to the body-fixed axes of the secondary, the effective torque must be perpendicular to the angular momentum. As a conceptual illustration, imagine a satellite undergoing torque-free tumbling. In this scenario, the satellite's angular momentum vector is constant, while dissipation reorients the satellite so that its principal axis is aligned with the angular momentum (and its kinetic energy is minimized). In the same sense, within the body-fixed frame of the secondary, its angular momentum will appear to rotate until its aligned with the principal axis, while maintaining a constant magnitude. This is accomplished by applying an effective torque perpendicular to the angular momentum, such that this torque only rotates the angular momentum vector, but does not scale it. Following [119], we define an intermediate vector

$$\vec{\kappa} = \vec{H}_B \times \hat{z} \tag{4.17}$$

where $\hat{z}$ is the secondary's maximum principal inertia axis. We then use this intermediate vector to define the torque unit vector

$$\hat{\Gamma} = \frac{\vec{H}_B \times \vec{\kappa}}{|\vec{H}_B \times \vec{\kappa}|}. \tag{4.18}$$

The effective torque will act to rotate the angular momentum vector $\vec{H}_B$ until it is aligned with the secondary's $\hat{z}$ direction. The effective torque is then calculated as

$$\vec{\Gamma}_{NPA} = \frac{\dot{E}}{\vec{\omega}_B \cdot \hat{\Gamma}}\hat{\Gamma}. \tag{4.19}$$

Note that in reality, the secondary angular momentum vector will not rotate and instead the body-fixed coordinate axes of the secondary will rotate to align $\hat{z}$ with the angular momentum vector. However, if we define our equations of motion in the secondary body-fixed frame as we have done, this torque will be appropriate to use.

### 4.2.3 Comparison

In order to compare our two methods of energy dissipation, we plot the rate of energy dissipation in the secondary as a function of the separation distance for a body rotating with a spin axis offset from its major principal axis by approximately 32°. This is near the switching point between long-axis and short-axis mode rotation, and thus NPA dissipation is near a maximum here. Fig. 4.1 shows the energy dissipation rates for the two mechanisms, highlighting that tidal dissipation is generally more than an order of magnitude stronger than NPA rotation for a close binary like Didymos. Despite this contrast, we still include the effects of NPA rotation as it does not significantly slow down the integration wall time.

While close systems like Didymos are dominated by tidal torque, wider systems see near-equal contributions from both tidal torque and NPA rotation, and NPA dissipation becomes dominant at very wide separations. The secondary shape and spin-axis obliquity will affect the rate of NPA rotation energy decay, but for Didymos the tidal torque will always be stronger owing to the close proximity of its secondary.

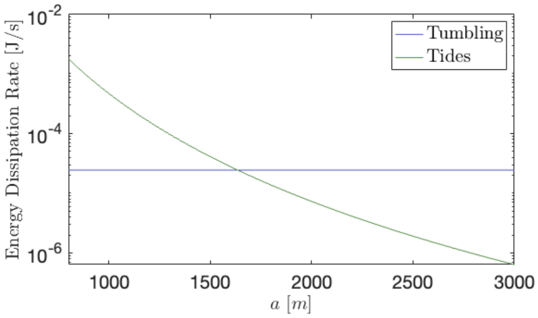

Figure 4.1: The rate of energy dissipation through tidal torque compared to NPA rotation as a function of separation. Tidal torque has orders of magnitude more of an effect than NPA rotation for a close binary system like Didymos.

Looking at a system with a semimajor axis of 1200 m, we next examine how the secondary's spin offset angle affects dissipation. Fig. 4.2 shows the dissipation rate as a function of the angle between the secondary's spin axis and its principal moment of inertia axis (we call this angle $\delta$, and a system with $\delta = 0°$ is in major principal axis spin). We see tidal dissipation is largely independent of the spin axis offset, but NPA rotation depends strongly on this angle. There is a discontinuity where the secondary switches from short-axis to long-axis mode rotation. Dissipation then quickly drops to zero as spin approaches either perfectly major ($\delta = 0°$) axis rotation.

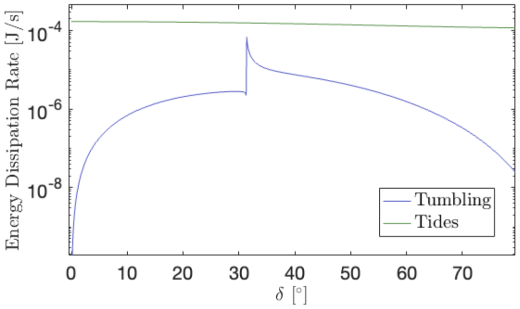

Figure 4.2: The rate of energy dissipation through tidal torque compared to NPA rotation as a function of secondary spin offset angle. The NPA dissipation is greatest near the discontinuity, where the secondary is switching between long-axis and short-axis rotation modes.

## 4.3 Dissipation Dynamics

In this work we will focus on two shapes of the secondary, one with $a/b = 1.2$, $b/c = 1.1$, and the other with $a/b = 1.4$, $b/c = 1.3$. In conjunction with the mean radius, we can solve for the semiaxes that define the ellipsoid, as well as the dimensionless shape parameter $S$ defined as

$$S = \frac{I_y - I_x}{I_z}. \tag{4.20}$$

Table 4.1 gives the dimensions of the two ellipsoids we will primarily use as Dimorphos, as well as their shape parameter $S$.

Table 4.1: Summary of the two triaxial ellipsoids used in this Section as the secondary shape.

| Shape | $a$ [m] | $b$ [m] | $c$ [m] | $S$ |
|---|---|---|---|---|
| $a/b = 1.2$, $b/c = 1.1$ | 95.6 | 79.7 | 72.4 | 0.18 |
| $a/b = 1.4$, $b/c = 1.3$ | 112 | 80.0 | 61.5 | 0.32 |

For this analysis, we will assume a perturbation equivalent to a $\beta$ value of 3, as this is large enough to excite unstable motion in some shapes of Dimorphos, but small enough to allow stable motion in other shapes. A perturbation of $\beta = 3$ is roughly equivalent to increasing the eccentricity to around 0.02-0.03, depending on the secondary shape and mass. This allows us to study both stable and unstable dynamical regimes without having to test multiple perturbation magnitudes. Note this selection is not grounded in the actual DART impact, as we are interested in how different secondary shapes affect dissipation rates within a system rather than making any quantitative predictions, as an accurate prediction is impossible without knowledge of the system's interior structure. Following Hera's survey, this analysis can be revisited with better constraints on the shape and mass of Dimorphos. We reproduce the results of [90] for $\beta = 3$ in Fig. 4.3 to show the unstable region of motion. While the size of Dimorphos is fixed by the bulk diameter, the shape of the triaxial ellipsoid is defined by the axis ratios $a/b$ and $b/c$, where $a$, $b$, and $c$ are the longest, intermediate, and shortest semiaxes of the ellipsoid, respectively. Fig. 4.3 shows the amplitude of the 1-2-3 Euler angles, corresponding to roll, pitch, and yaw, for each secondary shape. If a system is in a true equilibrium, these angles would remain zero. An unstable region is apparent in Fig. 4.3 where some secondary shapes result in tumbling. The unstable region in which the secondary begins to tumble is outlined by a yellow dashed line. This is not a formal boundary for this region and is only intended to aid interpretation. The unstable region is dependent on the system's eccentricity, so this boundary cannot be applied outside of our impact scenario.

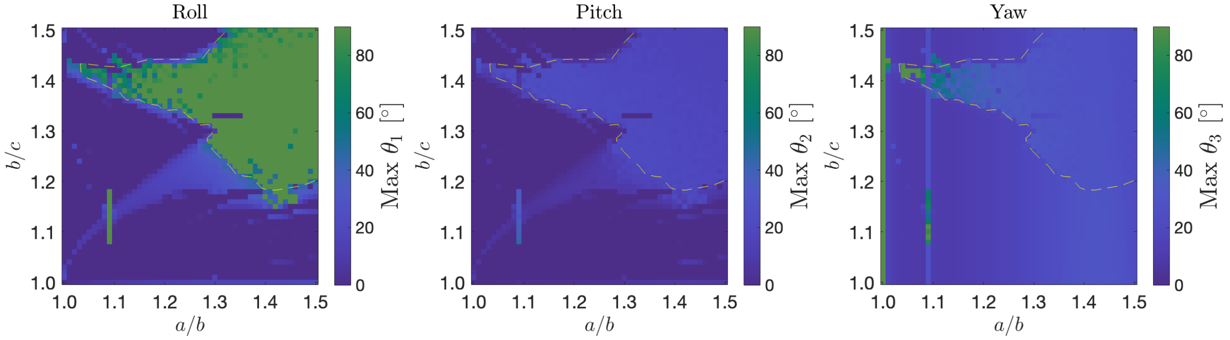

Figure 4.3: The maximum amplitude of the 1-2-3 Euler angles for an impact corresponding to $\beta = 3$ ($e \approx 0.02$), from the simulation set from [90]. The unstable regions, indicated by nonzero amplitudes in the roll and pitch angles, are governed by intersections of various resonances among fundamental frequencies of the system. The unstable region is outlined by the yellow dashed line; this is not a formal boundary and only serves to aid interpretation.

Due to the spin-orbit coupling in binary asteroids, these systems are non-Keplerian, and thus osculating Keplerian elements can be somewhat misleading. In an equilibrium configuration, the secondary may appear to be in a circular orbit to an external observer, but the Keplerian orbit is elliptical. In this configuration, the secondary is trapped at periapsis while the orbit itself precesses. Thus, there is a non-zero eccentricity at equilibrium and the semimajor axis is not the same as the separation distance [34]. However, these elements are still useful as they can give us an idea of the system's secular evolution over time, and we use the Keplerian osculating elements throughout this chapter.

In investigating the energy dissipation of a librating binary asteroid, we must consider two dynamical regimes: stable libration or NPA rotation. A system in the stable regime will only see fluctuations in secondary rotation about its major principal axis, whereas an unstable system will experience rotation about all three axes. For a uniform bulk density, the dynamical regime of the system depends on the shape of the secondary, as illustrated in Fig. 4.3. We will select a system from both the stable and unstable region to carry out long-term simulations to investigate how a system dissipates its libration and returns to a synchronous equilibrium. For the stable system, we select a secondary with axis ratios $a/b = 1.2$, $b/c = 1.1$, and for the unstable system we choose $a/b = 1.4$, $b/c = 1.3$. Note that energy dissipation in the primary is generally uniform across all reasonable secondary shapes, so we thus exclude it from our analysis for simplicity.

### 4.3.1 Stable System

For the stable system, we simulate the dynamics for 200 years ($\sim 150,000$ orbit periods), during which the system returns to an equilibrium and begins to secularly evolve. We first examine the system energy, shown in Fig. 4.4a. We plot the secondary rotational energy, the orbit energy, and the free energy. We define the free energy simply as the sum of the secondary rotational and orbit energies, or alternatively as the total energy sans the primary rotational energy. Since the primary rotational energy will uniformly decrease as a result of tides, the free energy is a better metric to examine the system's evolution. We see oscillations in the energy after the perturbation, which damp out as the system settles into a new equilibrium. Interestingly, the free energy decreases for a time before increasing. This indicates that dissipation acts to equilibrate the system faster than secularly evolve it. This is apparent in the exponential decrease in the secondary and orbit energy oscillations, as these values converge to a mean faster than the mean itself evolves.

This behavior is also apparent in Fig. 4.4b, where we plot the Keplerian semimajor axis and eccentricity, along with the secondary libration angle. Again, we see the oscillations in the semimajor axis exponentially damping before any secular evolution is apparent. These oscillations damp at the same rate the eccentricity approaches its equilibrium value (recall that due to spin-orbit coupling, the equilibrium eccentricity is small but non-zero). This is also the same rate the libration damps to zero. In the libration angle we again see an initial exponential decrease.

As a result of spin-orbit coupling and the unique dynamics of binary asteroids, we see a new dynamical regime not previously studied in tidal analyses. It appears dissipation first acts to drive the system back toward an equilibrium by damping the eccentricity and oscillations in the system caused by libration, before the more classical secular tidal behavior is seen. Thus, rather than eccentricity and semimajor axis evolving concurrently as in classical tidal theory (e.g. [38]), the eccentricity is damped to a minimum before the semimajor axis evolves.

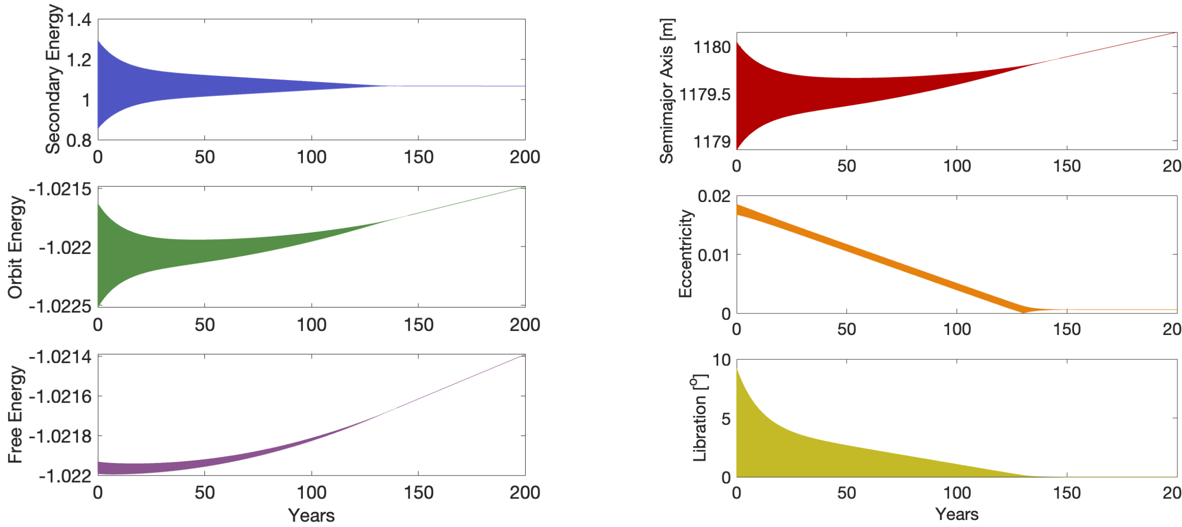

(a) Energy Dissipation in a Stable System

(b) Keplerian Elements in a Stable System Experiencing Dissipation

Figure 4.4: (a) The secondary rotational energy (top), orbit energy (middle), and free energy (bottom) of the stable system with secondary $a/b = 1.2$, $b/c = 1.1$. The energies are normalized by the respective pre-impact equilibrium values. The oscillations within the energy are damped at the same rate across the secondary, orbit, and free energies. Here $Q_A/k_A \approx 1e5$ and $Q_B/k_B \approx 2.5e4$. (b) The Keplerian semimajor axis (top), eccentricity (middle), and libration angle (bottom) of the stable system with the same secondary shape and dissipation parameters. The oscillations in semimajor axis and libration are damped at the same rate the eccentricity approaches its non-zero equilibrium value due to spin-orbit coupling.

### 4.3.2 Unstable System

We next perform the same simulation for the unstable system. The system energy is shown in Fig. 4.5a, where again we plot the secondary rotational energy, the orbit energy, and the free energy. Interestingly, on a comparable time scale as the stable system, the unstable system also returns to an equilibrium configuration. A notable difference is the oscillations in energy appear to converge linearly, unlike the stable system which experienced an exponential decay of oscillations.

In the unstable system we again see an initial decrease in the free energy before it begins to increase as the orbit expands.

In Fig. 4.5b, we plot the semimajor axis, eccentricity, and libration angle of the unstable system. Again we see a linear, rather than exponential, decay in these elements. Once more, the timescale of damping is approximately uniform across all these elements, also consistent with the energy envelope decay times, highlighting the strength of the spin-orbit coupling. The binary asteroid cannot settle into an equilibrium while the libration amplitude is nonzero, or equivalently the eccentricity is not equal to its equilibrium value.

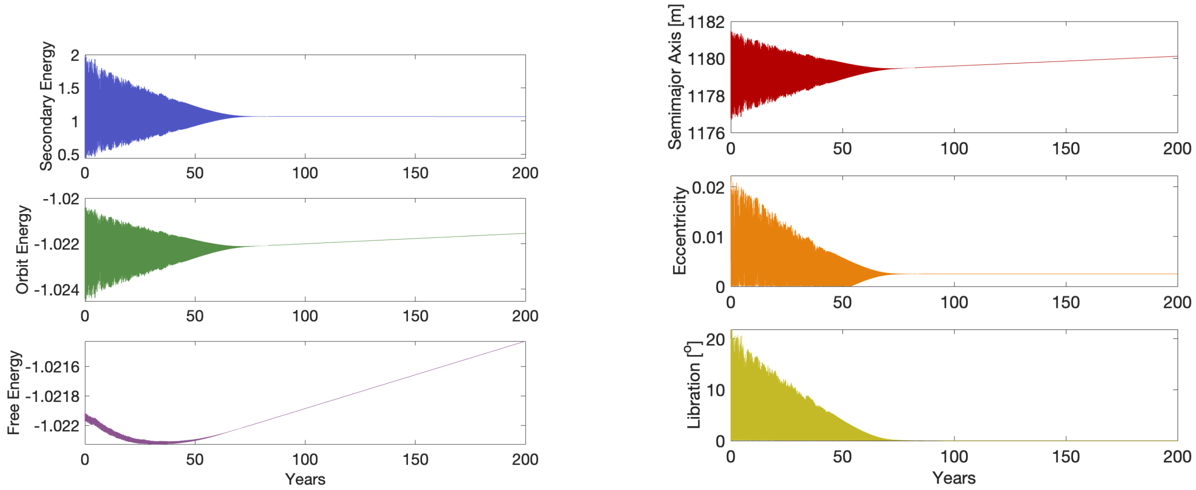

(a) Energy Dissipation in an Untable System

(b) Keplerian Elements in an untable System Experiencing Dissipation

Figure 4.5: (a) The secondary rotational energy (top), orbit energy (middle), and free energy (bottom) of the unstable system with secondary $a/b = 1.4$, $b/c = 1.3$. The energies are normalized by the respective pre-impact equilibrium values. The oscillations within the energy are damped at the same rate across the secondary, orbit, and free energies. Here $Q_A/k_A \approx 1e5$ and $Q_B/k_B \approx 2.5e4$. (b) The semimajor axis (top), eccentricity (middle), and libration angle (bottom) of the unstable system with the same secondary shape and dissipation parameters. The oscillations in semimajor axis and libration are damped at the same rate the eccentricity approaches its equilibrium value due to spin-orbit coupling.

An interesting takeaway from this result is both the stable and unstable systems reequilibrate on comparable timescales. While previous analyses have shown unstable rotation will slow dissipation [120, 92, 76], that applies to non-synchronous rotation, whereas our system never leaves an on-average synchronous configuration. [100] predict that tumbling within the synchronous state does not reduce energy dissipation and in fact can enhance it, and our results are consistent with that finding. However, a unique finding in our analysis is the close relationship between the eccentricity, libration, and oscillation within the semimajor axis. This is due to the spin-orbit coupling in binary asteroids, as any deviation from an equilibrium spin state of the secondary will also affect the orbit.

### 4.3.3 Analytic Models

An important question is how this numerical model compares to more classic analytical models of energy dissipation. Here, we focus only on tidal dissipation since this is the dominant mechanism. Analytic equations for the evolution of semimajor axis and eccentricity of a binary system with $e \ll 1$ undergoing tidal dissipation are reported in [38]:

$$\frac{\dot{a}}{a} = 3\frac{k_A}{Q_A}\frac{M_B}{M_A}\left(\frac{R_A}{a}\right)^5 n \tag{4.21}$$

$$\frac{\dot{e}}{e} = \frac{57}{8}\frac{k_A}{Q_A}\frac{M_B}{M_A}\left(\frac{R_A}{a}\right)^5 n - \frac{21}{2}\frac{k_B}{Q_B}\frac{M_A}{M_B}\left(\frac{R_B}{a}\right)^5 n \tag{4.22}$$

where $n$ is the mutual orbit mean angular velocity. Note in Eqs. 4.21 and 4.22, $a$ refers to the binary mutual orbit semimajor axis rather than the secondary's longest semiaxis as used elsewhere in this chapter. In Eq. 4.22 for the eccentricity we see two terms: the first is the contribution from tides raised on the primary and the second is the contribution from tides raised on the secondary. The semimajor axis and eccentricity evolution is compared between the analytic model and our numeric results in Fig. 4.6a for the stable system and Fig. 4.6b for the unstable system.

For both the stable and unstable systems, the analytic model does a good job describing the secular rate of change of semimajor axis, but fails to account for the initial oscillations in semimajor axis. The analytic model also fails to describe the eccentricity damping rate and predicts a much slower decrease in eccentricity than what we see in our numeric model. These results make sense

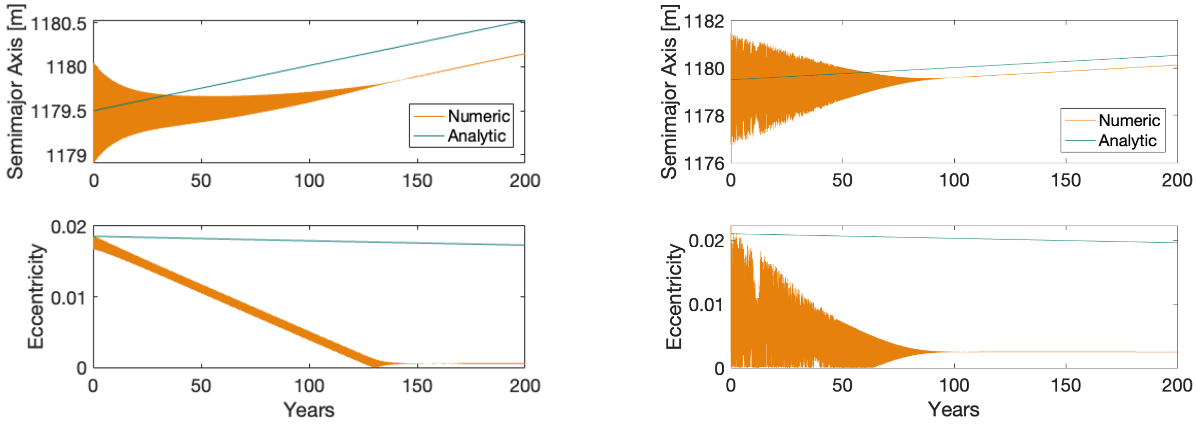

(a) Analytical Comparison for the Stable System (b) Analytical Comparison for the Unstable System

Figure 4.6: (a) The semimajor axis (top) and eccentricity (bottom) for the stable system ($a/b = 1.2$, $b/c = 1.1$), comparing the numeric results to an analytic model. While the secular trend of semimajor axis is consistent between the models, the analytic model does a poor job of describing the eccentricity evolution. (b) The semimajor axis (top) and eccentricity (bottom) for the unstable system ($a/b = 1.4$, $b/c = 1.3$), comparing the numeric results to an analytic model. While the secular trend of semimajor axis is consistent between the models, the analytic model does a poor job of describing the eccentricity evolution.

in the context of this problem; in our numeric model, the primary matches the assumptions in the analytic model: a rapidly rotating sphere. However, our secondary does not match the assumptions as it is neither spherical nor exactly tidally locked. Thus, we would expect to match the semimajor axis drift as this is driven by tides on the primary, but not the eccentricity damping rate, which has contributions from tides on the secondary. Furthermore, as the semimajor axis oscillations are driven by libration of the secondary, the analytic model does not capture this behavior. Note that our results have a non-negligible eccentricity, so we expect some error in the analytic model.

The analytic model of [38] makes no consideration of the secondary's libration. For this we turn to [42] who develop an expression for the damping rate of libration amplitude due to tides[1] :

$$\dot{\Phi}_B = -\frac{k_B \omega_l \Phi_B^2}{Q S \bar{I}_{B,z} \sin 2\Phi_B} \left( \frac{R_A}{\tilde{a}} \right)^3 \tag{4.23}$$

---

[1] The final result of this equation reported in [42] is missing the $1/\bar{I}_{B,z}$ term in the denominator.

where the libration frequency $\omega_l$ is defined as

$$\omega_l = \frac{\pi\omega_d\sqrt{3S(1+s)}}{2\mathrm{K}(\sin^2\Phi_B)}\left(\frac{R_A}{\tilde{a}}\right)^{3/2}. \tag{4.24}$$

Here, $\omega_d = \sqrt{4\pi\rho G/3}$ is the spin disruption limit, $\mathrm{K}(k^2)$ is the complete elliptic function of the first kind, $s = \bar{I}_{B,z}q^{2/3}(1+q)(R_A/\tilde{a})^2$ is the secondary perturbation term with mass fraction $q = m_B/m_A$. Here, $\tilde{a}$ is the binary mutual orbit semimajor axis in units of the primary radius, and recall $S = (I_{B,y} - I_{B,x})/I_{B,z}$. For the derivation and in-depth discussion of this model we refer the reader to [42].

While this formula is derived for a planar, circular orbit, it can still accurately be applied to our stable system as this remains essentially planar with a small eccentricity. We see in Fig. 4.7 that, for the stable system, there is good agreement between our numeric results and this analytic model. While the instantaneous dissipation rates can differ, the overall trend is similar and both models converge to zero in the same time frame. Applying this analytic model to the unstable system introduces error given the non-planar libration, but Fig. 4.8 still shows decent agreement. The biggest difference for the unstable system is the rate of dissipation, where the numeric model converges to zero faster than the analytic model. This indicates out-of-plane rotation of the secondary increases the rate of dissipation compared to purely planar libration, consistent with the findings of [100].

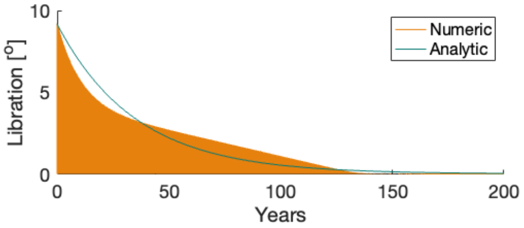

Figure 4.7: The libration amplitude for the stable system ($a/b = 1.2$, $b/c = 1.1$), comparing the numeric results to an analytic model. We see good agreement between the models, and both converge to zero on the same timescale.

While [42] use the same equations as [38] for the orbit evolution (semimajor axis and eccentricity), their derivation of the libration damping rate sidesteps the problem with the eccentricity

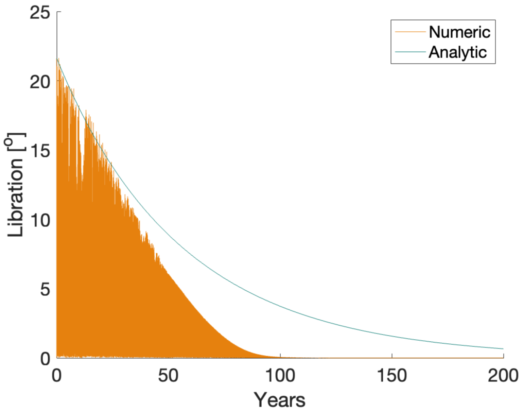

Figure 4.8: The libration amplitude for the unstable system ($a/b = 1.4$, $b/c = 1.3$), comparing the numeric results to an analytic model. The numeric model, experiencing non-planar libration, dissipates to zero faster than the analytic model predicts for planar libration.

damping equation. Thus, the formula for libration damping gives a good approximation for the eccentricity damping since these quantities are closely related in the coupled problem. Of course, this formula is more accurate for the stable, planar system. But a decent analytic approximation of the system's evolution can be made using only the semimajor axis and libration amplitude equations.

## 4.4 Effect of Tidal Parameters

As previously mentioned, there is considerable uncertainty surrounding the tidal parameters $Q/k$ for both the primary and secondary. We define three values for $Q_A/k_A$ to test: $10^4$, $10^5$, and $10^6$. We use these same values to test $Q_B/k_B$ as well. First, we vary $Q_A/k_A$ over these three values while holding $Q_B/k_B = 10^5$ constant. Then we perform the opposite test by varying $Q_B/k_B$ over the same values while holding $Q_A/k_A$ constant. In this way we can determine which behaviors in the system rely mainly on the primary or secondary. This range of $Q/k$ values for both bodies gives us an idea on how the tidal parameter affects the system evolution. We perform this analysis for both the stable and unstable systems.

### 4.4.1 Stable System

For the stable system ($a/b = 1.2$, $b/c = 1.1$), we first hold $Q_B/k_B = 10^5$ constant and vary $Q_A/k_A$ between $10^4$ and $10^6$. In Fig. 4.9, we plot the libration amplitude, free energy, semimajor axis, and eccentricity over 200 years. The free energy has been normalized by its pre-impact equilibrium value. Note this is not a long enough time span for the system to fully equilibrate, but it is long enough to see the secular behavior of the system.

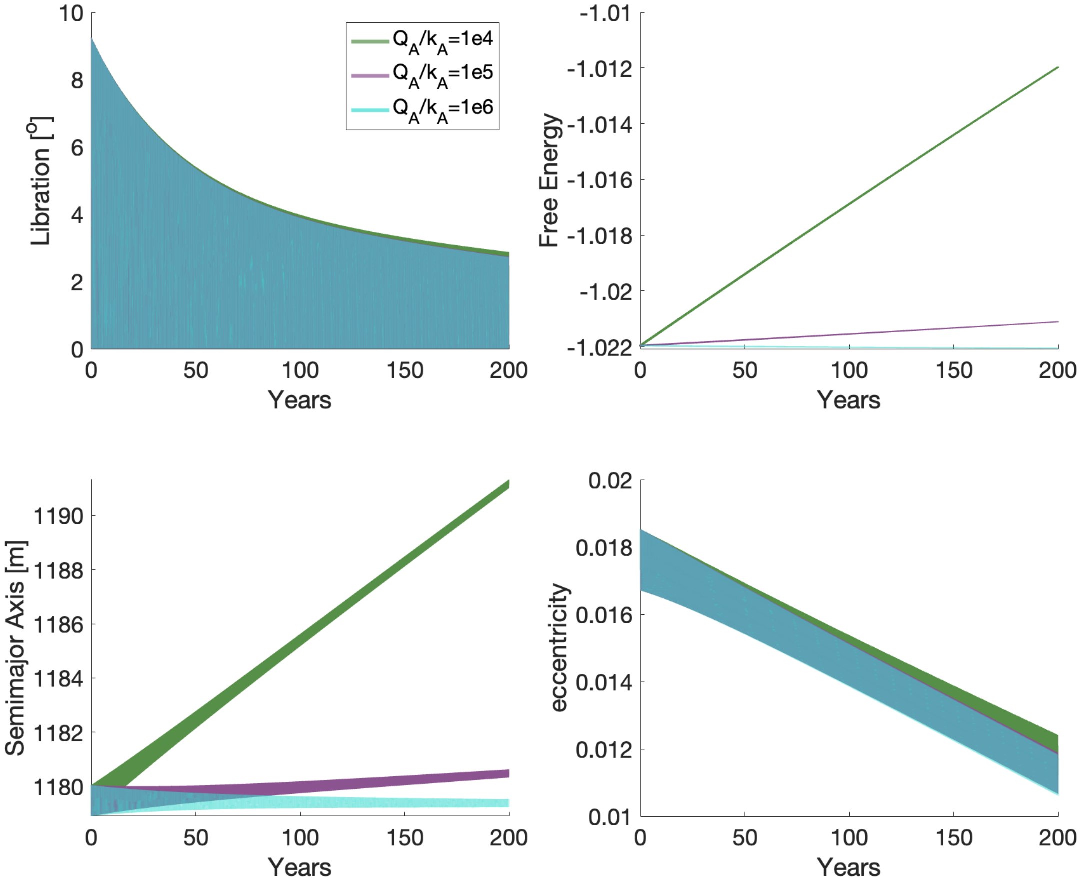

Figure 4.9: For the stable system $a/b = 1.2$, $b/c = 1.1$, we vary the value of $Q_A/k_A$ while keeping $Q_B/k_B = 10^5$ constant. For 200 years, we plot the libration angle (top left), normalized free energy (top right), semimajor axis (bottom left), and eccentricity (bottom right). While the rate of change of the semimajor axis and free energy strongly depend on $Q_A/k_A$, the libration amplitude and eccentricity are largely independent of primary tidal parameters.

From Fig. 4.9, we see the dissipation of the libration amplitude has very little dependence on $Q_A/k_A$, indicating it depends almost solely on $Q_B/k_B$. Conversely, the semimajor axis has a strong dependence on $Q_A/k_A$, as evidenced in the plot of free energy and semimajor axis. These dependencies are expected from classical tidal theory. Unsurprisingly, smaller $Q_A/k_A$ values (more dissipative systems) expand the orbit more rapidly than large values of $Q_A/k_A$. For small $Q_A/k_A$ values, the secular trend is faster than the dissipation in semimajor axis oscillations, whereas large $Q_A/k_A$ values see the opposite, where oscillations in semimajor axis are damped faster than the secular trend becomes dominant. In the plot of free energy, we see the least dissipative system slowly losing free energy while the other systems are monotonically increasing, which is consistent with the behavior seen in the semimajor axis. Overall this indicates that when $Q_A/k_A$ is larger than $Q_B/k_B$, the system contracts its orbit first to damp semimajor axis oscillations and libration amplitude, whereas when $Q_A/k_A$ is smaller than $Q_B/k_B$, the orbit expands faster than the secondary re-equilibrates. Lastly, the eccentricity damping also appears to have only a small dependence on $Q_A/k_A$, as there are only small differences in the trend between the values tested here.

Next, we perform the complement of this analysis by holding $Q_A/k_A = 10^5$ constant and varying $Q_B/k_B$ between $10^4$ and $10^6$. In Fig. 4.10, we plot the libration amplitude, the free energy, semimajor axis, and eccentricity over 200 years.

In Fig. 4.10, we see the dissipation of the libration amplitude has a strong dependence on $Q_B/k_B$, with smaller values (more dissipative) damping libration faster. Looking at the free energy, the secular trend appears to have only a small dependence on $Q_B/k_B$, but for small values of $Q_B/k_B$ we see the initial decrease in free energy. While the case $Q_B/k_B = Q_A/k_A = 10^5$ appears to have a slope different from the other cases, its slope is actually changing slowly and approaching the same rate as the others. The free energy corresponds to the semimajor axis, where the secular trend again sees only a small dependence on $Q_B/k_B$, but the rate of damping oscillations does have a strong dependence on $Q_B/k_B$. The most dissipative system ($Q_B/k_B = 10^4$) damps the oscillations fastest and appears to have an initial trend of decreasing semimajor axis (consistent with the decrease in free energy). This indicates that systems with a very dissipative secondary initially contract

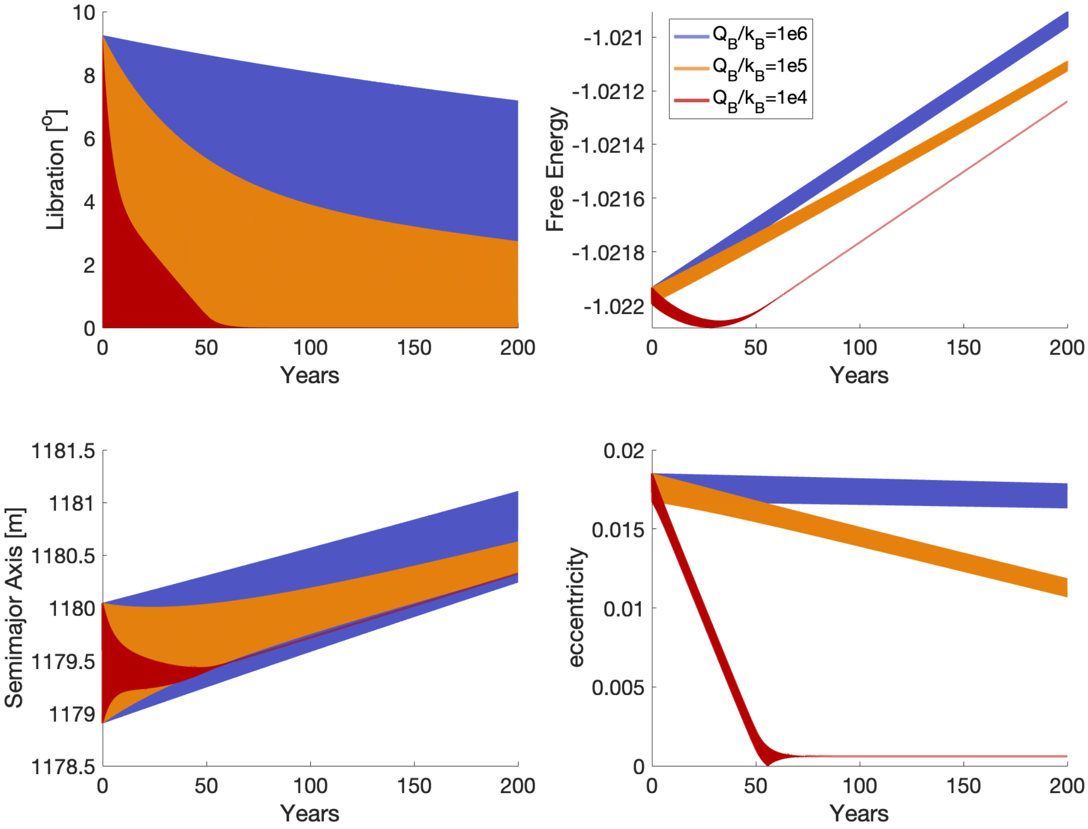

Figure 4.10: For the stable system $a/b = 1.2$, $b/c = 1.1$, we vary the value of $Q_B/k_B$ while keeping $Q_A/k_A = 10^5$ constant. For 200 years, we plot the libration angle (top left), normalized free energy (top right), semimajor axis (bottom left), and eccentricity (bottom right). The dissipation rates of the libration amplitude and eccentricity strongly depend on $Q_B/k_B$. For very dissipative secondaries, the free energy initially decreases, which is not the case for secondaries with larger $Q_B/k_B$ values. The secular rate of semimajor axis expansion seems independent of $Q_B/k_B$, but the damping rate of oscillations in semimajor axis does depend on $Q_B/k_B$.

the orbit to reestablish equilibrium. Lastly, we see a strong dependence of eccentricity damping on $Q_B/k_B$, with more dissipative systems unsurprisingly damping eccentricity the fastest. Again, these dependencies are expected from classical tidal theory.

### 4.4.2 Unstable System

We next repeat the same analysis by varying $Q_A/k_A$ and $Q_B/k_B$ for the unstable system ($a/b = 1.4$, $b/c = 1.3$). First, we hold $Q_B/k_B = 10^5$ constant while varying $Q_A/k_A$ between $10^4$

and $10^6$. We plot the libration amplitude, free energy, semimajor axis, and eccentricity for this analysis in Fig. 4.11.

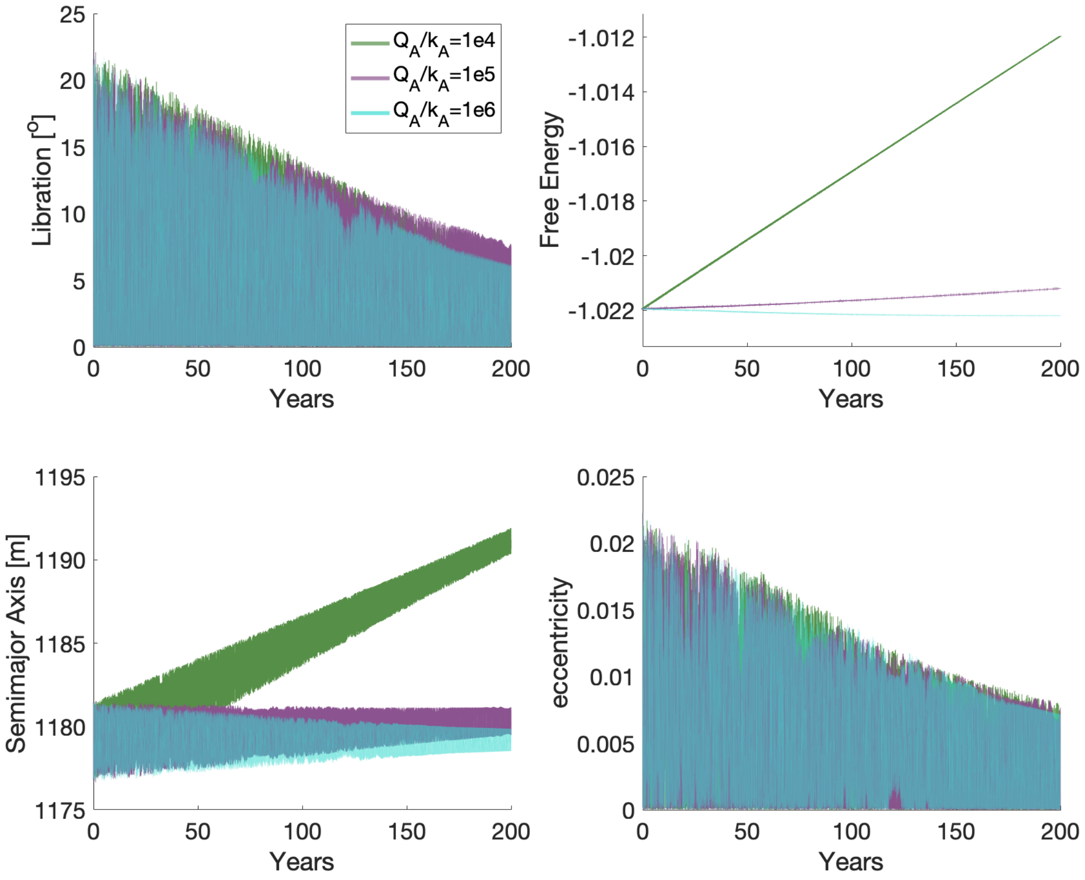

Figure 4.11: For the unstable system $a/b = 1.4$, $b/c = 1.3$, we vary the value of $Q_A/k_A$ while keeping $Q_B/k_B = 1e5$ constant. For 200 years, we plot the libration angle (top left), normalized free energy (top right), semimajor axis (bottom left), and eccentricity (bottom right). While the rate of change of the semimajor axis and free energy strongly depend on $Q_A/k_A$, the libration amplitude and eccentricity are largely independent of primary tidal parameters.

Overall, we see very similar behavior between the unstable and stable system. Consistent with classical tidal theory, it appears the libration amplitude and eccentricity damping are largely unaffected by the value of $Q_A/k_A$ during this time. Again, the secular trend of free energy and semimajor axis strongly depend on $Q_A/k_A$ as expected. When $Q_A/k_A > Q_B/k_B$ (i.e. $Q_A/k_A = 10^6$, $Q_B/k_B = 10^5$), the damping rate of semimajor axis oscillations is faster than the secular trend, and as a result we see an overall decrease in the free energy. At a longer timescale we expect both the semimajor axis and free energy to begin increasing as the orbit expands.

We next hold $Q_A/k_A = 10^5$ constant and vary $Q_B/k_B$ between $10^4$ and $10^6$. For this test, the libration amplitude, free energy, semimajor axis, and eccentricity are plotted in Fig. 4.12.

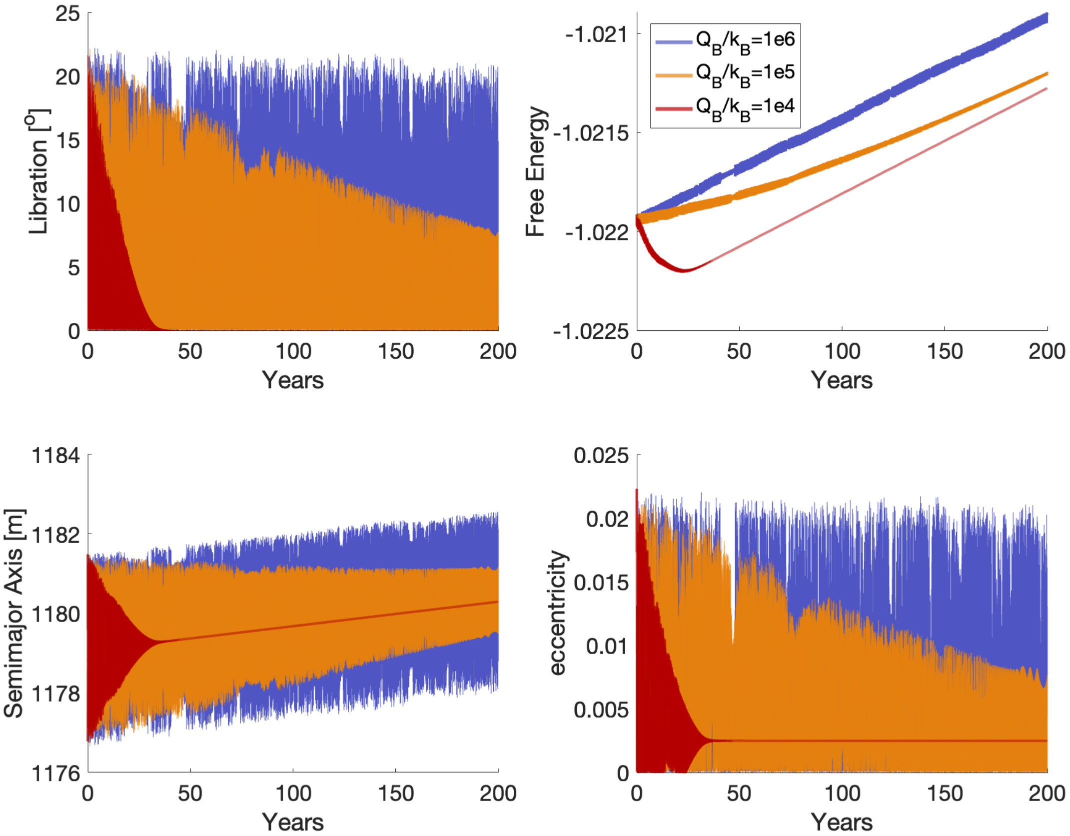

Figure 4.12: For the unstable system $a/b = 1.4$, $b/c = 1.3$, we vary the value of $Q_B/k_B$ while keeping $Q_A/k_A = 1e5$ constant. For 200 years, we plot the libration angle (top left), normalized free energy (top right), semimajor axis (bottom left), and eccentricity (bottom right). The dissipation rates of the libration amplitude and eccentricity strongly depend on $Q_B/k_B$. For very dissipative secondaries, the free energy initially decreases, which is not the case for secondaries with larger $Q_B/k_B$ values. The secular rate of semimajor axis expansion seems independent of $Q_B/k_B$, but the damping rate of oscillations in semimajor axis does depend on $Q_B/k_B$.

Again, there are strong similarities between the unstable and stable case. The damping rate of libration amplitude and eccentricity strongly depend on $Q_B/k_B$, while the secular trends in semimajor axis and free energy seem ignorant of $Q_B/k_B$, as expected from classical tidal theory. However, the damping rate of semimajor axis oscillations does depend heavily on $Q_B/k_B$, with more dissipative secondaries (small $Q_B/k_B$) damping these oscillations faster than the secular trend develops, and as a result the free energy of the system initially decreases.

Based on these analyses of $Q_A/k_A$ and $Q_B/k_B$, we can conclude that the libration amplitude, eccentricity, and oscillations in semimajor axis mostly depend on $Q_B/k_B$, while the secular trend of the orbit, i.e. semimajor axis expansion, is driven by $Q_A/k_A$. When systems have a more dissipative secondary, they re-enter equilibrium before any noticeable secular change in the orbit develops, whereas when systems have a more dissipative primary the re-equilibrization of the secondary takes longer than the secular evolution of the orbit.

## 4.5 Conclusion

We find that both stable and tumbling systems dissipate energy on comparable timescales to return to a synchronous configuration. Previous studies have claimed that tumbling greatly reduces the rate of energy dissipation [120, 76, 92], but this is only for the non-synchronous case. Our results agree with [100] in that tumbling within the synchronous state can increase energy dissipation, and the libration amplitude damps to zero before predicted for planar rotation. A unique result we find is that non-principal axis rotation can damp as quickly as planar libration for strongly coupled systems with efficient dissipation. We find in these systems the libration amplitude, both stable and unstable, is tied closely to the orbit eccentricity and oscillations in the semimajor axis, as all of these dissipate on the same timescale. For especially dissipative systems, the system returns to equilibrium before any substantial secular trend is apparent.

By varying $Q/k$ for both the primary and secondary, we find that the rate of libration and eccentricity damping are strongly dependent on the secondary's tidal parameters, but largely independent of the primary's. By extension, the oscillations in the semimajor axis also are mainly dependent on the secondary's tidal parameters. Conversely, the secular trend in the semimajor axis mainly depends on the primary's tidal parameters, but not the secondary's. Thus, we find systems with $Q_B/k_B < Q_A/k_A$ damp libration and eccentricity faster than secular changes in the orbit become apparent. This also corresponds to an initial decrease in the free energy before the semimajor axis begins expanding, unless the initial libration amplitude is small. On the other hand, when $Q_B/k_B > Q_A/k_A$, the secular trend in the orbit is immediately obvious and the damping of libration and eccentricity is relatively slow in comparison. Thus, if the secondary is very dissipative, Hera may be able to measure the damping of the libration amplitude and eccentricity. In these very dissipative systems, the coupling between eccentricity and libration means the eccentricity dissipates much faster than predicted by the analytic models of [38]. Consequently, we do not recommend using an analytic model to approximate evolution of a coupled system experiencing libration, unless this system is not very dissipative or is already in an equilibrium. This also suggests close binary asteroids with measured eccentricity have either a tumbling secondary or a stiff, non-dissipative secondary.

# Chapter 5

# Planetary Encounters

## 5.1 Introduction

The problem of binary encounters with perturbing bodies has been studied both analytically and numerically. [121] developed an analytic expression for the change in eccentricity of a binary star system encountering a third body. In addition to the change in eccentricity, [122] also derived the change in inclination. The change in energy of a perturbed binary system is studied by [123] and again in [124]. [125] combined all these results and compared them to numerical simulations at a variety of encounter geometries. All these studies consider the three bodies to be spherical; thus, they do not consider the spin-orbit coupling since gravitational torques are absent. In this chapter we correct this simplification and only consider the third perturbing body, the planet, to be spherical. Furthermore, we also investigate how planetary flybys affect the orientation of the secondary in its orbit.

We will first derive the spherical-restricted full three-body problem, and demonstrate how this can model binary asteroids under the influence of a perturbing gravitational body. In this analysis we consider the larger primary asteroid as an oblate spheroid, and the smaller secondary as a triaxial ellipsoid. The binary pair will be placed in a singly synchronous equilibrium and perturbed by an Earth flyby in our analysis to investigate how a flyby can disrupt the equilibrium configuration.

In the second half of this chapter we will apply this model to 1991VH in order to explain its current excited dynamical state. We will consider various singly synchronous progenitor systems

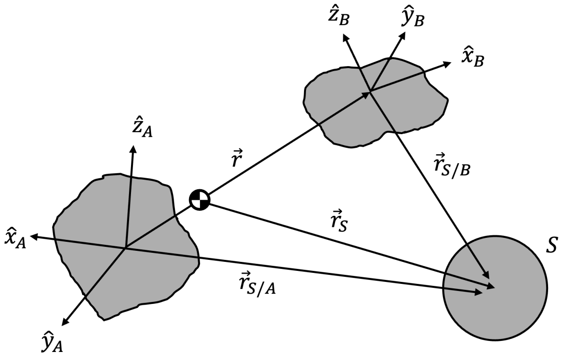

Figure 5.1: Relevant vectors in the spherical restricted full three-body problem.

and simulate close encounters with the Earth. Using a distribution of possible Earth encounter geometries, we will test the hypothesis that a previous close Earth flyby could cause a singly-synchronous binary asteroid to enter a dynamical state similar to the one 1991VH is observed in today.

## 5.2 Spherical Restricted Full 3-Body Problem

The F2BP equations of motion are modified by the effects of a third gravitational body, in our case a planet, leading to the spherical restricted full three-body problem (SRF3BP). This problem is spherical restricted in the sense that the third body is considered to be a sphere, as it is much larger than the two asteroids in the binary pair, and it is assumed the binary pair do not exhibit significant torques on the planet.

We first develop the equations of motion for a binary asteroid pair influenced by a third gravitational body. The larger primary asteroid is modeled as an oblate spheroid while the smaller secondary is modeled as a triaxial ellipsoid. Despite these assumptions, the equations of motion developed below do not assume any simplification to the geometry beyond the spherical planet and can be applied to any arbitrary asteroid shapes. A diagram of the SRF3BP is shown in Fig. 5.1.

In this illustration, $\vec{r}$ tracks the relative position of the secondary around the primary in the binary system. We define $\vec{r}_A$ to point from the center of gravity (cg) to the primary $A$, and $\vec{r}_B$ to point from cg to the secondary $B$. The vector $\vec{r}_S$ defines the position of the sphere relative to cg.

Finally, $\vec{r}_{S/A}$ is the position of the sphere relative to the binary primary and $\vec{r}_{S/B}$ similarly is the position of the sphere relative to the secondary.

Three potential energy terms are necessary to develop the equations of motion. The potential energy between the two asteroids is $U_{A/B}$, which we have already introduced in Sec. 2.2. We now add the subscript to avoid confusion with other potential energy terms. The potential energy between the sphere and the primary is $U_{S/A}$ and similarly between the sphere and the secondary is $U_{S/B}$. These potentials are much simpler than the binary asteroid mutual potential owing to the spherical shape of the third body; they are defined as the potential of body $A$ or $B$ multiplied by the mass of the sphere.

We describe the binary system using the relative position vector $\vec{r}$ and relative position of the sphere to cg, which is defined by the vector $\vec{r}_S$. The global coordinate frame is set with its origin at cg, and thus the acceleration of the coordinate frame must be considered. Modeling the binary system as a point mass at cg, the acceleration of cg is

$$\ddot{\vec{r}}_S = \frac{-1}{m_A + m_B}\left[\frac{\partial U_{S/A}}{\partial \vec{r}_{S/A}} + \frac{\partial U_{S/B}}{\partial \vec{r}_{S/B}}\right] \tag{5.1}$$

where $m_A$ is the mass of the binary system primary and $m_B$ is the mass of the secondary. To leading order, this can be well approximated as

$$\ddot{\vec{r}}_S = \frac{-\mu_S}{R_S^3}\vec{r}_S \tag{5.2}$$

where $\mu_S$ is the standard gravitational parameter of the spherical third body. This demonstrates that, to first order, the relative motion of cg and the sphere follows the classical two body problem.

The position vectors of each asteroid with respect to the center of gravity are

$$\vec{r}_A = \frac{-m_B}{m_A + m_B}\vec{r} \tag{5.3}$$

$$\vec{r}_B = \frac{m_A}{m_A + m_B}\vec{r}. \tag{5.4}$$

Note the relation $\vec{r} = \vec{r}_B - \vec{r}_A$. Accounting for the acceleration of cg, the equations of motion for each of the asteroids are:

$$\ddot{\vec{r}}_A = \frac{1}{m_A}\left(\frac{\partial U_{A/B}}{\partial \vec{r}} + \frac{\partial U_{S/A}}{\partial \vec{r}_{S/A}}\right) - \ddot{\vec{r}}_S \tag{5.5}$$

$$\ddot{\vec{r}}_B = \frac{1}{m_B}\left(\frac{-\partial U_{A/B}}{\partial \vec{r}} + \frac{\partial U_{S/B}}{\partial \vec{r}_{S/B}}\right) - \ddot{\vec{r}}_S. \tag{5.6}$$

Differentiating the relative position vector $\vec{r}$ yields

$$\ddot{\vec{r}} = \ddot{\vec{r}}_B - \ddot{\vec{r}}_A. \tag{5.7}$$

Substituting Eqs. 5.5 and 5.6 into Eq. 5.7 and rearranging terms gives the translational equation of motion for a binary pair. Note the acceleration of cg has dropped out of the equation, which is expected since we are only describing the relative motion of the asteroids:

$$\ddot{\vec{r}} = \frac{-1}{m_B}\frac{\partial U_{A/B}}{\partial \vec{r}} - \frac{1}{m_A}\frac{\partial U_{A/B}}{\partial \vec{r}} + \frac{1}{m_B}\frac{\partial U_{S/B}}{\partial \vec{r}_{S/B}} - \frac{1}{m_A}\frac{\partial U_{S/A}}{\partial \vec{r}_{S/A}}. \tag{5.8}$$

We can simplify this equation of motion by ignoring higher order terms in the force vectors between the sphere and the asteroids. Here we approximate the motion by assuming the force vectors between the sphere and each asteroid pass through the barycenters of the respective asteroids, ignoring the non-spherical terms of the bodies. This is a reasonable assumption considering the small sizes of the asteroids compared to the flyby distance. Using the standard gravitational parameter of the sphere, $\mu_S$, this approximation simplifies to

$$\ddot{\vec{r}} = -\frac{m_A + m_B}{m_A m_B}\frac{\partial U_{A/B}}{\partial \vec{r}} + \mu_S\left[\frac{\vec{r}_{S/B}}{R_{S/B}^3} - \frac{\vec{r}_{S/A}}{R_{S/A}^3}\right]. \tag{5.9}$$

The vectors $\vec{r}_{S/B}$ and $\vec{r}_{S/A}$ can be written in terms of $\vec{r}$ and $\vec{r}_S$ as:

$$\vec{r}_{S/B} = \vec{r}_S - \frac{m_A}{m_A + m_B}\vec{r} \tag{5.10}$$

$$\vec{r}_{S/A} = \vec{r}_S + \frac{m_B}{m_A + m_B}\vec{r}. \tag{5.11}$$

These expressions can be further simplified by introducing the mass fraction $\nu = \frac{m_B}{m_A+m_B}$:

$$\vec{r}_{S/B} = \vec{r}_S - (1-\nu)\vec{r} \tag{5.12}$$

$$\vec{r}_{S/A} = \vec{r}_S + \nu\vec{r}. \tag{5.13}$$

We can now write the final form of the translational equation of motion:

$$\ddot{\vec{r}} = -\frac{1}{m}\frac{\partial U_{A/B}}{\partial \vec{r}} + \mu_S \left[ \frac{\vec{r}_S - (1-\nu)\vec{r}}{|\vec{r}_S - (1-\nu)\vec{r}|^3} - \frac{\vec{r}_S + \nu\vec{r}}{|\vec{r}_S + \nu\vec{r}|^3} \right] \tag{5.14}$$

where we are using the reduced mass $m = \frac{m_A m_B}{m_A+m_B}$.

Next, the torque will be calculated. The rate of change of each asteroid's angular momentum is given by:

$$\dot{\vec{L}}_A = \vec{L}_A \times \vec{\omega}_A + \vec{M}_A + \vec{M}_{SA} \tag{5.15}$$

$$\dot{\vec{L}}'_B = \vec{L}'_B \times \vec{\omega}_A + \vec{M}'_B + \vec{M}'_{SB} \tag{5.16}$$

where the prime indicates a parameter of $B$ expressed in the body fixed frame of $A$. $\vec{L}'_B$ and $\vec{M}'_B$ are the rotational angular momentum of $B$ and the torque it receives from $A$, respectively. $\vec{M}_{SA}$ is the torque $A$ receives from the sphere, and similarly for $\vec{M}'_{SB}$. The quantities $\vec{M}_A$ and $\vec{M}'_B$ are discussed in Sec. 2.2. The torques caused by the sphere are:

$$\vec{M}_{SA} = \vec{r}_{S/A} \times \frac{\partial U_{S/A}}{\partial \vec{r}_{S/A}} \tag{5.17}$$

$$\vec{M}_{SB} = \vec{r}_{S/B} \times \frac{\partial U_{S/B}}{\partial \vec{r}_{S/B}}. \tag{5.18}$$

Note the leading terms of $U_{S/A}$ and $U_{S/B}$ do not contribute to the torques, and thus higher order terms must be included in these equations. The angular acceleration of each body can thus be written as:

$$\dot{\vec{\omega}}_A = \mathbf{I}_A^{-1} \left( \vec{L}_A \times \omega_A + \vec{M}_A + \vec{r}_{S/A} \times \frac{\partial U_{S/A}}{\partial \vec{r}_{S/A}} \right) \tag{5.19}$$

$$\dot{\omega}_B = \mathbf{I}_B^{-1} \left( \vec{L}'_B \times \omega_A + \vec{M}'_B + \vec{r}_{S/B} \times \frac{\partial U_{S/B}}{\partial \vec{r}_{S/B}} \right) \tag{5.20}$$

where $\mathbf{I}_A$ is the inertia tensor of $A$ and similarly for $\mathbf{I}_B$ for $B$.

The position and orientation of the binary asteroid pair can be completely described by Equations 5.14, 5.19, and 5.20. We modified GUBAS with these equations to account for the third body gravitational perturbations to numerically simulate a planetary flyby of the binary asteroid pair. The modifications necessary simply consist of calculating and adding the $\vec{F}_{S/A}$, $\vec{F}_{S/B}$, $\vec{M}_{SA}$, and $\vec{M}_{SB}$ terms to the relevant existing equations of motion [126].

## 5.3 Monte Carlo Flyby Simulations

For this analysis, a generic, representative binary asteroid is modeled as an oblate spheroid primary and a triaxial ellipsoid secondary. The oblate spheroid has an equatorial radius of 500 meters and a polar radius of 420 meters. The triaxial ellipsoid is 200 × 150 × 120 meters, with the long axis aligned with the primary-secondary line of centers and the short axis aligned with the primary's short axis. The relative separation of the two bodies' centers is 5 primary radii, and a fourth degree and order gravity field between the bodies is used. The primary is a fast-rotator, with a spin period of 3.5 hours, while the secondary is singly synchronous with a spin period equal to the orbit period. This system is similar to 1991VH, but we will compute more accurate simulations for 1991VH in Sec. 5.4

A hyperbolic flyby trajectory is generated by first selecting a closest approach distance, which we call $q$, between the binary asteroid barycenter and the perturbing planet. A suitable hyperbolic excess velocity of the flyby, $v_\infty$, is also chosen. These quantities define the eccentricity $e$ and semimajor axis $a$ of the hyperbolic trajectory via the following:

$$e = \frac{v_\infty^2 q}{\mu_s} + 1 \tag{5.21}$$

$$a = \frac{q}{1 - e}. \tag{5.22}$$

Now that the hyperbolic geometry is defined, it must be oriented in space. This is done using the angular Keplerian elements: Longitude of the ascending node $\Omega$, inclination $i$, and argument of periapsis $\omega$. In order to test the entire solution space, these angles are randomly drawn in a series of Monte Carlo simulations. The longitude of ascending node and argument of periapsis are randomly chosen between 0 and $2\pi$, and the inclination angle is chosen between 0 and $\pi$. These three angles are independently generated for each simulation in 100 Monte Carlo runs for defined values of $q$ and $v_\infty$. The full hyperbolic trajectory definition is illustrated in Fig. 5.2.

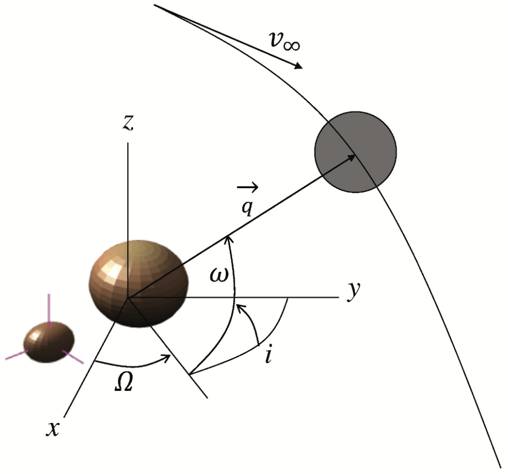

Figure 5.2: Diagram showing the hyperbolic trajectory. For a given closest approach distance $q$ and hyperbolic excess velocity $v_\infty$, the hyperbolic trajectory is oriented by selecting a longitude of ascending node $\Omega$, inclination $i$, and argument of periapsis $\omega$. The binary system barycenter is used as the origin.

### 5.3.1 Results

During each Earth flyby simulation, changes in the binary asteroid mutual orbit are characterized by the time history of its semimajor axis, eccentricity, and inclination, while the orientation of the secondary is characterized by its relative Euler Angles. An example of this time history is shown in Fig. 5.3, where ten simulations of the binary system, each with a randomly oriented geometry, are plotted over six days, with closest approach occurring at the start of the second day. The hyperbolic excess speed of these simulations is 10 km/s and the closest approach is 100,000 km. A six day integration time is sufficient to capture the impulsive nature of the planetary encounter. The only difference between these simulations is the randomly chosen geometry.

The flybys behave as a nearly impulsive change to the binary system. The orbit is changed from planar, circular, and synchronous to eccentric and inclined. While the secondary doesn't lose lock in any of these flybys, there are substantial increases in the libration angle.

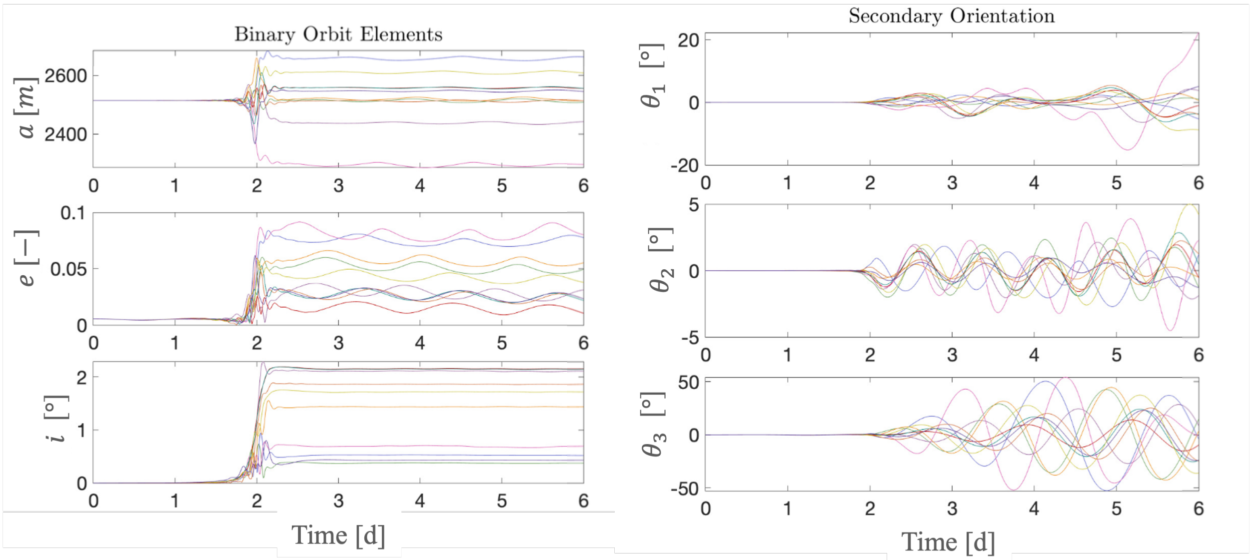

Figure 5.3: The time history of the binary asteroid mutual orbit semimajor axis (top left), eccentricity (middle left), and inclination (bottom left), along with the secondary roll (top right), pitch (middle right), and libration (equivalently yaw, bottom right) angles for a 10 km/s flyby with a closest approach distance of 100,000 km. The ten simulations each have a randomly generated flyby geometry, and the colors are arbitrarily chosen to distinguish these ten simulations.

This analysis is repeated for various values of flyby velocity, ranging from a relatively slow encounter of 7 km/s to a much faster 24 km/s for every flyby distance tested. The Earth flyby distances range from a very close flyby of 30,000 km to a more distant 500,000 km. One hundred Monte Carlo simulations are run for every combination of flyby distance and velocity to test the entire solution space of encounter geometry.

The resulting changes in binary mutual orbit and secondary orientation are averaged over all

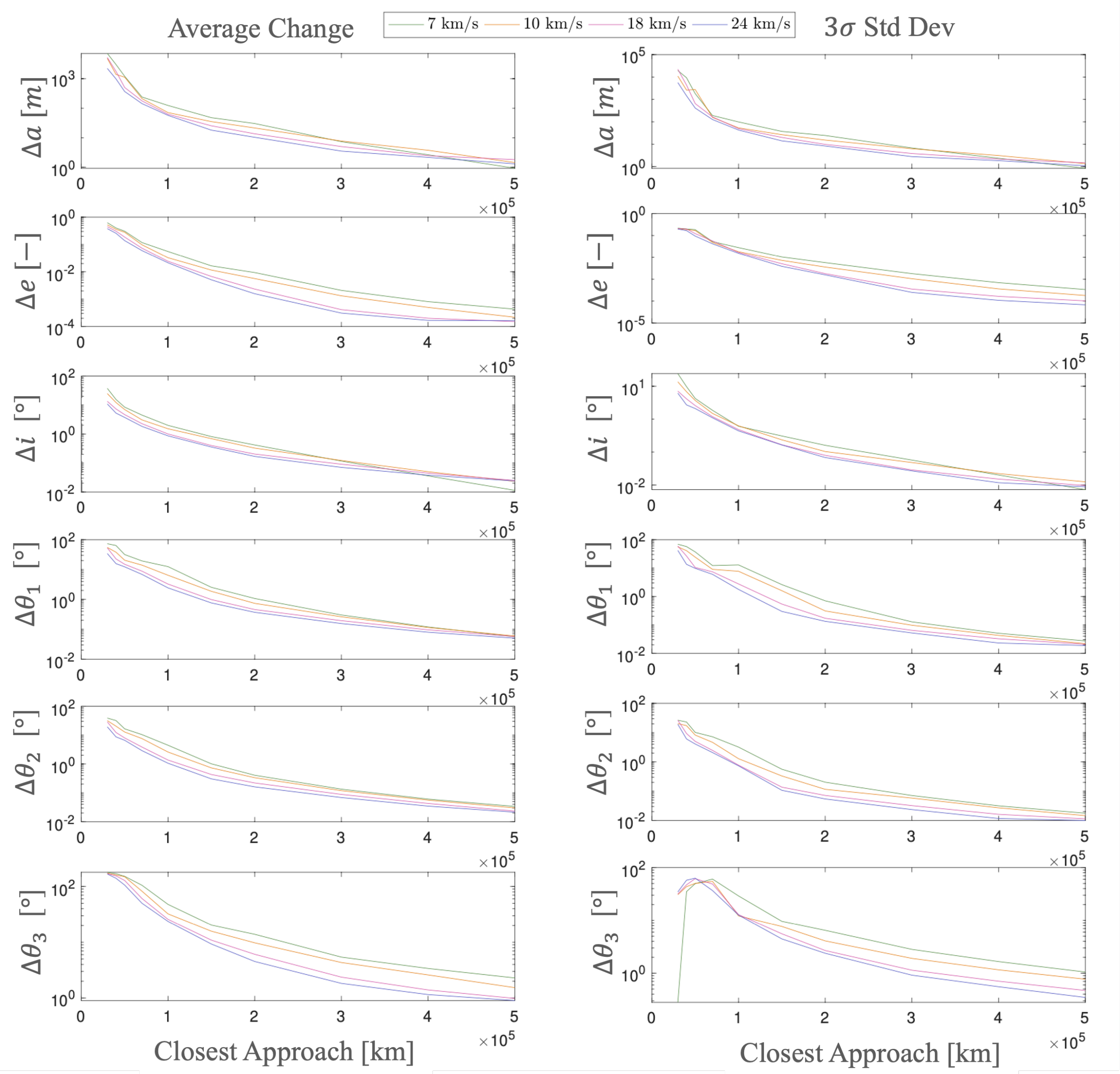

Figure 5.4: The average change in binary orbit element and secondary orientation (left column) and the associated $3\sigma$ standard deviation in changes (right column) as a function of closest approach distance. The left-hand column of plots give the average changes in 100 Monte Carlo simulations while the right-hand column gives the $3\sigma$ standard deviation of those same simulations for each flyby distance and velocity tested. Thus the large majority of the results of a series of simulations are captured between the two sets of plots and will fall within the range $\bar{x} \pm 3\sigma_x$.

encounter geometries for simulations in which the binary system remains stable (the secondary does not impact the primary or escape the mutual orbit). The average change in elements is found by differencing the average element in the final three days of the simulation and the average element in the first day of the simulation. In this way the strong dynamics within ±1 day of closest approach are not considered, but the fluctuations in the elements following the flyby are accounted for in the average change. Since initially the orbit elements are essentially unchanging, averaging over one day is sufficient to obtain a measure of these elements. After the flyby, the orbit period is unpredictable and not necessarily constant as the flyby changes the resulting dynamics in various ways. Thus, an average over three days is used, as this is long enough to ensure two full orbits are considered. The change in the secondary's Euler angles are found by differencing the maximum angle after the flyby with the angle prior to the flyby, which is zero in all cases. These results are then averaged over all 100 simulations to consider all flyby geometries in order to understand how the closest approach distance and flyby velocity affect the binary asteroid dynamics. The absolute value of the average change in element along with the $3\sigma$ standard deviation are shown in Fig. 5.4 as a function of closest approach distances for each value of flyby speed. As expected, the average change in elements decreases as the flyby distance increases and as the flyby speed increases. Additionally, the variance in these changes decreases as flyby distance increases and as flyby velocity increases. Thus, close, slow flybys have the largest change and the largest variance in these changes. Conversely, distant, fast flybys have the smallest change and smallest variance in these changes.

The simulation results see a large variance for the close flybys which drops off at far flybys. To explore this, we plot the changes in semimajor axis for 70,000 km flybys and 500,000 km flybys. Fig. 5.5 shows a histogram of the semimajor axis changes in these simulations. The changes from a 70,000 km flyby have a much broader range of outcomes than the 500,000 km results, illustrating the trend seen in Fig. 5.4.

The impulsive planetary flyby can significantly change the binary mutual orbit, as discussed in previous studies. However, this analysis also shows that close planetary encounters can cause the secondary to lose lock and tumble in its orbit. Even distant flybys can perturb the secondary's libration amplitude by a few degrees.

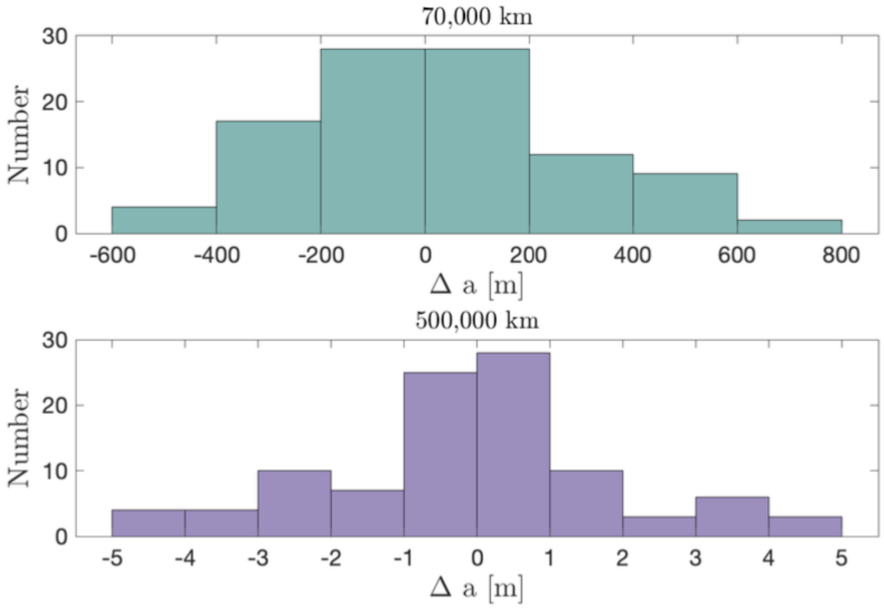

Figure 5.5: Histograms showing the various changes in semimajor axis for 70,000 km flybys (top) and 500,000 km flybys (bottom). The 70,000 km flybys see a much wider range in semimajor axis change than the 500,0000 km flybys, illustrating the larger variance in outcomes from close flybys.

The impulsive nature of these flybys is consistent with the assumptions made in previous studies of binary asteroid planetary encounters [123, 124, 125]. Given this consistency, we compare these high-fidelity numerical results to the analytic approximations developed by [122] and [124] and reported in a compact form in [125]. These analytic models are repeated here for convenience. Averaging over all encounter geometries, the changes in binary asteroid mutual orbit semimajor axis, eccentricity, and inclination can be approximated by

$$\Delta a \approx 1.48\sqrt{\frac{G}{(m_A + m_B)}}\frac{m_S a^{5/2}}{v_\infty q^2}, \tag{5.23}$$

$$\Delta e \approx 1.89\sqrt{\frac{G}{(m_A + m_B)}}\frac{m_S a^{3/2}}{v_\infty q^2}, \tag{5.24}$$

$$\Delta i \approx 0.75\sqrt{\frac{G}{(m_A + m_B)}}\frac{m_S a^{3/2}}{v_\infty q^2}. \tag{5.25}$$

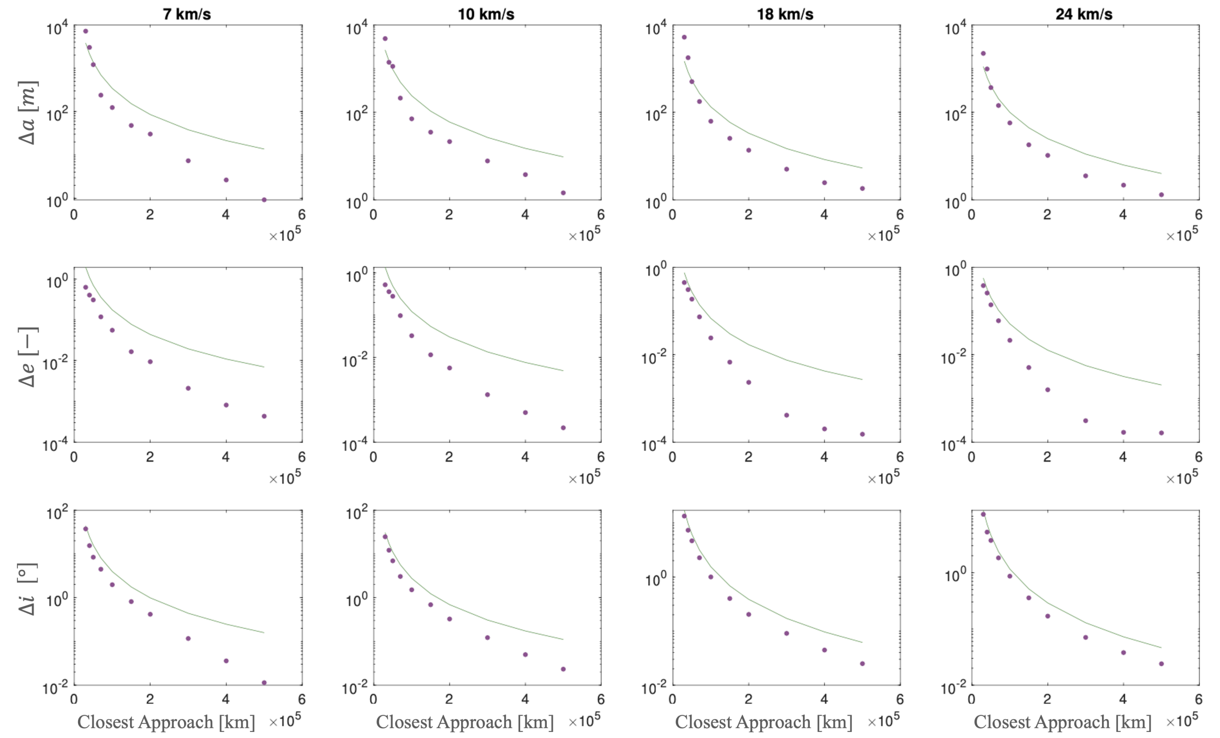

Figure 5.6: The analytic approximation for an impulsive change in semimajor axis, eccentricity, and inclination compared to the numeric averages. The analytic approximation is plotted as curves while the numeric results are shown as data points for the flyby distances tested. The two approaches generally agree to within an order of magnitude, with the analytic approximation almost always over-predicting the change in each element compared to the numeric results. Note the logarithmic scale in the y-axis, which leads to the apparent divergence between the numeric results and the analytic approximation at far flyby distances.

Fig. 5.6 compares the analytic curves of the approximate changes in binary mutual orbit elements to the numeric results. Overall, the analytic approximation is a relatively good fit to the numeric results, despite the fully coupled spin-orbit dynamics used in our numeric model. The two results agree to within about an order of magnitude over the entire domain, with the analytic approximation almost always over-predicting the change in each element, especially at further close approach distances. This discrepancy is unsurprising since the analytic model is only an approximation, and similar discrepancies are seen in the analysis in [125].

### 5.3.2 Disruptions

Some of the very close flybys, with a flyby distance less than 50,000 km, can disrupt the binary system. This includes changes that result in the binary secondary impacting the primary or escaping from the mutual orbit. The above results only consider cases in which the binary asteroid is perturbed but remains stable. Now we examine simulations that disrupt the system. For each flyby speed tested, the number of simulations that cause disruption are counted, and the percentage of very close flybys that cause disruptions are reported in Fig. 5.7.

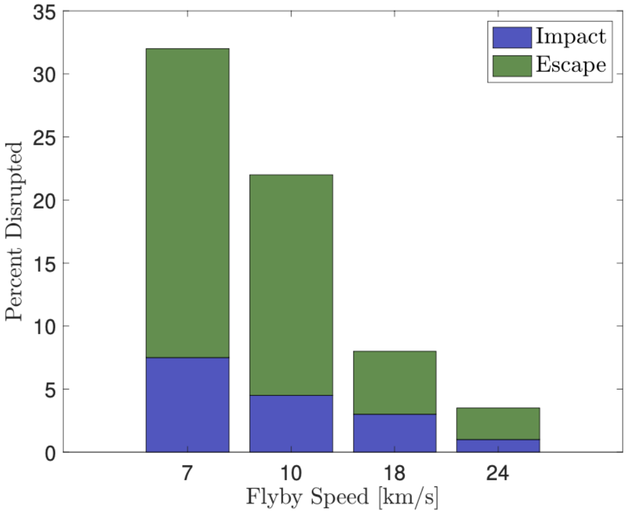

Figure 5.7: The percentage of very close flybys (closer than 50,000 km) that cause disruptions in the binary asteroid system. Disruptions include the secondary impacting the primary or escaping from the mutual orbit. No disruptions occurred with flybys further than 50,000 km.

As expected, as flyby speed increases, the number of disruptions decreases. This is consistent with smaller impulsive changes at faster flyby speeds.

### 5.3.3 Loss of Lock

Loss of lock occurs when the secondary's libration angle reaches 90 degrees [42]. We next examine the flyby conditions that will cause the secondary to reach a libration angle of 90 degrees and lose lock, causing the BYORP effect to terminate, in turn pushing the binary system into a new phase in its evolution. To do this we first define the flyby parameter, which is the coefficient used in the analytic model defined in [125]:

$$P = \sqrt{\frac{G}{(m_A + m_B)}} \frac{m_S a^{3/2}}{v_\infty q^2}. \tag{5.26}$$

This parameter characterizes the flyby by relating the closest approach distance, flyby speed, binary system mass and separation, and the planet's mass in one coefficient. We calculate the flyby parameter for all of the simulations, and plot the average change in libration angle for each of these simulations as a function of the flyby parameter, so that each data point is the average of all 100 Monte Carlo simulations at a specific combination of closest approach distance and flyby velocity. This investigation is plotted in Fig. 5.8, which has the shape of a sigmoid function. Based on this analysis, the secondary loses lock at a flyby parameter of approximately 0.1 on average. At a flyby speed of 10 km/s, this corresponds to a closest approach of 73,000 km for our binary system, which is consistent with the Monte Carlo results. Fig. 5.8 also shows the maximum change in libration angle over all simulations, demonstrating that encounters with a flyby parameter lower than this value can still lose lock, with a flyby parameter as low as 0.06 still losing lock.

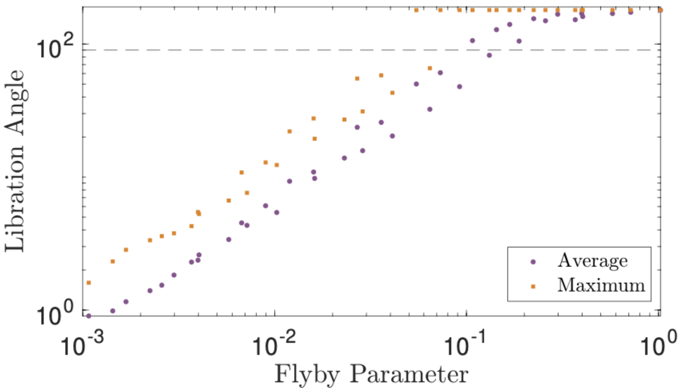

Figure 5.8: The change in libration angle for all simulations as a function of the flyby parameter. The dashed line shows a 90 degrees libration. The average change over all simulations is shown as purple circles, and the maximum change over all simulations is shown as orange squares.

In order to validate these results, we turn to the analytic model for secondary libration developed in [71]. This work uses the system's free energy to determine when the secondary has sufficient energy to begin circulation. The free energy is defined as the total energy of the system excluding the primary's rotational energy, since the primary's rotation is essentially unaffected by the secondary's dynamics. The general expression for the normalized free energy is

$$E_{free} = \frac{1}{2}\frac{(1-\nu)v^2}{\alpha^2 n^2} + \frac{1}{2}\frac{I_B\omega_B^2}{\alpha^2 n^2 m_B} + \mathcal{V} \tag{5.27}$$

where $\mathcal{V}$ is the normalized potential energy, and we have normalized using the secondary's mass, the maximum ellipsoid semiaxis, $\alpha$, and the mean motion at this distance, $n = \sqrt{G(m_A + m_B)/\alpha^3}$.

[71] introduce a simplified, planar form of this expression, given below

$$E_{free} = \frac{1}{2}\frac{K^2}{I_z} + \frac{1}{2}(1-\nu)\bar{r}'^2 + \frac{1}{2}\frac{\bar{I}_{B,z}(1-\nu)\bar{r}^2\phi_B'^2}{I_z} + \bar{V}(\bar{r}, \phi_B). \tag{5.28}$$

Here, $K$ is the free angular momentum, defined as $K = I_z\theta' + \bar{I}_{B,z}\phi_B'$. $I_z$ is the general moment of inertia, defined as $I_z = \bar{I}_{B,z} + \nu\bar{r}^2$. $\bar{I}_{B,z}$ is the nondimensional z-component of the secondary's inertia tensor, $\theta$ is the argument of longitude of the secondary and $\phi_B$ is the secondary's libration angle. The prime indicates differentiation with respect to nondimensional time, and the bar indicates a normalized quantity. Finally, $\bar{V}(\bar{r}, \phi_B)$ is the normalized potential of a system with an oblate primary, which is not repeated here. [71] define this potential energy using a second order expansion in the moments of inertia. For the singly synchronous system, $\phi_B = 0$. Note that [71] define their mass fraction as $1-\nu$, where $\nu$ is the mass fraction used in this work. It is also important to note that all these quantities are only defined in-plane.

In the analytic model, [71] derive a sufficient value of $\phi_B'$ required for the secondary to break lock and begin circulation. This value is defined as

$$\phi_B'^2 = \frac{I_z}{\bar{I}_{B,z}\bar{r}^5}\left[C_B^+ + \bar{I}_{A,z} - \bar{I}_{A,x} - (C_B^- + \bar{I}_{A,z} - \bar{I}_{A,x})\left(\frac{\bar{r}^3}{\bar{r}_m^3}\right)\right] \tag{5.29}$$

where

$$C_B^+ = -2\bar{I}_{B,x} + \bar{I}_{B,y} + \bar{I}_{B,z} \tag{5.30}$$

$$C_B^- = \bar{I}_{B,x} - 2\bar{I}_{B,y} + \bar{I}_{B,z} \tag{5.31}$$

and $r_m$ is the apoapsis radius of the mutual orbit if $C_B^+ + \bar{I}_{A,z} - \bar{I}_{A,x} > 0$ or the periapsis radius if $C_B^+ + \bar{I}_{A,z} - \bar{I}_{A,x} < 0$. In this analysis, we assume a circular orbit, so that $r_m = r$, which leads to a conservative estimate of the energy required to cause circulation. Substituting this value for $\phi'_B$ into Eq. 5.28 gives an analytic solution for the circulation energy. Since the system is initially locked, the initial value of $\phi'_B$ is zero. Thus, we have all the information required to estimate the change in energy that will result in circulation of the secondary. For our system, this change in nondimensional energy is approximately $1.444 \times 10^{-4}$.

Finally, we calculate the average change in energy for all simulations using Eq. 5.27. These values are plotted as a function of the flyby parameter in Fig. 5.9. This Figure also shows the analytic solution for the change in energy that will cause circulation, which is plotted as a dashed horizontal line. Fig. 5.9 shows that circulation can start at a flyby parameter near 0.1, with the possibility of circulation at flyby parameters smaller than this value. These results are consistent with those from Fig. 5.8.

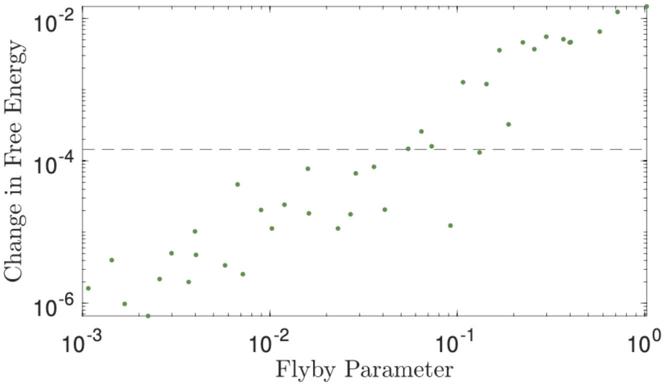

Figure 5.9: The change in free energy for all simulations as a function of the flyby parameter. The dashed line shows the analytic prediction of where circulation will begin.

## 5.4 1991VH Flybys

Binary asteroids are characterized by strong spin-orbit coupling [69, 34]. These internal dynamics can easily excite the secondary into a complex rotational state given an external perturbation [90, 84]. Variations of the spin and orbit period of a system experiencing only principal axis rotation are generally not large enough to explain the variations seen in the observations [96].

The lifecycle of NEAs is chaotic and driven by close encounters with the terrestrial planets, so a reasonable explanation for the excited dynamics of 1991VH is a recent close planetary encounter with the Earth. [127] showed that close Earth encounters with 1991VH are common, and it has also been shown that such close encounters can excite both the internal orbital and spin dynamics of binary asteroids [125, 126]. Thus, it seems the most natural explanation for the current dynamical state of 1991VH is NPA rotation within the secondary caused by an external perturbation and driven by the internal dynamics. This dynamical state has been postulated by [6] and [76], and here we provide a more quantitative analysis of this possibility. We test the hypothesis that the observed dynamical state of 1991VH can be explained by a single close Earth encounter in the past. To achieve this, we perform another suite of Monte Carlo simulations, where a singly-synchronous 1991VH-like system is perturbed by the Earth in a variety of encounter geometries. We then compare the orbit period, secondary rotation period, semimajor axis, and eccentricity of the post-flyby system to check for similarities with the current observations.

### 5.4.1 Earth Encounter Simulations

Our hypothesis is that 1991VH was previously in a singly-synchronous state, similar to the majority of observed binary steroids [6], before a close Earth encounter added eccentricity to the system and excited the system into its currently-observed chaotic state. To test this hypothesis, we vary possible pre-encounter orbit periods for the singly-synchronous state, then simulate a variety of Earth encounter conditions using the SRF3BP derived in this chapter.

In these simulations, we fix the bulk density of the system to be $\rho = 1.6\text{g/cm}^3$ [76], and set the primary and secondary densities equal to one another. Thus, when we choose the pre-encounter orbit period, this fixes the pre-encounter semimajor axis. Instead of using the Keplerian relationship to determine the semimajor axis, we adopt the approach defined in Appendix A, but inverted to calculate semimajor axis from orbit period.

In these simulations, we will use the F2BP dynamics, and thus allow for the primary to be aspherical. We set the primary $J_2 = 0.02$ (S. Naidu, personal communication, September 2020),

Table 5.1: The physical parameters used in the Monte Carlo simulations of Earth close encounters.

| Parameter | Symbol | Range |
|---|---|---|
| Pre-encounter Binary Orbit Period | $T_{pre}$ | 27-37 hr |
| Secondary Diameter | $D_B$ | 400-500 m |
| Secondary Prolateness | $a/b$ | 1.1-1.5 |
| Secondary Oblateness | $b/c$ | 1.1-1.5 |

and use a second degree-and-order expansion of the mutual potential. We fix the primary volume-equivalent diameter to 1.2 km.

We generate realistic flyby geometries of 1991VH relative to the Earth by propagating its orbit backward in time, taking into account the uncertainties in its ephemeris. We do this using the semi-analytic NEO propagation tool developed by [127]. The results of this propagation for the past $100,000$ years is shown in Fig. 5.10, showing every close approach within $150,000$ km of Earth.

There are a cluster of possible flybys around $25,000$ years ago, followed by another cluster around $40,000$ years ago. After these periods, uncertainties grow large enough that we have a more uniform distribution in flybys. The distribution of the longitude of the ascending note is generally uniform for all flybys, but the hyperbolic excess velocity has a clear evolution with time, generally decreasing into the past until around $80,000$ years ago. The inclination of the flybys appears roughly Gaussian, and centered around $90^\circ$. The argument of periapsis is centered around either $0/360^\circ$ or $180^\circ$. We also see a uniform distribution of the Earth-secondary phase angles at closest approach, indicating we are testing a wide range of possible geometries.

For the pre-encounter binary asteroid, we use the range of possible values outline in Table 5.1. This gives the pre-encounter orbit period, as well as the size and shape of the secondary. The separation distance is calculated from the orbit period such that the secondary is in a physically circular orbit, using the F2BP dynamics to eliminate pre-encounter libration from the secondary.

We use the SRF3BP dynamical model derived in this chapter. This model calculates the full spin-orbit coupling between the primary and secondary while also influenced by a distant and large spherical perturber, in our case the Earth. We simulate the flyby for 20 days with closest

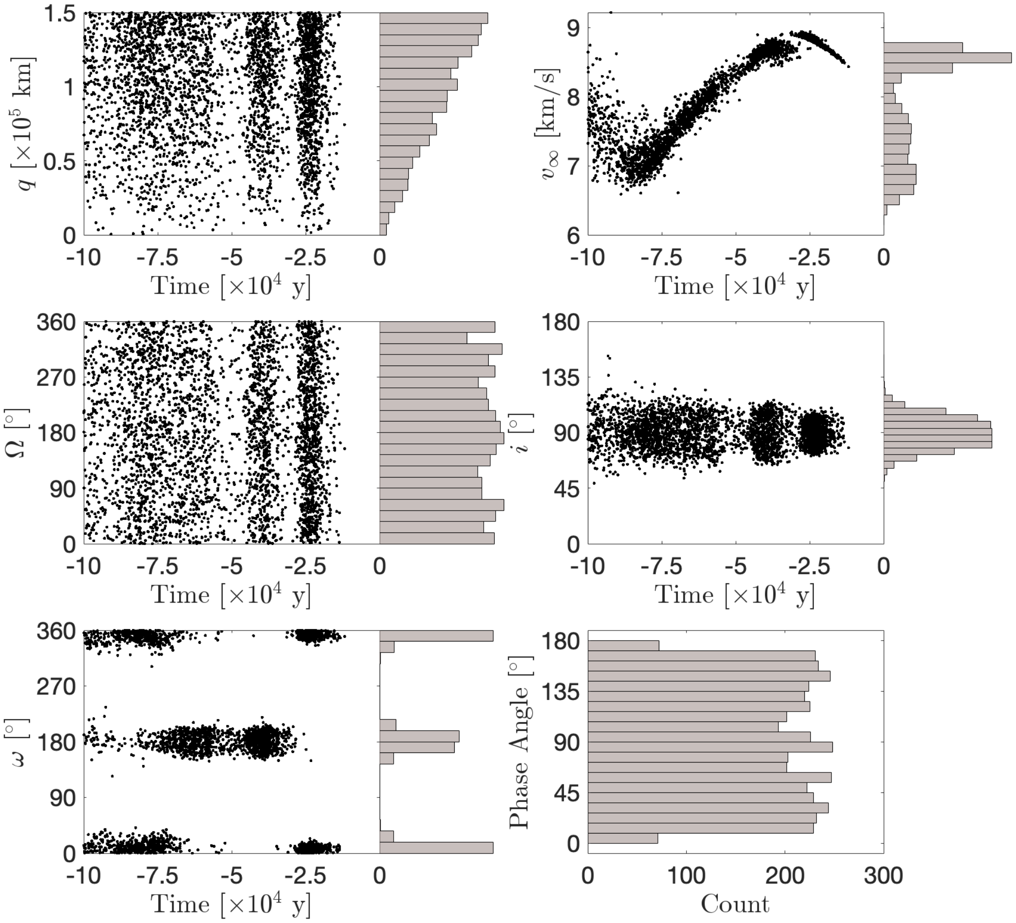

Figure 5.10: The close approach distance and hyperbolic excess speed, along with the Keplerian angles of the hyperbolic flyby trajectories as a function of time in the past. We also plot their overall distributions as histograms. These flybys are calculated by propagating the heliocentric orbit of 1991VH into the past and finding close approaches with Earth. We also plot the distribution of Earth-secondary phase angle at closest approach used in our Monte Carlo analysis.

approach centered at 10 days. After this, we hand off the results to the pure F2BP to speed up computational time without needing to track the effect of the Earth, and simulate the system for a full year.

### 5.4.2 Results

As shown in Sec. 2.2, Keplerian elements are inaccurate in describing binary asteroids. As such, we will also adopt the use of the ‘observable’ semimajor axis and eccentricity in our results. These quantities are defined using only the maximum and minimum separation distances within some time interval; in this analysis we will use a time interval of 5 days.

This still leaves the question of how best to calculate the secondary’s spin period, which is a key piece of information provided by observations. We are concerned with the dynamics of 1991VH that will reproduce these observations, so our approach should mimic how the spin period is calculated in these observations. Generally this is done using lightcurves of the secondary [6]. We define synthetic lightcurves, which we will calculate using the visible cross section of the secondary’s cross-sectional area:

$$A = \pi\sqrt{\hat{x}^2 b^2 c^2 + \hat{y}^2 a^2 c^2 + \hat{z}^2 a^2 b^2} \tag{5.32}$$

where $\hat{x}$, $\hat{y}$, and $\hat{z}$ is the direction of the observer defined in the body-fixed coordinates of the secondary, and $a > b > c$ are the semiaxes of the secondary ellipsoid.

After calculating the cross-section area, we perform a 1-degree Fourier fit over the same 5-day observation window. If the r-squared value of the fit is at least 0.5, we keep the fit as a measurement of half the secondary spin period. Due to the symmetry of the perfect ellipsoid, the Fourier fit will only measure half the spin period, so we correct by a factor of 2 to obtain the true spin period.

We perform $4,600$ Monte Carlo simulations of Earth close encounters. In each of these simulations we calculate the stroboscopic orbit period of the post-encounter system. To match the observations, we remove any results that have an average orbit period less than 30 hours or greater than 35 hours. After this removal, we obtain $1,866$ results, which are plotted in Fig. 5.11a. This plots the secondary spin period measurements as a function of closest approach distance, with dashed lines bracketing the observed values.

From Fig. 5.11a, we see a large grouping of secondary spin periods in the 30-35 hour range. These are the systems which remain synchronous with the orbit period after the flyby. We see most simulations fall in this category, but a significant number of simulations do have faster or shorter secondary spin periods, indicating these systems have become asynchronous. The number of results falling within the observed window is small but significant, indicating it is possible to reproduce the observed systems after a single Earth close encounter.

We see a narrow range of flyby conditions that are able to reproduce both the observed secondary rotation period and the orbital eccentricity. These flybys have a close approach distance within the range of $50,000$ - $80,000$ km. Closer than this produces an eccentricity that is too large, while further than this does not provide a sufficient perturbation to induce asynchronous rotation in the secondary.

In Fig. 5.11b, we plot the post-encounter observable semimajor axis as a function of pre-encounter orbit period. Again, the dashed lines bracket the observed values. Here we see to achieve the observed value, the pre-encounter orbit period of the system was likely between 28 and 35 hours. However, to match the observed eccentricity, the pre-encounter orbit period was likely not within the 30-33 hour range. This indicates the orbit period and semimajor axis of 1991VH have likely not changed very significantly as a result of a possible Earth encounter in its past, and the main change is the eccentricity and rotation of the secondary.

### 5.4.3 Example History

Next we present an example simulation providing a close match with observations. This system was initially in a circular orbit with a separation distance of 3.11 km and an orbit period of 29.9 hours. The secondary ellipsoid has a volume-equivalent diameter of 458 m, and axis ratios $a/b = 1.39$ and $b/c = 1.17$. This system undergoes an Earth encounter with a close approach distance of $46,580$ km with a hyperbolic excess speed of 7.6 km/s. The hyperbolic elements are $i = 78^\circ$, $\Omega = 217^\circ$, and $\omega = 193^\circ$.

To study this history, we integrate the system forward for 10 years after the flyby and plot the post-encounter secondary spin period and orbit period in Fig. 5.12. The results are not a perfect match, but lie very close to the observed values. The secondary spin period alternates between

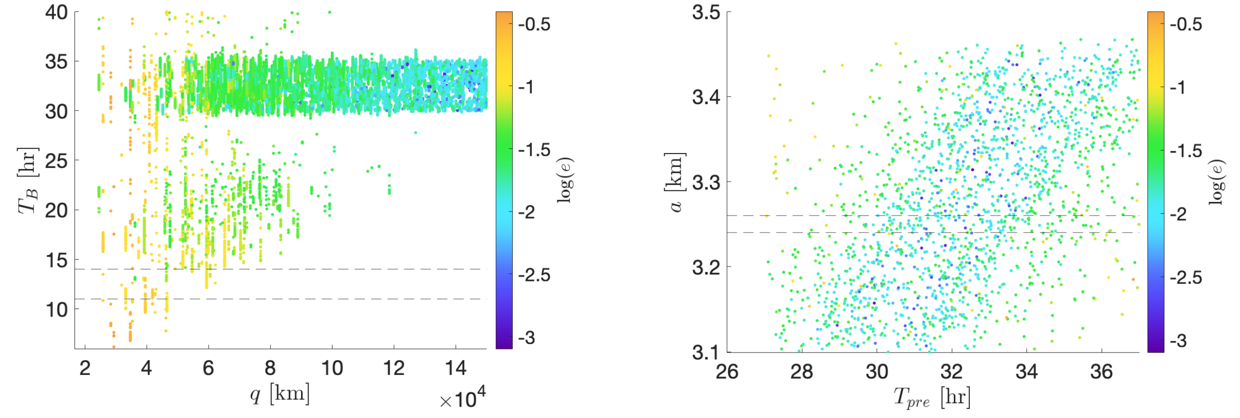

(a) Secondary Spin Period and Close Approach Distance (b) Semimajor Axis and Pre-Encounter Orbit Period

Figure 5.11: (a) The secondary spin periods as a function of Earth closest approach. The dashed lines bracket the range of observed values, and the color gradient shows eccentricity. (b) The observable semimajor axis as a function of pre-encounter orbit period. The dashed lines bracket the range of observed values, and the color gradient shows eccentricity.

epochs of more chaotic rotation and quasi-constant spin. The periods of quasi-constant spin last for several years at around a 10 hour spin period, generally consistent with observations. During the more chaotic epochs the spin period varies between 10 and 40 hours, and larger values are also possible. We note the actual observations of the secondary's rotation period in 1991VH do not see these longer rotation periods, although there is a possible estimate of a spin period up to 29 hours (see Table 2.1).

Likewise, the orbit period fluctuates between around 31.5 and 33 hours. The observed orbit period ranges between 32.5 and 32.8 hours. Thus, our simulated orbit period is not an exact match, but very close. There is a clear correlation with the secondary spin period. During the quasi-constant secondary spin period, the orbit period is slightly less than 32 hours, but increases during the periods of chaotic rotation.

In Fig. 5.13 we plot the observable semimajor axis and eccentricity. The semimajor axis ranges between 3.23 and 3.32 km. Similar to the orbit period, these values are a close match to the true observations of 32.4-32.6 km. Again there is a correlation with the secondary spin, with a lower semimajor axis during quasi-constant spin and a larger value during the chaotic rotation.

The eccentricity ranges between 0.02 and 0.15. The true eccentricity values range from 0.03 to 0.07. The periods of higher eccentricity correlate the the chaotic rotation and lower eccentricity during quasi-constant spin. So while our simulated eccentricity values can exceed these observations, they are overall generally consistent with observations.

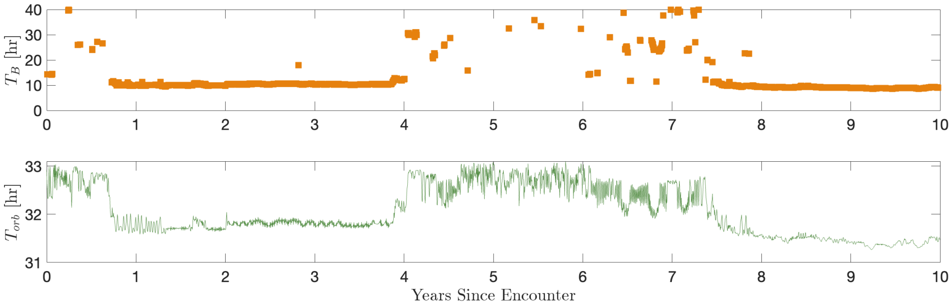

Figure 5.12: The fitted secondary spin periods (top) and stroboscopic orbit period (bottom) for one example simulation over 10 years after an Earth encounter.

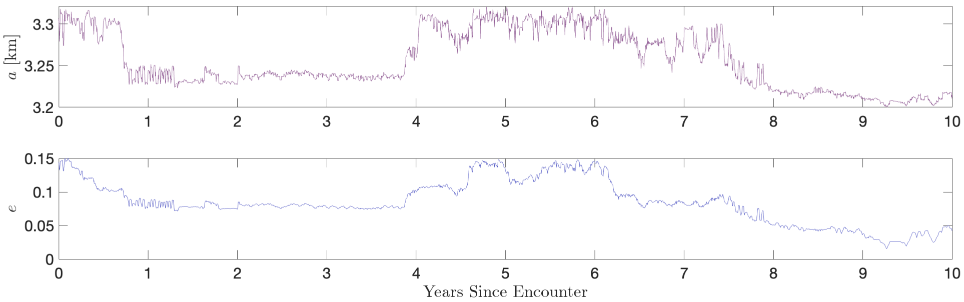

Figure 5.13: eriods (top) and stroboscopic orbit period (bottom) for one example simulation over 10 years after an Earth encounter. (b) The observable semimajor axis (top) and eccentricity (bottom) for one example simulation over 10 years after an Earth encounter.

We track the secondary's orientation with a set of 1-2-3 roll, pitch, yaw Euler angles relative to the rotating Hill frame. Fig. 5.14 shows these Euler angles over time for this example. During the period of quasi-constant spin, the secondary is generally only librating in its roll angle, either around 0° or 180°. However, the other angles are circulating, indicating even in this period of apparent stability the secondary is still fully tumbling. During the periods of chaotic rotation, all three angles are circulating.

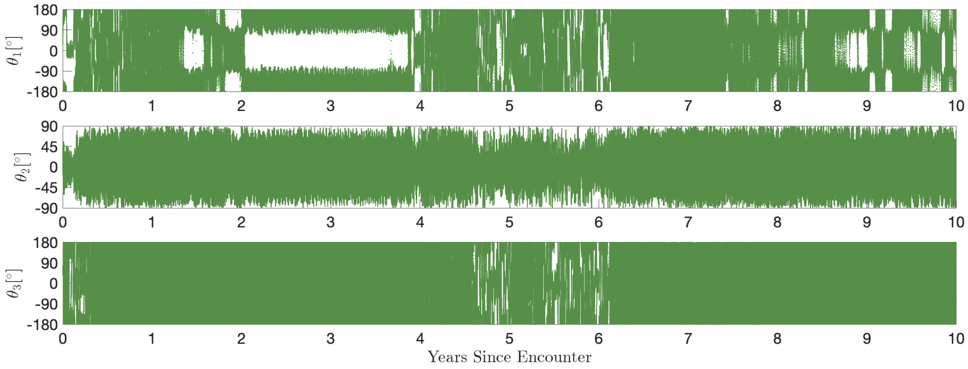

Figure 5.14: The roll (top), pitch (middle), and yaw (bottom) angles tracking the secondary's orientation relative to the singly-synchronous equilibrium.

In this simulation, the secondary enters a state of fully chaotic rotation. As this dynamical state closely reproduces the observations, this is another indicator that 1991VH is indeed experiencing chaotic rotation in the secondary.

Overall, this simulation demonstrates that due to the chaotic nature of binary asteroids, it is possible for a single Earth encounter to transform an equilibrated, singly-synchronous binary asteroid into a system that looks similar to the current 1991VH.

### 5.4.4 Secular Energy Dissipation

While we have demonstrated a close Earth encounter can create a system similar to 1991VH from a previously singly-synchronous binary asteroid, it is unclear how long-lived this excited state will last. The earliest Earth encounter sufficiently close to produce these dynamics was around 12,000 years ago [127].

In the singly-synchronous configuration, for a given spin rate of the primary the system's energy is minimized for the amount of angular momentum in the system. A perturbation such as a close planetary flyby will change the energy and angular momentum such that NPA rotation is allowable, precipitating an exchange of angular momentum between the secondary and the orbit. Since the secondary's angular momentum is much smaller than that of the orbit and primary, a small excess in energy at a given angular momentum level allows for NPA rotation.

In the minimum-energy configuration, the equilibrium spin rate is defined by Eq. 2.32. Because the secondary is in the 1:1 spin-orbit resonance in this configuration, its spin rate relative to an inertial frame is also defined by 2.32. Thus, the angular momentum for this configuration is simply written as:

$$H = (I_{Bz} + Mr^2)\sqrt{\frac{G(M_A + M_B)}{r^3}\left(1 + \frac{3}{2r^2}\mathcal{I}\right)} + I_{Az}\omega_A \tag{5.33}$$

where

$$\mathcal{I} = \bar{I}_{By} + \bar{I}_{Bz} - 2\bar{I}_{Bx} \tag{5.34}$$

and

$$M = \frac{M_A M_B}{M_A + M_B}. \tag{5.35}$$

Here we are explicitly assuming the primary is limited to principal-axis rotation about its major axis.

In the equilibrium configuration, the orbital velocity is $v = r\dot{\theta}$. Using this, the corresponding minimum energy can be written as [34]:

$$E^* = \frac{1}{2}(I_{Bz} + Mr^2)\frac{G(M_A + M_B)}{r^3}\left(1 + \frac{1}{3r^2}\mathcal{I}\right) - \frac{GM_AM_B}{r}\left(1 + \frac{1}{2r^2}\mathcal{I}\right) + \frac{1}{2}I_{Az}\omega_A^2. \tag{5.36}$$

When the system is perturbed away from this equilibrium, it will dissipate energy at a constant angular momentum. As the orbit expands and the primary's rotation rate slows, it will eventually be constrained to synchronous rotation in the secondary. This happens at the combination of separation and primary spin rate defined in Eq. 5.36. At this point energy dissipation will continue due to the rapidly rotating primary. However, there will not be enough energy to allow for a complex spin state in the secondary. As dissipation occurs, the separation distance $r$ will increase while the primary's spin rate $\omega_A$ will decrease. The primary methods of energy dissipation considered is tidal torques, and we implement the model defined in Sec. 4.2.1.

Using the results from Section 5.4.3, we integrate the equations of motion forward for another 100 years using the sphere-ellipsoid equations of motion. To improve numerical stability, we switch to a set of nondimenstional units, with the primary's mass as the mass unit, the initial separation as the length unit, and the Keplerian orbit period at this distance as the time unit. The total energy, free energy, and primary spin rate in these units are plotted in Fig. 5.15, demonstrating the energy dissipation. Here we are defining free energy as the total energy minus the contribution from the primary.

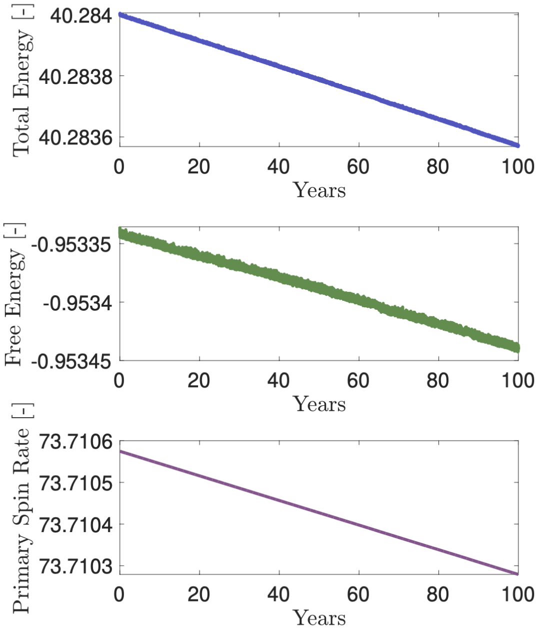

Figure 5.15: The total energy (top), free energy (middle), and the primary's spin rate (bottom), plotted in nondimensional units for 100 years.

Next, in Fig. 5.16, we also plot the total and free angular momentum. This ensures our system is conserving total angular momentum accurate to within $10^{-6}$. However, due to the secular evolution, the free angular momentum (the contribution of the secondary and the orbit) is increasing.

To predict the system's future behavior, we perform a linear fit to both the total energy and the primary spin rate. The linear fit is a conservative estimate, as dissipation will in reality slow as the separation distance increases. Using this fit, we can extrapolate the total energy and the primary's spin rate at a future time. Using the primary's spin rate, numerically solving Eq. 5.33 provides the separation distance required to conserve angular momentum, then Eq. 5.36 at these

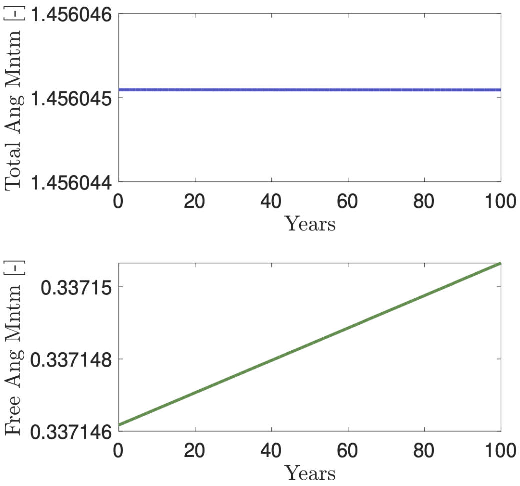

Figure 5.16: The total angular momentum (top) and free angular momentum (bottom) plotted in nondimensional units for 100 years.

values gives the energy for the singly-synchronous configuration at this angular momentum level, what we call the minimum energy. The difference between the total energy and this minimum energy is the excess energy, which is plotted in Fig. 5.17.

As we see, the excess energy is greater than 0 only for around $5,000$ years in this case, suggesting NPA rotation would in fact be relatively short lived for these tidal parameters. Indeed, a close Earth encounter for 1991VH did not occur within the past $12,000$ years [127].

To validate this predicted time for NPA rotation, we integrate the system for $10,000$ years. The results of this integration are shown in Fig. 5.18, plotting the libration angle, semimajor axis, and eccentricity. In this plot, the libration angle is the angle between the secondary's body-fixed $x$-axis and the position vector of the secondary relative to the primary.

From Fig. 5.18, we see very good agreement with the predicted duration of NPA rotation and these fully numerical results. The libration angle stops circulation a little before $5,000$ years, very similar to the prediction by our linear extrapolation. In this example, the secondary settles into the anti-synchronous case where it has flipped 180° from its initial orientation. This plot also shows the reduction of eccentricity, which happens much faster than predicted in analytical models [39, 128]. During this initial energy dissipation, the eccentricity is dissipating quicker than the

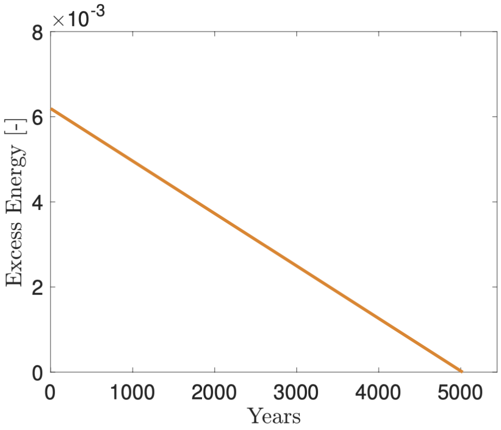

Figure 5.17: The excess energy of the system at this level of angular momentum. When the curve reaches zero, there is no longer any excess energy and the system must be in the singly-synchronous configuration.

semimajor axis is expanding, although we do see a secular increasing trend in the semimajor axis envelope toward the end of the simulation.

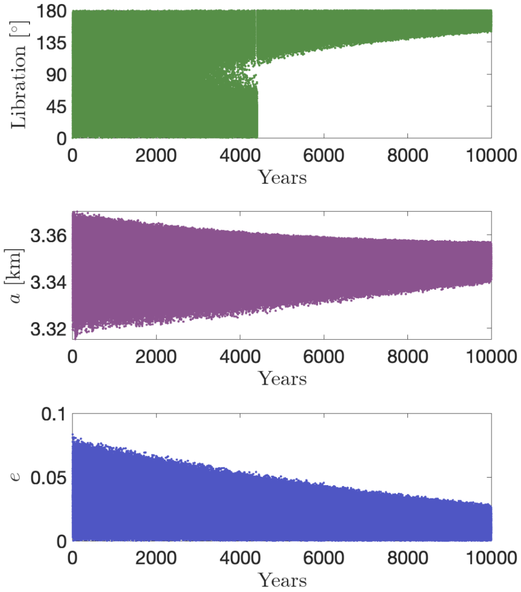

Figure 5.18: The libration angle (top), semimajor axis (middle), and eccentricity (bottom) of our example system undergoing tidal dissipation.

With the linear dissipation model validated by this detailed numerical integration, we now extend the analysis to different values of secondary tidal parameters. The secondary's libration dissipation is driven primarily by the parameters of the secondary [70, 128], so we can limit our analysis to only these parameters while keeping the primary's parameters constant.

Fig. 5.19 plots the total time for which NPA rotation is permissible as a function of secondary tidal parameters. The latest a flyby could have occurred was around $12,000$ years ago, which is plotted as a dashed black line. Assuming it was an Earth encounter that provided the excitation to place 1991VH in an excited dynamical state, this places a lower bound on $Q_B/k_B$ of around $2\times10^5$, although in reality it would likely be higher. This is relatively large for a rubble pile secondary [61], and using the model of [115] would require a 15 m or smaller dissipative regolith layer or less around the secondary. However, these values are still within the realm of possibility.

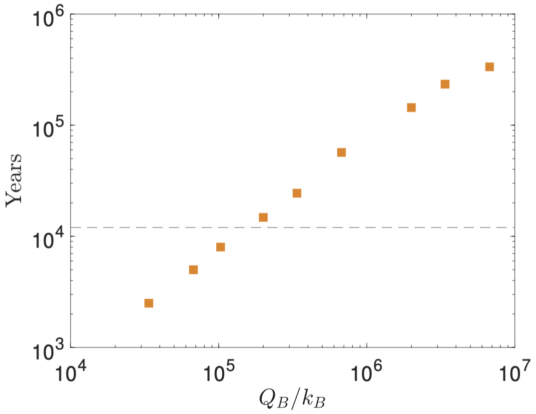

Figure 5.19: The permissible time of NPA rotation as a function of secondary tidal parameters. Close Earth encounters were possible starting around 12,000 years ago, which is marked as a dashed black line. This places a minimum boundary on secondary tidal parameters assuming 1991VH was excited by a past Earth encounter.

## 5.5 Conclusion

The dynamical evolution of binary asteroid systems is not fully understood. In this chapter we have shown that planetary encounters could play a significant role in this process. Due to the spin-orbit coupling present in binary asteroids, planetary flybys exert both gravitational forces and torques on the individual asteroids. The forces cause an impulsive change in the binary asteroid mutual orbit, while the torques can significantly perturb the secondary away from a synchronous orbit. The effect of these perturbations drop off exponentially as the flyby distance increases, and have a smaller effect at faster flyby speeds. Planetary encounters not only perturb the mutual orbit of a binary asteroid system, they also can significantly affect the spin state of the secondary, causing large libration amplitudes and even breaking lock after close flybys. While we have focused exclusively on close planetary encounters in this chapter, these equations can also be applied to study the solar effects of the heliocentric orbit on the binary asteroid dynamics.

We have also investigated the feasibility that the current excited dynamical state of 1991VH is the result of a previous close encounter with Earth. We find that it is relatively easy to excite NPA rotation of the secondary of 1991VH. This analysis reveals it is most likely that 1991VH was in a singly-synchronous configuration with an orbit period between 28 and 35 hours, although likely not within the 30-33 hour range. A single close Earth encounter around between $50,000$ km and $80,000$ km could have then placed the system into its current dynamical state. Because the current eccentricity of 1991VH is relatively small, this indicates the semimajor axis and orbit period of the system did not significantly change as a result of the flyby. However, the spin-orbit coupled dynamics are sufficient to place the secondary into its currently excited rotation state as a result of this flyby. A flyby closer than $50,000$ km is possible if secular dissipation has reduced the eccentricity into the range observed today. This excited state could then persist to the current day without energy dissipation returning it to the archetypal singly-synchronous state, provided the secondary is not very efficient at energy dissipation, or sequential close encounters counteract dissipation.

# Chapter 6

# The DART Impact

## 6.1 Introduction

In the first planetary defense test of a kinetic impactor, the NASA Double Asteroid Redirection Test (DART) spacecraft impacted Dimorphos, the secondary in the Didymos binary asteroid system, on September 26, 2022 [12]. The impact altered the trajectory of Dimorphos around Didymos, reducing the orbit period by around 33 minutes [60]. Studying and understanding the effects of the DART impact is one of the main motivations for this thesis. We will use numerical simulations to study the post-impact system, and connect this to the pre-impact system using the momentum transfer from the spacecraft to the asteroid. We outline the algorithm used in some detail in Appendix A. This relies on the use of observable elements and the stroboscopic orbit period to connect real-world observations to numerical simulations in GUBAS and other models. The case study of Didymos after the DART impacts demonstrates the usefulness of studying the perturbed dynamics of binary asteroids, as we are able to glean new information using this approach.

Ground-based observations of the system have shown a possible reduction in eccentricity and a loss of the precession signal [129]. From our analyses thus far, we know these are indicators of NPA rotation in Dimorphos. This Chapter will explore this possibility in depth with a quantitative analysis. The observable elements introduced in Chapter 2, and the stroboscopic orbit period in particular, have been used by the DART team to calculate the momentum enhancement factor $\beta$ of the impact [75], one of the level one objectives of the mission [59].

## 6.2 Problem Setup

The system parameters initially used in this analysis for the pre- and post-impact Didymos system are given in Table 6.1, estimated from the initial measurements after the DART impact. In calculating the axis ratios for Didymos and Dimorphos, we use the shape extents defined in [12]. For a conservative approach, we triple the uncertainties in the extents to ensure we sample the full $3\sigma$ parameter space. We limit $a/b > 1.01$ for both shapes to avoid cases where $b > a$, which corresponds to an unstable pre-impact equilibrium [87], or $a = b$, in which the system decouples and the spin-orbit equilibrium vanishes. We employ a suite of Monte Carlo simulations that sample over the uncertainties in the pre- and post-impact orbits as well as the uncertainties in the body shapes.

Note the considerable uncertainty on the pre-impact semimajor axis, which is equal to the separation between Didymos and Dimorphos at the impact time under the (physically) circular orbit assumption. While DART imaged the system before the impact, there are significant uncertainties in the positions of the bodies' centers of mass since the internal density distributions are unknown, which manifests in a large uncertainty in the pre-impact semimajor axis. Thus, the pre-impact separation is instead measured with radar data in [60].

For this work, we develop a method of ensuring our models are accurately capturing the behavior of the real system, outlined in Appendix A. In the simulations, we first numerically determine the required density of the primary to achieve an equilibrated randomly selected pre-impact system. This is done using a secant search algorithm. We then iterate an instantaneous $\Delta\vec{v}$ on the secondary's orbital velocity until the system converges to the post-impact orbit period using a second secant search. This allows us to connect the pre-impact system to the post-impact system. We include radial and out-of-plane $\Delta\vec{v}$ components such that the full $\Delta\vec{v}$ vector is anywhere within 30° of the orbit tangent direction, consistent with the impact and ejecta geometries discussed in [12] and [75], respectively.

We assume uniform density distributions of the asteroids and an equilibrated pre-impact orbit

Table 6.1: Parameters for the Didymos binary asteroid system. Uncertainties are reported as $1\sigma$ Gaussian unless noted as a uniform distribution. The secondary diameter and axis ratios are from the pre-impact body, and truncated at a lower limit of a/b = 1.01.

| Parameter | Value | Uncertainty/Note | Source |
|---|---|---|---|
| Pre-impact orbit period [hr] | 11.92148 | ±0.000044 | [82] |
| Post-impact orbit period [hr] | 11.372 | ±0.0057 | [60] |
| Pre-impact semimajor axis [m] | 1206 | ±35 | [60] |
| Pre-impact eccentricity | 0 | *assumed* | [82] |
| Primary diameter [m] | 761 | ±26 | [12] |
| Secondary diameter [m] | 151 | ±5 | [12] |
| Primary a/b axis ratio | 1.01-1.11 | *uniform* ($3\sigma$) | [12] |
| Primary b/c axis ratio | 1.21-1.56 | *uniform* ($3\sigma$) | [12] |
| Secondary a/b axis ratio | 1.01-1.13 | *uniform* ($3\sigma$) | [12] |
| Secondary b/c axis ratio | 1.32-1.69 | *uniform* ($3\sigma$) | [12] |
| Secondary density [kg/m$^3$] | 1500-3300 | *uniform* ($3\sigma$) | [12] |

with zero observable eccentricity and zero secondary libration. [80] and [75] outline justifications for these assumptions. In this work we initially ignore any torque applied to Dimorphos from the impact, as we are mainly concerned with the orbital dynamics. However, we will later consider the libration and stability of the secondary while including torque.

In our GUBAS simulations, both Didymos and Dimorphos are modeled as triaxial ellipsoids with semiaxes $a \geq b \geq c$. We use a second-degree and -order gravity expansion between these bodies. Given the uncertainties in the body shapes and their unknown internal mass distributions, there is no advantage to using a higher-order gravity expansion.

## 6.3 Effect of the DART Impact

From the approach in Sec. 3.2, we can calculate the change in specific orbital angular momentum to predict if the true anomaly should be librating or circulating. Assuming a circular pre-impact orbit and a planar, head-on impact with the secondary, the impulsive change in specific orbital angular momentum is easily calculated:

$$\Delta h = r\Delta v_T. \tag{6.1}$$

For the initial calculation of $\Delta v_T = -2.7$ mm/s [75], the change in specific orbit angular momentum is about $-3.2$ m$^2$/s. While the actual impact conditions are more complicated than this simple analysis, this value is sufficiently beyond the circulation threshold of roughly $-2$ m$^2$/s from Fig. 3.1 and Eq. 3.3 that we can confidently predict that the DART impact changed the system's momentum sufficiently to push it out of an equilibrium state.

### 6.3.1 Change in Velocity

Next, we calculate the along-track $\Delta v_T$ necessary to achieve the observed post-impact orbit period. While we include three-dimensional components in our analysis, we find essentially only the along-track change in velocity has an effect on the orbit period. As a function of the pre-impact observable semimajor axis, the along-track $\Delta v_T$ is plotted in Fig. 6.1a. Based on the Keplerian relationship, we fit $\Delta v_T$ as a function of the square-root of the pre-impact semimajor axis: $\Delta v_T \approx -5.86\sqrt{\frac{a_0}{1206\text{ m}}} + 3.19$ mm/s, where again $a_0$ is the pre-impact observable semimajor axis in meters. This numerical fit only applies to the range of data shown in Fig. 6.1a and should not be extrapolated out of this domain. Our results agree with those presented in [75], with a $\Delta v_T = -2.7 \pm 0.1$ mm/s, however here we highlight the dependence on the pre-impact observable semimajor axis. This also demonstrates that any component of the full $\Delta v$ vector not aligned with the orbit tangent direction does not appreciably affect the post-impact orbit period and is thus unobservable from the ground.

Besides the dependence of $\Delta v_T$ on the pre-impact observable semimajor axis, we also find a smaller dependence on Didymos's oblateness, or its $J_2$ gravity term. This is shown in Fig. 6.1b, where as Didymos becomes more oblate (larger $J_2$ values), the magnitude of $\Delta v_T$ needed to achieve the post-impact orbit period decreases. While the dependence of $\Delta v_T$ on the pre-impact semimajor axis dominates, it's also important to estimate Didymos's $J_2$ coefficient to fully understand the effects of the DART impact.

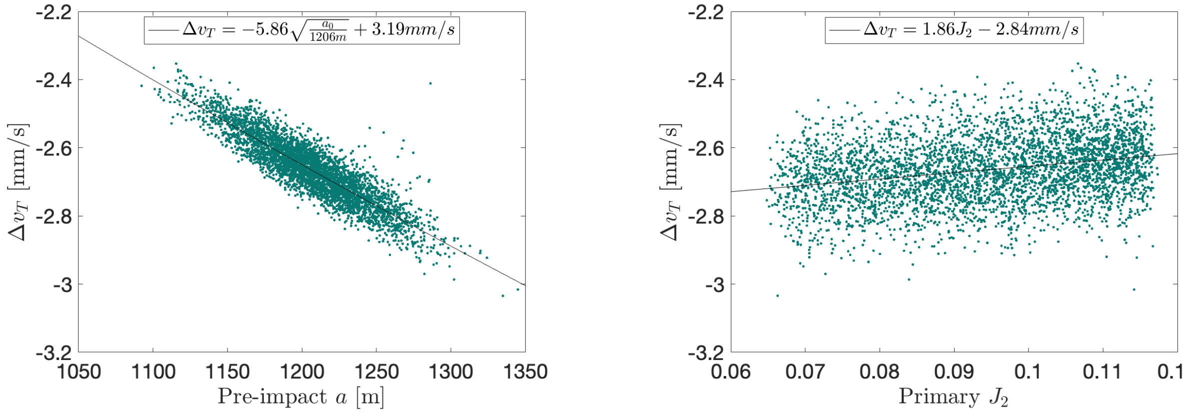

(a) Change in Velocity as a Function of Semimajor Axis

(b) Change in Velocity as a Function of Oblateness

Figure 6.1: (a) Change in along-track velocity as a function of the possible pre-impact observable semimajor axis. There is a strong relationship between $\Delta v_T$ and pre-impact observable semimajor axis. (b) Change in along-track velocity as a function of Didymos's possible $J_2$ gravity coefficient. The magnitude of $\Delta v_T$ decreases slightly as Didymos's $J_2$ increases.

By calculating the $\Delta v_T$ caused by the DART impact, we are able to convert this to a change in momentum. Unfortunately, the mass of Dimorphos is unobservable based on current measurements. However, the change in momentum can be reported as a function of this unknown parameter, as we did in [130]. This work satisfies the level one requirement of calculating the momentum enhancement of the DART impact.

### 6.3.2 Change in Semimajor Axis

Next, we calculate the change in the observable semimajor axis. From the Monte Carlo simulations we calculate the post-impact observable semimajor axis and solve for the change in the observable semimajor axis. We find $\Delta a = -37 \pm 1$ m ($1\sigma$), but the change in semimajor axis depends on the pre-impact observable semimajor axis, as illustrated in Fig. 6.2. Again, using a simple linear fit, we find $\Delta a \approx -37.64\left(\frac{a_0}{1206\text{ m}}\right) + 0.91$ m. From the Monte Carlo simulations, the post-impact observable semimajor axis is also directly calculated, equal to $1170 \pm 34$ m ($1\sigma$).

Thanks to the linear relationship between the pre- and post-impact observable semimajor axis, it is simple for measurements of the post-impact semimajor axis to add additional constraints

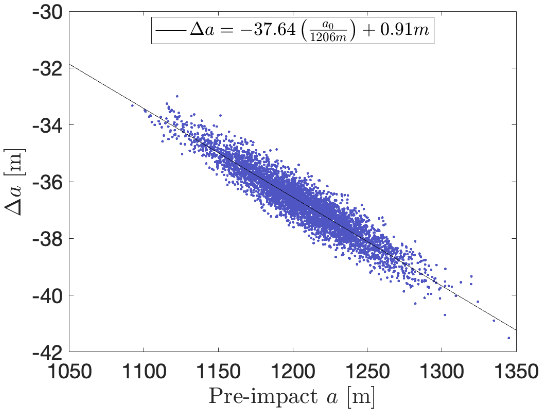

Figure 6.2: The change in observable semimajor axis as a function of the possible pre-impact observable semimajor axis. There is a strong linear relationship between the post- and pre-impact semimajor axes.

to the pre-impact value. This is important, as we have already seen the importance of tightening the constraints on the pre-impact observable semimajor axis, as $\Delta v_T$ strongly depends on this quantity. Thus, a major advantage and contribution of ESA's Hera mission, planned to return to Didymos to study the post-impact system in early 2027, is the ability to precisely measure the current semimajor axis [64].

This linear relationship is expected from basic Keplerian dynamics. From Kepler's third law, we know the following relationship between orbital period and semimajor axis for a common barycenter:

$$\frac{P_1^2}{a_1^3} = \frac{P_2^2}{a_2^3}. \tag{6.2}$$

This can be rearranged and, substituting in the parameters from Table 6.1, we find

$$a_2 = a_1\left(\frac{P_2}{P_1}\right)^{2/3} = 1168.65\left(\frac{a_1}{1206\text{ m}}\right)\text{ m}. \tag{6.3}$$

Even though the F2BP dynamics are non-Keplerian in reality, applying Kepler's third law provides a relatively accurate estimate for the relationship between the pre- and post-impact semimajor axis. Furthermore, this illustrates the linear relationship. Thus, precise measurements from Hera of the post-impact semimajor axis also provide estimates for the pre-impact semimajor axis. This in turn leads to a more accurate estimate for the system's mass and the $\Delta v_T$ of the DART impact, provided the orbit has only experienced minimal secular evolution since the impact.

### 6.3.3 Change in Eccentricity

Finally, we discuss the post-impact eccentricity. The change in observable eccentricity is plotted in Fig. 6.3a as a function of the pre-impact observable semimajor axis. Notably, while previous quantities have depended strongly on the pre-impact observable semimajor axis, the eccentricity is largely independent of this quantity. From an initial orbit with zero observable eccentricity, the post-impact eccentricity is $0.031 \pm 0.002$.

It is worth discussing the skewed distribution in Fig. 6.3a, in which the change in observable eccentricity is occasionally much smaller than the representative value of 0.031. Each data point in Fig. 6.3a is the average post-impact observable eccentricity over the full simulation time of 100 days. The lower averages correspond to simulations in which the secondary enters a state of non-principal axis (NPA) rotation, as discussed in Sec. 3.6.2. Approximately 18% of our simulation runs result in this attitude instability.

Next, we relax the initially circular orbit assumption. Using only the nominal system (i.e., the parameters from Table 6.1 without the uncertainties), we vary the pre-impact observable eccentricity. Fig. 6.3b shows the post-impact observable eccentricity as a function of the pre-impact observable eccentricity. In these simulations, we only apply a tangential $\Delta v_T$, and the perturbation occurs when the secondary is either at apoapsis or periapsis of the now-eccentric pre-impact orbit. This means the two curves in Fig. 6.3b define an envelope of permissible eccentricity values. Depending on where in the orbit the secondary is at the time of the impact, the resulting eccentricity can lie anywhere in the area bounded by the two curves. Thus, measuring the post-impact eccentricity can give constraints to the pre-impact eccentricity. However, if the pre-impact orbit was eccentric, it is unknown where in its orbit Dimorphos was at the time of the impact, so a precise relationship between pre- and post-impact eccentricity is impossible.

To illustrate the change in Dimorphos's orbit, we plot the system with the nominal pre- and post-impact orbits ignoring the uncertainties in Table 6.1 in Fig. 6.4. This shows the differences

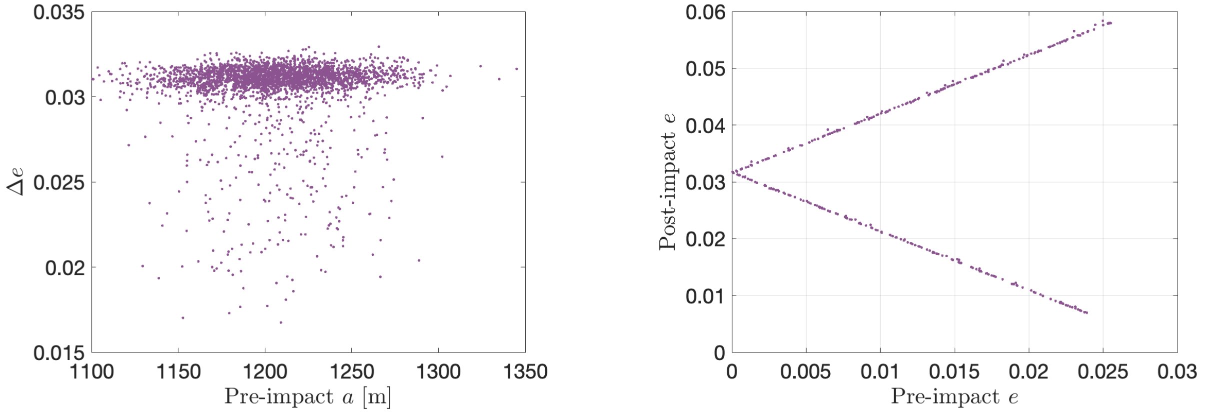

(a) Change in Eccentricity Caused by DART (b) Range of Possible Eccentricities Caused by DART

Figure 6.3: (a) Change in observable eccentricity as a function of the possible pre-impact observable semimajor axis. The change in eccentricity is largely independent of the pre-impact semimajor axis. The pre-impact orbit is assumed physically circular. The simulation runs with a skewed smaller eccentricity change are the result of tumbling in the secondary. (b) The post-impact observable eccentricity as a function of the pre-impact observable eccentricity. The two curves define an envelope in which the post-impact observable eccentricity may exist, depending on where in its orbit the secondary was at the time of the perturbation.

in the mutual orbit caused by the DART impact. For illustration purposes we use the radar shape model from [81] scaled to the size calculated by [12] for Didymos, and the DRACO shape model of Dimorphos from [12]. The outer orbit is the pre-impact, and the inner orbit is the post-impact. Only the first full orbit after the impact is plotted, and over time this orbit will precess around Didymos.

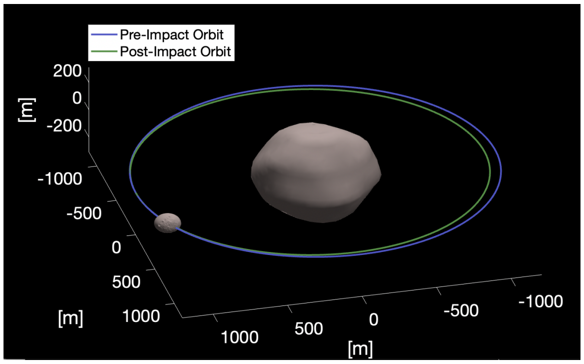

Figure 6.4: The pre- and post-impact orbits for the nominal system plotted to scale. For illustration purposes, the scaled radar shape model is used to show Didymos [81] and the [12] shape model is used to show Dimorphos.

## 6.4 Dimorphos Mass Loss and Reshaping

We now relax our assumption of no mass loss or reshaping of Dimorphos from the DART impact. This is an important consideration, as [131] showed that reshaping of Dimorphos can contribute to the momentum enhancement factor estimate. To achieve this, we modify our algorithm so that after the system's mass is calculated to match the pre-impact orbit period, we re-sample the secondary size and shape, keeping its density the same. DART impacted roughly along the intermediate axis of Dimorphos [12], so any reshaping will decrease the ellipsoid's $b$ axis to first order. This is equivalent to increasing the $a/b$ ratio and decreasing the $b/c$ ratio. In reality, reshaping may result in an asymmetric secondary [132]. However, while our secondary is still an ellipsoid shape, we are in effect changing its moments of inertia, which are the dominant quantities in calculating the mutual potential.

We re-sample $a/b$ and $b/c$ for Dimorphos, raising the upper limit of $a/b$ to 1.3 and decreasing the lower limit of $b/c$ to 1.1. To reflect the reality of decreasing the $b$ axis, in re-sampling the axis ratios, we adjust the uniform distribution so that the lower limit of $a/b$ is equal to its pre-impact value (so it always increases) and the upper limit of $b/c$ is equal to its pre-impact value (so it always decreases). The new limits on post-impact $a/b$ and $b/c$ are somewhat arbitrary but allow for relatively large changes in the secondary shape.

To account for mass loss, we also re-sample the volume-equivalent radius of Dimorphos. We center our sampling on the pre-impact value and draw from a half-normal distribution with a standard deviation of 0.1 m, ensuring we do not increase the radius. The standard deviation of the post-impact radius was chosen to approximately match the initial mass-loss estimate of [133], around 0.3-0.5% of the assumed Dimorphos pre-impact mass.

Accounting for mass loss and reshaping slightly reduces the magnitude of $\Delta v_T$ needed to achieve the post-impact orbit period. Our new estimate is $\Delta v_T \approx -2.6 \pm 0.1$ mm/s. This effect was not considered in [75], and thus they may have over-approximated the impact-induced $\Delta v_T$, as reshaping is likely significant as we will show later in the chapter. To explore this shift, we plot $\Delta v_T$

as a function of the mass loss in Fig. 6.5a and as a function of reshaping $a/b$ in Fig. 6.5b. We find $\Delta v_T$ has a negligible dependence on the mass loss, likely given the minimal percent change of the mass. However, the magnitude of $\Delta v_T$ slightly decreases with larger changes to $a/b$, consistent with results from [131], who showed reshaping of the secondary changes the mutual potential between the bodies, which contributes to changes in the orbit period. We find no trend with $\Delta v_T$ and the $b/c$ ratio.

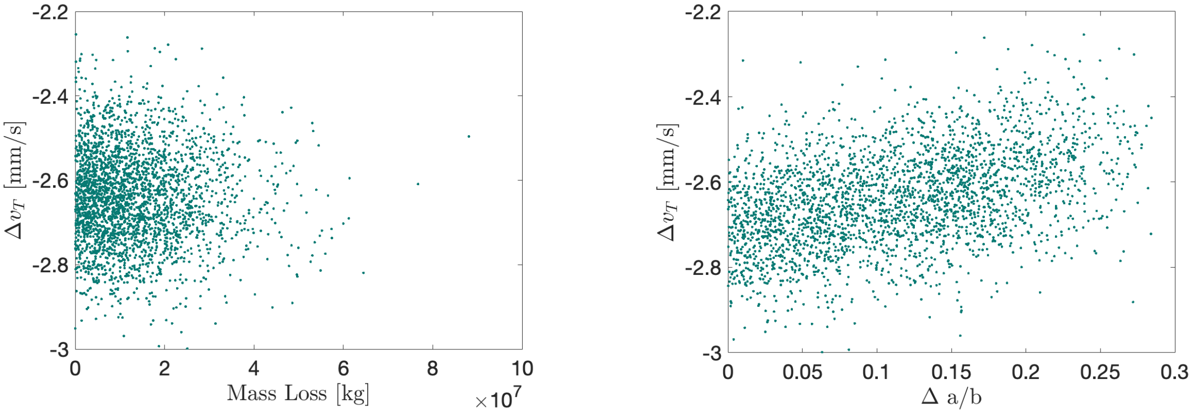

(a) Change in Velocity Accounting for Mass Loss

(b) Change in Velocity Accounting for Reshaping

Figure 6.5: (a) Calculated $\Delta v_T$ as a function of Dimorphos's mass loss. Within reasonable values for mass loss, there is no strong trend in $\Delta v_T$. (b) Calculated $\Delta v_T$ as a function of Dimorphos's reshaping of its $a/b$ ratio. For impacts that cause more reshaping, the required $\Delta v_T$ magnitude to achieve the post-impact orbit period is smaller on average.

We also find a relationship between reshaping of $a/b$ and the post-impact observable eccentricity. For larger changes in $a/b$, the change in observable eccentricity slightly decreases on average. This is another important consideration to make when interpreting the system's current eccentricity. Fig. 6.6 shows this relationship.

## 6.5 Precession

As discussed in Sec. 3.5, the shape and spin state of the secondary has a significant effect on the orbital apsidal precession rate. Using the estimated apsidal precession rate in Didymos [134], we can place constraints on the secondary shape and libration. We refine our inputs, so

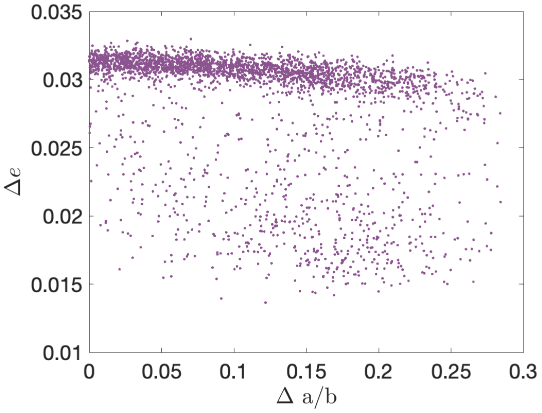

Figure 6.6: Calculated observable $\Delta e$ as a function of Dimorphos's reshaping of its a/b ratio. For impacts that cause more reshaping, the change in eccentricity is on-average reduced.

rather than using the full range of values in Table 6.1, we use $J_2 = 0.09$ for Didymos and the separation of the orbit at the time of the DART impact of 1.189 km [134]. We assume Dimorphos was in a circular orbit about Didymos prior to the perturbation, and fix the Dimorphos $b/c = 1.2$. From observations the estimated apsidal precession rate in Didymos is $\dot{\varpi} = 6.7°/\text{day}$ [134]. In the analysis of precession, we limit the orbital motion to planar, so we switch our model to the planar F2BP.

In our algorithm, we iterate a tangential and instantaneous $\Delta v_T$ on the orbital speed of Dimorphos until our post-impact system matches the measured post-DART orbital period of 11.37 hours. Once this is achieved, we perform a second iteration to the secondary's rotation rate: we add a $\delta\dot{\phi}_2$ to correctly achieve the estimated apsidal precession rate.

In Fig. 6.7a, we plot curves that represent combinations of secondary elongation and spin perturbation that replicate the apsidal precession rate in Didymos. For a given Dimorphos $C_{22}$, or equivalently an $a/b$ value, there are two values of spin perturbation $\delta\dot{\phi}_2$ that can reproduce the observed precession rate. Thus, some knowledge of the perturbation's geometry is required to resolve the ambiguity between the two curves. For the geometry of the DART impact, we likely have a negative value of $\delta\dot{\phi}_2$ [134], corresponding to the lower of the two curves in Fig. 6.7a.

These curves demonstrate that for the nominal system (ignoring uncertainties on the shape of Didymos and the orbit geometry), we are required to have an $a/b \gtrsim 1.25$, equivalent to having $C_{22} \gtrsim 0.018$. This is a purely dynamical constraint indicating significant reshaping in Dimorphos as a result of the DART impact, which complements the physical argument for the same phenomenon by [135]. This is also consistent with the estimation of the system parameters by [134].

We can also use this approach to investigate the allowable libration amplitude in the system. Here we see uniformly increasing libration amplitude with increasing $C_{22}$. The minimum $C_{22}$ results in a libration amplitude of around 10°, indicating the system has at least this libration amplitude. Smaller values are permissible given the uncertainties in the system, but most combinations of parameters will result in a libration amplitude larger than this value.

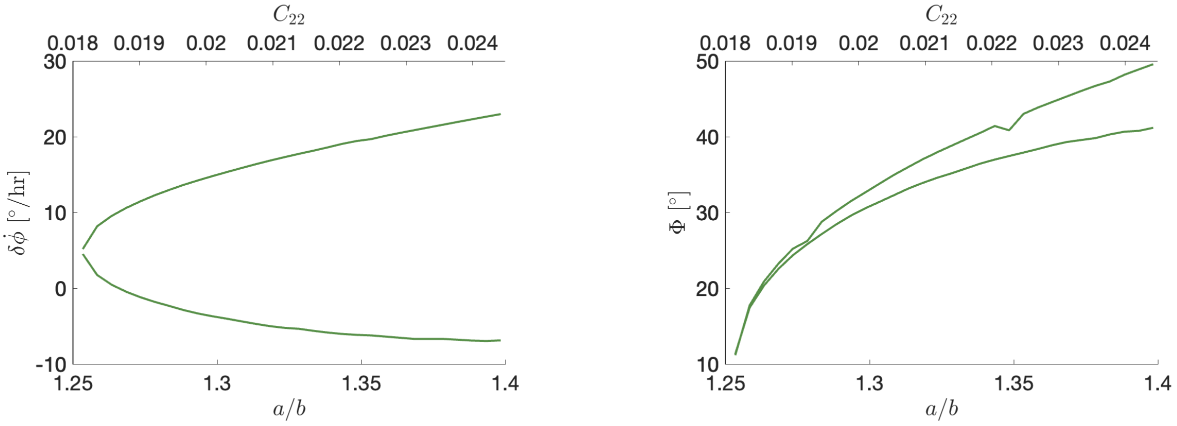

(a) Required Spin Perturbation

(b) Required Libration Amplitude

Figure 6.7: Plots of numeric results showing (a) The required spin perturbation and (b) the required libration amplitude as functions of Dimorphos prolateness necessary to reach the measured precession rate.

## 6.6 Dissipation

One question of interest is how quickly will energy dissipate from Didymos following the DART impact? This is important to understand, as the system may have evolved before the arrival of Hera. To investigate this, we integrate the system forward for 10 years and plot the eccentricity over that time using the sphere-ellipsoid model while incorporating dissipation from three-dimensional tidal torque and NPA rotation. We test a variety of combinations of tidal parameters. For a system which remains in stable, principal-axis rotation, the results are shown in Fig. 6.8

In the stable case, we see the fastest eccentricity dissipation occurs for very small values of $Q_s/k_s$, which is expected from the literature [70]. We also see if $Q_s/k_s \gg Q_p/k_p$, the eccentricity increases, which is also a classical result. In all cases, there is still significant eccentricity by the time of Hera's arrival, about 5 years after the DART impact. However, for the extremely dissipative cases, the eccentricity is around half its value immediately after the DART impact. If Hera measures an eccentricity much smaller than the value obtained from ground-based measurements, this will constrain the tidal parameters of the system. However, if the tidal parameters are larger, there will not be a significant change in eccentricity by the time of Hera's arrival.

Next, we repeat the same analysis for a case in which Dimorphos enters NPA rotation, plotted in Fig. 6.9. In this case, we see the systems which are very efficient at dissipating energy are able to return to a circular orbit prior to Hera's arrival, as eccentricity is essentially eliminated within 5 years. This is due to the NPA rotation providing another mechanism to dissipate energy, resulting in a faster secular change to the orbit. However, as tidal parameters increase and the system becomes less efficient at energy dissipation, the eccentricity again can see very little change, and any secular trend may be dominated by chaotic fluctuations due to the angular momentum exchange with the tumbling secondary.

Here, we have demonstrated the possibility of Hera measuring secular changes to Didymos. This is only possible in a select few cases, and provided the system is in principal axis rotation. If Dimorphos enters NPA rotation, it is very unlikely Hera will be able to measure any secular changes within the system during its limited mission duration.

## 6.7 Lightcurve Analysis

Following the DART impact, lightcurves of Dimorphos were detected spanning from December 2022 into January 2023 at 7 distinct epochs. Upon analysis, the amplitude of the cross-section

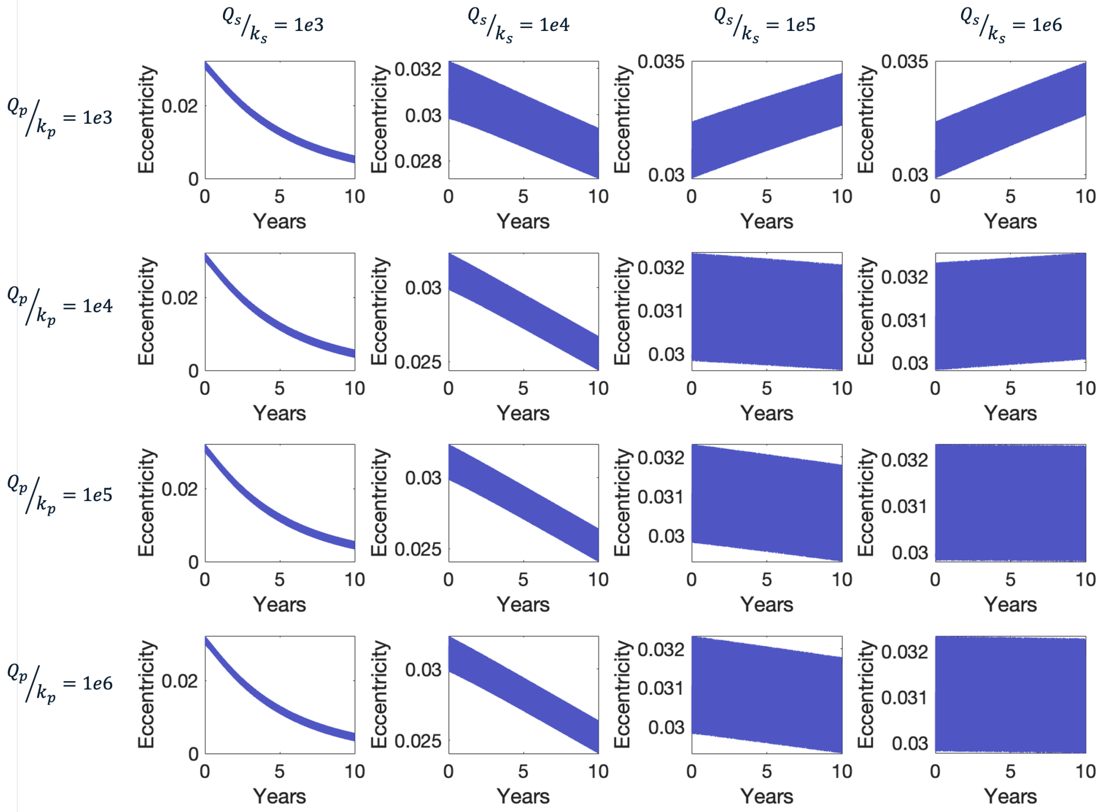

Figure 6.8: The eccentricity over 10 years for various combinations of tidal parameters in a system remaining in stable rotation.

variation over Dimorphos's rotation and the offset in mean anomaly between the minimum of the secondary lightcurve and the center of the mutual event varied across these epochs [136]. These measurements are shown in Table 6.2, where $C$ is the visible cross sectional area of Dimorphos and $M$ is its mean anomaly. These variations are intriguing, so to provide more context to the observations we utilize high-fidelity GUBAS simulations to generate synthetic lightcurves and compare to the data.

### 6.7.1 Numerical Simulations of the Dimorphos Lightcurves

Due to the uncertainties surrounding the parameters of the Didymos system, we again adopt a Monte Carlo approach. After further refinement incorporating newer observations, the new inputs

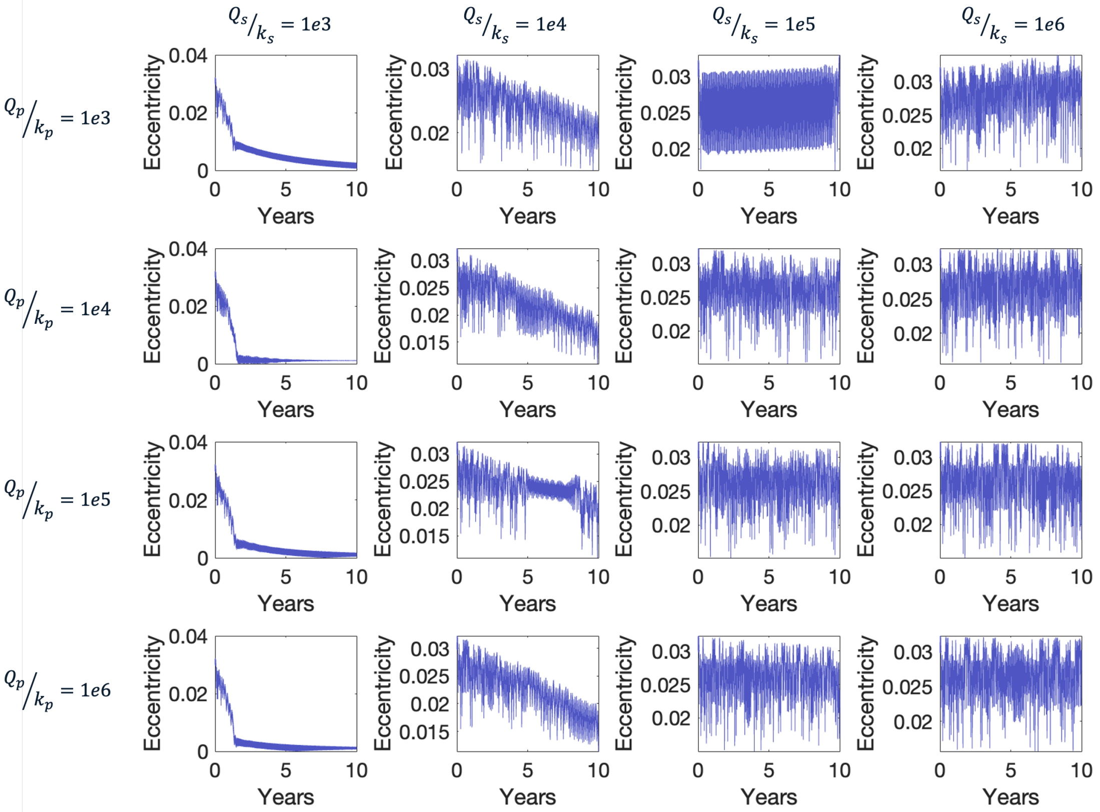

Figure 6.9: The eccentricity over 10 years for various combinations of tidal parameters for a system in NPA rotation.

to the simulation are given in Table 6.3. Given the small uncertainties in the pre- and post-impact orbit period, we fix these values at 11.9215 and 11.3675 hours, respectively [129]. We also fix the diameter of Didymos $D_1 = 711.4$ m and its elongation $a_1/b_1 = 1$ since it is very nearly axisymmetric and its rapid rotation will average out the effect of any minor elongation [134]. Thus, Didymos is modeled as an oblate spheroid. We model Dimorphos as a triaxial ellipsoid with an instantaneous shape change at the time of the impact. The spin period of Didymos is 2.26 hr and the initial spin period of Dimorphos is taken to be the same as the initial orbit period [129]. The remaining system parameters have an associated uncertainty and are detailed in Table 6.3.

The initial velocity of the pre-impact system is determined by the separation at impact. The

Table 6.2: Dimorphos lightcurves post-DART impact.

| Epoch | $\Delta C/C_{mean}$ | $\Delta M$ [°] |
|---|---|---|
| 2022-12-14 to 15 | 0.12 | -11.9 |
| 2022-12-22 | 0.12 | +4.2 |
| 2022-12-28 to 31 | 0.07 | +5.3 |
| 2023-01-11 | 0.17 | -0.7 |
| 2023-01-14 to 16 | 0.13 | -26.3 |
| 2023-01-18 | 0.12 | +15.5 |
| 2023-01-28 to 29 | 0.24 | +4.6 |

Table 6.3: Parameters of the Didymos system and their uncertainties used in our Monte Carlo simulations. Most estimates are from [134], except for the estimates of off-tangent velocity angle and the momentum enhancement factor, which come from [130]. We chose $b_1/c_1$ to approximately match the estimate of Didymos $J_2$. To accommodate our assumption of uniform density distributions and a second order gravity expansion, we inflate our shape uncertainties.

| Parameter | Symbol | Estimate | Distribution |
|---|---|---|---|
| Separation at impact | $r_0$ | $1189 \pm 25$m | Normal |
| Didymos $b/c$ | $b_2/c_2$ | $1.35 \pm 0.08$ | Normal |
| Dimorphos effective diameter | $D_2$ | $150 \pm 7.5$m | Normal |
| Dimorphos pre-impact $a/b$ | $a_{2,0}/b_{2,0}$ | $1.02 \pm 0.02$ | Normal |
| Dimorphos pre-impact $a/c$ | $a_{2,0}/c_{2,0}$ | $1.52 \pm 0.02$ | Normal |
| Dimorphos post-impact $a/b$ | $a_2/b_2$ | $1.1 - 1.4$ | Uniform |
| Dimorphos post-impact $b/c$ | $b_2/c_2$ | $1.0 - 1.6$ | Uniform |
| Velocity perturbation | $\delta v$ | $0.98 - 1.02$ | Uniform |
| Off-tangent velocity angle | $\theta$ | $0° - 30°$ | Uniform |
| Momentum enhancement factor | $\beta$ | $2.5 - 4.5$ | Uniform |

velocity is calculated as

$$v_0 = \delta v \times \frac{2\pi}{T_0} r_0 \tag{6.4}$$

where $T_0$ is the pre-impact orbit period. The velocity perturbation $\delta v$ allows for some amount of pre-impact eccentricity. The algorithm takes the initial state and iterates the bulk density of the system using a secant search algorithm to match the pre-impact orbit period, as described in Appendix A. Then, the instantaneous effects of the impact are applied. We pick a new shape for Dimorphos, and iterate the tangential $\Delta v_T$ using another secant search algorithm to match the post-impact orbit period. Along with the $\Delta v_T$, we also apply an off-tangent $\Delta v$ and a torque imparted by the off-center impact and the net ejecta momentum. The radial $\Delta v_r$ and out-of-plane $\Delta v_z$ are calculated using the off-tangent velocity angle:

$$\Delta v_r = \Delta v_z = \Delta v_T \sin\theta. \tag{6.5}$$

The torque is calculated using the relative location and velocity of the DART impact. DART impacted at a position relative to the center-of-figure, which is equal to the center-of-mass given our uniform density assumption, given in [12]:

$$\vec{r}_{rel} = [-8.31, -83.2, -13]^{\mathrm{T}} \text{ m} \tag{6.6}$$

and a relative velocity:

$$\vec{v}_{rel} = [-1062.71, 5963.7, 1032.0]^{\mathrm{T}} \text{ m/s}. \tag{6.7}$$

The perturbation to the spin rate of Dimorphos caused by the torque of the DART spacecraft and ejecta is calculated by

$$\Delta\vec{\omega} = \mathbf{I}_B^{-1}\beta m_{DART}(\vec{r}_{rel} \times \vec{v}_{rel}). \tag{6.8}$$

Note this approach involves the implicit assumption that the ejecta momentum is aligned with the incoming DART velocity vector. In reality this is not the case, but here we are only using this approach to apply a spin perturbation to the secondary. Without a spin perturbation, we would under-estimate the likelihood of inducing significant NPA rotation.

We run a total of 15,743 Monte Carlo simulations in GUBAS sampling over the uncertainties listed in Table 6.3. We use a second degree-and-order expansion of the mutual potential for computational efficiency. Given the uncertainties in the mass distributions, there is no added benefit to using a higher order gravity expansion.

### 6.7.2 Synthetic Lightcurves

Beginning with the geometry at the moment of the DART impact, we integrate forward 130 days. Starting 79 days into the simulation we begin generating synthetic lightcurves. This matches the first observation of a Dimorphos lightcurve on 14 December 2022. To keep our individual synthetic lightcurves uncorrelated and to approximately match the strategy of the real lightcurves, we generate a synthetic lightcurve once every 3 days, with each lightcurve spanning about 8 hours. The lightcurves are generated using a spin pole of Didymos of $\lambda = 310°$ and $\delta = -80.4°$ [129].

In the synthetic lightcurves, we use ray tracing within our numerical simulations to calculate the time of mutual events. We measure a mutual event as anytime the two asteroids overlap or cast a shadow on the other (corresponding to occultations and eclipses, respectively). We measure the time of the mutual event as the time at the center of the event.

For direct comparison with observations, we calculate the total visible cross section of Dimorphos. This eliminates the need to assume any scattering law in these simulations. For the shapes, we use a polyhedron shape model for Didymos and a triaxial ellipsoid for Dimorphos since there is no shape model of Dimorphos post-impact. The shape parameters are sampled in the Monte Carlo. To calculate the visible cross section of Dimorphos, we use the expression of the visible area of an ellipsoid, given in Eq. 5.32.

Following the approach of lightcurve decomposition, we also fit a first degree Fourier series to the Dimorphos lightcurve. From this Fourier fit we can easily find the minimum and the amplitude of the lightcurve. The amplitude is converted to $\Delta C/C_{mean}$ and the minimum is compared to the mutual event time to calculate the timing offset. We can then compare these parameters to the measured values of the actual lightcurves. An example of one of these synthetic lightcurves is shown in Fig. 6.10, along with the relevant information we calculate from each generated lightcurve.

The epochs in which Dimorphos lightcurves were obtained span 46 days. Generating a synthetic lightcurve every 3 days results in 16 synthetic lightcurves for each Monte Carlo GUBAS simulation. This results in a total of 251,888 synthetic lightcurves.

### 6.7.3 Simulation Results

Of the 15,743 simulations, about 73% are in NPA regime 2 (epicyclic tumbling), and the rest in NPA regime 1 (no tumbling), discounting the few cases that could be considered in NPA regime 3 (constant tumbling), as it is difficult for the DART perturbation to place the system into

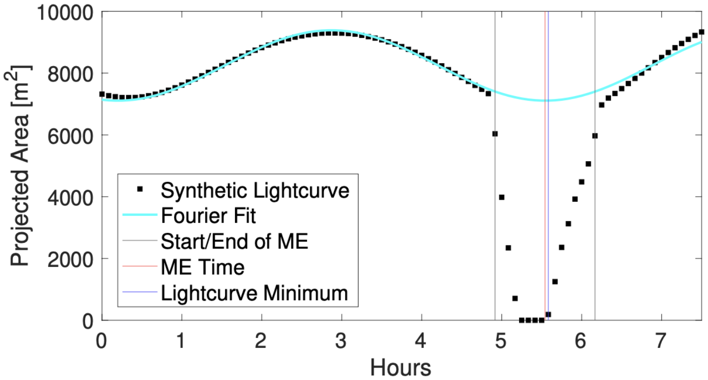

Figure 6.10: An example of a synthetic lightcurve generated using our numerical approach. We fit a first degree Fourier series to the numerical data, then use this fit to calculate the timing offset from the mutual event. The time of the mutual event is the time at the center of the event.

this state. However, not all of these systems match the observed apsidal precession rate. [134] estimate a precession rate of $6.7 \pm 0.2^\circ$/day using a combination of lightcurves and radar data. [129] estimate a precession rate of $7.3 \pm 2^\circ$/day using lightcurves. Given the uncertainties already involved in our Monte Carlo approach, we eliminate any systems with a precession rate outside the range of $5 - 9^\circ$/day for the first 30 days after impact, consistent with the larger uncertainties from [129]. Only about 20% of systems (52,128 synthetic lightcurves) are consistent with this observed precession rate. For the remainder of this work, we only deal with these systems.

We first look at the statistics for the event offset timings, which are shown as a histogram in Fig. 6.11. We break the simulations into two groups: those with rotation in NPA regime 1 and those in NPA regime 2. The actual measurements from Table 6.2 are shown as red vertical lines. Overall, the two populations are overlapping, with those in NPA regime 2 having a slightly wider distribution in event offsets, as expected. However, both populations cover all 7 observations, so it is unlikely we will be able to determine the level of attitude instability in Dimorphos from event offset timings alone.

Next we examine $\Delta C/C_{\text{mean}}$ calculated from the synthetic lightcurves. Fig. 6.12 shows a histogram of $\Delta C/C_{\text{mean}}$, again split into regime 1 and regime 2 NPA rotation. Notably, these

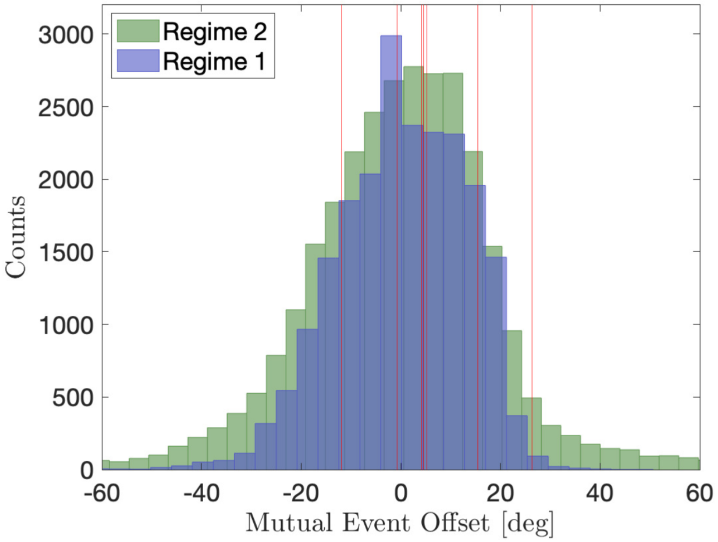

Figure 6.11: A histogram of the mutual event offsets calculated from the synthetic lightcurves, measured in degrees. We split the simulations into NPA rotation regime 1 and regime 2. The actual measurements are plotted as red lines.

two populations have distinct distributions, with those in regime 1 following a pseudo-normal distribution, whereas the regime 2 distribution has a skewed distribution covering higher values of $\Delta C/C_{\mathrm{mean}}$. This difference in distribution means only those systems in regime 2 NPA rotation are able to span all 7 observations listed in Table 6.2, again shown as red lines. This indicates we may be able to distinguish between regime 1 and regime 2 of NPA rotation using the observed $\Delta C/C_{\mathrm{mean}}$.

To further investigate how $\Delta C/C_{\mathrm{mean}}$ may differentiate between the two possible regimes of NPA rotation, we plot our simulation results in greater detail. Fig. 6.13 shows the synthetic $\Delta C/C_{\mathrm{mean}}$ for each lightcurve as a function of the secondary's $a_2/b_2$. Thus, each value of $a_2/b_2$ will correspond to 16 realizations of $\Delta C/C_{\mathrm{mean}}$, one for each synthetic lightcurve generated from a single GUBAS run. We see a general linear trend for both regimes, where increasing $a_2/b_2$ leads to generally increasing $\Delta C/C_{\mathrm{mean}}$, which is expected since more elongated secondaries will have a bigger difference between their maximum and minimum cross sections. Fig. 6.13 demonstrates that no system in NPA regime 1 is able to span the full width of observed $\Delta C/C_{\mathrm{mean}}$, but systems

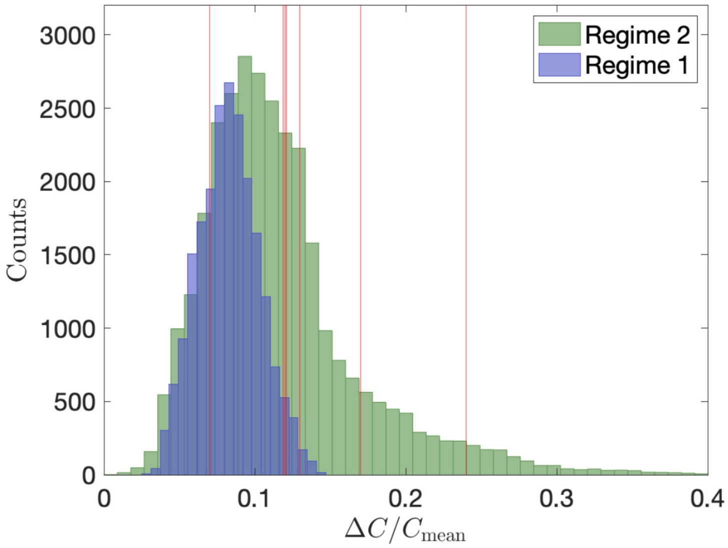

Figure 6.12: A histogram of synthetic $\Delta C/C_{\rm mean}$ values. We split the simulations into NPA rotation regime 1 and regime 2. The actual measurements are plotted as red lines.

with an $a_2/b_2$ around 1.32-1.35 overlap with the cluster of observed $\Delta C/C_{\rm mean}$ values of around 0.12-0.13.

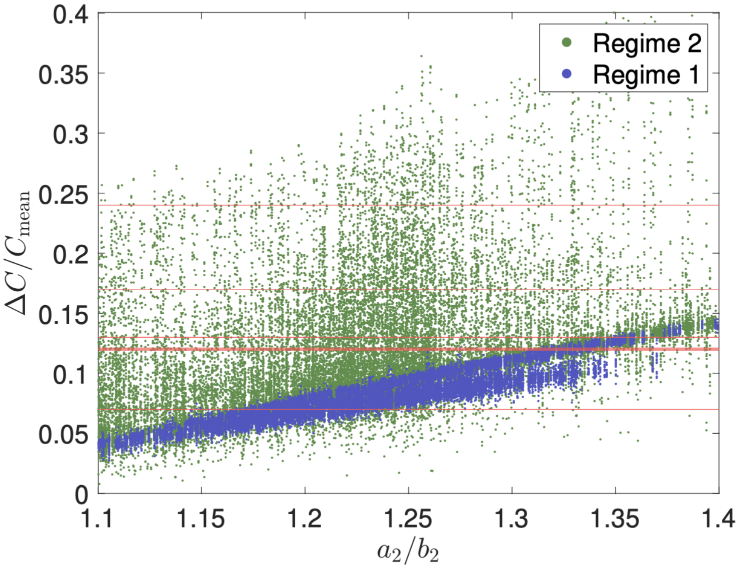

Figure 6.13: A scatter plot of synthetic $\Delta C/C_{\rm mean}$ values as a function of $a_2/b_2$. We split the simulations into NPA rotation regime 1 and regime 2. The actual measurements are plotted as red lines.

In Fig. 6.13, we see a bifurcation within regime 1 as $a_2/b_2$ increases. To investigate this, we plot the same for $b_2/c_2$ in Fig. 6.14a and for $a_2/c_2$ in Fig. 6.14b. This reveals a more complicated domain. There are clear islands within $b_2/c_2$ for which regime 1 rotation is impossible, and similarly for $a_2/c_2$. This can help us place additional constraints on the secondary shape. Small values of $b_2/c_2$ are unlikely to reproduce the observed distribution. For $a_2/c_2$, we see a range between $\sim 1.4$ and 1.8 have $\Delta C/C_{\text{mean}}$ distributions most similarly to the observed.

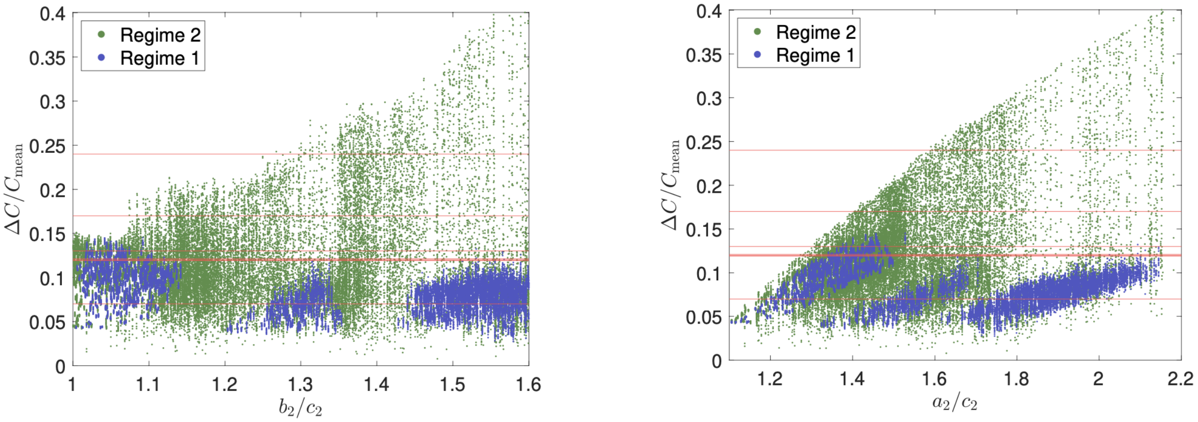

(a) Scatter Plot of Cross Section Variation As a Function of $b_2/c_2$

(b) Scatter Plot of Cross Section Variation As a Function of $a_2/c_2$

Figure 6.14: A scatter plot of the synthetic $\Delta C/C_{\text{mean}}$ as a functin of (a) $b_2/c_2$ and (b) $a_2/c_2$. We split the simulations into NPA rotation regime 1 and regime 2. The actual measurements are plotted as red lines.

The question of the source of these regions of instability still remains. There are clear regions of secondary shapes which do not permit regime 1 rotation. A likely cause is resonances among the natural frequencies of the system as discussed in Sec. 3.6. To investigate this, we plot our shapes as a function of $a_2/b_2$ and $b_2/c_2$, still broken up into the two NPA regimes, in Fig. 6.15. On top of this we also plot resonant curves calculated from the natural frequencies within the linearized system. This is the same approach presented in Sec. 3.6. Immediately we see wherever the resonant curves overlap, regime 1 of NPA rotation is not permitted. To clarify, we note that domains for which NPA regime 1 is permitted do not preclude NPA regime 2, as there is overlap within those areas. In Fig. 6.15, we also see a large empty domain for large values of $a_2/b_2 \gtrsim 1.3$ and for values of

$b_2/c_2$ between $\sim 1.1$ and 1.4. Shapes within this region are inconsistent with the estimated apsidal precession rate of the orbit and have thus been eliminated from the system. This places additional shape constraints on the system. Very elongated shapes (having a large $a_2/b_2$) are only permissible of $b_2/c_2$ is large or small.

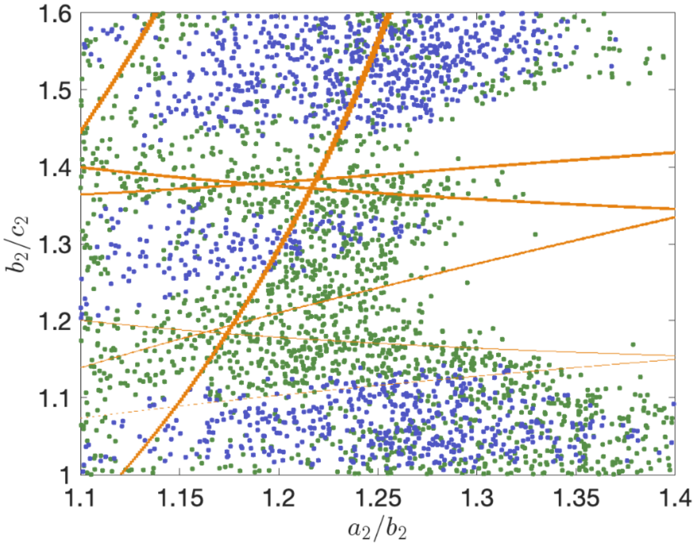

Figure 6.15: A scatter plot of the secondary shapes as a function of $a_2/b_2$ and $b_2/c_2$, broken into the two NPA regimes. Resonances up to 3:1 are plotted as curves, and we see overlap of these resonance curves does not permit regime 1 rotation.

Plotting these simulation results suggests we should focus on $\Delta C/C_{\text{mean}}$ as the most promising method of determining the attitude stability of Dimorphos. However, we cannot formally discount the use of mutual event offset timings, nor have we formally shown our observations are definitively consistent with regime 2 of NPA rotation. For this, we must apply a rigorous statistical test to compare our simulations with the observed data.

### 6.7.4 Statistical Tests

Our goal is to determine which of our simulated distributions is consistent with the observed distribution, both for mutual event offsets and $\Delta C/C_{\text{mean}}$. For each simulation we have two discrete sample populations (one simulated and one observed) from a continuous distribution. Thus, we choose the two-sample Kolmogorov-Smirnov test (hereafter KS2 test), which is a non-parametric test used to determine how likely is it that the two samples come from the same distribution [137, 138]. The null hypothesis of the KS2 test is that the two samples are from the same continuous distribution. We note that a high $p$ value from the KS2 test indicates it is more likely that the two samples are consistent with the same underlying distribution than a low $p$ value, as a small $p$ value indicates one should reject the null hypothesis and a large $p$ value means we do not have enough evidence to reject the null hypothesis. Thus, by construction of the KS2 test (and all other rank tests), we cannot definitively prove our simulated samples come from the same distribution as the observed, merely that they are not inconsistent with one another.

We first apply the KS2 test to the simulated sample of mutual event offsets compared to the observed sample. Fig 6.16a plots the $p$ value of the KS2 test for each simulation as a function of secondary shape. We see simulations in both NPA regime 1 and regime 2 span the full breadth of possible $p$ values, and thus we are unable to separate these populations statistically. This is consistent with our expectations from Fig. 6.11, and indicates both possible rotational states will produce a similar distribution of observed mutual event offset timings. Thus, we cannot practically use these observations to determine the rotational stability of the secondary.

Next, we apply the same approach to the cross section variation $\Delta C/C_{\mathrm{mean}}$ from our simulated and observed lightcurves. Fig. 6.16b plots the $p$ value obtained from the KS2 test as a function of secondary shape. Here we see distinct differences in the distributions, where systems in NPA regime 1 are limited to smaller $p$ values, entirely less than 0.25. On the other hand, systems in NPA regime 2 span the full breadth of $p$ values, with some systems having $p > 0.9$. This indicates the systems with the least evidence for rejection of the null hypothesis are in NPA regime 2; in other words NPA regime 2 is more consistent with the observed samples than NPA regime 1. Again, this is consistent with our expectations from Fig. 6.12.

The systems in NPA regime 1 with the largest $p$ values are clustered between $a_2/b_2 = 1.3$ to 1.35. Recall this is the region in Fig. 6.13 where the linear slope of the simulated $\Delta C/C_{\mathrm{mean}}$ crosses with the clustered observed values around $0.12 - 0.13$. But overall, there is not a single simulation in which a system in NPA regime 1 is able to span the full width of observed $\Delta C/C_{\mathrm{mean}}$ values. This is consistent with the conclusions drawn from Fig. 6.16b.

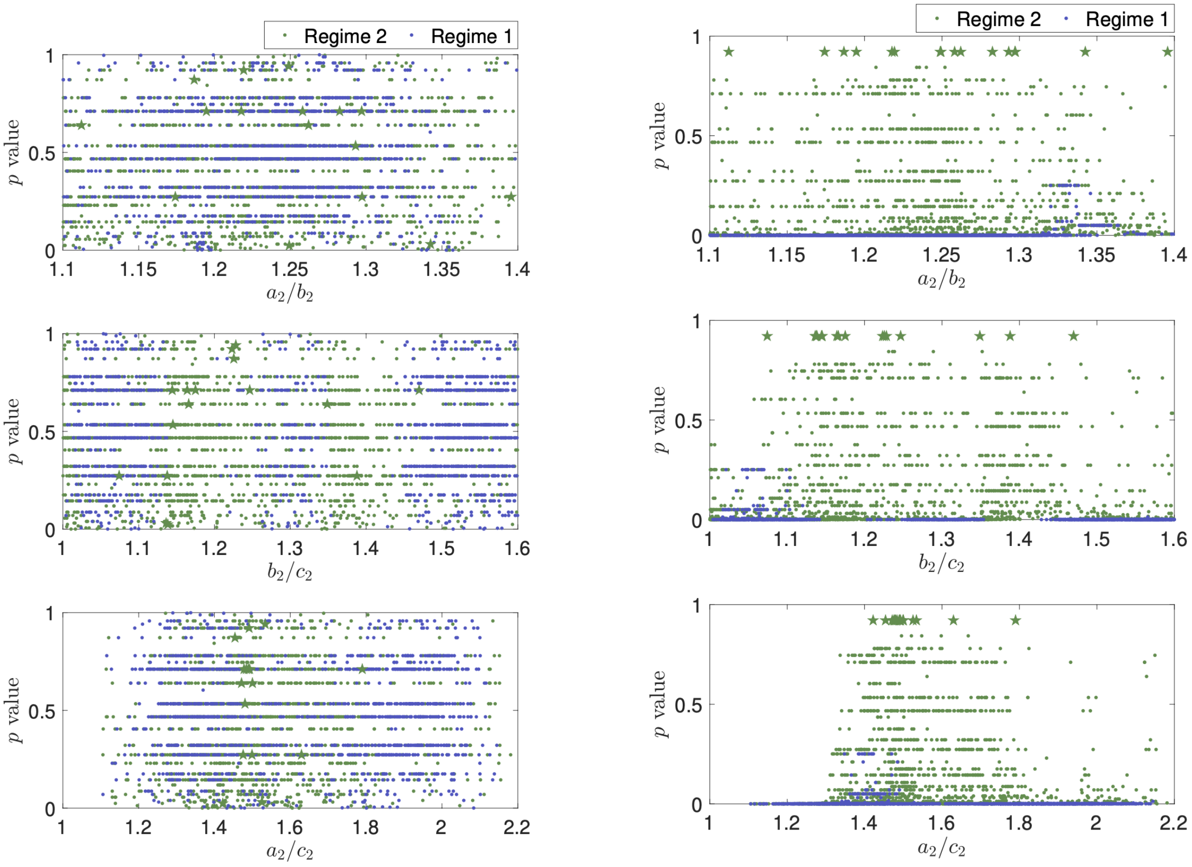

(a) Scatter of $p$-values for Mutual Event Offsets

(b) Scatter of $p$-values for Cross Section Variation

Figure 6.16: (a) The KS2 test $p$ value for the mutual event timing offsets of each simulation compared to the observed data as a function of Dimorphos shape ratios. Both regime 1 and regime 2 have similar distributions of $p$ values. (b) The KS2 test $p$ value for the $\Delta C/C_{\mathrm{mean}}$ values of each simulation compared to the observed data as a function of Dimorphos shape ratios. Here we see regime 1 only has small $p$ values, but regime 2 can have large or small $p$ values. The simulations with the highest $p$ values in $\Delta C/C_{\mathrm{mean}}$ are shown as stars in both plots.

From Fig. 6.16b, we see there are 16 systems with $p > 0.9$. In theory, these systems should be the most consistent with the observed distribution of $\Delta C/C_{\mathrm{mean}}$ values. We plot these 16 systems' $\Delta C/C_{\mathrm{mean}}$ as a function of their $a_2/b_2$ in Fig. 6.17. In general we see good agreement between the simulated and observed data and acceptable $a_2/b_2$ values ranging between 1.1 and 1.4. All of these systems are in regime 2 of NPA rotation.

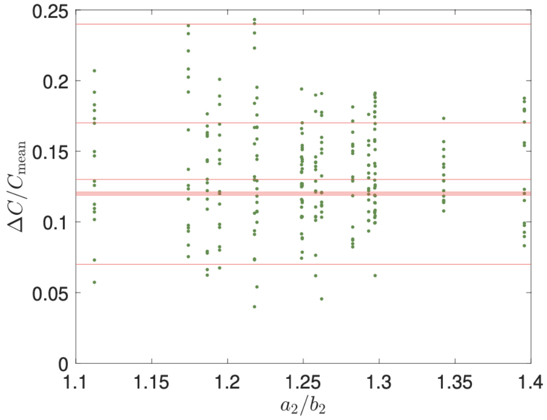

Figure 6.17: The 16 systems with the best match to the observations, showing the simulated $\Delta C/C_{\mathrm{mean}}$ for each $a_2/b_2$. The actual observations are shown as red lines.

### 6.7.5 Example Dynamics

Next we will take a closer look at a few representative cases of these systems. An additional constraint from observations we have not yet applied is the apparent disappearance of the precession rate about 70 days after the impact [129]. [129] hypothesizes this is caused by a reduction in the eccentricity due to the onset of secondary NPA rotation, as we discussed in Sec. 3.6.4. This behavior will help evaluate the feasibility of our simulations in reproducing the observations.

#### 6.7.5.1 Case 1

In the first example case we plot the simulated $\Delta C/C_{\mathrm{mean}}$ over time compared to the observed values in Fig. 6.18. This system is our best match to the data overall, as it has the largest $p$ value for both the mutual event offsets and cross section variation. While this simulation generally exhibits a similar distribution as that observed, it does not reach the largest observed $\Delta C/C_{\mathrm{mean}}$ value, 0.24. In fact, generally this large $\Delta C/C_{\mathrm{mean}}$ value is the most difficult to reproduce with simulations. However, it is possible the system is capable of reproducing this value and we simply haven't sampled it, which is why it is not statistically ruled out.

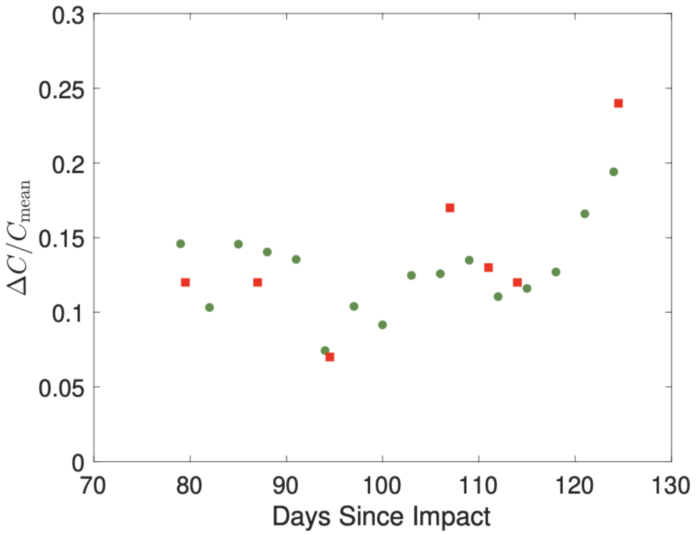

Figure 6.18: The synthetic $\Delta C/C_{\text{mean}}$ for this simulation plotted over time. The true observed values are shown as red squares. Generally we see good agreement, however, the synthetic data do not reach the maximum observed value.

We also plot the 1-2-3 Euler angles of the secondary, corresponding to roll, pitch, yaw, in Fig. 6.19. This shows the onset of the barrel instability around 120 days into the simulation. Throughout the full simulation time the secondary is in NPA rotation within the synchronous configuration, demonstrated by $\theta_2, \theta_3 < 90°$. The precession rate, as plotted in Fig. 6.20, increases rapidly around 80 days into the simulation, consistent with the observations of the system. This corresponds to a change in the system, where the eccentricity quickly decreases causing the true anomaly to return to a state of libration and the longitude of periapsis measures the angular position of the secondary. This mimics the observations reported by [129], who see a disappearance of the eccentricity and precession rate about 70 days after the impact. These results corroborate their argument that this is due to NPA rotation. Here, we specify that this must be NPA rotation in regime 2.

#### 6.7.5.2 Case 2

We show another example case, in which the simulated $\Delta C/C_{\text{mean}}$ does fully span the range of observed values. This is shown in Fig. 6.21, where we plot the simulated $\Delta C/C_{\text{mean}}$ against the

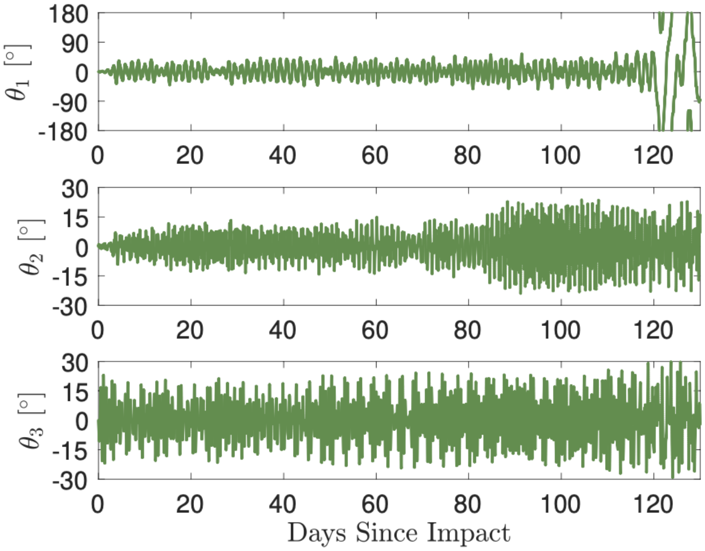

Figure 6.19: The 1-2-3 (roll, pitch, yaw) Euler angles for the simulation. We see the secondary in NPA rotation about the synchronous configuration, with the barrel instability starting about 70 days into the simulation.

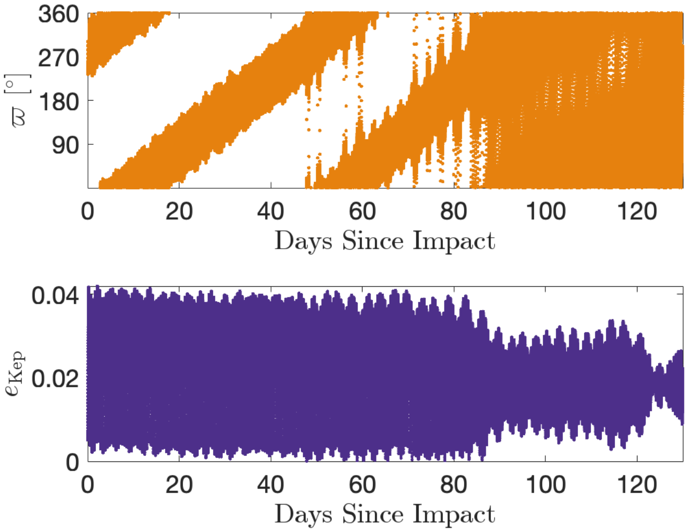

Figure 6.20: The longitude of periapsis and Keplerian eccentricity for the simulation. The precession rate is constant for the first 70 days of the simulation, where it then jumps and varies as angular momentum is exchanged in the system. This corresponds to a change in the eccentricity.

observed. Once again, we see a good match between the observed and simulated cross sectional variation, and the distributions are consistent.

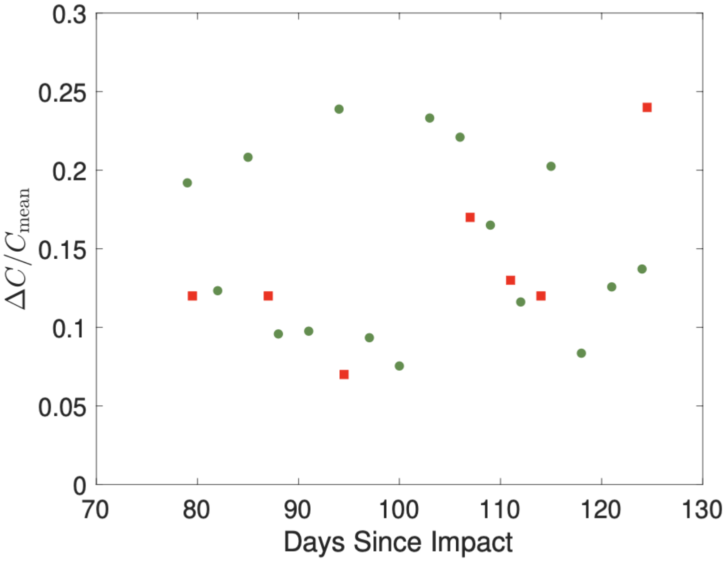

Figure 6.21: The synthetic $\Delta C/C_{\text{mean}}$ for this simulation plotted over time. The true observed values are shown as red squares. This demonstrates that the synthetic data span the full width of observed values.

Plotting the secondary's 1-2-3 Euler angles in Fig. 6.22 reveals that in this case the barrel instability occurs much sooner. Additionally, this corresponds to the secondary switching to NPA rotation around the anti-synchronous configuration, demonstrated by $\theta_3 > 90°$. The secondary switches between the synchronous and anti-synchronous configuration several times throughout the simulation. Furthermore, the longitude of periapsis, plotted in Fig 6.23, shows several instances of switching between slow and rapid precession as angular momentum is exchanged between the secondary and the orbit.

## 6.8 Conclusion

In this Chapter we have provided a detailed analysis of the effects of the DART impact. Using the F2BP in a Monte Carlo approach, we are able to calculate the change to Didymos's orbit, including the tangential $\Delta v_T$, along with the semimajor axis and eccentricity of the post-impact orbit. We found reshaping of Dimorphos caused by the DART impact requires a smaller $\Delta v_T$ than would otherwise be required. The reshaping also reduces the post-imapct eccentricity of

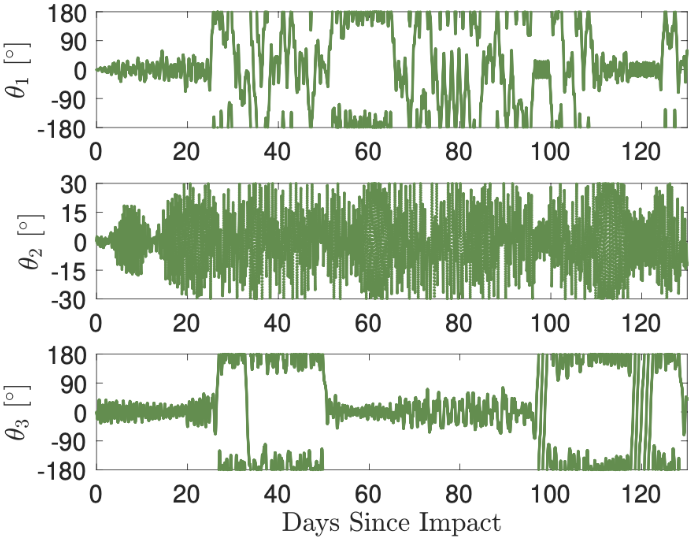

Figure 6.22: The 1-2-3 (roll, pitch, yaw) Euler angles for the simulation. We see the secondary start in NPA rotation about the synchronous configuration, but at the onset of the barrel instability about 25 days into the simulation it switches to NPA rotation about the anti-synchronous configuration. Over the simulation it switches between the synchronous and anti-synchronous configuration several times.

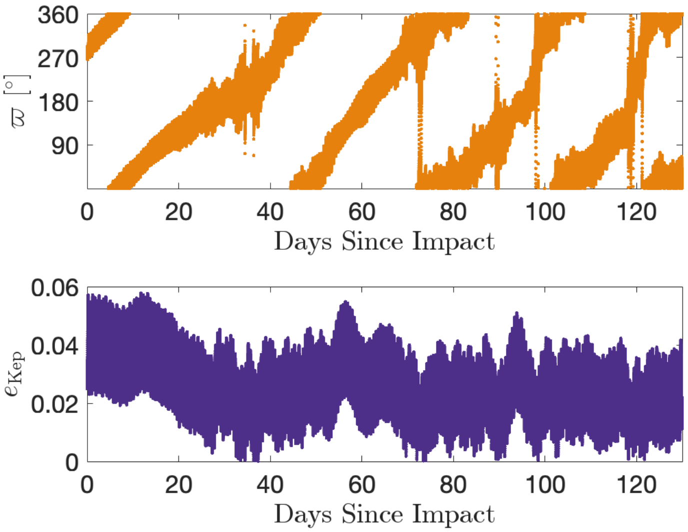

Figure 6.23: The longitude of periapsis and Keplerian eccentricity for the simulation. The precession rate is constant for the first 35 days of the simulation, where it then fluctuates as angular momentum is exchanged in the system. This corresponds to a change in the eccentricity.

the orbit.

We can use estimates of the apsidal precession rate to estimate the reshaping in Dimorphos. Because the precession rate depends on the shape and spin of the secondary, there are only certain combinations of elongation and spin rate that result in the observed value. As a result of this constraint, we place a nominal lower bound on the post-impact $a_2/b_2$ of Dimorphos of roughly 1.25, although smaller values are possible when considering uncertainties within the system. This is consistent with observations and impact simulations [135, 134].

Finally, by generating synthetic lightcurves of the post-impact orbit and rotational dynamics of the system, we argue Dimorphos is currently in a state of NPA rotation experiencing epicyclic tumbling. A detailed statistical analysis reveals the changing amplitude of Dimorphos's lightcurve is best explained by this NPA rotation.

We need to note that Didymos is still subjected to considerable uncertainties. The only realistic way to handle this is by making assumptions regarding the system and the DART impact. While Hera will help alleviate this issue, our predictions made here are only a best guess, limited by the uncertainty.

Thus, this Chapter demonstrates how a thorough understanding and study of the perturbed dynamics of binary asteroids reveals additional information from observations. This dynamical analysis has revealed significant reshaping in Dimorphos caused by the DART impact, as well as a perturbation to its spin rate. This change in shape and spin likely results in significant NPA rotation within Dimorphos.

The tools and methods developed throughout this thesis have been used to help complete the objectives of the DART mission. Thanks to these analyses, we are able to calculate the momentum enhancement factor of the DART impact [75], and we have an idea of what Hera will find when it arrives at Didymos. This ultimately leads to a deeper understanding of the dynamical evolution of binary asteroids.

# Chapter 7

# Conclusion

In this thesis, we have provided a detailed analysis of the dynamics of near-Earth binary asteroids. These binary asteroids are common, particularly among fast rotators, and have been the target of several recent, upcoming, and proposed missions. Their coupled dynamics make them a dynamically rich and complicated subject of study. We developed a variety of tools to investigate these dynamics, and applied these tools to a diversity of systems.

## 7.1 Thesis Summary

In Chapter 2, we introduced the common dynamical models that have been developed in the literature to study the full two-body problem (F2BP). The highest-fidelity of these models is limited to a purely numerical implementation due to the complexity of the dynamics. However, limiting the motion to purely planar, or assuming one of the bodies to be spherical, are simplifications that allow for an analytical consideration of the spin-orbit coupled problem. We also introduced three archetypal binary asteroids: 1996FG3 as an example of a system in equilibrium; Didymos as an example of a recently perturbed system; and 1991VH as an example of an asynchronous and chaotic system.

We also analyzed the dynamics of a binary asteroid in equilibrium and pointed out the shortcomings of a traditional Keplerian treatment of these dynamics. We introduced a set of observable elements that can be used to easily relate real-world measurements of these systems to numerical models. These elements are vital to gaining an understanding of the behavior of real-world systems.

Chapter 3 then delved into an analysis of the dynamics of these systems once they've been perturbed out of an equilibrium. This begins with a discussion of the true anomaly within these systems; when the system is in the singly-synchronous configuration, the true anomaly is trapped at periapsis while the longitude of periapsis circulates with the secondary. We calculated the threshold to break this configuration, beyond which perturbations are sufficient to allow the true anomaly to begin circulating with the secondary around the primary. Once the system is perturbed, the secondary is able to librate around the synchronous spin rate. This libration results in fluctuations in its spin rate, which are compensated by fluctuations in the orbit rate to conserve angular momentum. These variations in the orbit period are driven by the natural frequencies within the system, and can thus provide information on the moments of inertia of the secondary if these variations are measured. A rendezvous mission such as Hera at Didymos may be able to leverage this phenomenon to help understand the interior structure of the secondary.

The apsidal precession of the orbit can also help provide information on the secondary. Our investigation demonstrated how the shape and spin of the secondary play an important role in the orbital precession rate. As the precession rate can be observed by ground-based observations, this is an important quantity to consider in any analysis of binary asteroids. We also demonstrated the complex relationship between these parameters in determining the precession rate, and thus analyses are limited to a numerical approach.

We also analyzed how resonances among natural frequencies within these binary asteroids can induce non principal-axis (NPA) rotation in the secondary. This means certain shapes of the secondary are naturally unstable, and small perturbations can result in large changes to the spin state, also leading to perturbations to the orbit due to spin-orbit coupling. When the secondary enters NPA rotation, the resulting change in its angular momentum leads to an on-average decrease in the orbit's eccentricity. This means a decrease in orbital eccentricity is an indicator of NPA rotation within the system. Chaotic rotation within the secondary also leads to chaotic variations within the orbit period as angular momentum is passed between the secondary and the orbit.

Lastly, the precession rate can vary rapidly and widely as a result of this angular momentum exchange. Thus, observations of the eccentricity and precession rate can elucidate the spin state of the secondary, making these important observables.

Due to secular energy dissipation, any non-equilibrated binary asteroid will eventually return to a minimum-energy configuration. We studied this process in Chapter 4. In this chapter we generalized classical tidal torques to three dimensions for applications to binary asteroids with a secondary in NPA rotation. We also applied a model to incorporate dissipation as a result of NPA rotation, in which flexure results in internal dissipation in the non rigid-body dynamics case. We applied these models to Didymos to investigate how an excited binary asteroid returns to an equilibrium. We found the eccentricity dissipates much faster than predicted, sometimes resulting in an initial decrease in the semimajor axis before tidal torques result in a secular increase in this parameter. We also found NPA rotation in the secondary is not necessarily long lived, and the system can relatively quickly transition back into synchronous, principal axis rotation depending on the dissipation parameters of the system.

In Chapter 5, we analyzed how close planetary encounters affect the dynamics of binary asteroids. To accomplish this, we derived a high-fidelity dynamical model in which the gravitational forces and torques from a distant spherical planet are incorporated into the internal dynamics of a binary asteroid. Using this model, we simulated a wide variety of flyby conditions, and calculated the flyby conditions sufficient to cause the secondary to become asynchronous with the orbit rate. While close flybys have a large impact on the dynamics, the effect rapidly drops off as the periapsis distance increases; we find the effect becomes weaker than predicted by analytical models as the flyby distance increases.

We also tested the hypothesis that the excited dynamics of 1991VH are the result of a past close encounter with the Earth. In this analysis, we found a relaxed, synchronous 1991VH-like system can be excited into a dynamical state similar to the one observed today as a result of such a flyby. In particular, flybys closer than 100,000 km are able to achieve this level of perturbation, provided the shape of the secondary is near a resonance. This allows the internal dynamics to evolve the secondary spin rate close to the values currently observed for the system. When incorporating our energy dissipation model, we found the excited dynamics of 1991VH are not necessarily long-lived. This makes arguments for the system to be relatively inefficient at dissipating energy and for the flyby to be relatively recent. Alternatively, successive flybys could slow energy dissipation. The most recent possible close encounter with the Earth was about 12,000 years ago, which constrains the dissipation parameters of the secondary.

Finally, in Chapter 6, we applied the tools developed throughout this thesis to Didymos in order to understand the effects of the DART impact. As we developed the most accurate method of connecting observational data to numerical models, we are able to accurately model the post-impact system. By matching our models to the observations, we calculated a change in velocity, semimajor axis, and eccentricity of the spin-orbit coupled system. This approach was used in calculating the momentum enhancement factor of the DART impact, one of the mission's level-one science goals. Using the analyses we developed, we concluded that the DART impact likely caused massive reshaping of Dimorphos, and the shape of the body found by Hera will likely by significantly different than the shape estimated by DART.

By generating synthetic lightcurves of the post-impact system, we also argued that Dimorphos is probably in a state of NPA rotation as a result of the impact. This comes from an observed variation in its cross section, which is best explained by significant out-of-plane rotation. Other observations point to a reduction in eccentricity and a loss of the precession signal, which are also indicators of NPA rotation.

To conclude, this thesis has developed a thorough understanding of the dynamical evolution of perturbed near-Earth binary asteroids. This work was used in NASA's DART mission to calculate the momentum transfer of the impact, as well as to understand the dynamics of the post-impact system. We also are able to show how the dynamical state of 1991VH is easily explained as the result of a previous close planetary encounter. Beyond these two examples, this work has led to a better understanding of the behavior within binary asteroids, which improves the scientific return of ground-based observations and flyby missions.

## 7.2 Future Work

The research carried out for this thesis opens several doors for future work. This includes the role played by inclination, the effects of a third body in a triple system, the dynamical environment around binary asteroids, and incorporating higher-order dissipation effects driven by motion on and within the asteroid.

### 7.2.1 Inclination

One major subject which would benefit from additional research is the consideration of inclination within the binary asteroid mutual orbit. Even with the inclusion of full three-dimensional motion in the systems studied in this work, these systems are still considered to have effectively planar orbits. To be specific, the angular momentum vectors of the orbit plane and the primary's rotation are essentially aligned. In simulating planetary encounters, some of the most perturbed systems did end with a few degrees of inclination, as seen in Sec. 5.4. However, we never performed an in-depth analysis of these effects. Some preliminary analyses on this topic have revealed some intriguing results, however. In carrying out a classical averaged analysis of the Lagrangian Planetary Equations, the secular rates of change of the eccentricity, inclination, and argument of periapsis are written as

$$\frac{\mathrm{d}\bar{e}}{\mathrm{d}t} = \frac{-3C_{30}r_0^3\mu\sin i\cos\omega\left(\frac{5}{4}\sin^2 i - 1\right)}{2a^6 n\left(e^2-1\right)^2} \tag{7.1}$$

$$\frac{\mathrm{d}\bar{i}}{\mathrm{d}t} = \frac{3C_{30}r_0^3 e\mu\cos i\cos\omega\left(5\cos^2 i - 1\right)}{8a^6 n\left(e^2-1\right)^3} \tag{7.2}$$

$$\frac{\mathrm{d}\bar{\omega}}{\mathrm{d}t} = \frac{-3\mu\left(2C_{20}r_0^2 ae\sin i(e^2-1)(4-5\sin^2 i) + C_{30}r_0^3\sin\omega\left(4(e^2-\sin^2 i)+5\sin^4 i+35e^2\sin^2 i(\sin^2 i-1)\right)\right)}{8a^6 en\sin i(e^2-1)^3} \tag{7.3}$$

when considering up to the third zonal gravity term. Typically, these analyses only include up to the second zonal term, as this is the dominating perturbation. But with the inclusion of the third degree term, the eccentricity and inclination are no longer constant on average, and we see an additional term in the apsidal precession rate. This suggests a pseudo-Kozai effect in play, where the eccentricity and inclination trade off. With irregular shapes in asteroids, the third degree zonal term could be significant in some systems, leading to a fluctuation of eccentricity in non-planar binary asteroids. Due to spin orbit coupling, this fluctuation is compensated by an additional precession of the primary's spin pole. This is just one effect of adding inclination to the system, and future research is necessary to fully understand how mutual inclination affects both the orbital dynamics and the rotational dynamics of the primary.

### 7.2.2 Triple Systems

The work carried out thus far has exclusively focused on binary systems. However, NEA triples have been found to exist, and even quadruple systems. There are two well-characterized NEA triples: 2001 SN263 and 1994 CC. An interesting aspect of these systems is they both have non-negligible eccentricities within the mutual orbits, and the orbital planes of the two satellites are not co-planar [139]. Given the paradigm of the singly-synchronous binary system, one would expect triple systems to be an extension of this, with both satellites tidally locked in circular orbits. A suitable explanation has been proposed in the form of close planetary encounters perturbing these systems. But then, why don't we see more binary asteroids with eccentricity and inclination? Are triple systems simply more susceptible to these perturbations, or are these effects easier to detect in triples? Are these examples just a selection bias? There are many questions to be answered surrounding the evolution of NEA triples. Furthermore, the discovery of the contact binary satellite of Dinkinesh opens a new possibility about two moons that collide and formed a single moon [140]. How frequent are these contact binary satellites, and is is possible Dinkinesh used to be a triple system that experienced some evolution or perturbation that destabilized the system, causing the collision of its moons? This is a highly relevant line of questioning necessary to understand the evolution of rubble piles in general.

### 7.2.3 Dynamical Environment

Lastly, another area of future work is understanding the dynamical environment around binary asteroid systems. This is applicable both to natural dynamics and artificial satellite navigation and mission design. One major question to answer is the evolution of a possible debris disk around Didymos after the DART impact. In the short term this helps us unravel the mystery of post-collision dynamics within rubble piles. In the longer term, this helps us investigate the possibility of quasi-satellites within binary systems. A highly relevant problem in this field is the possibility of Dimorphos debris remaining in the Didymos system until the arrival of Hera, which could potentially provide an unknown source of risk to the mission. Related, this is also applicable to the mission design of Hera itself in finding stable orbits around the system. The two cubesats carried by Hera will attempt to land on Dimorphos, and these maneuvers will require an in-depth understanding of the dynamical environment. This problem is essentially the restricted full three-body problem, which has primarily only been studied in the literature when confined to a circular orbit. However, as we have shown, Dimorphos is now on an eccentric orbit, and perhaps even more importantly, it is experiencing chaotic NPA rotation. These characteristics provide challenges to the Hera mission and should be comprehensively studied.

### 7.2.4 Structural Dissipation

While we have considered the effects of internal energy dissipation in this thesis, our analysis only considered simple models for tidal torques and NPA dissipation. Additional effects may play an equally important, or perhaps an even more important role. These depend on the physical structure of rubble piles. The main example of this is landslides, which could be an efficient method of dissipating energy. These have the dual effect of removing energy via friction, but also changing the shape of the asteroid. If the post-impact shape of Dimorphos is unstable, it could be susceptible to such landslides. Perhaps post-DART Dimorphos is experiencing rapid energy dissipation as its new shape settles into a minimum energy configuration, serving to reduce the time required to return the system to a singly-synchronous state. The literature has begun to discuss this phenomenon, particularly how NPA rotation could induce surface movement [109]. However, much work remains on this problem, and Hera may be able to identify recent landslides on the surface of Dimorphos. Larger shape changes, resulting from structural failure on a larger scale, could also decrease the time required for the system to return to an equilibrium state. A mechano-dynamical model is required to investigate this effect, which can simultaneously simulate the rotational dynamics and the stress state of the asteroid.

# Bibliography

[1] E. Rabe, “On the formation of rapidly rotating asteroids.,” Astrophysical Journal, vol. 131, p. 231, vol. 131, p. 231, 1960.

[2] T. Van Flandern, E. Tedesco, and R. Binzel, “Satellites of asteroids.,” Asteroids, pp. 443–465, 1979.

[3] S. Weidenschilling, “Hektor: Nature and origin of a binary asteroid,” Icarus, vol. 44, no. 3, pp. 807–809, 1980.

[4] F. Marchis, J. Durech, J. Castillo-Rogez, F. Vachier, M. Cuk, J. Berthier, M. H. Wong, P. Kalas, G. Duchene, M. A. Van Dam, et al., “The puzzling mutual orbit of the binary trojan asteroid (624) hektor,” The Astrophysical journal letters, vol. 783, no. 2, p. L37, 2014.

[5] C. Chapman, J. Veverka, P. Thomas, K. Klaasen, M. Belton, A. Harch, A. McEwen, T. Johnson, P. Helfenstein, M. Davies, et al., “Discovery and physical properties of dactyl, a satellite of asteroid 243 ida,” Nature, vol. 374, no. 6525, pp. 783–785, 1995.

[6] P. Pravec, P. Scheirich, P. Kušnirák, K. Hornoch, A. Galád, S. Naidu, D. Pray, J. Világi, Š. Gajdoš, L. Kornoš, et al., “Binary asteroid population. 3. secondary rotations and elongations,” Icarus, vol. 267, pp. 267–295, 2016.

[7] J. Agarwal, D. Jewitt, M. Mutchler, H. Weaver, and S. Larson, “A binary main-belt comet,” Nature, vol. 549, no. 7672, pp. 357–359, 2017.

[8] D. Nesvornỳ, D. Vokrouhlickỳ, W. F. Bottke, H. F. Levison, and W. M. Grundy, “Very slow rotators from tidally synchronized binaries,” The Astrophysical Journal Letters, vol. 893, no. 1, p. L16, 2020.

[9] K. S. Noll, H. F. Levison, W. M. Grundy, and D. C. Stephens, “Discovery of a binary centaur,” Icarus, vol. 184, no. 2, pp. 611–618, 2006.

[10] S. Kern and J. Elliot, “The frequency of binary kuiper belt objects,” The Astrophysical Journal, vol. 643, no. 1, p. L57, 2006.

[11] M. Ćuk and D. Nesvornỳ, “Orbital evolution of small binary asteroids,” Icarus, vol. 207, no. 2, pp. 732–743, 2010.

[12] R. T. Daly, C. M. Ernst, O. S. Barnouin, N. L. Chabot, A. S. Rivkin, A. F. Cheng, E. Y. Adams, H. F. Agrusa, E. D. Abel, A. L. Alford, et al., “Successful kinetic impact into an asteroid for planetary defense,” Nature, pp. 1–3, 2023.

[13] S. J. Ostro, J.-L. Margot, L. A. Benner, J. D. Giorgini, D. J. Scheeres, E. G. Fahnestock, S. B. Broschart, J. Bellerose, M. C. Nolan, C. Magri, et al., "Radar imaging of binary near-earth asteroid (66391) 1999 kw4," Science, vol. 314, no. 5803, pp. 1276–1280, 2006.

[14] D. J. Scheeres, E. G. Fahnestock, S. J. Ostro, J.-L. Margot, L. A. Benner, S. B. Broschart, J. Bellerose, J. D. Giorgini, M. C. Nolan, C. Magri, et al., "Dynamical configuration of binary near-earth asteroid (66391) 1999 kw4," Science, vol. 314, no. 5803, pp. 1280–1283, 2006.

[15] J.-L. Margot, M. Nolan, L. Benner, S. Ostro, R. Jurgens, J. Giorgini, M. Slade, and D. Campbell, "Binary asteroids in the near-earth object population," Science, vol. 296, no. 5572, pp. 1445–1448, 2002.

[16] P. Pravec, P. Scheirich, P. Kušnirák, L. Šarounová, S. Mottola, G. Hahn, P. Brown, G. Esquerdo, N. Kaiser, Z. Krzeminski, et al., "Photometric survey of binary near-earth asteroids," Icarus, vol. 181, no. 1, pp. 63–93, 2006.

[17] P. Pravec, D. Vokrouhlickỳ, D. Polishook, D. J. Scheeres, A. W. Harris, A. Galad, O. Vaduvescu, F. Pozo, A. Barr, P. Longa, et al., "Formation of asteroid pairs by rotational fission," Nature, vol. 466, no. 7310, pp. 1085–1088, 2010.

[18] P. Pravec, P. Fatka, D. Vokrouhlickỳ, P. Scheirich, J. Ďurech, D. Scheeres, P. Kušnirák, K. Hornoch, A. Galád, D. Pray, et al., "Asteroid pairs: a complex picture," Icarus, vol. 333, pp. 429–463, 2019.

[19] A. K. Virkki, S. E. Marshall, F. C. Venditti, L. F. Zambrano-Marín, D. C. Hickson, A. McGilvray, P. A. Taylor, E. G. Rivera-Valentín, M. Devogèle, E. F. Díaz, et al., "Arecibo planetary radar observations of near-earth asteroids: 2017 december–2019 december," The Planetary Science Journal, vol. 3, no. 9, p. 222, 2022.

[20] P. A. Taylor and J.-L. Margot, "Tidal end states of binary asteroid systems with a nonspherical component," Icarus, vol. 229, pp. 418–422, 2014.

[21] B. Gladman, P. Michel, and C. Froeschlé, "The near-earth object population," Icarus, vol. 146, no. 1, pp. 176–189, 2000.

[22] K. J. Walsh, "Rubble pile asteroids," Annual Review of Astronomy and Astrophysics, vol. 56, pp. 593–624, 2018.

[23] W. F. Bottke Jr and H. J. Melosh, "Formation of asteroid satellites and doublet craters by planetary tidal forces," Nature, vol. 381, no. 6577, pp. 51–53, 1996.

[24] K. J. Walsh and D. C. Richardson, "Binary near-earth asteroid formation: Rubble pile model of tidal disruptions," Icarus, vol. 180, no. 1, pp. 201–216, 2006.

[25] K. J. Walsh and D. C. Richardson, "A steady-state model of nea binaries formed by tidal disruption of gravitational aggregates," Icarus, vol. 193, no. 2, pp. 553–566, 2008.

[26] K. J. Walsh, D. C. Richardson, and P. Michel, "Rotational breakup as the origin of small binary asteroids," Nature, vol. 454, no. 7201, pp. 188–191, 2008.

[27] D. P. Rubincam, "Radiative spin-up and spin-down of small asteroids," Icarus, vol. 148, no. 1, pp. 2–11, 2000.

[28] D. J. Scheeres, “Landslides and mass shedding on spinning spheroidal asteroids,” Icarus, vol. 247, pp. 1–17, 2015.

[29] H. F. Agrusa, Y. Zhang, D. C. Richardson, P. Pravec, M. Ćuk, P. Michel, R.-L. Ballouz, S. A. Jacobson, D. J. Scheeres, K. Walsh, et al., “Direct n-body simulations of satellite formation around small asteroids: Insights from dart’s encounter with the didymos system,” The Planetary Science Journal, vol. 5, no. 2, p. 54, 2024.

[30] T. S. Statler, “Extreme sensitivity of the yorp effect to small-scale topography,” Icarus, vol. 202, no. 2, pp. 502–513, 2009.

[31] S. A. Jacobson and D. J. Scheeres, “Dynamics of rotationally fissioned asteroids: Source of observed small asteroid systems,” Icarus, vol. 214, no. 1, pp. 161–178, 2011.

[32] D. J. Scheeres, “Rotational fission of contact binary asteroids,” Icarus, vol. 189, no. 2, pp. 370–385, 2007.

[33] Y. Zhang, D. C. Richardson, O. S. Barnouin, P. Michel, S. R. Schwartz, and R.-L. Ballouz, “Rotational failure of rubble-pile bodies: influences of shear and cohesive strengths,” The Astrophysical Journal, vol. 857, no. 1, p. 15, 2018.

[34] D. J. Scheeres, “Stability of the planar full 2-body problem,” Celestial Mechanics and Dynamical Astronomy, vol. 104, pp. 103–128, 2009.

[35] K. J. Walsh and S. A. Jacobson, “Formation and evolution of binary asteroids,” Asteroids IV, vol. 375, 2015.

[36] Y. Zhang, P. Michel, O. S. Barnouin, J. H. Roberts, M. G. Daly, R.-L. Ballouz, K. J. Walsh, D. C. Richardson, C. M. Hartzell, and D. S. Lauretta, “Inferring interiors and structural history of top-shaped asteroids from external properties of asteroid (101955) bennu,” Nature Communications, vol. 13, no. 1, p. 4589, 2022.

[37] A. J. Meyer and D. J. Scheeres, “The strength and shapes of contact binary objects,” The Astrophysical Journal Letters, vol. 963, no. 1, p. L14, 2024.

[38] P. Goldreich et al., “Tidal evolution of rubble piles,” The Astrophysical Journal, vol. 691, no. 1, p. 54, 2009.

[39] P. A. Taylor and J.-L. Margot, “Binary asteroid systems: Tidal end states and estimates of material properties,” Icarus, vol. 212, no. 2, pp. 661–676, 2011.

[40] P. A. Taylor and J.-L. Margot, “Tidal evolution of close binary asteroid systems,” Celestial Mechanics and Dynamical Astronomy, vol. 108, pp. 315–338, 2010.

[41] M. Ćuk and J. A. Burns, “Effects of thermal radiation on the dynamics of binary neas,” Icarus, vol. 176, no. 2, pp. 418–431, 2005.

[42] S. A. Jacobson, D. J. Scheeres, and J. McMahon, “Formation of the wide asynchronous binary asteroid population,” The Astrophysical Journal, vol. 780, no. 1, p. 60, 2013.

[43] S. A. Jacobson and D. J. Scheeres, “Long-term stable equilibria for synchronous binary asteroids,” The Astrophysical Journal Letters, vol. 736, no. 1, p. L19, 2011.

[44] H.-S. Wang and X.-Y. Hou, "Break-up of the synchronous state of binary asteroid systems," Monthly Notices of the Royal Astronomical Society, vol. 505, no. 4, pp. 6037–6050, 2021.

[45] G. Duboshin, "The differential equations of translational-rotational motion of mutally attracting rigid bodies.," Soviet Astronomy, Vol. 2, p. 239, vol. 2, p. 239, 1958.

[46] A. J. Maciejewski, "Reduction, relative equilibria and potential in the two rigid bodies problem," Celestial Mechanics and Dynamical Astronomy, vol. 63, pp. 1–28, 1995.

[47] D. Scheeres, "The dynamics of neo binary asteroids," Proceedings of the International Astronomical Union, vol. 2, no. S236, pp. 177–190, 2006.

[48] R. A. Werner and D. J. Scheeres, "Mutual potential of homogeneous polyhedra," Celestial Mechanics and Dynamical Astronomy, vol. 91, pp. 337–349, 2005.

[49] E. G. Fahnestock and D. J. Scheeres, "Simulation of the full two rigid body problem using polyhedral mutual potential and potential derivatives approach," Celestial Mechanics and Dynamical Astronomy, vol. 96, pp. 317–339, 2006.

[50] E. G. Fahnestock and D. J. Scheeres, "Simulation and analysis of the dynamics of binary near-earth asteroid (66391) 1999 kw4," Icarus, vol. 194, no. 2, pp. 410–435, 2008.

[51] M. Hirabayashi and D. J. Scheeres, "Recursive computation of mutual potential between two polyhedra," Celestial Mechanics and Dynamical Astronomy, vol. 117, pp. 245–262, 2013.

[52] P. Tricarico, "Figure–figure interaction between bodies having arbitrary shapes and mass distributions: a power series expansion approach," Celestial Mechanics and Dynamical Astronomy, vol. 100, pp. 319–330, 2008.

[53] X. Hou, D. J. Scheeres, and X. Xin, "Mutual potential between two rigid bodies with arbitrary shapes and mass distributions," Celestial Mechanics and Dynamical Astronomy, vol. 127, pp. 369–395, 2017.

[54] A. B. Davis and D. J. Scheeres, "Doubly synchronous binary asteroid mass parameter observability," Icarus, vol. 341, p. 113439, 2020.

[55] A. B. Davis and D. J. Scheeres, "Gubas: General use binary asteroid simulator," Astrophysics Source Code Library, pp. ascl–2107, 2021.

[56] H. F. Agrusa, D. C. Richardson, A. B. Davis, E. Fahnestock, M. Hirabayashi, N. L. Chabot, A. F. Cheng, A. S. Rivkin, P. Michel, D. D. W. Group, et al., "A benchmarking and sensitivity study of the full two-body gravitational dynamics of the dart mission target, binary asteroid 65803 didymos," Icarus, vol. 349, p. 113849, 2020.

[57] A. Ho, M. Wold, M. Poursina, and J. T. Conway, "The accuracy of mutual potential approximations in simulations of binary asteroids," Astronomy & Astrophysics, vol. 671, p. A38, 2023.

[58] H. F. Agrusa, F. Ferrari, Y. Zhang, D. C. Richardson, and P. Michel, "Dynamical evolution of the didymos- dimorphos binary asteroid as rubble piles following the dart impact," The Planetary Science Journal, vol. 3, no. 7, p. 158, 2022.

[59] A. F. Cheng, A. S. Rivkin, P. Michel, J. Atchison, O. Barnouin, L. Benner, N. L. Chabot, C. Ernst, E. G. Fahnestock, M. Kueppers, et al., "Aida dart asteroid deflection test: Planetary defense and science objectives," Planetary and Space Science, vol. 157, pp. 104–115, 2018.

[60] C. A. Thomas, S. P. Naidu, P. Scheirich, N. A. Moskovitz, P. Pravec, S. R. Chesley, A. S. Rivkin, D. J. Osip, T. A. Lister, L. A. Benner, et al., "Orbital period change of dimorphos due to the dart kinetic impact," Nature, pp. 1–3, 2023.

[61] L. Pou and F. Nimmo, "Tidal dissipation of binaries in asteroid pairs," Icarus, vol. 411, p. 115919, 2024.

[62] D. DellaGiustina, R. Ballouz, K. Walsh, A. Marusiak, V. Bray, and S. Bailey, "Seismology of rubble-pile asteroids in binary systems," Monthly Notices of the Royal Astronomical Society, p. stae325, 2024.

[63] D. J. Scheeres, J. McMahon, E. B. Bierhaus, J. Wood, L. Benner, C. M. Hartzell, P. Hayne, R. Jedicke, L. Le Corre, A. Meyer, et al., "Janus: A nasa simplex mission to explore two neo binary asteroids," in 7th IAA Planetary Defense Conference, p. 55, 2021.

[64] P. Michel, M. Küppers, A. C. Bagatin, B. Carry, S. Charnoz, J. De Leon, A. Fitzsimmons, P. Gordo, S. F. Green, A. Hérique, et al., "The esa hera mission: detailed characterization of the dart impact outcome and of the binary asteroid (65803) didymos," The Planetary Science Journal, vol. 3, no. 7, p. 160, 2022.

[65] H. F. Levison, C. B. Olkin, K. S. Noll, S. Marchi, J. F. Bell III, E. Bierhaus, R. Binzel, W. Bottke, D. Britt, M. Brown, et al., "Lucy mission to the trojan asteroids: Science goals," The Planetary Science Journal, vol. 2, no. 5, p. 171, 2021.

[66] M. Barucci, M. Yoshikawa, P. Michel, J. Kawagushi, H. Yano, J. Brucato, I. Franchi, E. Dotto, M. Fulchignoni, S. Ulamec, et al., "Marco polo: near earth object sample return mission," Experimental Astronomy, vol. 23, pp. 785–808, 2009.

[67] R. Dissly, D. J. Scheeres, E. Nilsen, S. Roark, W. Frazier, T. Bank, D. Rosing, E. Jordan, B. S. Team, et al., "The binary asteroid in-situ explorer (basix) mission," in AAS/Division for Planetary Sciences Meeting Abstracts# 42, vol. 42, pp. 49–28, 2010.

[68] D. H. Eckhardt, "Theory of the libration of the moon," The Moon and the planets, vol. 25, no. 1, pp. 3–49, 1981.

[69] D. J. Scheeres, "Relative equilibria for general gravity fields in the sphere-restricted full 2-body problem," Celestial Mechanics and Dynamical Astronomy, vol. 94, no. 3, pp. 317–349, 2006.

[70] C. D. Murray and S. F. Dermott, Solar system dynamics. Cambridge university press, 2000.

[71] J. W. McMahon and D. J. Scheeres, "Dynamic limits on planar libration-orbit coupling around an oblate primary," Celestial Mechanics and Dynamical Astronomy, vol. 115, no. 4, pp. 365–396, 2013.

[72] P. Scheirich, P. Pravec, S. Jacobson, J. Ďurech, P. Kušnirák, K. Hornoch, S. Mottola, M. Mommert, S. Hellmich, D. Pray, et al., "The binary near-earth asteroid (175706) 1996 fg3—an observational constraint on its orbital evolution," Icarus, vol. 245, pp. 56–63, 2015.

[73] P. Pravec, C. Thomas, A. Rivkin, P. Scheirich, N. Moskovitz, M. Knight, C. Snodgrass, J. de León, J. Licandro, M. Popescu, et al., "Photometric observations of the binary near-earth asteroid (65803) didymos in 2015–2021 prior to dart impact," The Planetary Science Journal, vol. 3, no. 7, p. 175, 2022.

[74] P. Scheirich and P. Pravec, "Preimpact mutual orbit of the dart target binary asteroid (65803) didymos derived from observations of mutual events in 2003–2021," The Planetary Science Journal, vol. 3, no. 7, p. 163, 2022.

[75] A. F. Cheng, H. F. Agrusa, B. W. Barbee, A. J. Meyer, T. L. Farnham, S. D. Raducan, D. C. Richardson, E. Dotto, A. Zinzi, V. Della Corte, et al., "Momentum transfer from the dart mission kinetic impact on asteroid dimorphos," Nature, pp. 1–3, 2023.

[76] S. P. Naidu and J.-L. Margot, "Near-earth asteroid satellite spins under spin–orbit coupling," The Astronomical Journal, vol. 149, no. 2, p. 80, 2015.

[77] S. Naidu, J.-L. Margot, L. Benner, P. A. Taylor, M. C. Nolan, C. Magri, M. Brozovic, M. W. Busch, and J. Giorgini, "Radar observations and characterization of binary near-earth asteroid (35107) 1991 vh," in AAS/Division for Planetary Sciences Meeting Abstracts# 50, vol. 50, pp. 312–09, 2018.

[78] P. Pravec, P. Scheirica, D. Scheeres, J. McMahon, A. Meyer, P. Kušnirák, K. Hornoch, H. Kučáková, P. Fatka, R. McMillan, et al., "Photometric observations of the unrelaxed binary near-earth asteroid (35107) 1991 vh in support of the nasa janus space mission–detection of a spin-orbit interaction," in 7th IAA Planetary Defense Conference, p. 24, 2021.

[79] A. S. Rivkin, N. L. Chabot, A. M. Stickle, C. A. Thomas, D. C. Richardson, O. Barnouin, E. G. Fahnestock, C. M. Ernst, A. F. Cheng, S. Chesley, et al., "The double asteroid redirection test (dart): planetary defense investigations and requirements," The Planetary Science Journal, vol. 2, no. 5, p. 173, 2021.

[80] D. C. Richardson, H. F. Agrusa, B. Barbee, W. F. Bottke, A. F. Cheng, S. Eggl, F. Ferrari, M. Hirabayashi, Ö. Karatekin, J. McMahon, et al., "Predictions for the dynamical states of the didymos system before and after the planned dart impact," The Planetary Science Journal, vol. 3, no. 7, p. 157, 2022.

[81] S. Naidu, L. Benner, M. Brozovic, M. Nolan, S. Ostro, J. Margot, J. Giorgini, T. Hirabayashi, D. Scheeres, P. Pravec, et al., "Radar observations and a physical model of binary near-earth asteroid 65803 didymos, target of the dart mission," Icarus, vol. 348, p. 113777, 2020.

[82] S. P. Naidu, S. R. Chesley, D. Farnocchia, N. Moskovitz, P. Pravec, P. Scheirich, C. Thomas, and A. S. Rivkin, "Anticipating the dart impact: Orbit estimation of dimorphos using a simplified model," The Planetary Science Journal, vol. 3, no. 10, p. 234, 2022.

[83] R. T. Daly, C. M. Ernst, O. S. Barnouin, R. W. Gaskell, H. Nair, H. Agrusa, N. L. Chabot, A. F. Cheng, E. Dotto, E. M. Epifani, et al., "An updated shape model of dimorphos from dart data," The Planetary Science Journal, vol. 5, no. 1, p. 24, 2024.

[84] A. J. Meyer, H. F. Agrusa, D. C. Richardson, R. T. Daly, O. Fuentes-Muñoz, M. Hirabayashi, P. Michel, C. C. Merrill, R. Nakano, A. F. Cheng, et al., "The perturbed full two-body problem: Application to post-dart didymos," The Planetary Science Journal, vol. 4, no. 8, p. 141, 2023.

[85] S. P. Naidu, J. Margot, M. Busch, P. Taylor, M. Nolan, E. Howell, J. Giorgini, L. Benner, M. Brozovic, and C. Magri, "Dynamics of binary near-earth asteroid system (35107) 1991 vh," in AAS/Division of Dynamical Astronomy Meeting# 43, vol. 43, pp. 7–07, 2012.

[86] N. Borderies-Rappaport and P.-Y. Longaretti, "Test particle motion around an oblate planet," Icarus, vol. 107, no. 1, pp. 129–141, 1994.

[87] J. Bellerose and D. J. Scheeres, "Energy and stability in the full two body problem," Celestial Mechanics and Dynamical Astronomy, vol. 100, pp. 63–91, 2008.

[88] R. Moeckel, "Counting relative equilibrium configurations of the full two-body problem," Celestial Mechanics and Dynamical Astronomy, vol. 130, no. 2, p. 17, 2018.

[89] M. Jafari-Nadoushan, "Surfing in the phase space of spin–orbit coupling in binary asteroid systems," Monthly Notices of the Royal Astronomical Society, vol. 520, no. 3, pp. 3514–3528, 2023.

[90] H. F. Agrusa, I. Gkolias, K. Tsiganis, D. C. Richardson, A. J. Meyer, D. J. Scheeres, M. Ćuk, S. A. Jacobson, P. Michel, Ö. Karatekin, et al., "The excited spin state of dimorphos resulting from the dart impact," Icarus, vol. 370, p. 114624, 2021.

[91] M. Ćuk, S. A. Jacobson, and K. J. Walsh, "Barrel instability in binary asteroids," The Planetary Science Journal, vol. 2, no. 6, p. 231, 2021.

[92] A. C. Quillen, A. LaBarca, and Y. Chen, "Non-principal axis rotation in binary asteroid systems and how it weakens the byorp effect," Icarus, vol. 374, p. 114826, 2022.

[93] P. Tan, H.-s. Wang, and X.-y. Hou, "Attitude instability of the secondary in the synchronous binary asteroid," Icarus, vol. 390, p. 115289, 2023.

[94] N. Borderies and C. Yoder, "Phobos' gravity field and its influence on its orbit and physical librations," Astronomy and Astrophysics (ISSN 0004-6361), vol. 233, no. 1, July 1990, p. 235-251., vol. 233, pp. 235–251, 1990.

[95] R. Jacobson, "The orbits and masses of the martian satellites and the libration of phobos," The Astronomical Journal, vol. 139, no. 2, p. 668, 2010.

[96] A. J. Meyer, I. Gkolias, M. Gaitanas, H. F. Agrusa, D. J. Scheeres, K. Tsiganis, P. Pravec, L. A. Benner, F. Ferrari, and P. Michel, "Libration-induced orbit period variations following the dart impact," The planetary science journal, vol. 2, no. 6, p. 242, 2021.

[97] J. A. Burns, "Elementary derivation of the perturbation equations of celestial mechanics," American Journal of Physics, vol. 44, no. 10, pp. 944–949, 1976.

[98] J. A. Burns, "Erratum:"an elementary derivation of the perturbation equations of celestial mechanics"," American Journal of Physics, vol. 45, no. 12, pp. 1230–1230, 1977.

[99] A. J. Fleig, On the libration of a gravity gradient stabilized spacecraft in an eccentric orbit. National Aeronautics and Space Administration, 1970.

[100] A. C. Quillen, M. Lane, M. Nakajima, and E. Wright, "Excitation of tumbling in phobos and deimos," Icarus, vol. 340, p. 113641, 2020.

[101] J. A. Burns, V. Safronov, and T. Gold, "Asteroid nutation angles," Monthly Notices of the Royal Astronomical Society, vol. 165, no. 4, pp. 403–411, 1973.

[102] S. Breiter, A. Rożek, and D. Vokrouhlickỳ, "Stress field and spin axis relaxation for inelastic triaxial ellipsoids," Monthly Notices of the Royal Astronomical Society, vol. 427, no. 1, pp. 755–769, 2012.

[103] A. Molina, F. Moreno, and F. Martínez-López, "Energy dissipation by internal stresses in a free-rotating symmetric ellipsoid: Application to comet p/halley," Astronomy & Astrophysics, vol. 398, no. 3, pp. 809–817, 2003.

[104] S. V. Ershkov and D. Leshchenko, "On the dynamics of non-rigid asteroid rotation," Acta Astronautica, vol. 161, pp. 40–43, 2019.

[105] P. Pravec, A. W. Harris, P. Scheirich, P. Kušnirák, L. Šarounová, C. W. Hergenrother, S. Mottola, M. Hicks, G. Masi, Y. N. Krugly, et al., "Tumbling asteroids," Icarus, vol. 173, no. 1, pp. 108–131, 2005.

[106] M. S. Tiscareno, P. C. Thomas, and J. A. Burns, "The rotation of janus and epimetheus," Icarus, vol. 204, no. 1, pp. 254–261, 2009.

[107] M. Efroimsky, "Dissipation in a tidally perturbed body librating in longitude," Icarus, vol. 306, pp. 328–354, 2018.

[108] M. Hirabayashi, "Dynamics of a deforming planetary body," Icarus, vol. 389, p. 115258, 2023.

[109] H. Agrusa, R. Ballouz, A. J. Meyer, E. Tasev, G. Noiset, Ö. Karatekin, P. Michel, D. C. Richardson, and M. Hirabayashi, "Rotation-induced granular motion on the secondary component of binary asteroids: Application to the dart impact on dimorphos," Astronomy & Astrophysics, vol. 664, p. L3, 2022.

[110] A. W. Harris, E. G. Fahnestock, and P. Pravec, "On the shapes and spins of "rubble pile" asteroids," Icarus, vol. 199, no. 2, pp. 310–318, 2009.

[111] D. N. Brack and J. W. McMahon, "Modeling the coupled dynamics of an asteroid with surface boulder motion," Icarus, vol. 333, pp. 96–112, 2019.

[112] F. Mignard, "The evolution of the lunar orbit revisited. i," The Moon and the planets, vol. 20, no. 3, pp. 301–315, 1979.

[113] P. Hut, "Tidal evolution in close binary systems," Astronomy and Astrophysics, vol. 99, pp. 126–140, 1981.

[114] M. Efroimsky, "Tidal evolution of asteroidal binaries. ruled by viscosity. ignorant of rigidity," The Astronomical Journal, vol. 150, no. 4, p. 98, 2015.

[115] F. Nimmo and I. Matsuyama, "Tidal dissipation in rubble-pile asteroids," Icarus, vol. 321, pp. 715–721, 2019.

[116] S. Ferraz-Mello, "Tidal synchronization of close-in satellites and exoplanets. a rheophysical approach," Celestial Mechanics and Dynamical Astronomy, vol. 116, no. 2, pp. 109–140, 2013.

[117] R. Brasser, "Efficient tidal dissipation in deimos," Icarus, vol. 347, p. 113791, 2020.

[118] P. Scheirich, P. Pravec, P. Kušnirák, K. Hornoch, J. McMahon, D. Scheeres, D. Čapek, D. Pray, H. Kučáková, A. Galád, et al., "A satellite orbit drift in binary near-earth asteroids (66391) 1999 kw4 and (88710) 2001 sl9—indication of the byorp effect," Icarus, vol. 360, p. 114321, 2021.

[119] D. Vokrouhlickỳ, S. Breiter, D. Nesvornỳ, and W. Bottke, "Generalized yorp evolution: Onset of tumbling and new asymptotic states," Icarus, vol. 191, no. 2, pp. 636–650, 2007.

[120] J. Wisdom, S. J. Peale, and F. Mignard, "The chaotic rotation of hyperion," Icarus, vol. 58, no. 2, pp. 137–152, 1984.

[121] D. C. Heggie and F. A. Rasio, "The effect of encounters on the eccentricity of binaries in clusters," Monthly Notices of the Royal Astronomical Society, vol. 282, no. 3, pp. 1064–1084, 1996.

[122] B. F. Collins et al., "Levy flights of binary orbits due to impulsive encounters," The Astronomical Journal, vol. 136, no. 6, p. 2552, 2008.

[123] P. Farinella and B. Chauvineau, "On the evolution of binary earth-approaching asteriods," Astronomy and Astrophysics, vol. 279, pp. 251–259, 1993.

[124] B. Chauvineua, P. Farinella, and A. Harris, "The evolution of earth-approaching binary asteroids: A monte carlo dynamical model," Icarus, vol. 115, no. 1, pp. 36–46, 1995.

[125] J. Fang and J.-L. Margot, "Binary asteroid encounters with terrestrial planets: Timescales and effects," The Astronomical Journal, vol. 143, no. 1, p. 25, 2011.

[126] A. J. Meyer and D. J. Scheeres, "The effect of planetary flybys on singly synchronous binary asteroids," Icarus, vol. 367, p. 114554, 2021.

[127] O. Fuentes-Muñoz, A. J. Meyer, and D. J. Scheeres, "Semi-analytical near-earth objects propagation: the orbit history of (35107) 1991 vh and (175706) 1996 fg3," The Planetary Science Journal, vol. 3, no. 11, p. 257, 2022.

[128] A. J. Meyer, D. J. Scheeres, H. F. Agrusa, G. Noiset, J. McMahon, Ö. Karatekin, M. Hirabayashi, and R. Nakano, "Energy dissipation in synchronous binary asteroids," Icarus, vol. 391, p. 115323, 2023.

[129] P. Scheirich, P. Pravec, A. J. Meyer, H. F. Agrusa, D. C. Richardson, S. R. Chesley, S. P. Naidu, C. Thomas, and N. A. Moskovitz, "Dimorphos orbit determination from mutual events photometry," The Planetary Science Journal, vol. 5, no. 1, p. 17, 2024.

[130] A. F. Cheng, H. F. Agrusa, B. W. Barbee, A. J. Meyer, T. L. Farnham, S. D. Raducan, D. C. Richardson, E. Dotto, A. Zinzi, V. Della Corte, et al., "Momentum transfer from the dart mission kinetic impact on asteroid dimorphos," Nature, vol. 616, no. 7957, pp. 457–460, 2023.

[131] R. Nakano, M. Hirabayashi, H. F. Agrusa, F. Ferrari, A. J. Meyer, P. Michel, S. D. Raducan, P. Sánchez, and Y. Zhang, "Nasa's double asteroid redirection test (dart): Mutual orbital period change due to reshaping in the near-earth binary asteroid system (65803) didymos," The Planetary Science Journal, vol. 3, no. 7, p. 148, 2022.

[132] S. D. Raducan and M. Jutzi, “Global-scale reshaping and resurfacing of asteroids by small-scale impacts, with applications to the dart and hera missions,” The planetary science journal, vol. 3, no. 6, p. 128, 2022.

[133] A. Graykowski, R. A. Lambert, F. Marchis, D. Cazeneuve, P. A. Dalba, T. M. Esposito, D. O. Peluso, L. A. Sgro, G. Blaclard, A. Borot, et al., “Light curves and colors of the ejecta from dimorphos after the dart impact,” Nature, pp. 1–3, 2023.

[134] S. P. Naidu, S. R. Chesley, N. Moskovitz, C. Thomas, A. J. Meyer, P. Pravec, P. Scheirich, D. Farnocchia, D. J. Scheeres, and M. Brozovic, “Orbital and physical characterization of asteroid dimorphos following the dart impact,” The planetary science journal, vol. 5, no. 3, p. 74, 2024.

[135] S. Raducan, M. Jutzi, A. Cheng, Y. Zhang, O. Barnouin, G. Collins, R. Daly, T. Davison, C. Ernst, T. Farnham, et al., “Physical properties of asteroid dimorphos as derived from the dart impact,” Nature Astronomy, pp. 1–11, 2024.

[136] P. Pravec, A. J. Meyer, P. Scheirich, D. J. Scheeres, C. Benson, and H. F. Agrusa, “Rotational lightcurves of dimorphos and constraints on its post-dart impact spin state,” Icarus, vol. In Revision, 2024.

[137] J. W. Pratt, J. D. Gibbons, J. W. Pratt, and J. D. Gibbons, “Kolmogorov-smirnov two-sample tests,” Concepts of nonparametric theory, pp. 318–344, 1981.

[138] G. Marsaglia, W. W. Tsang, and J. Wang, “Evaluating kolmogorov’s distribution,” Journal of statistical software, vol. 8, pp. 1–4, 2003.

[139] J. Fang, J.-L. Margot, M. Brozovic, M. C. Nolan, L. A. Benner, and P. A. Taylor, “Orbits of near-earth asteroid triples 2001 sn263 and 1994 cc: properties, origin, and evolution,” The Astronomical Journal, vol. 141, no. 5, p. 154, 2011.

[140] H. F. Levison, S. Marchi, K. S. Noll, J. R. Spencer, T. S. Statler, J. F. Bell III, E. B. Bierhaus, R. Binzel, W. F. Bottke, D. Britt, et al., “A contact binary satellite of the asteroid (152830) dinkinesh,” Nature, vol. 629, no. 8014, pp. 1015–1020, 2024.

[141] A. Meyer, D. Scheeres, S. Naidu, L. Benner, P. Pravec, and P. Scheirich, “Modeling fully coupled dynamics of janus binary asteroid mission targets,” AAS/Division of Dynamical Astronomy Meeting, vol. 53, no. 5, pp. 405–06, 2021.

[142] S. Renner and B. Sicardy, “Use of the geometric elements in numerical simulations,” Celestial Mechanics and Dynamical Astronomy, vol. 94, pp. 237–248, 2006.

[143] O. Fuentes-Muñoz, A. J. Meyer, and D. J. Scheeres, “Semi-analytical near-earth objects propagation: the orbit history of (35107) 1991 vh and (175706) 1996 fg3,” The Planetary Science Journal, vol. 3, no. 11, p. 257, 2022.

[144] P. Pravec, M. Wolf, and L. Šarounová, “Occultation/eclipse events in binary asteroid 1991 vh,” Icarus, vol. 133, no. 1, pp. 79–88, 1998.

[145] N. L. Chabot, A. S. Rivkin, A. F. Cheng, O. S. Barnouin, E. G. Fahnestock, D. C. Richardson, A. M. Stickle, C. A. Thomas, C. M. Ernst, R. T. Daly, et al., “Achievement of the planetary defense investigations of the double asteroid redirection test (dart) mission,” The Planetary Science Journal, vol. 5, no. 2, p. 49, 2024.

[146] P. Pravec and A. W. Harris, “Binary asteroid population: 1. angular momentum content,” Icarus, vol. 190, no. 1, pp. 250–259, 2007.

[147] L. Dell’Elce, N. Baresi, S. Naidu, L. Benner, and D. Scheeres, “Numerical investigation of the dynamical environment of 65803 didymos,” Advances in Space Research, vol. 59, no. 5, pp. 1304–1320, 2017.

# Appendix A

## Observation Fitting Algorithm

One of the main tools developed in this thesis is an algorithm to match numerical simulations to observations. This is important to ensure accurate representations of real-world systems. This algorithm was used to calculate the momentum change in Dimorphos as a result of the DART impact, and can also be used to estimate the mass of a binary asteroid, since a traditional Keplerian approach will give an erroneous estimate.

From lightcurve and radar data, the most accurate measurement of NEA binaries is the orbital period. Thus, this is the parameter we should match. We will call this parameter $T_{obs}$. An observation of the semimajor axis is used as the initial separation distance.

(1) **Velocity.** For a physically circular orbit, we set the velocity equal to $v = R\frac{2\pi}{T_{obs}}$ where $R$ is the separation distance. To add eccentricity to the system, we can add a scalar multiplier to this, and tune it until the desired observable eccentricity is achieved.

(2) **Secondary Rotation.** We set the rotation period of the secondary equal to $T_{obs}$ to ensure the system is singly synchronous. If there is eccentricity in the system, we can iterate this value to tune the libration within the system. The minimum libration amplitude in this case is the forced libration.

(3) **Density.** Next we iterate the density $\rho$ through a secant search algorithm while minimizing the error in orbit period. We calculate the stroboscopic orbit period, which we call $T_{sim}$.

The iteration is defined as

$$\rho_n = \rho_{n-1} - T(\rho_{n-1})\frac{\rho_{n-1} - \rho_{n-2}}{T(\rho_{n-1}) - T(\rho_{n-2})} \tag{A.1}$$

where the function $T(\rho) = T_{obs} - T_{sim}(\rho)$. We can assume both bodies have equal densities, or fix one body's density and calculate the density of the other.

(4) **Change in Velocity**. To model the DART impact, we perform another iteration on tangential velocity to match the new orbit period. We now have a new value of $T_{obs}$, which we use in the algorithm,

$$v_n = v_{n-1} - T(v_{n-1})\frac{v_{n-1} - v_{n-2}}{T(v_{n-1}) - T(v_{n-2})}. \tag{A.2}$$

(5) **Orbit Precession**. We can also match the precession of the orbit. If the shape of the primary and secondary are fixed, we can iterate over the secondary's spin rate. This iteration takes the form

$$\dot{\phi}_n = \dot{\phi}_{n-1} - T(\dot{\phi}_{n-1})\frac{\dot{\phi}_{n-1} - \dot{\phi}_{n-2}}{T(\dot{\phi}_{n-1}) - T(\dot{\phi}_{n-2})}, \tag{A.3}$$

where now our error function is $T(\dot{\phi}) = \dot{\varpi}_{obs} - \dot{\varpi}_{sim}(\dot{\phi})$, where $\dot{\varpi}$ is the apsidal precession of the orbit.

Using all of these steps, we can accurately match our numerical simulations to the observations of the real system. This allows us to accurately model any system, provided we have information about the orbit period, separation distance, and size and shape information about the asteroids.